



UNIVERSITÉ DE REIMS CHAMPAGNE-ARDENNE
ÉCOLE DOCTORALE SCIENCES FONDAMENTALES SANTÉ

THÈSE EN CO-TUTELLE

Pour obtenir le grade de

DOCTEUR DE L'UNIVERSITÉ D'ÉTAT DE MOSCOU LOMONOSSOV

Discipline : CHIMIE

Et

DOCTEUR DE L'UNIVERSITÉ DE REIMS CHAMPAGNE-ARDENNE

Discipline : CHIMIE

Spécialité : Pharmacie - SFS

Présentée et soutenue publiquement par

Pavel LINKOV

Le 19 décembre 2018

SYNTHÈSE ET CARACTÉRISATION PHYSICO-CHIMIQUE ET OPTIQUE DE NANOCRISTAUX FLUORESCENTS POUR DES APPLICATIONS BIOMÉDICALES

Thèse dirigée par **M. Lev SIDOROV, Professeur, l'Université d'Etat de Moscou**

Et par **M. Igor NABIEV, Professeur, et Janos SAPI, Professeur, Université de Reims Champagne-Ardenne**

JURY

M. Fabrice FLEURY,	Professeur,	Université de Nantes,	Président
M. Igor NABIEV,	Professeur,	Université de Reims Champagne - Ardenne,	Directeur de thèse
M. Janos SAPI,	Professeur,	Université de Reims Champagne - Ardenne,	Co-Directeur de thèse
M. Lev SIDOROV,	Professeur,	l'Université d'Etat de Moscou	Co-Directeur de thèse
M. Vitaliy MARKOV,	Professeur,	l'Université d'Etat de Moscou	Rapporteur
M. Pavel SAMOKHVALOV,	Docteur,	Université Nationale de Recherche Nucléaire	Examineur

Acknowledgments

I would first like to thank my supervisors, Prof. Igor NABIEV from The University of Reims Champagne-Ardenne (URCA) and Prof. Lev SIDOROV from the Moscow State University (MSU), for all their support over the course of my PhD project, as well as my co-supervisor, Prof. Janos SAPI, for invaluable help and discussions regarding the organic-chemistry part of this research and for his ongoing support throughout my work in URCA.

Special thanks to Prof. Jacques H.M. COHEN and my supervisors Prof. Igor NABIEV and Prof. Janos SAPI, for the organization of the joint international postgraduate study.

My sincere thanks also go to my colleagues in the Laboratory of Nano-Bioengineering of the Moscow Engineering Physics Institute (MEPhI), especially Dr. Pavel SAMOKHVALOV, who has been my research director during all my research work over the past six years.

I thank Dr. Marie LARONZE-COCHARD, without whose careful and patient guidance on the organic synthesis this project would have come to naught.

I would like to thank Prof. Alyona SUKHANOVA for her assistance in the implementation of biological aspects of the project in URCA, as well as specially thank Dr. Maria BARYSHNIKOVA for the integrated biological evaluation of samples in the Laboratory of Nano-Bioengineering of MEPhI and Blokhin Russian Cancer Research Center.

Also special thanks to Prof. Alexey GORYUNKOV, the head of the Laboratory of Thermochemistry of MSU, for his help in the implementation of my PhD project.

I also thank Dr. Bertrand BRASSART for biological evaluations and interpretation of data on novel organic molecules and Dr. Victor KRIVENKOV for carrying out the two-photon characterization of samples.

Many thanks to all researchers at the Faculty of Pharmacy of URCA, Institute of Molecular Chemistry of Reims, Chemical Faculty of MSU, and Laboratory of Nano-Bioengineering of MEPhI who have helped me along the way.

My thanks to Vladimir USHAKOV for his valuable advice proofreading of my thesis to correct all my English mistakes.

Also many thanks to all the staff of the Doctoral School of the University of Reims Champagne-Ardenne, in particular, Nathalie LE BARCH, the administrative director of the Doctoral School, for all their help over the past four years.

I would like to thank my family for understanding and tremendous moral support.

I would also like to acknowledge the financial support of the Région Champagne-Ardenne, the Laboratory of Nano-Bioengineering of MEPhI and the Ministry of Education and Science of the Russian Federation, State Contract no. 16.1034.2017/ПЧ.

Résumé

Le développement des nanoparticules fluorescentes, appelées quantum dots (QDs) est devenu l'un des domaines les plus prometteurs de la science des matériaux, influençant fortement la société moderne en raison de leurs nombreuses applications allant de la production d'énergie au diagnostic de maladies et à l'administration de médicaments.

Ces dernières années, beaucoup d'efforts ont été consacrés à la résolution des problèmes se rapportant aux technologies liées aux QDs, telles que la réduction de leur taille, la maximisation du rendement quantique et la stabilité colloïdale dans les solutions biologiques.

Dans cette étude une procédure avancée de synthèse contrôlable de QDs a été mise au point, comprenant (1) la synthèse de noyaux ultra-minces de CdSe, (2) la purification de noyau haute performance par la chromatographie de perméation de gel et (3) le revêtement central avec une coquille épitaxiale en ZnS d'une épaisseur déterminée.

Cette approche a permis d'obtenir des QDs d'une taille de 1,5 nm possédant un rendement quantique supérieur à 70% et également d'améliorer considérablement leurs propriétés colloïdales.

Les QDs développés ont été utilisés : (1) pour concevoir des conjugués de QDs compacts avec les nouveaux dérivés d'acridine synthétisés dans cette étude, ayant une affinité élevée pour le G-quadruplex des télomères; (2) pour démontrer l'efficacité fonctionnelle des conjugués lors des essais avec des acides nucléiques et des cellules, ainsi que leur effet inhibiteur sur la télomérase, une cible importante du traitement du cancer; et aussi (3) pour accélérer la pénétration transmembranaire des QDs ultracompacts dans les cellules cancéreuses tout en conservant une brillance élevée et une stabilité colloïdale.

Les résultats de cette étude ouvrent la voie à l'ingénierie de nanosondes multifonctionnelles possédant une meilleure pénétration intracellulaire, une plus forte brillance et une stabilité colloïdale plus importante, permettant leur utilisation dans une multitude d'applications allant de l'administration de médicaments au diagnostic.

Mots-clefs: *nanocristaux photoluminescents, « quantum dots », acridine, G-quadruplex, bioconjugaison, nanoprobés multifonctionnelles.*

The synthesis and physico-chemical and optical characterisation of fluorescent nanocrystals for biomedical applications.

Abstract

Development of the fluorescent nanoparticles referred to as quantum dots (QDs) has become one of the most promising areas of materials sciences, strongly influencing modern society due to their numerous applications ranging from disease diagnostics to drug delivery. In recent years, much effort was concentrated on solving problems of QD-related technologies, such as minimizing their size and maximizing the quantum yield and colloidal stability in biological solutions.

In this study, an advanced procedure of controllable synthesis of QDs, which includes

- (1) the synthesis of ultrasmall CdSe cores,
- (2) high-performance core purification by gel permeation chromatography, and
- (3) core coating with an epitaxial ZnS shell of a specified thickness has been developed.

This approach has allowed obtaining 1.5-nm-core QDs with a quantum yield exceeding 70% and significantly improved their colloidal properties.

The QDs developed have been used:

(1) to engineer compact conjugates of QDs with the novel acridine derivatives synthesized in this study, which have a high affinity for the telomere G-quadruplex;

(2) to demonstrate the functional effectiveness of the conjugate in tests with nucleic acids and cells, as well as their inhibitory effect on telomerase, an important target of anticancer therapy; and

(3) to accelerate transmembrane penetration of ultrasmall QDs into cancer cells while retaining a high brightness and colloidal stability.

The results of this study pave the way to the engineering of multifunctional nanoprobes with improved intracellular penetration, brightness, and colloidal stability, which will find use in a plethora of drug delivery and diagnostic applications.

Keywords: *photoluminescent nanocrystals, quantum dots, acridine, G-quadruplex, bioconjugation, multifunctional nanoprobes.*

Contenu en français

Remerciements	1
Résumé en français	2
Résumé en anglais	3
Contenu en français	4
Contenu en anglais	7
Liste des figures	10
Liste des tableaux	13
Liste des annexes	14
Liste des abréviations	15
Résumé substantiel en français	17
Conclusions et perspectives en français	51
Introduction	56
Chapitre 1. Revue de la littérature	61
1.1. Sondes photoluminescentes pour l'imagerie et l'administration de médicaments	61
1.2. <i>Quantum dots</i> (« boîtes quantiques ») photoluminescents	63
1.2.1. Propriétés physico-chimiques des <i>Quantum dots</i> photoluminescents	64
1.2.2. Synthèse de <i>Quantum dots</i> à base de CdSe	70
1.2.3. Synthèse de <i>Quantum dots</i> cœur/coquille	72
1.2.4. Modification de la surface des points quantiques	79
1.2.5. Bioconjugaison à la surface des <i>Quantum dots</i>	81
1.2.6. Cytotoxicité par <i>Quantum dots</i>	84
1.3. Ligands de l'ADN G-quadruplexe à base d'hétérocycles polyaromatiques azotés	86
1.3.1. Télomères de l'ADN G-quadruplex	86
1.3.2. Étude des interactions des ligands avec le G-quadruplex	88
1.3.3. Ligands G-Quadruplex comme inhibiteur de la télomérase	88
Chapitre 2. Matériels et méthodes	96
2.1. Préparation des matériaux	96
2.2. Caractérisation des matériaux	96
2.2.1. Microscopie électronique à transmission (TEM)	96
2.2.2. Spectroscopie optique en régime permanent	97
2.2.3. Spectroscopie à deux photons	100
2.2.4. Chromatographie d'exclusion stérique, chromatographie en couche mince et chromatographie flash	101
2.2.5. Spectroscopie de résonance magnétique nucléaire (^1H NMR)	101

2.2.6.	Spectrométrie de masse	102
2.2.7.	Diffusion dynamique de la lumière (DLS) et mesures du potentiel zeta	102
2.2.8.	Essai de fusion par transfert d'énergie de résonance en fluorescence (FRET)	102
2.2.9.	Test de TRAP (Protocole d'amplification télomérique répétée)	103
2.2.10.	Essai de viabilité cellulaire (essai colorimétrique de MTT)	103
2.2.11.	Microscopie confocale	104
2.3.	Synthèse des <i>Quantum dots</i> (boîtes quantiques) de type CdSe	104
2.4.	Synthèse de <i>Quantum dots</i> cœur/coquille	106
2.5.	Préparation de <i>Quantum dots</i> hydrosolubles	108
2.6.	Synthèse de dérivés d'acridine 4,5,9-trisubstituée	110
2.6.1.	Synthèse de la 4,5-bis(bromométhyl)acridine (19)	110
2.6.2.	Synthèse de la 4,5-(dihydroxyméthyl)acridine (20)	111
2.6.3.	Synthèse de l'acide 9-oxo-9,10-dihydroacridine-4,5-dicarboxylique (21)	111
2.6.4.	Synthèse du 4-aminobutylcarbamate de tert-butyle (27)	112
2.6.5.	Synthèse du dichlorure de l'acide 9-chloroacridine-4,5-dicarboxylique (23)	113
2.6.6.	Synthèse d'acridines 9-substituées avec des anilines substituées(24a-c)	114
2.6.7.	Synthèse de dérivés d'acridines 4,5,9-trisubstituées (25a-c)	117
2.7.	Assemblage des nanosondes multifonctionnelles	120
2.8.	Absorption cellulaire des QD de type CdSe/ZnS	120
Chapitre 3. Synthèse de <i>Quantum dots</i> de haute qualité à base de CdSe		122
3.1.	Synthèse de nanocristaux de CdSe colloïdale par injection à chaud	122
3.1.1.	Développement et optimisation de la méthode de synthèse des QDs colloïdales	122
3.1.2.	Synthèse de QDs de type CdSe ultrapetits	132
3.1.3.	Développement du modèle de croissance des QDs à base de CdSe	137
3.2.	Synthèse de QDs cœur/coquille à base de CdSe	141
3.2.1.	Synthèse de QDs cœur/coquille à base de CdSe/ZnS	141
3.2.2.	Synthèse de QDs à multicoquilles	147
3.3.	Solubilisation de très petits QDs dans l'eau	155
	Résumé	157
Chapitre 4. Synthèse et caractérisation fonctionnelle, structurale et biologique des dérivés 4,5,9-trisubstituée de acridine		160

4.1. Synthèse de dérivés 4,5,9-trisubstitués de l'acridine	160
4.2. Évaluation biochimique des dérivés de l'acridine 4,5,9-trisubstituée	165
Résumé	169
Chapitre 5. Ingénierie, propriétés et application des nanosondes PL	170
5.1. Synthèse des nanosondes multifonctionnelles	170
5.2. Propriétés optiques des nanosondes	173
5.3. Toxicité et absorption cellulaire des nanosondes et de leurs composants	178
5.3.1. Évaluation de la cytotoxicité par essai de viabilité cellulaire	178
5.3.2. Analyse in vitro de l'absorption de très petits QD de type CdSe/ZnS	179
Résumé	180
Conclusions et perspectives	182
Bibliographie	186
Annexes	209
Liste de publication	212

Contents	
Acknowledgments	1
Résumé	2
Abstract	3
Contenu en français	4
Contents	7
List of Figures	10
List of Tables	13
List of Annexes	14
List of Abbreviations	15
Résumé substantiel en français	17
Conclusions et perspectives en français	51
Introduction	56
Chapter 1. Review of the literature	61
1.1. Photoluminescent probes for imaging and drug delivery	61
1.2. Photoluminescent quantum dots	63
1.2.1. Physico-chemical properties of photoluminescent quantum dots	64
1.2.2. Synthesis of CdSe-based quantum dots.....	70
1.2.3. Synthesis of core/shell quantum dots	72
1.2.4. Quantum dot surface modification	79
1.2.5. Quantum dot bioconjugation	81
1.2.6. Quantum dot cytotoxicity	84
1.3. G-quadruplex DNA ligands, based on nitrogen-containing polyaromatic heterocycles	86
1.3.1. G-quadruplex DNA telomeres.....	86
1.3.2. Study of ligand interactions with the G-quadruplex.....	88
1.3.3. G-Quadruplex ligands as telomerase inhibitor	88

Chapter 2. Materials and methods	96
2.1. Material preparation.....	96
2.2. Material characterization	96
2.2.1. Transmission electron microscopy (TEM).....	96
2.2.2. Steady state optical spectroscopy	97
2.2.3. Two-photon spectroscopy	100
2.2.4. Thin-layer, flash and gel-penetration chromatography.	101
2.2.5. Nuclear magnetic resonance (¹ H NMR) spectroscopy	101
2.2.6. Mass spectrometry	102
2.2.7. Dynamic light scattering (DLS) and zeta-potential measurements.....	102
2.2.8. Fluorescence resonance energy transfer (FRET) melting assay.....	102
2.2.9. Telomeric repeat amplification protocol (TRAP) assay.....	103
2.2.10. Cell viability assay (colorimetric MTT assay)	103
2.2.11. Confocal microscopy	104
2.3. Synthesis of CdSe quantum dots	104
2.4. Synthesis of core/shell quantum dots.....	106
2.5. Preparation of water-soluble quantum dots	108
2.6. Synthesis of 4,5,9-trisubstituted acridine derivatives	110
2.6.1. Synthesis of 4,5-bis(bromomethyl)acridine (19).....	110
2.6.2. Synthesis of acridine-4,5-(dihydroxymethyl)acridine (20).....	111
2.6.3. Synthesis of 9-oxo-9,10-dihydroacridine-4,5-dicarboxylic acid (21).....	111
2.6.4. Synthesis of <i>tert</i> -butyl 4-aminobutylcarbamate (27).....	112
2.6.5. Synthesis of 9-chloroacridine-4,5-dicarbonyl dichloride (23)	113
2.6.6. Synthesis of 9-substituted acridines with substituted anilines (24a-c).....	114
2.6.7. Synthesis of 4,5,9-trisubstituted acridines derivatives (25a-c).....	117
2.7. Assembling of multifunctional nanoprobe.....	120
2.8. Cellular uptake of CdSe/ZnS QDs.....	120
Chapter 3. High quality CdSe-based quantum dots	122

3.1. Hot-injection synthesis of colloidal CdSe nanocrystals.	122
3.1.1. Development and optimisation of hot injection method for QD synthesis.	122
3.1.2. Synthesis of ultrasmall CdSe QDs.....	132
3.1.3. Development of CdSe nanocrystals growth model	137
3.2. Synthesis of CdSe-based core/shell QDs.....	141
3.2.1. Synthesis of CdSe/ZnS core/shell QDs	141
3.2.2. Synthesis of multishell QDs	147
3.3. Water-solubilization of ultrasmall QDs	155
Summary.....	157
Chapter 4. Synthesis and structural and biological functional characterization of 4,5,9-trisubstituted acridine derivatives	160
4.1. Synthesis of 4,5,9-trisubstituted acridine derivatives	160
4.2. Biochemical evaluation of 4,5,9-trisubstituted acridine derivatives.....	165
Summary.....	169
Chapter 5. Engineering, properties and application of the PL nanoprobe. 170	
5.1. Engineering of multifunctional nanoprobe	170
5.2. Optical properties of nanoprobe	173
5.3. Toxicity and cellular uptake of nanoprobe and components.....	178
5.3.1. Assessment of cytotoxicity by cell viability assay	178
5.3.2. Uptake analysis of ultrasmall CdSe/ZnS QDs <i>in vitro</i>	179
Summary.....	180
Conclusions and prospects	182
Bibliography	186
Annexes.....	209
Publication list	212

List of Figures

Figure 1: Schematic representation of the quantum confinement effect on the energy level structure of a semiconductor. The lower panel shows colloidal suspensions of CdSe NCs of different sizes under UV excitation.	65
Figure 2: LaMer curve describing three stages of metal nanocrystal formation in a solution. Stage I, atom production; stage II, nucleation; and stage III, seed formation and growth	67
Figure 3: The growth rate as a function of the nanocrystal radius	68
Figure 4: Crystal growth processes and key factors determining the crystal shape	69
Figure 5: The mechanism of the chemical reaction used to obtain CdSe NCs	72
Figure 6: Changes in the typical (a) absorbance and (b) photoluminescence spectra of CdS/ZnS QDs in the course of shell formation	75
Figure 7: Small molecule ligands with affinity towards the surface of QDs.	80
Figure 8: Strategies for bioconjugation of QDs via (A) EDC/NHS coupling, (B) the thiol–maleimide reaction, (C) streptavidin–biotin binding, and (D) interaction between Ni-NTA and histidine	83
Figure 9: Telomeres in an eukaryote cell.	86
Figure 10: (A) The arrangement of guanine bases in the G-quartet, shown together with a centrally placed metal ion. (B) The possible conformations of the intramolecular G-quadruplex formed by human telomeric DNA	87
Figure 11: Examples of the binding modes of a small molecule with a G-quadruplex	89
Figure 12: Structures of quindoline derivatives.	90
Figure 13: Structures of porphyrin derivatives.....	91
Figure 14: Structures of macrocyclic alkaloids and their derivatives.	91
Figure 15: Structures of acridine and acridone derivatives.	93
Figure 16: Synthesis route to benzylamino-substituted acridines.	94
Figure 17: (a) The three lowest electron (E^e) and hole (E^h) energy levels in a semiconductor QD. (b) Assignment of the transitions in the absorption spectrum of colloidal QDs.	98
Figure 18: Experimental dependence of the integrated PL intensity from the optical density of the QD solution.	100
Figure 19: Reaction apparatus of CdSe core and core/shell QD synthesis.	106
Figure 20: Schematic of chemical synthesis.	106
Figure 21: Scheme of gel filtration of CdSe cored using Bio-Beads SX-1 (Bio-RAD) as a stationary phase.	107
Figure 22: Absorption spectra of CdSe QDs in different solvents.....	124

Figure 23: Absorption spectra of CdSe QDs obtained from various precursors.	126
Figure 24: Photoluminescence spectra of CdSe QDs obtained from various precursors.	127
Figure 25: (a) Absorption spectra after 5 min of QD growth and (b) changes in the average size of CdSe QDs obtained at different injection temperatures.	129
Figure 26: Photoluminescence of the solutions of CdSe QDs with the size varying from 1.8 to 5 nm.	130
Figure 27: Absorption and PL spectra of CdSe core QDs.	131
Figure 28: (a) A STEM image of CdSe core QDs. (b) Histogram of size distribution.	132
Figure 29: Evolution of the absorption spectra during CdSe QD growth.	134
Figure 30: The PL spectra of the CdSe/ZnS QD synthesis reaction mixture, with the shell grown in situ in the presence of a residual amount of the cadmium precursor.	134
Figure 31: The absorption (Abs) and photoluminescence (PL) spectra of CdSe quantum dots prepared using different procedures.	136
Figure 32: Key elements of the QD growth model: (a) spherical model of a QDs; (b) TEM images of synthesized CdSe QDs; (c) geometrical model of a QD, a hexagonal bipyramid; (d) step-by-step growth of a CdSe QD, starting from the monomer; (e) model layer-by-layer shell growth.	139
Figure 33: (a) Evolution of the extinction spectra at different stages of wurtzite-CdSe QD growth. (b) Comparison of the exciton absorption maximum wavelengths calculated using the QD growth model and the experimental data for different stages of growth.	141
Figure 34: A STEM image of the CdSe/ZnS QD sample in which shell growth was performed at 200°C.	144
Figure 35: Absorption and fluorescence spectra of CdSe/ZnS QDs based on the cores purified using different procedures.	145
Figure 36: (a) An HRTEM image of CdSe/ZnS QDs; the inset shows the histogram of the size distribution based on the analysis of HRTEM images; (b) a STEM image of CdSe/ZnS QDs.	146
Figure 37: EDS spectrum of a CdSe/ZnS QDs.	147
Figure 38: Schematic structure and energy-level diagrams of different core/shell QDs.	148
Figure 39: (a) The energy-level diagram of the novel core/multishell CdSe/ZnS/CdS/ZnS quantum dot; (b) the schematic structure of the core/multishell colloidal QD.	149
Figure 40: The (a) absorption and (b) emission spectra of QDs with different shells. (c) A DF-STEM image of different shell structure QDs.	150
Figure 41: Evolution of the PL QY during shell growth of the three samples studied.	151

Figure 42: (a) Absorption and PL spectra of CdSe/ZnS/CdS/ZnS QD-540, QD-570, and QD-610. (b) Evolution of PL QY during shell growth.....	153
Figure 43: The (a) absorption and (b) PL spectra of three CdSe/MS lots with different reactor loadings (150 and 600 mmol) fabricated from different lots of CdSe cores and different lots of shell precursors.	154
Figure 44: Size distribution of PEG-stabilized CdSe/ZnS QDs in a phosphate buffer after GPC from the excess of the PEG derivatives.	156
Figure 45: Zeta-potential distribution of PEG-QDs	157
Figure 46: Proposed structure of the acridine ligand.....	161
Figure 47: Synthetic pathway of 4,5,9-trisubstituted acridine derivatives.....	162
Figure 48: Gel retardation analysis of the binding of the potential inhibitors with the telomere nucleotide sequence.....	168
Figure 49: Elution chromatogram of acridine ligand–QD c and their components. A GPC chromatographic column with Sephadex G100 as a stationary phase.	171
Figure 50: Size distribution of the original CdSe/ZnS QDs and AL–QD complexes in phosphate buffer	172
Figure 51: Zeta-potential distribution of AL–QD complexes.....	172
Figure 52: The (a) absorbance and (b) photoluminescence spectra of the acridine ligand and QDs with different shell structures and numbers of shell monolayers.....	174
Figure 53: Dependence of CdSe/ZnS/CdS/ZnS QDs fluorescence quenching on the amounts of excess AL.	175
Figure 54: Changes in quenching of PL of different QDs with an increase in the amount of excess AL.	176
Figure 55: Schematic illustration of the photoinduced electron transfer mechanism from a core/shell QD to the acridine ligand.....	177
Figure 56: Cell viability in the presence of the conjugate and its components.....	179
Figure 57: Confocal fluorescence microscopy images.....	180

List of Tables

Table 1: Characteristics of some bulk semiconductor materials.	73
Table 2: Optical properties of the reference dyes.....	100
Table 3: Properties of solvents used in the synthesis of QDs.....	124
Table 4: Properties of cadmium salt precursors.	125
Table 5: Atomic composition and basic properties of CdSe QDs at different stages of growth.....	140
Table 6: Main optical properties of CdSe/ZnS QDs with cores purified using different procedures.....	145
Table 7: The main optical characteristics of the different core/shell structure QD samples....	152
Table 8: Telomeric G-quadruplex stabilization measured by FRET and TRAP inhibition.	167
Table 9: Human monocyte viability	179

List of Annexes

Annex 1: Mass spectrum of 9-chloroacridine-4,5-dicarbonyl dichloride (23).....	209
Annex 2: N4,N5-bis(<i>tert</i> -butyl-4-aminobutylcarbamate)-9-(3,4-difluorophenylamino)acridine-4,5-dicarboxamide (24a).	210
Annex 3: N4,N5-bis(<i>tert</i> -butyl-4-aminobutylcarbamate)-9-(4-(dimethylamino)phenylamino)acridine-4,5-dicarboxamide (24c).	210
Annex 4: N4,N5-bis(4-aminobutyl)-9-(3,4-difluorophenylamino)acridine-4,5-dicarboxamide (25a).	211
Annex 5: N4,N5-bis(4-aminobutyl)-9-(4-fluorophenylamino)acridine-4,5-dicarboxamide (25b).....	211

List of Abbreviations

AL	Acridine ligand
Cys	DL-cysteine
DLS	Dynamic light scattering
ED	Electron diffraction
EDC	<i>N</i> -Ethyl- <i>N'</i> -(3-dimethylaminopropyl) carbodiimide
EDS	Energy dispersive X-ray spectroscopy
FRET	Fluorescence resonance energy transfer
FWHM	The full width at half maximum
GPC	Gel-penetration chromatography
HDA	1-Hexadecylamine
HOMO	Highest molecular orbital occupied
HRMS	High resolution mass spectrometry
HRTEM	High resolution transmission electronic microscopy
IR	Infrared region
LUMO	Lowest unoccupied molecular orbital
MES	2-(<i>N</i> -morpholino)ethanesulfonic acid buffer
ML	Monolayer
MPA	3-Mercaptopropionic acid
MS	Multishell
NHS	<i>N</i> -Hydroxysuccinimide
Ni-NTA	Nickel nitrilotriacetic acid
OA	Oleic acid
ODE	1-Octadecene
OLE	Oleylamine
PEG	Polyethylene glycol
PET	Photo-induced electron transfer
PL	Photoluminescence (fluorescence)
QD	Quantum dot
QY	Quantum yield
SILAR	Successive ion layer adsorption and reaction
SMCC	<i>N</i> -hydroxysuccinimideester
STEM	Scanning transmission electron microscopy

TEM	Transmission electron microscopy
TEGDME	Triethylene glycol dimethyl ether
TLC	Thin layer chromatography
TOA	Tri-n-octylamine
TOP	Tri-n-octylphosphine
TOPO	Tri-n-octylphosphine oxide
TPACS	Two-photon absorption cross section
TPECS	Two-photon emission cross section
TRAP	Telomeric repeat amplification protocol
UV-vis	Ultraviolet-visible

Résumé substantiel en français

Introduction générale

Le taux d'incidence des tumeurs malignes est en augmentation constante, environ six millions de nouveaux cas de cancer sont diagnostiqués chaque année dans le monde. L'une des stratégies actuelles pour le développement des méthodes de traitement avancées est axée sur l'administration ciblée de médicaments aux cellules tumorales, ce qui garantit de faibles concentrations de médicaments toxiques dans les tissus sains. Dans ce cas, en plus du ciblage hautement spécifique, le médicament peut être conjugué à un marqueur, généralement magnétique, radioactif ou photoluminescent. L'imagerie optique, relativement peu coûteuse et facile à mettre en œuvre, constitue actuellement la principale tendance en matière de la thérapie guidée par l'imagerie. Elle repose sur la détection des photons transmis à travers des tissus et fournit un suivi non invasif des véhicules de médicaments et une surveillance du traitement. La liaison d'un agent d'imagerie (photoluminescent, PL) à une molécule reconnaissant les biomarqueurs et à un agent pharmacologique assure un suivi en temps réel de l'administration de la substance active. Bien que les fluorophores organiques (colorants et protéines photoluminescents) traditionnellement utilisés pour l'ingénierie des sondes diagnostiques ou thérapeutiques présentent certains avantages, tels qu'un rendement quantique élevé (QY) et une bonne compatibilité avec le milieu aqueux, il existe également des inconvénients importants qui limitent leur utilisation: notamment la faible photostabilité et le spectre d'absorption étroit empêchent l'excitation de la photoluminescence de différents fluorophores organiques à une seule longueur d'onde.

Les *quantum dots* (QD ; boîtes quantiques) sont des nanocristaux (NC) semi-conducteurs de quelques nanomètres, capables d'émettre de la lumière (photoluminescence, PL) dans une large gamme spectrale. La structure énergétique, les caractéristiques d'absorption de la lumière et la photoluminescence (PL) dépendent fortement de la taille du QD en raison de l'effet de confinement quantique, ce qui explique leurs caractéristiques optiques uniques: notamment, la longueur d'onde de l'émission et la luminosité élevée du signal sont reliés à leur taille [1]. En particulier, en utilisant le QD le plus courant à base de séléniure de cadmium (CdSe), on peut obtenir des matériaux avec une PL intense dans la région visible du spectre (450–650 nm).

À l'heure actuelle, les QDs les plus répandus sont ceux du type cœur / coquille, où une couche épitaxiale, mince d'un semi-conducteur à bande interdite plus large (par exemple, CdS ou ZnS) est déposée sur le noyau / cœur CdSe photoluminescent afin de renforcer le confinement des porteurs de charges à l'intérieur du noyau et de protéger ce dernier des réactions chimiques avec le milieu ambiant. De plus, l'application de cette coquille protectrice simplifie sensiblement

la fonctionnalisation de la surface des QDs avec des ligands hydrophiles pour leur transfert dans un milieu aqueux et facilite également la conjugaison avec des médicaments pour l'obtention de nanosondes multifonctionnelles.

Les QDs peuvent être utilisés dans une grande variété d'applications et de technologies, ce qui a stimulé les efforts visant à développer et à étudier des matériaux de type QD et à contrôler leur morphologie à l'échelle nanométrique. Une application biomédicale typique des QDs est leur utilisation en tant que marqueurs photoluminescents, qui sont avantageux en raison de leurs propriétés optiques uniques par rapport aux colorants organiques, couramment utilisés.

L'utilisation des QDs comme sondes de la photoluminescence en biologie a été limitée par les contraintes suivantes:

- les difficultés de solubilisation,
- la faible stabilité colloïdale des QDs en milieu aqueux,
- la non-homogénéité des propriétés de l'ensemble des QDs et
- une forte « quenching » de luminescence en présence des molécules d'eau polaires.

L'optimisation des caractéristiques des QDs inclut le développement des méthodes de fabrication visant à garantir l'uniformité des particules, des bandes d'émission étroites et symétriques, une photoluminescence élevée avec efficacité quantique et un clignotement minimal des QDs individuels.

La modélisation assistée par ordinateur et les simulations théoriques de la physique et de la chimie des QDs, des études de l'influence de la couche du ligand et des défauts du réseau cristallin du système cœur / coquille sur les propriétés optiques, le contrôle de la croissance de cristaux, etc. sont ensemble les préoccupations majeures du monde de la recherche.

En termes de synthèse chimique, les dernières avancées dans la matière sont des modifications des coquilles inorganiques passivées à l'aide de nouvelles structures de coquilles et le développement de nouvelles approches pour assurer la croissance de la coquille. Ces résultats ont permis une amélioration significative des propriétés des QDs, néanmoins, leurs applications en recherche biomédicale souffrent de l'absence de techniques de production simples, polyvalentes et reproductibles permettant de préparer des QDs hautement stables avec une efficacité quantique proche de 100%.

La croissance incontrôlée des cellules cancéreuses est liée généralement à des facteurs stimulant la prolifération cellulaire. Les médicaments anticancéreux tuent les cellules cancéreuses ou modifient leur croissance. Parmi eux, les inhibiteurs des enzymes, responsables de la réplication de l'ADN sont devenus les cibles privilégiées de la recherche de nouveaux traitements du cancer [2]. Les systèmes hétérocycliques fusionnés avec des noyaux aromatiques comportant divers hétéroatomes (N, S et O), possèdent un large spectre d'activités

pharmacologiques. La synthèse des composés hétérocycliques azotés bioactifs a suscité un grand intérêt en raison de leurs rôles importants dans le contrôle de divers processus en biologie cellulaire, notamment la réplication, la transcription de l'ADN et la ségrégation des chromosomes au cours de la mitose.

L'inhibition d'enzymes par stabilisation de l'ADN simple et double-brin peut déclencher des voies de signalisation cellulaire menant à la mort des cellules cancéreuses. Assurer la distribution ciblée de molécules biologiquement actives dans la cellule est l'une des tâches essentielles du développement moderne de médicaments anticancéreux. Par le fait que les mécanismes de défense exercés par les membranes cellulaires limitent la distribution intracellulaire des agents thérapeutiques [3], l'administration intracellulaire à l'aide de vecteurs membranaires (molécules ayant une affinité pour les membranes cellulaires) est une méthode prometteuse, déjà utilisée avec succès pour transporter divers agents fonctionnels. Un vecteur convenablement choisi peut transporter le médicament ou la nanoparticule dans la cellule ou dans le noyau [4]. Diverses polyamines naturelles (putrescine, spermine, spermidine) sont des vecteurs convenables pour l'introduction d'agents cytotoxiques dans des cellules cancéreuses. Le principal moyen de créer des sondes pour l'administration ciblée de médicaments consiste à modifier l'agent pharmacologique avec le vecteur. L'assemblage d'un agent pharmacologique avec un agent d'imagerie par fluorescence [5] assurerait à la fois la libération du principe actif dans une cellule cancéreuse et son suivi spatio-temporel.

L'objectif et l'originalité de la thèse consistent en la synthèse de QDs photoluminescents de type cœur / coquille avec des propriétés optiques optimales pour les applications biomédicales. À cette fin, les tâches suivantes ont été accomplies: (1) la modélisation de la croissance de la QD en s'appuyant sur des principes physiques de la conception des matériaux; (2) la synthèse des cœurs de QD homogènes et sans défauts; (3) leur revêtement avec des coquilles de différentes compositions chimiques; (4) la synthèse de nouveaux ligands d'ADN capables de se conjuguer avec des QDs solubles dans l'eau; et (5) l'assemblage des nanosondes multifonctionnelles et leur évaluation biologique in-vitro.

Ces travaux de recherche ont été réalisés dans le cadre d'un projet de doctorat international en co-tutelle entre l'Université de Reims Champagne-Ardenne et l'Université d'État de Moscou. Ce projet, co-supervisé par le groupe de recherche français, dirigé par les Professeurs Nabiev (EA 4682) et Sapi (ICMR, UMR CNRS 7312) et par le groupe de recherche russe, dirigé par le Professeur Sidorov (Laboratoire de Thermochimie de *Moscou State University*) porte sur le développement des QDs dotés de propriétés colloïdales et optiques avancées pour des applications biologiques. Ainsi, il était prévu l'ingénierie de structures conjuguées compactes

entre les QDs et des dérivés d'acridine, nouveaux agents pharmacologiques, capables de stabiliser efficacement les G-quadruplexes télomériques de l'ADN humain.

La **partie nanotechnologique** de ce projet visait à adapter la structure des nanocristaux photoluminescents au cours de leur préparation afin d'obtenir les propriétés suivantes: (1) une taille minimale des QDs, indispensable pour une pénétration rapide dans les cellules; (2) un rendement quantique de la photoluminescence (PL QY) supérieur à 90%; et (3) une grande homogénéité de la taille des QDs dans son ensemble. Le groupe de recherche du Professeur Nabiev avait obtenu des résultats décisifs dans la synthèse des QDs colloïdales et également dans la fonctionnalisation de la surface des QDs. Le laboratoire du Professeur Sidorov a beaucoup d'expériences dans la simulation de nanoparticules optimales ainsi que dans la caractérisation de biomolécules à la surface de nanoparticules par spectrométrie de masse et par des méthodes en résonance magnétique nucléaire. La combinaison des résultats et des expériences des deux groupes de recherche a permis de mener une étude approfondie sur la modélisation de structures optimales de QDs, de valider les modèles théoriques expérimentalement par la synthèse des QDs colloïdales de haute qualité et par leur caractérisation ultérieure.

La **partie thérapeutique** du projet, liée aux applications biomédicales des QDs avancés, porte sur (1) la conception d'agents anticancéreux, dérivés de l'acridine et leur conjugaison à des véhicules spécifiques, assurant leur internalisation dans les cellules tumorales et (2) sur la fixation des QDs à la structure conjuguée (acridine+véhicule), ce qui permettra la visualisation de cette nanosonde. L'équipe du Professeur Sapi s'est spécialisée dans la synthèse de molécules aza-hétérocycliques polyaromatiques, ayant une haute affinité pour les G-quadruplexes télomériques de l'ADN. La synthèse de nouveaux agents anticancéreux potentiels, de type de dérivés de l'acridine, et leur conjugaison avec des QDs à l'aide des approches développées par l'équipe du professeur Nabiev ont permis l'obtention de nanosondes multifonctionnelles. L'évaluation biologique des agents pharmacologiques et des sondes pour l'imagerie, menée respectivement par le Dr Brassart (Médyc, UMR 7369) et le Dr Baryshnikova (Centre de Recherche Russe sur le Cancer Blokhin), a permis de prouver l'efficacité aussi bien des QDs à propriétés avancées que des nanosondes multifonctionnelles.

Le **premier chapitre** de cette thèse est une revue de la littérature, consacrée à la conception de sondes photoluminescentes multifonctionnelles. Il est divisé en trois sections principales. Dans la première section, ils sont passés en revue les principaux types de sondes photoluminescentes portant un agent diagnostique ou thérapeutique et les agents pour l'imagerie, tels que les colorants organiques ou les nanocristaux photoluminescents (NC). La deuxième partie du chapitre examine en détail les propriétés physiques et chimiques générales des QDs et les stratégies visant à améliorer le confinement quantique, notamment la croissance des coquilles

géantes (épaisses), des coquilles à multicouche et des coquilles épitaxiales, composées d'alliages. La troisième partie du chapitre traite les différentes méthodes de stabilisation des G-quadruplexes télomériques avec des petites molécules. Une attention particulière est accordée aux dérivés de l'acridine, y compris à des dérivés disubstitués en position 4,5 et à des analogues 3,6,9-trisubstitués, en tant qu'inhibiteurs potentiels de la télomérase dans les cellules cancéreuses. Les principales approches de l'évaluation biologique concernant l'efficacité de la stabilisation des G-quadruplexes et la sélectivité de l'inhibition de la télomérase sont brièvement présentées.

Dans le **deuxième chapitre** sont présentés les protocoles détaillés ainsi que les méthodes de caractérisation, utilisées tout au long de cette thèse. Premièrement, ils sont décrites les méthodes de synthèse des cœurs colloïdaux de type CdSe et celles des QDs de type cœur / coquille avec différentes compositions de la coquille, obtenues en utilisant l'approche dite « couche par couche ».

En résumé, elles sont décrites les méthodes exactes pour développer une coquille inorganique d'une épaisseur spécifiée sur des cœurs de CdSe, ainsi qu'une coquille organique pour la solubilisation de QD de type cœur / coquille. Deuxièmement, ils sont présentés en détails les protocoles de la synthèse à multi-étape, permettant de préparer des dérivés 4,5,9-trisubstitués de l'acridine. Tout naturellement les résultats de la caractérisation des molécules synthétisées (spectroscopie de résonance magnétique nucléaire et spectrométrie de masse, chromatographie en couche mince) sont aussi présentés. La suite de la présentation concerne le protocole de conjugaison entre des QDs solubles dans l'eau et des nouveaux ligands à base d'acridine, utilisant la chimie du carbodiimide. Enfin, sont décrites les différentes techniques de caractérisation des propriétés physiques, chimiques et biologiques des conjugués et de leurs composants.

Dans le **troisième chapitre**, les résultats de la synthèse colloïdale de cœurs de type CdSe et celle de QDs cœur / coquille, de structure différente sont discutés en détail. L'influence des principaux paramètres de réaction sur l'homogénéité du noyau / cœurs de type CdSe et sur les propriétés des QDs obtenus est analysée. Les paramètres variables sont: les différents types de précurseurs utilisés, les différents types de milieu réactionnel pour la synthèse organique, la température d'injection, la durée de la réaction et le rapport entre les précurseurs de cadmium et de sélénium. Les propriétés spectrales dépendantes de la taille des QDs de type CdSe sont analysées en fonction de la synthèse des cœurs ultra-petits. Nous avons pu confirmer la nécessité et l'efficacité de la chromatographie à gel pénétration pour la purification de haute performance des noyaux ultra-minces. Nous avons également mis en évidence expérimentalement l'importance du calcul précis de la quantité des précurseurs de la coquille. La taille, la morphologie, la structure cristalline et la composition chimique des meilleurs échantillons de

QDs ont été analysées. Finalement, les QDs ultra-petits ont été solubilisés dans un milieu aqueux à l'aide des échanges de ligands en deux étapes.

Dans le **quatrième chapitre**, les structures des ligands d'ADN proposés sont passées en revue et la sélection des groupements substituant le noyau d'acridine est expliquée en détail. La voie de synthèse permettant d'obtenir des dérivés d'acridine 4,5,9-trisubstitués est décrite. L'évaluation biologique est menée à l'aide de l'analyse de fusion liée à la méthode *FRET* (transfert d'énergie par résonance et fluorescence) et par le protocole *TRAP* (*telomeric repeat amplification protocol*)

Le **cinquième chapitre** porte sur la conjugaison des QDs de type CdSe / ZnS solubles dans l'eau avec des dérivés 4,5,9 trisubstitués de l'acridine. La conjugaison des deux unités a été réalisée utilisant des réactifs de couplage de type carbodiimide et sous forme de complexes électrostatiques ont été préparées par mélange direct de deux composants à pH 7.2. Le succès du processus de bioconjugaison est analysé et discuté en détail. Les toxicités cellulaires des conjugués ainsi obtenus et celles de leurs composants sont mesurées à l'aide d'un dosage colorimétrique permettant d'évaluer l'activité métabolique des cellules. L'internalisation cellulaire des structures bioconjuguées est étudiée par microscopie confocale.

Chapitre 1. Revue de la littérature

Le premier chapitre de ce manuscrit présente une étude bibliographique, comprenant l'ingénierie de pointe des sondes photoluminescentes de diagnostic ou de thérapie à base de colorants organiques et les QDs avec leurs composants. Ce chapitre est divisé en trois sections principales. Ensuite, elles sont décrites la synthèse des QDs de type cœur/coquille pour les applications biologiques, la stratégie visant à atteindre le rendement maximum quantique (QY) de la photoluminescence (PL) en optimisant la structure de la coquille. Ce chapitre résume également les principales classes de composés organiques polyaromatiques azotés, y compris les dérivés d'acridine di- et trisubstitués comme ligands du G-quadruplexe les plus prometteurs. La synthèse des QDs et des biomolécules ainsi que les problèmes de leur stabilité colloïdale et de leur toxicité sont brièvement décrits.

Sondes photoluminescentes pour l'imagerie et l'administration de médicaments

Les méthodes sensibles de détection des biomarqueurs du cancer, comme les protéines et les acides nucléiques, sont importantes pour le diagnostic, le pronostic et le contrôle thérapeutique. Lorsque des biomarqueurs sont identifiés, des capteurs à haute sensibilité, sélectivité et stabilité deviennent nécessaires. Ces dernières décennies ont connu un énorme progrès dans le développement des sondes luminescentes de diagnostic. Comparativement aux outils d'analyse plus conventionnels, les sondes optiques offrent l'avantage d'être peu invasives et

peuvent être préparées dans une variété de formats, y compris des sondes à petites molécules ou des nanosondes. En utilisant les propriétés fluorescentes adaptées des nanocristaux photoluminescents appelés points quantiques ou boîtes quantiques ou *quantum dots* comme marqueurs fluorescents, fonctionnalisés par la molécule de reconnaissance, nous pouvons obtenir une nanosonde multifonctionnelle compacte de diagnostic et de thérapie.

Les quantum dots (QD) (boîtes quantiques) sont des cristaux de semi-conducteurs de forme sphérique dont les dimensions ne dépassent pas quelques nanomètres. Les QD ont des propriétés optiques hors du commun qui permettent de dépasser plusieurs limitations inhérentes aux marqueurs fluorescents organiques (fluorescéine, rhodamine, GFP, green fluorescent protein, etc.), comme la faible résistance au photoblanchiment (c'est-à-dire la perte d'émission de fluorescence après une certaine durée d'excitation), ou la difficulté de visualiser simultanément des colorants de couleur différente. Un QD unique peut être visualisé en fluorescence pendant plusieurs dizaines de minutes, ce qui permet de pousser la détection jusqu'à la visualisation de molécules uniques. Par ailleurs, pour des raisons de confinement quantique, la longueur d'onde d'émission des QDs est directement reliée à leur taille. En effet, la 'taille caractéristique' de l'onde associée à l'exciton -responsable de l'émission de fluorescence- créé dans le cœur du QD, est plus grande que le QD lui-même.

Le suivi fonctionnel et l'interaction de surface avec des molécules, tout particulièrement des substances pharmacologiquement actives avec leurs cibles physiologiques (enzymes, récepteurs, ADN...) et le trafic intracellulaire qui en découle, sont de mieux en mieux réalisés par les technologies nouvelles en imagerie utilisant de molécules marquées. Parmi les outils, les systèmes de marquages par nanoparticules (QDs) fluorescentes se sont révélés particulièrement intéressants ces derniers temps.

Malgré les propriétés optiques uniques, l'utilisation des QDs en tant que marqueurs fluorescents en biologie a été limitée par

- les difficultés de solubiliser les QDs en milieu aqueux tout en conservant des propriétés essentielles comme leur bonne fluorescence, leur stabilité colloïdale et une faible adsorption non spécifique,
- le clignotement de QD lié à la variation de la constante diélectrique à leur surface dans les solutions complexes et dans les milieux biologiques.

Boîtes quantiques (QDs) photoluminescentes

L'optimisation des caractéristiques des QDs concerne l'uniformité des particules, le rendement quantique (QY) de la photoluminescence (PL), les bandes d'émissions étroites et symétriques et le clignotement minimal d'un QD individualisé. Les dernières avancées ont été réalisées en ce qui concerne la modification de coquilles inorganiques passivées en trouvant de

nouveaux précurseurs de couches, par l'ajustement de la structure de la coquille ou par l'application de coquilles géantes, obtenues par un dépôt « couche-par-couche » via la procédure contrôlée SILAR. Néanmoins, les applications dans les domaines de l'industrie ou de la recherche souffrent du manque de techniques de production faciles, générales et reproductibles permettant de préparer des QDs hautement stables, « non-clignotants » avec un rendement quantique proche de 100%. Aussi modélisations et simulations théoriques, les études de l'influence des défauts du réseau cristallin du système cœur/coquille sur les propriétés optiques et le contrôle de la croissance des cristaux, sont les principales préoccupations futures de la communauté des chercheurs-nanotechnologistes.

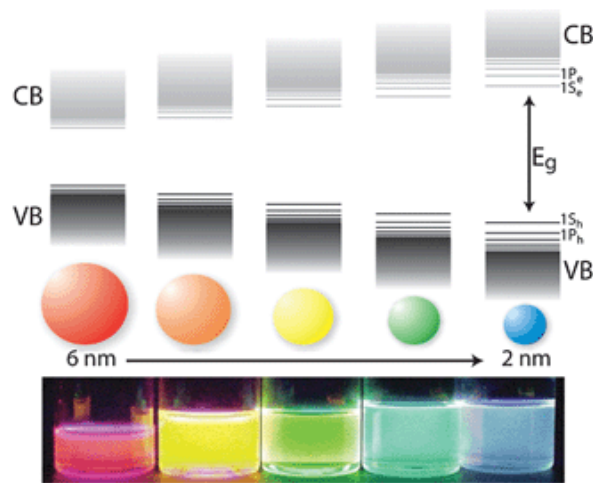


Figure 1: Évolution de la structure du niveau d'énergie d'une nanocristaux semi-conducteurs.

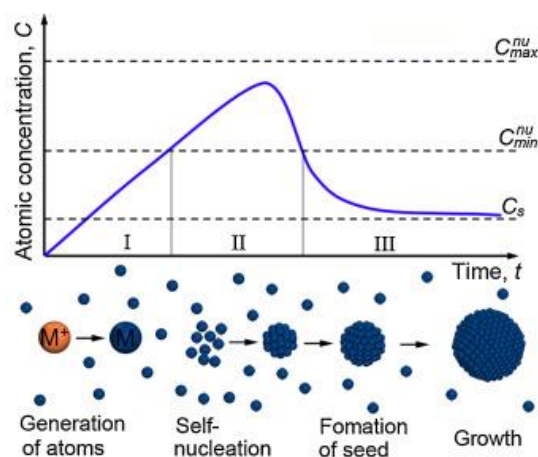


Figure 2: Courbe de LaMer décrivant trois étapes de la formation des nanocristaux métalliques dans un système en solution. Stade I : production d'atomes, stade II : nucléation, et stade III : formation et croissance des germes.

Le diagramme de LaMer révèle comment la barrière énergétique agit pour induire un "nucléation en rafale". Au stade I, certains noyaux peuvent se former dans des conditions sursaturées d'espèces atomiques ou moléculaires actives (monomères). Par contre, ces noyaux sont instables du point de vue thermodynamique et sont facilement redissous. Au stade II, une nucléation en rafale est initiée en augmentant brusquement la concentration du monomère au-dessus du seuil. Lorsque la concentration en monomère est épuisée par le processus de nucléation, le système passe au stade de croissance (taux de nucléation = 0, stade III).

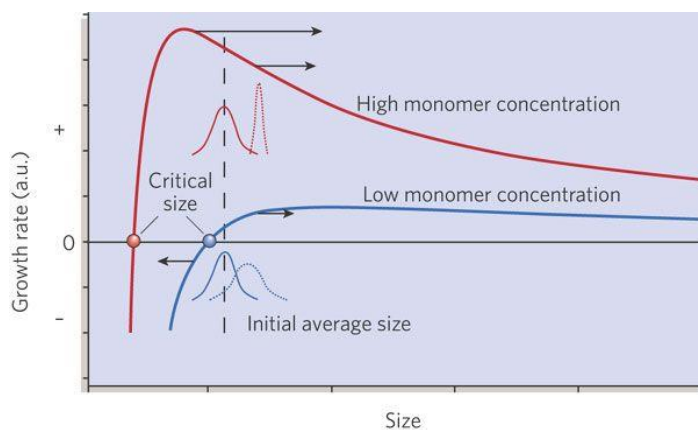


Figure 3: Cinétique de croissance des nanocristaux.

La figure illustre le taux de croissance en fonction du rayon nanocristallin. Le processus de croissance des nanoparticules peut être "contrôlé par diffusion" ou "contrôlé par cinétique" et dépend fortement de la concentration du monomère présent. À des concentrations élevées de monomères, la taille critique, qui est la taille minimale d'un noyau qui peut se développer spontanément dans la solution sursaturée, est petite afin que toutes les particules se développent.

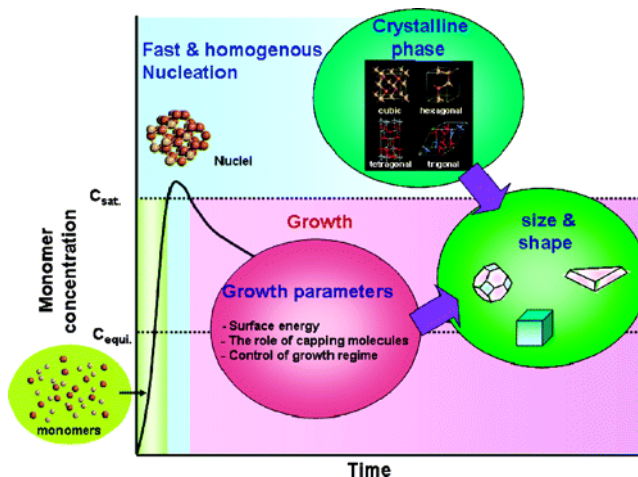


Figure 4: Processus de croissance des cristaux et les facteurs clés pour la détermination de la forme.

La figure montre que la forme géométrique des nanocristaux colloïdaux est déterminée par trois facteurs critiques : (1) la phase cristalline de la germe au stade de la nucléation ; (2) l'effet de l'énergie de surface et (3) le contrôle du régime de croissance au stade de croissance.

Tableau 1: Caractéristiques de certains matériaux semi-conducteurs massifs

Material	Structure [300K]	Type	E_{gap} [eV]	Lattice parameter [Å]	Density [kg m ⁻³]
ZnS	Zinc blende	II-VI	3.61	5.41	4090
ZnSe	Zinc blende	II-VI	2.69	5.668	5266
ZnTe	Zinc blende	II-VI	2.39	6.104	5636
CdS	Wurtzite	II-VI	2.49	4.136/6.714	4820
CdSe	Wurtzite	II-VI	1.74	4.3/7.01	5810
CdTe	Zinc blende	II-VI	1.43	6.482	5870
GaN	Wurtzite	III-V	3.44	3.188/5.185	6095
GaP	Zinc-blende	III-V	2.27	5.45	4138
GaAs	Zinc blende	III-V	1.42	5.653	5318
GaSb	Zinc blende	III-V	0.75	6.096	5614
InN	Wurtzite	III-V	0.8	3.545/5.703	6810
InP	Zinc blende	III-V	1.35	5.869	4787
InAs	Zinc blende	III-V	0.35	6.058	5667
InSb	Zinc blende	III-V	0.23	6.479	5774
PbS	Rocksalt	IV-VI	0.41	5.936	7597
PbSe	Rocksalt	IV-VI	0.28	6.117	8260
PbTe	Rocksalt	IV-VI	0.31	6.462	8219

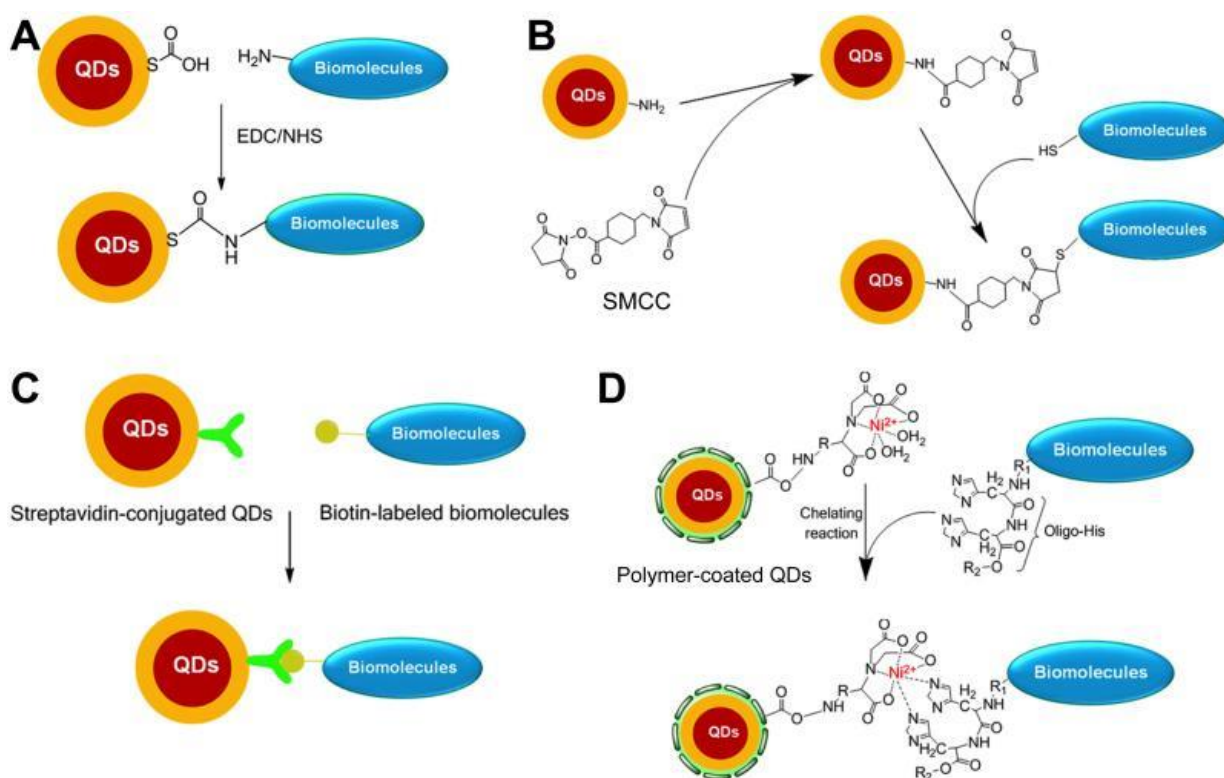


Figure 8: Stratégies représentatives de la bioconjugaison des DQ par couplage EDC/NHS (A), réaction thiol-maléimide (B), liaison streptavidine-biotine (C) et interaction entre Ni-NTA et histidine (D).

Le tableau 1 montre les principales caractéristiques, y compris la structure cristallographique et le paramètre du réseau, de certains composés semi-conducteurs massifs qui sont pris en compte dans le choix du matériau de la coquille. On distingue trois types de structure énergétique de QD en fonction de la disposition des niveaux d'énergie cœur/coquille. Les QDs à base de CdSe, revêtus avec les coquilles constituées de matériaux à large bande interdite, tels que le ZnS et le CdS, garantissant que les porteurs de charge (électrons et trous) sont retenus dans le cœur de CdSe, sont les plus couramment utilisés.

La figure illustre plusieurs approches pour lier des molécules biologiques (peptides, protéines, médicaments, ligands d'ADN aux QD), y compris l'adsorption non spécifique, l'interaction électrostatique, l'échange mercapto (-SH) et la liaison covalente.

Ligands de l'ADN G-quadruplexe à base d'hétérocycles polyaromatiques azotés

Chez les eucaryotes, les extrémités des chromosomes sont protégées par des structures particulières, les télomères. Chez l'Homme, ceux-ci contiennent des séquences répétées (TTAGGG)_n formant des complexes avec des protéines spécifiques (Figure 9). Les télomères permettent à la fois de stabiliser les chromosomes mais aussi d'en maintenir l'individualité. Dans les cellules saines somatiques, l'absence d'activité télomérase, une transcriptase inverse, occasionne un raccourcissement progressif des télomères à chaque mitose cellulaire. Lorsque les télomères ont atteint une taille critique, il se produit un arrêt du cycle cellulaire (sénescence répliquative).

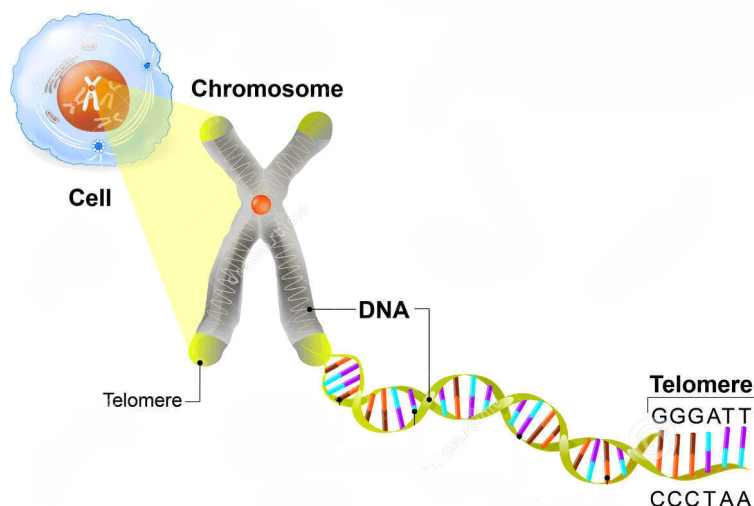


Figure 9: Télomères dans une cellule eucaryote.

Par contre, les cellules tumorales peuvent se diviser indéfiniment et cette propriété coïncide avec le maintien de la longueur des télomères par induction de la télomérase à un

niveau élevé d'expression. La télomérase, présente dans 85% des cellules tumorales, est donc devenue une cible intéressante pour le développement de molécules antitumorales.

Les télomères comportent une région simple brin proéminente à leur extrémité 3' (brin G). Le brin G est présent au niveau de toutes les extrémités chromosomiques et est susceptible d'adopter plusieurs conformations telles que la T-loop ou le quadruplexe de guanine (G4). Le brin G peut former un quadruplexe dans lequel quatre séries de répétitions de guanines sont engagées dans trois quartets adjacents stabilisés par des liaisons de type Hoogsteen et par la chélation d'un cation (K^+ ou Na^+) (Figure 10).

In vitro, l'activité optimale de la télomérase, l'enzyme responsable de la synthèse des extrémités télomériques, ne s'effectue que sur une structure du brin G linéaire et la stabilisation d'un G-quadruplexe bloque cette activité enzymatique. La recherche de molécules stabilisant le G4 télomérique et inhibant la réplication des télomères est apparue comme une stratégie originale et sélective pour induire la sénescence ou la mort des cellules cancéreuses. Quatre groupes de molécules parmi les nombreux ligands du G-quadruplexe présentent un intérêt particulier : la quinoléine, la porphyrine, les dérivés macrocycliques et l'acridine. Ces ligands G4 sont souvent des hétérocycles azotés parmi lesquels figure l'acridine 3,6,9-trisubstituée, le BRACO-19, actuellement en phase préclinique. Récemment, Neidle et al. ont déterminé par des méthodes physico-chimiques, les sites d'interactions entre une séquence d'ADN télomérique humaine formant deux G-quadruplexes consécutifs, et le BRACO-19; il s'agit d'interactions électrostatiques (phosphates de l'ADN télomérique), de réseaux de liaisons hydrogène, d'interactions des systèmes aromatiques du BRACO-19 avec ceux des bases de l'ADN télomérique.

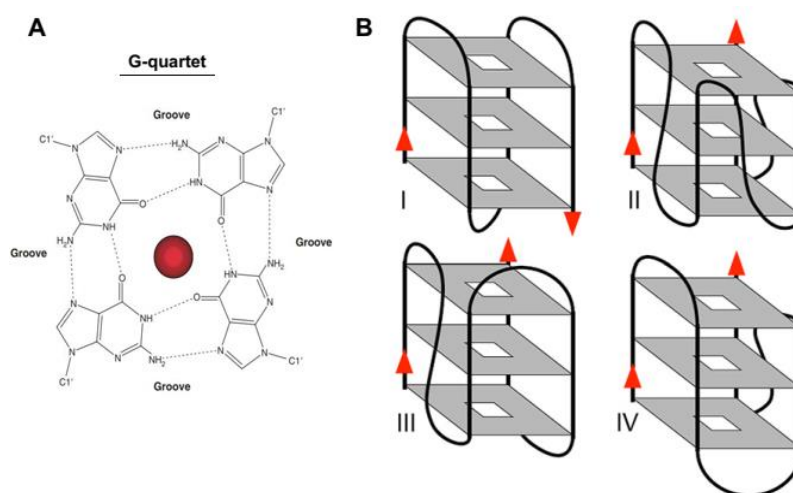


Figure 10: (A) La disposition des bases de guanine dans le G-quartet, représentée avec un ion métallique placé au centre. (B) Les conformations possibles du G-quadruplexe intramolécule formé par l'ADN télomérique humain.

La figure illustre la structure du G-quadruplex et les options de formation.

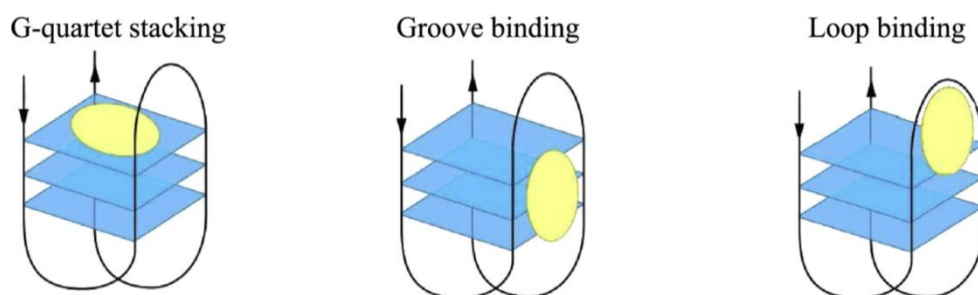


Figure 11: Exemples de modes de liaison d'une petite molécule avec un G-quadruplexe. La figure montre les modes de liaison de base des ligands G-quadruplexe.

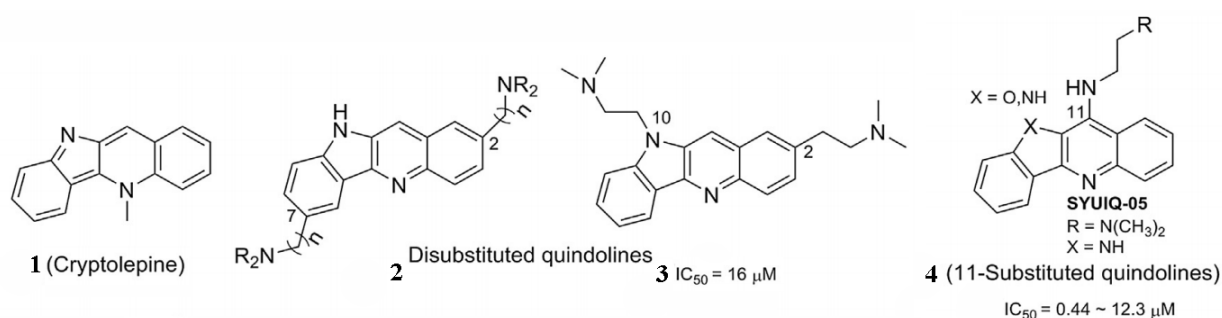


Figure 12: Structures des dérivés de la quindoline.

La figure montre quatre dérivés de la quinoléine, importants puisque les quinoléines sont largement utilisées comme composés "parents" pour synthétiser des molécules ayant des applications médicales, en particulier pour les activités antipaludienne, antimicrobienne et anti-cancéreuse.

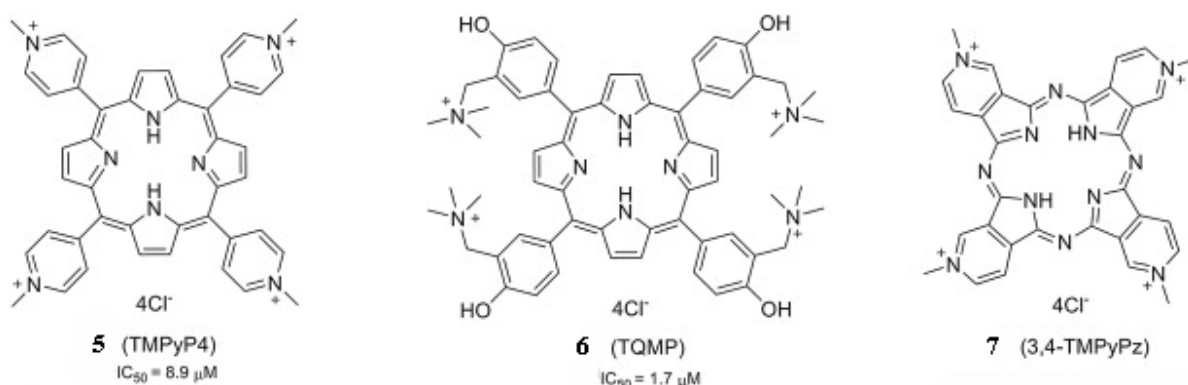


Figure 13: Structures des dérivés de la porphyrine. Les porphyrines présentent un groupe de composés organiques naturels, qui étaient à l'origine bien connus comme des agents de liaison de l'ADN duplex avec une grande sélectivité vers le G-quadruplexe vs. l'ADN duplex.

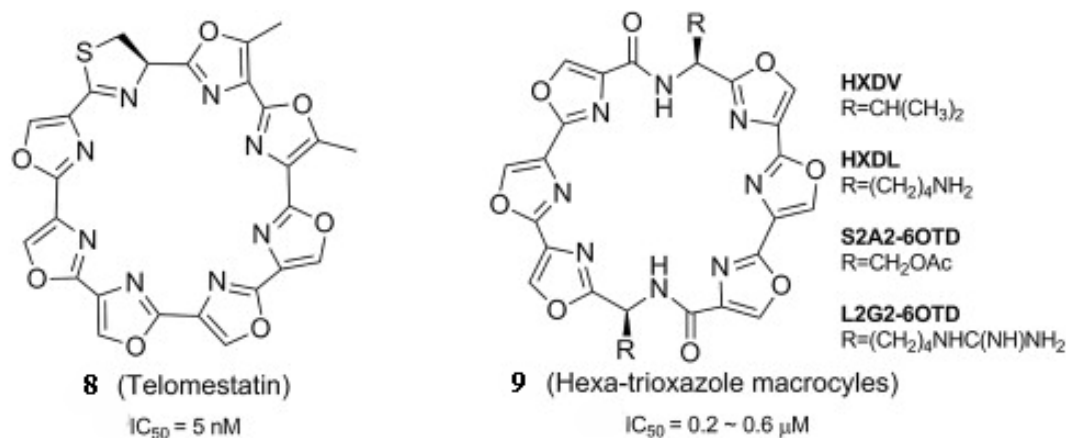


Figure 14: Structures des alcaloïdes macrocycliques et leurs dérivés.

La télomestatine est un composé macrocyclique naturel, c'est un autre ligand stabilisateur efficace du G-quadruplexe télomérique.

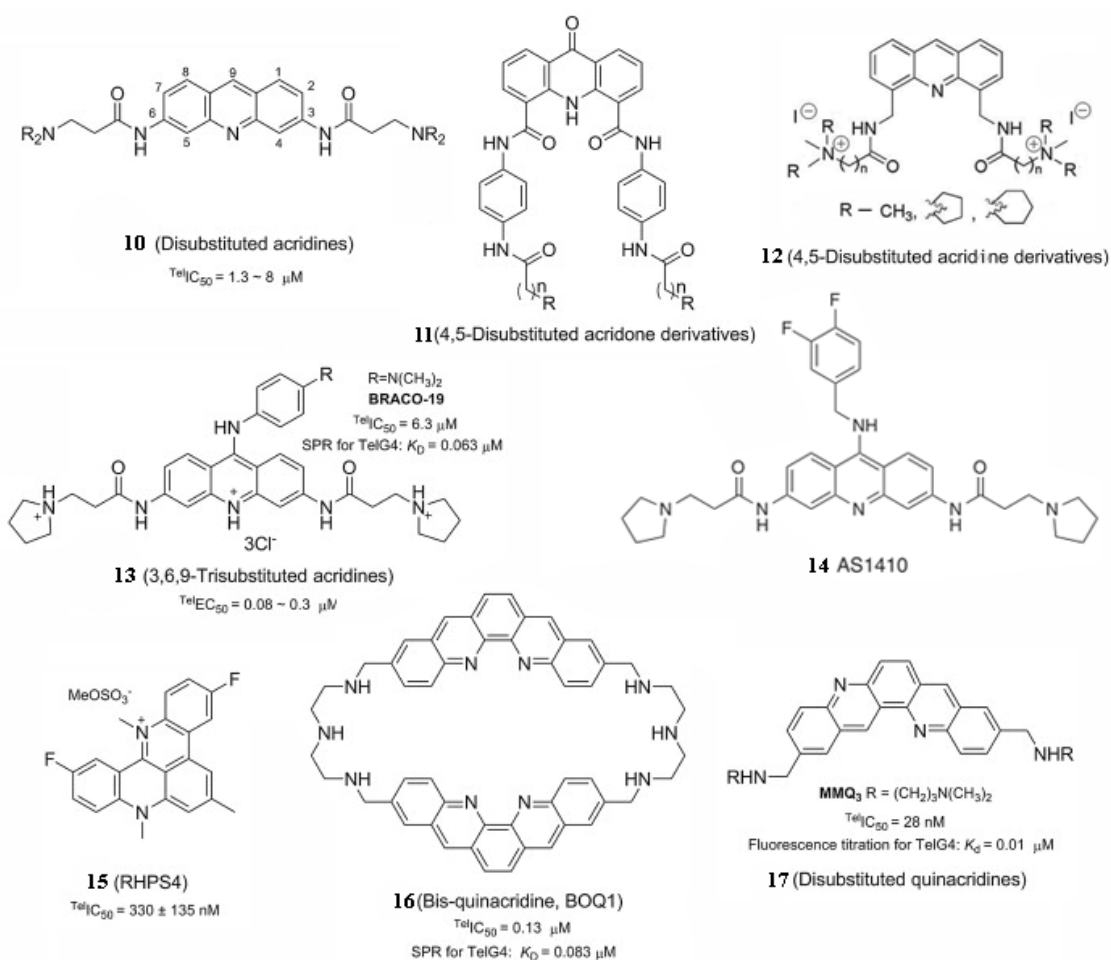


Figure 15 : Structures de l'acridine et de ses dérivés.

Tous les dérivés de l'acridine présentés dans la figure montrent une activité élevée contre les lignées cellulaires tumorales, en partie due à la structure plane du système tricyclique qui

confère la capacité de s'intercaler dans l'ADN et d'interférer avec les processus métaboliques des cellules eucaryotes.

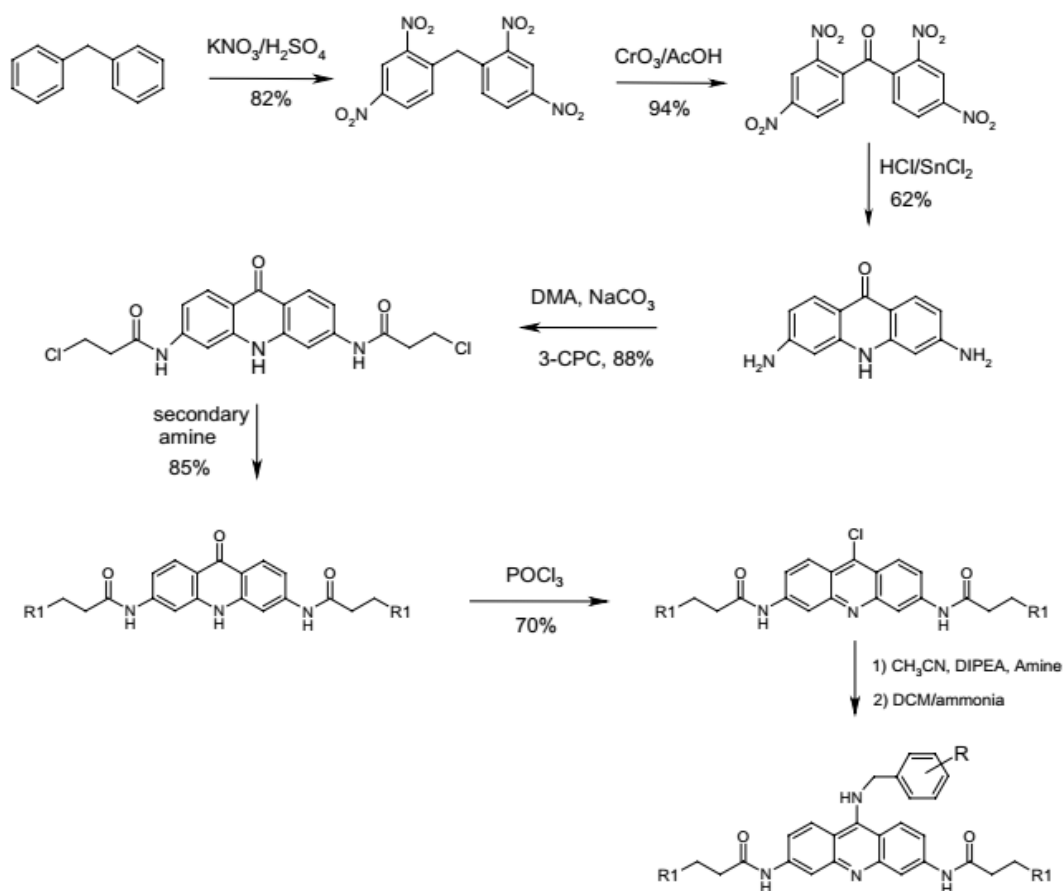


Figure 16 : Voie de synthèse vers les acridines benzylamino-substituées.

La figure illustre la voie de synthèse par l'intermédiaire de l'acridone, l'un des composés les plus remarquables de cette série est le BRACO-19 - un dérivé 3,6,9-trisubstitué de l'acridine.

Bien que des progrès considérables aient été réalisés dans la conception de nanosondes multifonctionnelles, il reste encore beaucoup à faire pour améliorer les propriétés pharmacodynamiques et pharmacocinétiques des acridines, ainsi que la stabilité colloïdale et la photoluminescence des QD.

Chapitre 2. Matériels et méthodes

Dans le deuxième chapitre, les protocoles détaillés et les méthodes de caractérisation utilisées tout au long de cette thèse sont présentés. Ils sont décrits en détail la voie de synthèse colloïdale des QDs de type cœur/coquille de haute qualité, la synthèse des dérivés 4,5,9-trisubstitués de l'acridine, ainsi que l'assemblage des dérivés conjugués.

Caractérisation des matériaux

Les échantillons obtenus dans cette thèse ont été caractérisés par des méthodes physico-chimiques et biologiques. La spectroscopie ultraviolet-visible (UV-Vis) et la spectroscopie de photoluminescence (PL) ont été utilisées pour mesurer les propriétés optiques des QDs initiaux sous forme soit cœur, soit cœur/coquille et des échantillons conjugués. Le QY PL des QDs a été déterminé (voir la méthode sur la figure 18) à l'aide de différents colorants organiques dont la valeur de QY PL connue est indiquée sur le tableau 2. La résonance magnétique nucléaire et la spectroscopie de masse ont été appliquées pour caractériser les molécules organiques.

Tableau 2: Propriétés optiques des colorants de référence.

Spectral region, nm	Dye	PL excitation wavelength, nm	Dye PL QY, % / solvent
<500	Cymarine 102	365	76 / ethanol
500-550	Fluorescein	460	90 / 0.1 M NaOH
550-590	Rhodamine 6G	500	95 / ethanol
570-600	Rhodamine 101	532	95 / Ethanol
600-650	Cresyl violet	580	58 / methanol

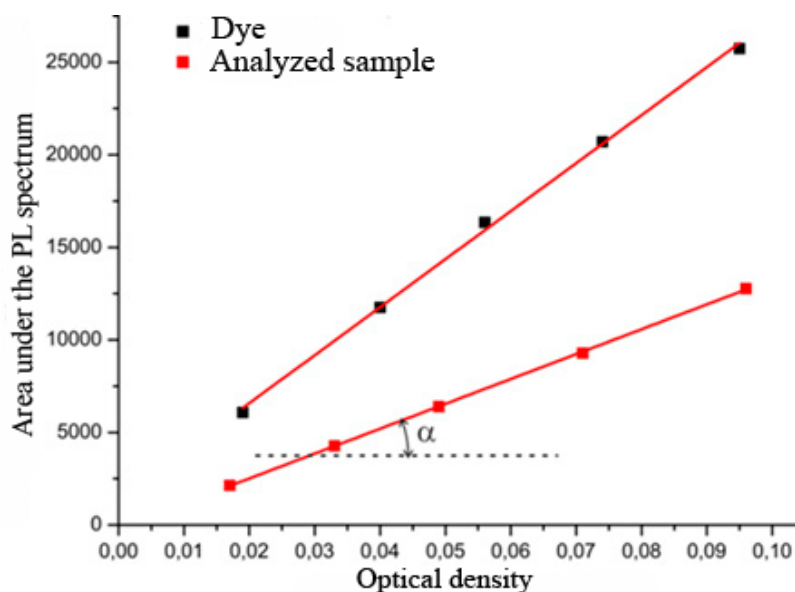


Figure 18: Dépendance expérimentale de l'intensité PL intégrée par rapport à la densité optique de la solution du QD.

La dispersion granulométrique d'une suspension colloïdale de QD a été analysée par DLS. Pour les évaluations biologiques de nouveaux agents pharmacologiques potentiels, on a utilisé à la fois le transfert d'énergie par résonance en fluorescence (FRET) et le protocole TRAP

(*telomeric repeat amplification protocol*). Un test de viabilité cellulaire a également été appliqué pour évaluer la cytotoxicité des molécules, des QDs et des dérivés conjugués.

La microscopie électronique en transmission (TEM), et les techniques auxiliaires de EDS ont été les principales techniques de caractérisation utilisées dans cette thèse. Ces techniques sont considérées comme des outils puissants pour déterminer une gamme de paramètres de matériaux tels que : la morphologie de l'échantillon à fort grossissement, la structure cristalline et la composition. Les études HRTEM ont fourni des informations détaillées sur la structure et l'orientation cristallographique de l'échantillon. L'EDS a été utilisé pour déterminer la composition élémentaire des échantillons.

Synthèse des boîtes quantiques (QDs) de type CdSe

Des cœurs composés de CdSe de différentes tailles ont été synthétisés par la méthode d'injection à chaud dans le solvant organique, le 1-octadécène ayant un point d'ébullition élevé et une faible polarité (Figure 19). Les cœurs CdSe ont été obtenus à partir du *n*-hexadécylphosphonate de cadmium et du complexe de tri-*n*-octylphosphine de sélénium comme précurseurs en présence de la tri-*n*-octylamine comme agent stabilisant. Pour la nucléation des QDs, le précurseur du sélénium a été injecté rapidement dans la solution du précurseur du cadmium.

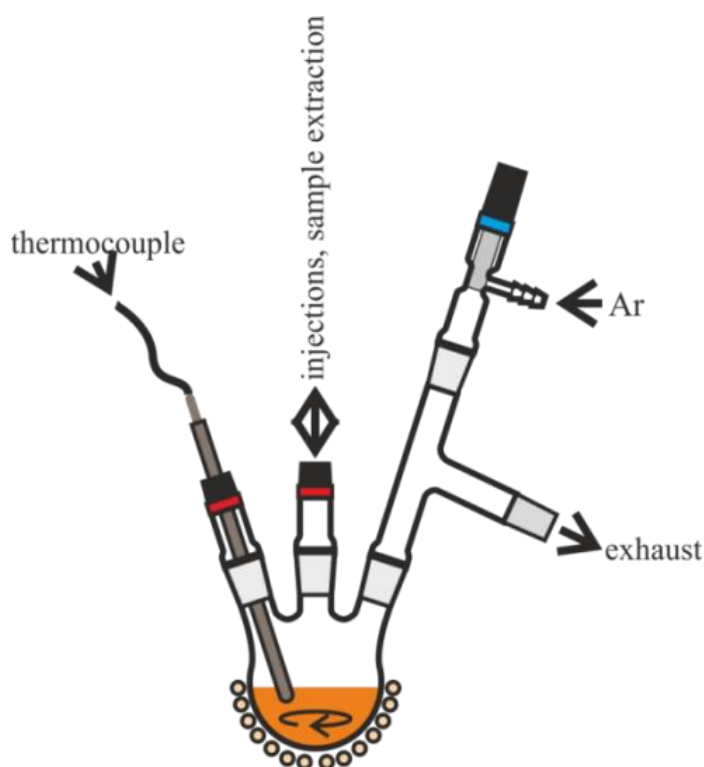


Figure 19: Appareil de réaction pour la synthèse des QDs de CdSe de type cœur et cœur/coquille.

Des cœurs CdSe de différentes tailles ont été obtenus par la méthode d'injection à chaud dans le 1-octadécène. Les Figures 19 et 20 illustrent respectivement l'appareil utilisé et le schéma de synthèse.

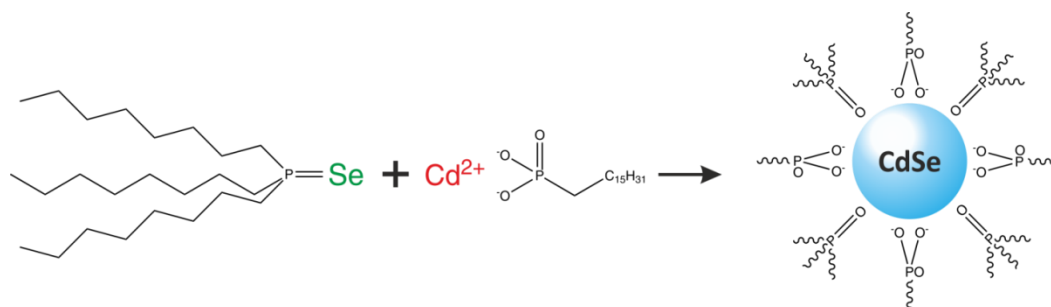


Figure 20: Schéma de la synthèse chimique.

Ensuite, la purification du mélange réactionnel des précurseurs et la préparation de la surface NC pour la croissance de la coquille ont été effectuées. Une solution de QD a été purifiée par chromatographie à perméation de gel en utilisant des billes de polystyrène réticulé SX-1 (BIO-RAD) comme phase stationnaire (Figure 21). Le revêtement du cœur a été réalisé selon le procédé SILAR en mode thermocyclique. Les quantités des réactifs ont été calculées à l'aide de notre modèle de croissance conçu pour les QDs pour éviter l'accumulation excessive de précurseurs dans le mélange réactionnel. Une fois la croissance de la coquille terminée, les QDs résultants ont été isolés de la solution brute par précipitation.

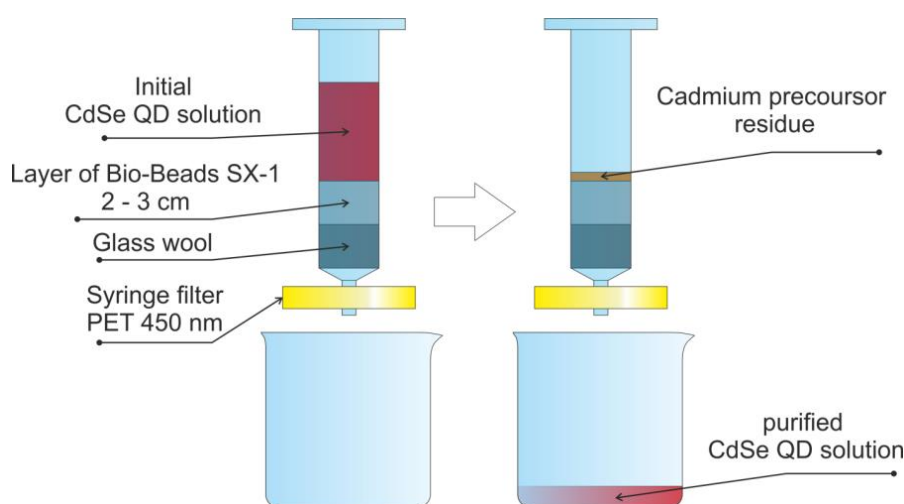


Figure 21: Schéma de filtration de CdSe sur gel Bio-Beads SX-1 (Bio-RAD) utilisée comme phase stationnaire.

La figure illustre le schéma de purification des QDs par chromatographie d'exclusion stérique par taille pour éliminer l'excès du surfactant, du solvant, les impuretés et les sous-produits.

La détermination de la taille de (la coquille) du cœur et de la concentration en QD a été effectuée par spectroscopie UV-Vis en utilisant les dépendances de la première position du pic d'absorption excitonique de la taille de QD et le lien entre son intensité et le coefficient d'extinction de QD. Le revêtement multicouche a été réalisé selon la procédure SILAR en mode thermocyclique, avec les quantités de réactifs calculées à l'aide de notre modèle de croissance de QDs pour éviter l'accumulation excessive de précurseurs dans le mélange réactionnel.

Préparation de boîtes quantiques (QDs) hydrosolubles

La solubilisation des DQs a été effectuée en utilisant l'approche d'échange de ligands en deux étapes. Dans un premier temps, les ligands hydrophobes ont été échangés contre la DL-cystéine ; dans un deuxième temps, la DL-cystéine a été échangée contre un mélange de deux dérivés du polyéthylène glycol (PEG). Les dérivés du PEG avec QD ont été incubés pendant la nuit et pré-nettoyés par centrifugation à l'aide d'unités de filtration Amicon Ultra-15 avec une coupure de 10 kDa dans un tampon phosphate.

Synthèse de dérivés 4,5,9-trisubstitués de l'acridine

La synthèse a été réalisée en sept réactions consécutives, à partir de l'acridine. L'étape clé a été la synthèse de l'intermédiaire acridone 4,5-disubstituée. Cette étape a été suivie par la substitution des carbones C-4 et C-5 par deux chaînes putrescines, qui avaient un groupement protecteur *tert*-butoxycarbonyle en position terminal (Boc), et par la fonctionnalisation de la position C-9 avec l'une des trois anilines. Le précurseur de la fonctionnalisation des carbones C-4 et C-5, la putrescine monoprotégée avec une fonction Boc, a été obtenue en ajoutant du dicarbonate de di-*tert*-butyle (Boc_2O) à l'amine primaire dans un milieu aqueux alcalin. La purification des composés finaux a été réalisée par chromatographie flash sur colonne ou chromatographie en phase liquide à haute performance.

Assemblage de nanosondes multifonctionnelles

Les complexes électrostatiques des QDs et le ligand d'acridine ont été synthétisés spontanément sans agent de réticulation en milieu neutre (tampon phosphate). La solution conjuguée purifiée a été caractérisée et ensuite utilisée pour l'internalisation cellulaire.

Internalisation cellulaire des QDs de type CdSe/ZnS

Pour analyser l'interaction des QD-PEG-OH hydrosolubles avec les monocytes, les QDs ont été ajoutés aux cellules monocytes humaines. Après incubation à 37 °C pendant 10 min, l'internalisation des QDs par les monocytes humains a été étudiée au microscope confocal à balayage laser LSM-710-NLO.

Chapitre 3. Boîtes quantiques (QDs) de haute qualité à base de CdSe

Dans le troisième chapitre, les résultats de la synthèse colloïdale des QDs de CdSe de type cœur et cœur/coquille ayant de structures différentes, sont discutés en détail. L'influence des principaux paramètres réactionnels sur l'homogénéité de l'ensemble du cœur composé de CdSe et les propriétés des QDs est analysée. Les paramètres variables sont : les différents types de précurseurs utilisés, les différents types de milieu de synthèse organique, la température d'injection, la durée de réaction, le rapport entre les précurseurs du cadmium et du sélénium. Les propriétés spectrales dépendantes de la taille des QDs de type CdSe sont analysées en fonction de la synthèse des cœurs ultra petits. Nous avons confirmé expérimentalement la nécessité et l'efficacité de la chromatographie par perméation de gel pour la purification de haute performance des cœurs ultra petits, ainsi l'importance du calcul précis des quantités de précurseurs de la coquille. La taille, la morphologie, la structure cristalline et la composition chimique des meilleurs échantillons QD sont analysés. Enfin, les DQs de taille minimale ont été solubilisés avec des dérivés du PEG.

La synthèse des cœurs de CdSe de haute qualité comprend :

- Développement de la méthode de synthèse des QDs par injection colloïdale à chaud, par investigation et optimisation des paramètres critiques de la réaction, permettant d'obtenir des QDs de haute qualité avec une taille faciles à régler et une longueur d'onde d'émission de PL bien définie.
- Synthèse de QDs de type CdSe compacts pour l'application biologique par la terminaison rapide de leur croissance et leur purification en plusieurs étapes, permettant d'isoler des cœurs de QDs ultra petits de 1,5 nm avec une distribution de taille étroite.
- Développement du modèle de croissance des QDs pour la prédiction précise des propriétés optiques et l'augmentation de la reproductibilité de la synthèse des QDs.

Le développement des QDs de type cœur/coquille solubles dans l'eau comprend :

- Synthèse des QDs de type CdSe/ZnS, compacts avec les cœurs ultra petits de 1,5 nm, et utilisation des calculs précis de la quantité de précurseurs appliquant le modèle de croissance de QDs, développé pour la croissance épitaxiale de la coquille.
- Conception de la nouvelle structure multicouche avec la localisation optimisée du support de charge pour obtenir une valeur maximale de l'efficacité de PL et une fonctionnalisation pratique de la surface ultérieurement.

Synthèse colloïdale par injection à chaud de nanocristaux de CdSe

Les principaux paramètres de la réaction de synthèse des QDs ont été optimisés: les types de précurseurs "chauds" et "froids" ; le type de solvant organique ; le type de sel de cadmium ; la température d'injection ; la durée de réaction ; le rapport entre les précurseurs du cadmium et ceux du sélénium.

Nous avons trouvé les conditions optimales pour la synthèse des QDs de type CdSe de haute qualité par injection à chaud. Les conditions optimales de la formation des QDs sont celles où le système réactionnel devrait former une quantité relativement faible de cœurs dans une courte durée, et ces cœurs donc ne consomment pas les monomères restants, car ils se développent rapidement à la taille souhaitée. Dans ce but, des précurseurs relativement moins réactifs seraient utiles. Des cœurs de QD de haute qualité ont été synthétisés selon le protocole adapté dans la publication [242] en utilisant du Cd-HDPA en présence de TOA et de 2-EHA pour stabiliser les QDs en croissance et limiter leur croissance rapide dans la solution ODE. La manipulation avec la température d'injection, la durée de croissance et la quantité de ligands permet d'obtenir des QDs sans défaut et de taille comprise entre 1,8 et 5 nm avec une distribution de taille étroite et une bande d'émission accordable.

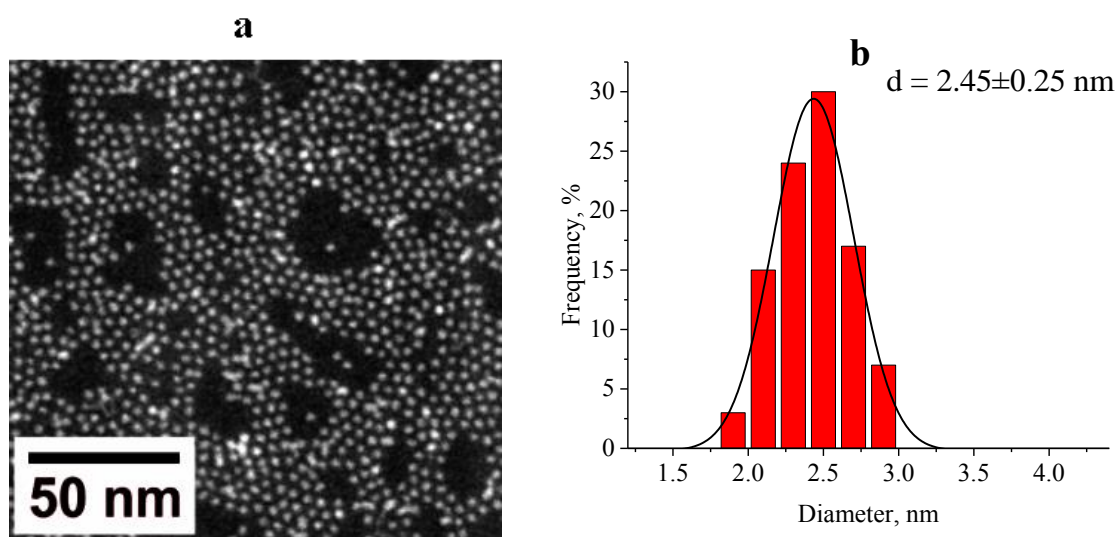


Figure 28 : a) Image STEM des QDs à base de CdSe. (b) La distribution de la taille de l'échantillon analysée.

Les images STEM des QDs de type CdSe montrent que ces QDs ont une morphologie uniforme : la distribution des tailles est de $2,45 \pm 0,25$ nm, la forme est proche de la distribution normale, ce qui confirme l'homogénéité de l'ensemble.

Synthèse des QDs de type CdSe ultra petits

Nous proposons une méthode efficace de terminaison ultra-rapide de la réaction par congélation du mélange réactionnel avec de l'azote liquide, ce qui permet d'obtenir des QDs dès les premiers stades de croissance. La purification efficace de ces petits QDs du précurseur du cadmium et des ligands adsorbés en excès ne se fait qu'en combinant la méthode traditionnelle de dispersion/précipitation et la chromatographie d'exclusion stérique. Grâce à la purification en plusieurs étapes, nous avons pu isoler des QDs de type CdSe ultra petits, très uniformes avec le premier pic d'absorption excitonique à 401 nm, ce qui correspond au diamètre des QDs de 1,5 nm.

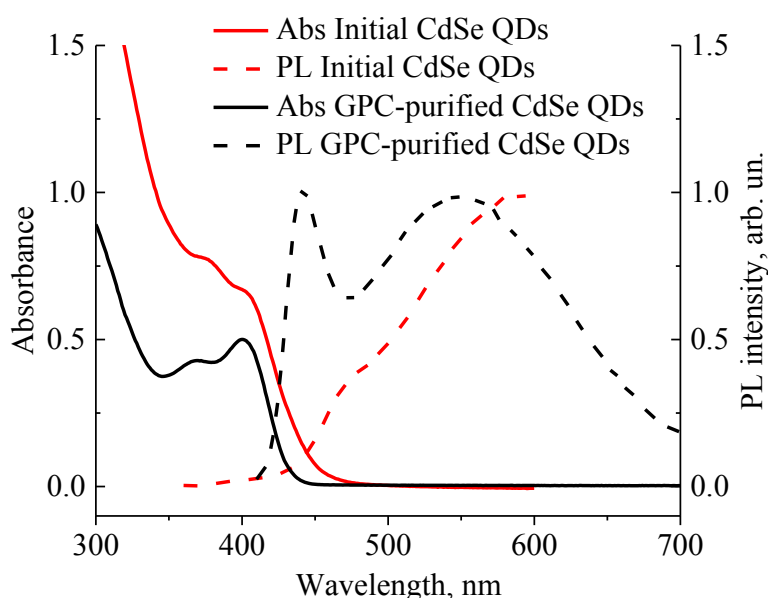


Figure 31 : Spectres d'absorption et de photoluminescence des boîtes quantiques de CdSe préparées selon différents procédés.

La figure montre qu'une purification supplémentaire par chromatographie par perméation de gel a amélioré la qualité des QDs résultants.

Développement du modèle de croissance des nanocristaux de CdSe

En tenant compte des défauts du modèle sphérique de croissance des QDs, nous avons proposé un modèle NC optimisé, basé sur les caractéristiques cristallographiques du matériau NC et la morphologie des cœurs de CdSe de type wurtzite, qui permet une description plus précise de la croissance des QDs.

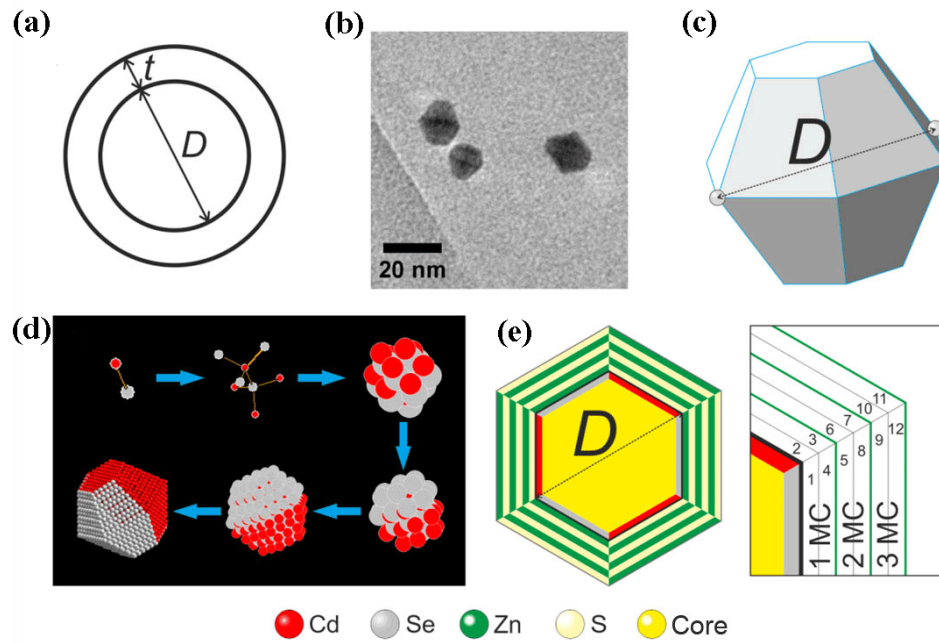


Figure 32 : Éléments clés du modèle de croissance des QDs : a) modèle sphérique d'un QD ; b) Images TEM des QDs de CdSe synthétisés ; c) modèle géométrique d'un QD, un bipyramide hexagonal ; d) croissance étape par étape d'un QD de CdSe, à partir du monomère ; e) modèle de croissance couche par couche ;

Tableau 5 : Composition atomique et propriétés principales des QDs de type CdSe à différents stades de croissance.

# iter	Cd atoms	Se atoms	total atoms	diameter, nm	abs λ_{\max} , nm
1	1	1	2		
2	3	3	8		
3	9	9	26		
4	16	16	58	1,51	404
5	28	28	114	1,84	441
6	39	39	192	2,3	489
7	57	57	306	2,66	518
8	73	73	452	3,12	546
9	97	97	646	3,48	563
10	117	117	880	3,94	580
11	147	147	1174	4,3	591
12	172	172	1518	4,76	603
13	208	208	1934	5,12	611
14	237	237	2408	5,58	621
15	279	279	2966	5,95	628
16	313	313	3592	6,41	636
17	361	361	4314	6,77	641
18	399	399	5112	7,23	648

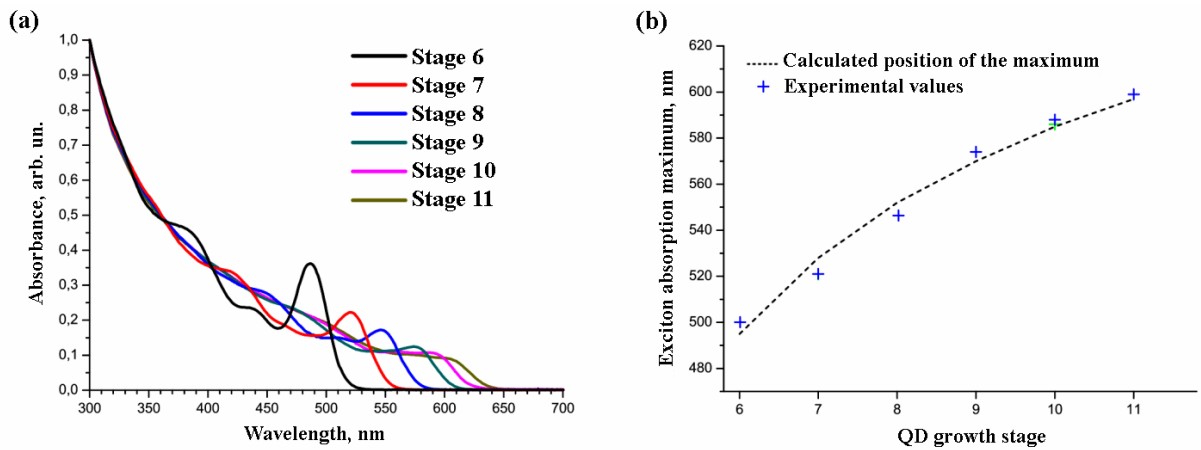


Figure 33 : a) Évolution des spectres d'extinction à différents stades de croissance des QD de CdSe de type wurtzite. b) Comparaison des longueurs d'onde maximales d'absorption de l'exciton calculées à l'aide du modèle de croissance des QDs et des données expérimentales pour différents stades de croissance.

La figure illustre la corrélation entre le maximum de l'absorption d'exciton obtenu expérimentalement et les données prédites par le modèle.

Synthèse de QD cœur/coquille à base de CdSe

Le modèle de croissance des QDs de CdSe a été utilisé pour calculer avec une grande précision les quantités de précurseurs nécessaires à la croissance d'une coquille épitaxiale protectrice de différentes compositions. Le calcul précis des quantités de précurseurs nécessaires (3 mL au total) tient compte de l'épaisseur de la coquille, de la concentration des précurseurs et des coefficients d'extinction molaire. La croissance épitaxiale de la coquille a été réalisée en utilisant l'approche SILAR, basée sur l'injection séquentielle de petites portions d'un métal et de précurseurs chalcogènes dans le mélange réactionnel. La cristallinité élevée des QDs de type cœur/coquille permet d'augmenter significativement le QY de PL et la stabilité colloïdale et rend les QDs appropriés pour une fonctionnalisation ultérieure.

Le rendement quantique des QDs à base de CdSe/ZnS est limité par l'ampleur de la barrière potentielle pour les porteurs de charge excités, créée par la coquille. La nouvelle génération des QDs cœur/multicoquille (MS) développée dans le cadre de ce projet présente un confinement très efficace des porteurs de charge dans les cœurs luminescents en raison de la structure énergétique spécifique de la coquille multicomposante (ZnS/CdS/ZnS). Il a été démontré que les QDs de cœur/MS de différentes tailles présentent le QY de PL proche de 100% quelle que soit la taille du cœur. De plus, la structure de la coquille est parfaitement compatible

avec les protocoles courants permettant l'échange de ligands de surface pour la solubilisation des QDs et leur fonctionnalisation pour les applications biomédicales.

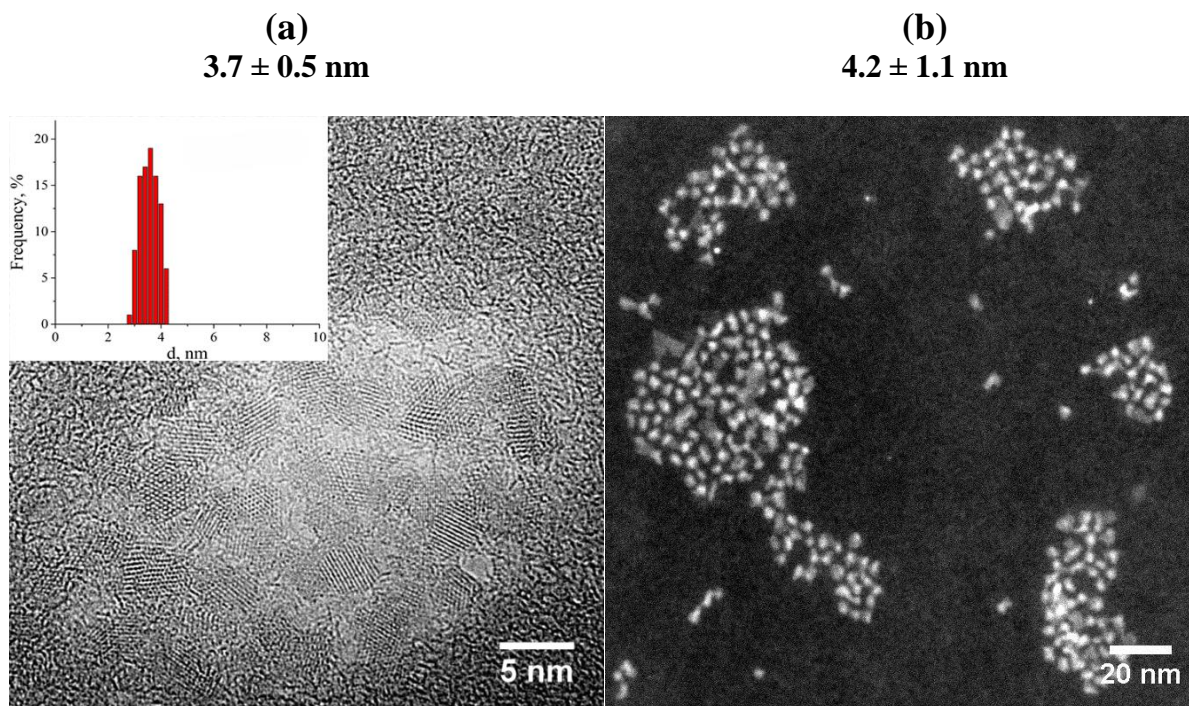


Figure 36 : Images HRTEM (à gauche) et STEM (à droite) des QDs de type CdSe/ZnS.

Les images illustrent l'existence de franges du réseau, l'absence de défauts visibles du réseau cristallin et la cristallinité élevée.

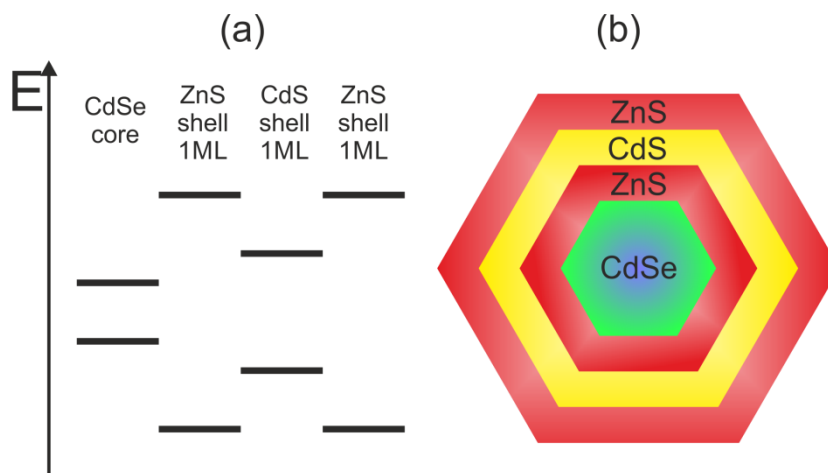


Figure 39 : a) Diagramme des niveaux d'énergie des nouveaux boîtes quantiques (QDs) de type cœur /multicoquille à base de CdSe/ZnS/CdS/ZnS/ZnS; b) Structure schématique de QD colloïdal cœur/multicoquille.

La figure montre la nouvelle structure de QD de type cœur /multicoquille à base de CdSe/ZnS/CdS/ZnS, qui est fondamentalement différente des structures classiques.

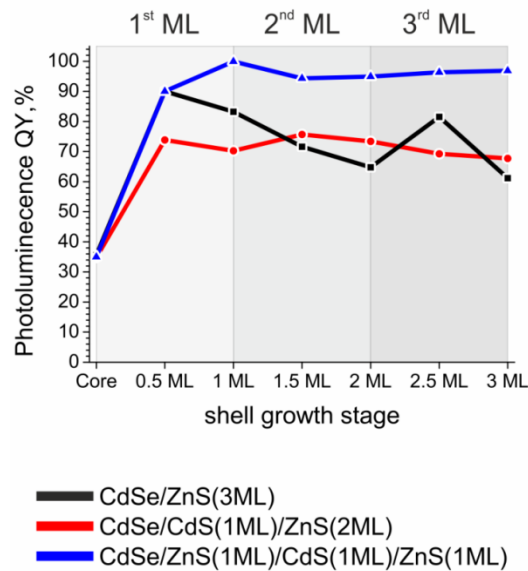


Figure 41: Evolution du QY de PL au cours de la croissance de la coquille des trois échantillons.

Tableau 7: Propriétés d'absorption et de photoluminescence des différents échantillons QD de structure cœur/coquille. Les résultats prouvent la supériorité de la structure des QDs multicoquilles par rapport à la structure classique. Le QY de PL de la structure QD multicoquille est de 97 %.

Sample type	Abs. _{max} , nm / PL _{max} , nm / FWHM, nm	PL QY, %
CdSe/ZnS	502 / 527 / 41	60
CdSe/CdS/ZnS	540 / 575 / 52	68
CdSe/ZnS/CdS/ZnS	541 / 563 / 39	97

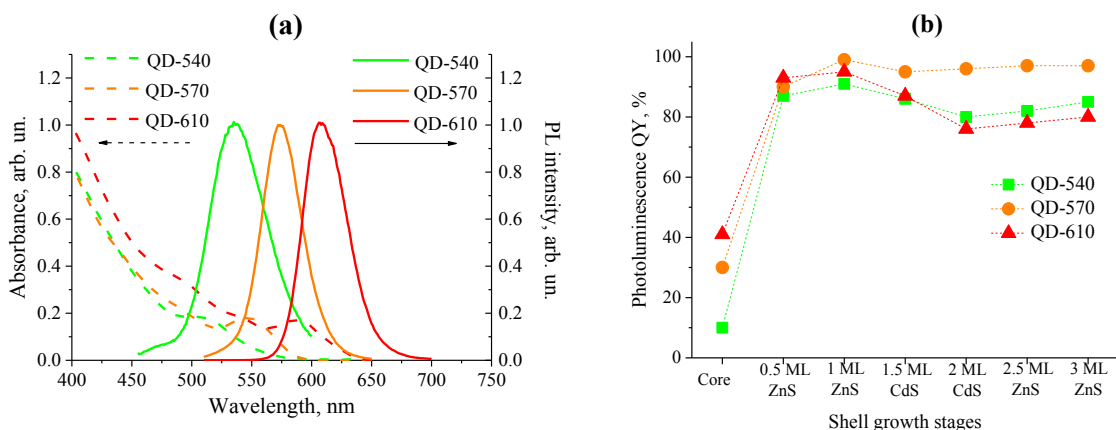


Figure 42: (a) Absorption et spectres de PL de QD-540, QD-570 et QD-610 (CdSe/ZnS/CdS/ZnS). (b) Évolution du QY de PL au cours de la croissance de la coquille des trois échantillons étudiés.

La figure illustre l'efficacité de la structure multicoquille quel que soit la taille des QDs et la longueur d'onde d'émission.

Solubilisation des très petits QDs dans l'eau

La méthode de transfert de phase des QDs organosolubles a été réalisée selon la réf. [250,251] avec quelques modifications, y compris le calcul des équivalents des ligands nécessaires et la maîtrise des conditions de solubilisation plus douces pour éviter l'agrégation des QDs ultra petits. La solubilisation des QDs a été effectuée en utilisant l'approche d'échange de ligands en deux étapes. Dans un premier temps, les ligands hydrophobes ont été échangés contre des résidus de DL-cystéine ; dans un deuxième temps, les DL-cystéines ont été échangées contre un mélange de deux dérivés PEG avec des groupes hydroxyle ou carboxyle terminaux.

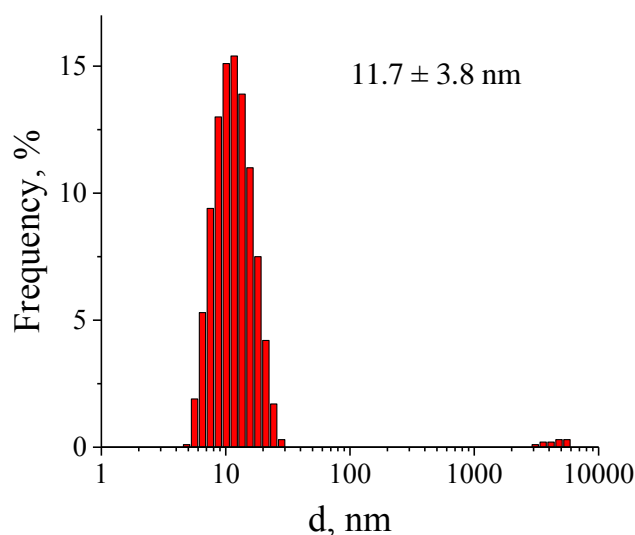


Figure 44 : Distribution granulométrique des QDs de type CdSe/ZnS, stabilisés avec du PEG dans un tampon phosphate (pH 8, 0.1 M) après purification de l'excès des dérivés du PEG.

	Mean (mV)	Area (%)	Width (mV)
Zeta Potential (mV): -12,6	Peak 1: -12,0	100,0	6,24
Zeta Deviation (mV): 13,3	Peak 2: 0,00	0,0	0,00
Conductivity (mS/cm): 0,160	Peak 3: 0,00	0,0	0,00

Result quality : Good

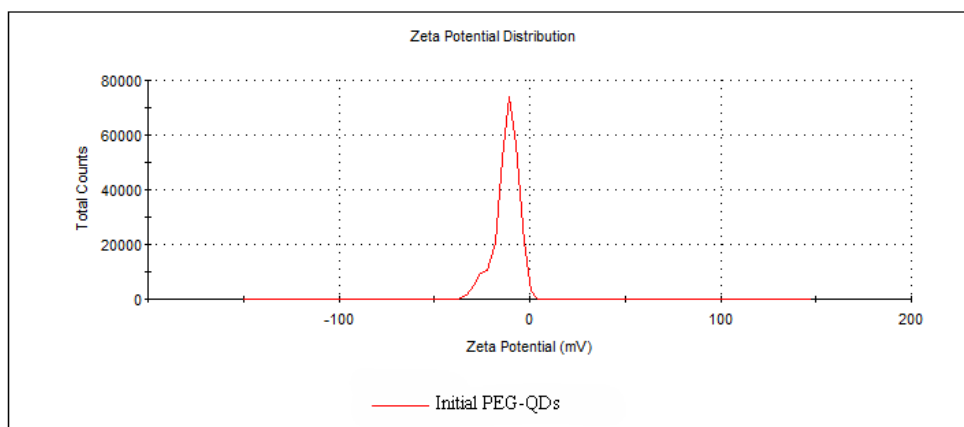


Figure 45 : Distribution du potentiel zêta des PEG-QDs. Les principales caractéristiques (distribution granulométrique et potentiel zêta) ont démontré la monodispersité de l'ensemble et la grande stabilité colloïdale des QDs en milieu aqueux.

Nous avons mis au point une méthode avancée pour la synthèse des QDs inférieurs à 2 nm, qui comprend l'arrêt de la croissance des QDs dès les premiers stades par congélation ultra-rapide du mélange réactionnel avec de l'azote liquide, suivie d'une chromatographie par perméation de gel pour la purification de haute performance des cœurs. Une augmentation du QY de PL de ces petits QDs a été obtenue par la croissance d'une coquille épitaxiale. Nous avons développé un modèle avancé de croissance des QDs, qui prend en compte les paramètres cristallographiques du matériau et la géométrie réelle des QDs. Le modèle est conforme à la fois à la littérature et à nos propres données, et il prédit avec précision les propriétés optiques des QDs et permet de calculer les quantités des précurseurs nécessaires à la croissance des QDs. L'exactitude du modèle proposé a été confirmée expérimentalement par la synthèse d'une série de QDs à plusieurs stades de croissance successifs dans l'intervalle de taille de 2,3-4,3 nm. L'applicabilité de ce modèle a été confirmée au cours des expériences de croissance épitaxiale de la coquille de ZnS. Le revêtement des cœurs de taille minimale avec des coquilles à trois couches a permis d'obtenir des QDs ultrapetits, très uniformes avec un QY de PL de 69%. Le revêtement des cœurs de CdSe avec une nouvelle structure de coquille multicouche assure l'obtention d'un QY de PL de plus de 80 % quelle que soit la taille des QDs. Le procédé d'échange de ligands en deux étapes a permis d'obtenir des QDs avec des dérivés de PEG, solubles dans l'eau.

Chapitre 4. Synthèse et caractérisation fonctionnelle, structurale et biologique des dérivés 4,5,9-trisubstitués de l'acridine

Le quatrième chapitre est consacré à la présentation de la voie de synthèse des dérivés 4,5,9-trisubstitués de l'acridine qui peuvent avoir une grande affinité pour les G-quadruplexes de l'ADN et une activité inhibitrice contre l'enzyme télomérase, qui est une cible importante du traitement antitumoral.

Synthèse des dérivés 4,5,9-trisubstitués de l'acridine

Ce composant biologiquement actif de la nanosonde devrait répondre aux exigences suivantes : (i) une forte affinité pour les structures stabilisées de l'ADN télomérique, appelées G-quadruplexes, qui est une condition préalable pour l'inhibition de l'activité enzymatique de la télomérase ; (ii) la possibilité de conjugaison avec la coquille organique des QDs par une liaison covalente directe. L'hydrophilie de la molécule, qui assure la solubilité dans un milieu aqueux et ne perturbe pas la stabilité colloïdale de la nanosonde, est également une condition importante pour le ligand.

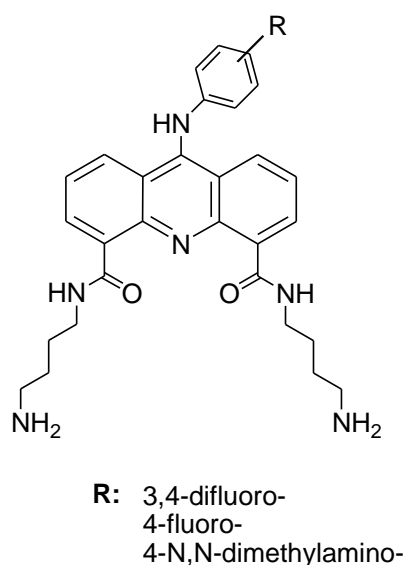


Figure 46 : Structures proposées des ligands acridiniques.

Les inhibiteurs potentiels ont été synthétisés à partir de la structure acridine (squelette), qui a été fonctionnalisée successivement aux positions C-4 et C-5 avec des chaînes de putrescines et sur le C-9 avec un noyau aniline, nécessaire à une meilleure stabilisation des G-quadruplexes de l'ADN. Les deux chaînes polyamine primaires sont censées augmenter la biocompatibilité et fournir la possibilité de conjugaison avec des QDs à fonction carboxyle.

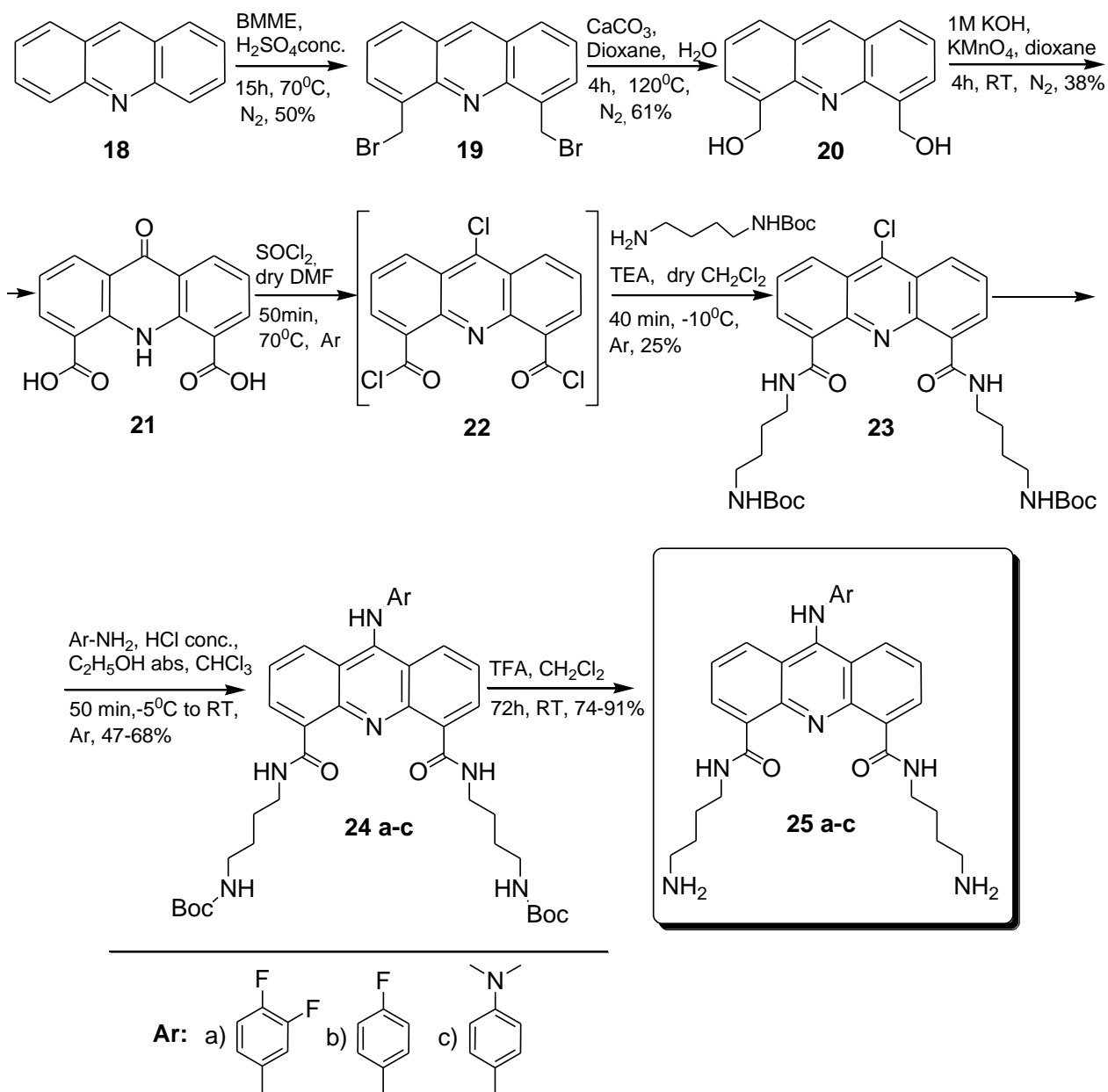


Figure 47 : Voie synthétique des dérivés 4,5,9-trisubstitués de l'acridine.

La figure illustre la voie synthétique de la molécule cible, qui se compose de sept réactions consécutives à partir de l'acridine. Les principales conditions réactionnelles sont également retrouvées sur la figure 50 : précurseurs, solvants, température et durée ainsi que le rendement des réactions.

La voie de synthèse comprend certaines étapes et approches qui ont été développées à l'Institut de Chimie Moléculaire de Reims (France) et qui ont déjà été décrites dans la littérature. L'étape clé est la synthèse de l'intermédiaire acridone 4,5-disubstituée. Elle est suivie d'une part la substitution des carbones C-4 et C-5 par deux chaînes putrescines, qui ont un groupe protecteur *tert*-butoxycarbonyl terminal (Boc), et d'autre part la fonctionnalisation de la

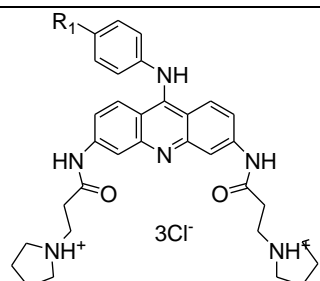
position C-9 par une des trois anilines (4-fluoroaniline, 3,4-difluoroaniline, *N,N*-diméthyl-*p*-phénylènediamine).

Évaluation biochimique des dérivés 4,5,9-trisubstitués de l'acridine

Afin d'augmenter la stabilité des dérivés 4,5,9-trisubstitués de l'acridine synthétisés, nous avons cristallisé les composés initiaux sous forme des sels de chlorhydrate, ce qui a assuré l'isolement des composés finaux sous une forme plus pure, ainsi que leur solubilité accrue dans les milieux aqueux. Par conséquent, trois dérivés 4,5,9-trisubstitués de l'acridine ont été synthétisés et caractérisés avec succès. Une gamme de molécules synthétisées est présentée sur le tableau 8.

Tableau 8 : Stabilisation du G-quadruplexe télomérique mesurée par les protocoles FRET et TRAP.

Compound		FRET, ΔT_m				TRAP
		20 μM	10 μM	5 μM	1 μM	IC ₅₀ , μM
(25a)		-	-	37.4	10.55	-
(25b)		-	-	38.01	12.1	4.20
(25c)		-	-	-	11.15	3.88

<p>BRACO 19 (reference)</p>		-	-	-	29.1	0.09
--	---	---	---	---	------	------

Nous évaluons également les dérivés de l'acridine synthétisés à l'aide des deux tests *in vitro* les plus populaires: (i) mesure de l'affinité des dérivés d'acridine synthétisés pour le G-quadruplexe télomérique de la séquence monobrin d'ADN (test FRET) et (ii) évaluation de la capacité des dérivés d'acridine à inhiber l'activité enzymatique de la télomérase (test TRAP). Les résultats de l'évaluation biologique ont montré des affinités élevées de toutes les molécules synthétisées (25a-c) pour les G-quadruplexes télomériques de l'ADN aux concentrations micromolaires. Dans le deuxième test, les capacités d'inhibition de la télomérase par des ligands ont été estimées en utilisant la séquence d'ADN télomérique humaine. Parmi les trois dérivés de l'acridine, le composé (25c) présente l'activité d'inhibition (mesurée par le protocole TRAP) micromolaire la plus élevée ($CI_{50} = 3.88$ mM). Les résultats des deux essais sont présentés sur le tableau 8.

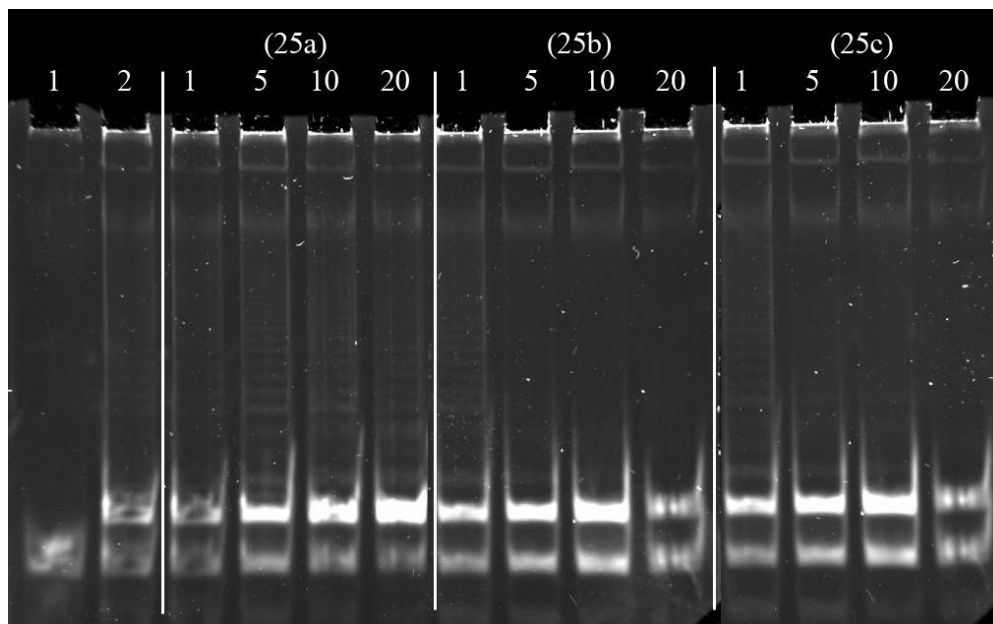


Figure 48 : Analyse du retard de gélification de la liaison des inhibiteurs potentiels avec la séquence nucléotidique du télomère. 1, Taq polymérase ; 2, séquence télomérique initiale avec Taq polymérase ; les voies restantes contiennent l'inhibiteur potentiel à différentes concentrations et un mélange de la séquence télomérique avec la Taq polymérase.

La figure illustre la capacité des molécules synthétisées à inhiber l'activité enzymatique de la télomérase.

Ainsi, les résultats ont confirmé la synthèse réussie d'un agent pharmacologique potentiel, et les essais basés sur l'évaluation biologique ont permis de sélectionner le composé le plus actif, qui a ensuite été utilisé pour l'assemblage de nanosondes multifonctionnelles.

Chapitre 5. Ingénierie, propriétés et application des nanosondes PL

Le cinquième chapitre est consacré à l'assemblage de nanosondes multifonctionnelles ainsi qu'à l'étude de leurs propriétés optiques et de l'étude cellulaire.

Synthèse des nanosondes multifonctionnelles

Initialement, le projet avait pour objectif de lier de manière covalente des QD soluble dans l'eau et de l'AL pour obtenir des nanosondes. Cependant, nous avons constaté que les QD et les AL peuvent former des complexes même sans réactif de couplage tel que la carbodiimide. Les nanosondes composées des QDs hydrosolubles et des dérivés d'acridine sous forme de complexes électrostatiques ont été préparées par le mélange direct des deux composants à pH 7.2. Les complexes électrostatiques obtenus ont été purifiés au moyen du GPC en utilisant le Sephadex G100 comme support stationnaire qui avait des limites optimales de poids moléculaire pour les QD. Par conséquent, il a été démontré que, malgré la nature électrostatique de l'interaction des composants, la nanosonde est très stable et ne se décompose pas dans les conditions physiologiques.

La formation de complexes a entraîné une légère augmentation de la taille hydrodynamique de 11.2 à 14.7 nm, tandis que la forme de la distribution n'a pas changé, ce qui indique l'absence d'agrégats et une grande homogénéité de la distribution des molécules ligands sur l'ensemble des QDs. Une augmentation du potentiel zêta, causée par une modification de la composition des ligands sur la surface des QDs a également été observée. On peut donc conclure une compensation pour la charge de surface négative des QDs et une diminution de sa valeur absolue due à la charge positive des groupes amines de l'AL.

Propriétés optiques des nanosondes

Les propriétés de la PL des nanosondes ont un rôle important pour leurs applications biologiques. Les ligands à base d'acridine sont des systèmes efficaces de transfert de charges en raison de leur structure polyaromatique, qui conduit à l'extinction de la PL des QDs. Nous avons constaté que la structure de la coquille du QD a un rôle déterminant sur le transfert d'électrons photo-induit (TEP) du QD sur le ligand acridine, ce qui conduit à l'extinction de la photoluminescence des QDs.

Le transfert de charge des molécules de QD aux molécules de ligands entraîne la diminution de PL du QD et, par conséquent, l'extinction de la fluorescence du QD. Nous supposons que dans le système étudié, l'extinction est causée par le transfert d'électrons du QD à l'AL, en raison de la proximité des niveaux d'énergie LUMO des deux composants (Figure 56). Nous avons constaté que la structure du QD de type CdSe/ZnS/CdS/ZnS à coquilles multiples offre une réduction minimale du rendement quantique de photoluminescence à une épaisseur de coquille minimale comparativement aux coquilles minces classiques, composées du ZnS ou aux coquilles "géantes". Ainsi, notre approche de l'ingénierie à haut potentiel de confinement par la création d'une nouvelle structure QD "multicoquilles" permet de supprimer le PET avec une grande efficacité contrairement aux structures classiques.

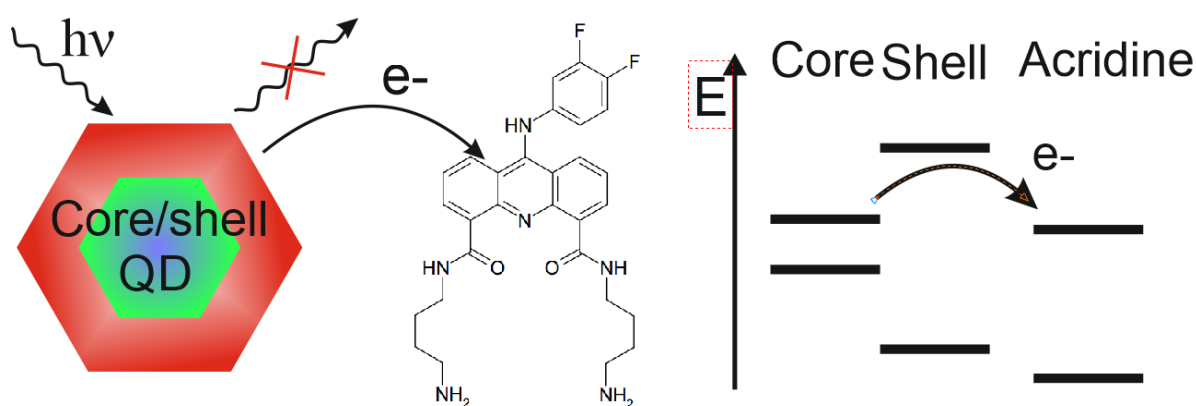


Figure 55: Illustration schématique du mécanisme de transfert d'électrons photoinduit du QD cœur/coquille vers le ligand acridine.

Toxicité et absorption cellulaire des nanosondes et de leurs composants

Les QDs sont les composants les plus toxiques du système, ce qui détermine la toxicité de la nanosonde. Notamment, la concentration de toxicité de l'AL était inférieure à celle de la plupart des autres dérivés de l'acridine étudiés précédemment (1 - 50 μM), ce qui rend ce composé prometteur en tant qu'agent pharmacologique pour la suppression de l'activité de la télomérase dans les cellules cancéreuses et nécessite des études biochimiques supplémentaires.

Les résultats obtenus sur la toxicité des QDs dans une culture de monocytes nous permettent d'étudier les QDs de structure CdSe/ZnS cœur/coquille dans les conditions *in vitro* par microscopie confocale au laser. Le résultat montre que les QD avec une concentration de $8 \cdot 10^{-8}$ M peuvent être détectés dans les cellules monocytes après 10 min d'incubation.

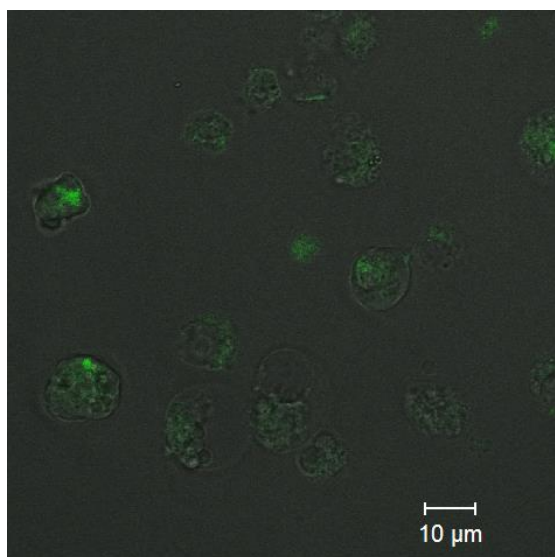


Figure 57: Images au microscope confocale à fluorescence.

Des expériences d'imagerie fluorescentes des cellules ont montré que des QDs ultra-petits de 3,7 nm pouvaient pénétrer rapidement dans les cellules après 10 min d'incubation en maintenant une PL intense. Ainsi, les QDs ultrapetits à cœur/coquille peuvent être utilisés comme agent fluorescent de sondes compactes pour la mise au point de systèmes d'administration de médicaments et de diagnostic du cancer. Ce travail nécessite la poursuite et l'étude complète du comportement de la nanosonde et de ses composants *in vitro*.

Sachant que les QDs sont « englutis » par une culture de monocytes sans perdre leurs propriétés fluorescentes, nous pouvons considérer les QDs de CdSe/ZnS cœur/coquille comme un outil utile pour l'imagerie *in vitro* des processus cellulaires, la détection des cellules cancéreuses et le développement des systèmes de libération des médicaments. L'utilisation des QDs dans les outils d'imagerie pourrait amener le diagnostic du cancer à un autre niveau en raison des propriétés physico-chimiques uniques et de la petite taille des QDs.

Conclusions et perspectives en français

Les résultats présentés dans cette étude démontrent la faisabilité de nouvelles approches pour la synthèse des QDs ultrapetits avec un QY de PL maximum et une stabilité colloïdale élevée pour la synthèse des nanosondes pharmacologiques photoluminescentes, à base de QDs et de nouveaux dérivés de l'acridine, considérés comme inhibiteurs potentiels de l'activité de la télomérase dans les cellules cancéreuses.

Le premier chapitre présente un aperçu de la littérature, qui comprend l'ingénierie de pointe des sondes PL à base de colorants organiques et des QDs. Nous avons présenté la synthèse des QDs cœur/coquille pour les applications biologiques et la stratégie visant à atteindre le QY de PL maximal en optimisant la structure de la coquille. Ensuite les principales classes des composés

organiques polyaromatiques contenant de l'azote, y compris des dérivés di- et trisubstitués de l'acridine comme les ligands du G-quadruplex les plus prometteurs, sont examinées en détail. La synthèse des QDs et des biomolécules ainsi que les problèmes de leur stabilité colloïdale et de leur toxicité sont brièvement décrits.

Dans le deuxième chapitre, les protocoles et les méthodes de caractérisation utilisées tout au long de cette thèse sont présentés. La voie de synthèse colloïdale des QDs cœur/coquille de haute qualité, la synthèse des dérivés 4,5,9-trisubstitués de l'acridine, ainsi que l'assemblage des nanosondes sont décrits en détail.

Le troisième chapitre traite la synthèse des QDs. Les QDs idéaux pour les applications biologiques devraient être compacts et avoir une PL brillante et une stabilité colloïdale élevée. Nous avons mis au point une méthode avancée pour la synthèse des QDs inférieurs à 2 nm, qui comprend l'arrêt de la croissance des QDs dès les premiers stades par congélation ultra-rapide du mélange réactionnel avec de l'azote liquide, suivie d'une chromatographie par perméation de gel pour la purification de haute performance des cœurs. Une augmentation du QY de PL de ces petits QDs a été obtenue par la croissance d'une coquille épitaxiale. Le modèle traditionnel de la croissance de la coquille couche par couche en supposant une géométrie sphérique des QDs présente des inconvénients importants et ne permet pas un contrôle précis de la croissance des QDs. Nous avons développé un modèle avancé de la croissance des QDs, qui prend en compte les paramètres cristallographiques du matériau et la géométrie réelle des QDs. Le modèle est conforme à la fois à la littérature et à nos propres données, et il prédit avec précision les propriétés optiques des QDs et permet de calculer les quantités des précurseurs nécessaires à la croissance des QDs. La précision du modèle proposé a été confirmée expérimentalement par la synthèse d'une série de QDs à plusieurs stades de croissance successifs dans un intervalle de taille entre 2,3 et 4,3 nm dont les spectres PL se chevauchent pour couvrir toute la gamme de la lumière visible. L'applicabilité de ce modèle a été confirmée lors des expériences de croissance épitaxiale de la coquille de ZnS. Le revêtement des cœurs de taille minimale avec des coquilles à trois couches a permis d'obtenir des QDs ultrapetits, très uniformes avec un QY de PL de 69%. La grande reproductibilité de cette méthode ouvre de nouveaux horizons pour l'utilisation des QDs à base de CdSe à cœur/coquille ultrapetit dans la synthèse de nanosondes photoluminescentes, compactes pour l'imagerie intracellulaire.

L'efficacité de PL des QDs de type CdSe/ZnS n'est pas optimale, ce qui indique qu'il y a quelques inconvénients de la structure énergétique des QDs cœur/coquille. Pour résoudre ce problème, nous avons développé la nouvelle structure CdSe/ZnS/CdS/ZnS/ZnS à cœur/multicoquilles avec un confinement très efficace des porteurs de charge. Dans cette structure, la première monocouche de la coquille de ZnS constitue la barrière potentielle la plus

élevée pour les paires électron-trou, assurant ainsi le résultat maximal de l'émission photoluminescente. La seconde, une coquille de CdS avec une barrière de potentiel importante, sépare deux monocouches de la coquille de ZnS et augmente l'épaisseur de la coquille, réduisant ainsi la probabilité d'un effet tunnel d'un porteur de charge. La dernière coquille en ZnS crée une barrière potentielle supplémentaire et est en outre parfaitement compatible avec les protocoles courants d'échange de ligands de surface pour la solubilisation des QDs et leur fonctionnalisation pour les applications biomédicales. La nouvelle structure « multicoquille » a permis d'augmenter le QY de PL à plus de 79% pour toutes les séries de QDs de différentes tailles, ce qui confirme l'efficacité de la nouvelle structure de la coquille. Les résultats présentés dans ce chapitre prouvent l'efficacité des approches novatrices, proposées pour la synthèse des QDs ultrafins pour des applications biomédicales.

La synthèse des petits QDs à faible taux de nucléation est inextricablement liée au problème du faible rendement de la réaction. Le procédé de synthèse par injection à chaud pourrait convenir à la synthèse des QDs en batch, sinon à la faible reproductibilité, qui est le principal défaut de l'approche. De plus, des conditions réactionnelles optimisées peuvent simplifier la procédure de synthèse, en excluant les étapes longues et complexes du traitement et de l'isolement des nanoparticules. En fin de compte, cela augmenterait la reproductibilité des techniques et réduirait le temps et le coût de leur préparation. Pour les travaux futurs, des combinaisons de différents types de solvants, de précurseurs et d'agents de surface peuvent être testées afin de mettre au point des méthodes simples et reproductibles pour la synthèse de QDs de haute qualité en quantités de batch.

De plus, les problèmes de clignotement et d'extinction de la PL causés par le transfert de charge à l'intérieur des QDs ou par un donneur ou accepteur externe en tant qu'agent pharmacologique sont des inconvénients significatifs de tous les QDs semi-conducteurs. L'étude des mécanismes de charge des QDs et la recherche de nouveaux moyens de les supprimer permettront d'accroître la stabilité de la PL des QDs individuels, ce qui, sur le plan pratique, ouvre de nouvelles perspectives pour les systèmes de diagnostic précoce utilisant la détection des signaux des QDs individuels.

Le quatrième chapitre traite la synthèse des dérivés 4,5,9-trisubstitués de l'acridine qui peuvent avoir une grande affinité pour les G-quadruplexes de l'ADN et une activité inhibitrice contre l'enzyme télomérase, qui est une cible importante du traitement antitumoral. Ce composant potentiel biologiquement actif de la nanosonde devrait répondre aux exigences suivantes : (i) une forte affinité pour les structures stabilisées de l'ADN télomérique, appelées G-quadruplexes, qui est une condition préalable à l'inhibition de l'activité télomérase ; (ii) la possibilité de conjugaison avec la coquille organique des QDs par liaison covalente directe entre

elles. L'hydrophilie de la molécule, qui assure la solubilité dans un milieu aqueux et ne perturbe pas la stabilité colloïdale de la nanosonde, est également une condition importante pour le ligand.

Les inhibiteurs potentiels ont été synthétisés à partir de l'acridine, qui a été fonctionnalisée successivement aux positions C-4 et C-5 avec des chaînes putrescine et à la position C-9 avec un fragment aniline, nécessaire à une meilleure stabilisation des G quadruplexes de l'ADN. Les deux chaînes polyamine primaires sont censées augmenter la biocompatibilité et fournir la possibilité de conjugaison avec des QDs portant des fonctions acide carboxylique. Afin d'augmenter la stabilité des dérivés 4,5,9-trisubstitués de l'acridine, nous avons cristallisé les composés initiaux sous forme des sels de chlorhydrate, ce qui a assuré l'isolement des composés finaux sous une forme plus pure, ainsi que leur solubilité accrue dans les milieux aqueux. Par conséquent, trois dérivés 4,5,9-trisubstitués de l'acridine ont été synthétisés et caractérisés avec succès.

Nous avons également étudié les dérivés de l'acridine synthétisés à l'aide des deux tests *in vitro* les plus populaires : (i) mesure de l'affinité des dérivés d'acridine synthétisés pour le G-quadruplexe télomérique de la séquence monobrin de l'ADN (test FRET) et (ii) évaluation de la capacité des dérivés d'acridine à inhiber l'activité enzymatique de la télomérase (test TRAP). Les résultats de l'évaluation biologique ont montré des affinités élevées de toutes les molécules synthétisées (**25a-c**) pour le G-quadruplexe télomérique de l'ADN aux concentrations micromolaires. Dans le deuxième test, les capacités d'inhibition de la télomérase par des ligands ont été estimées en utilisant la séquence d'ADN télomérique humaine. Parmi les trois dérivés de l'acridine, le composé (**25c**) présente l'activité inhibitrice micromolaire la plus élevée ($CI_{50} = 3.88$ mM) utilisant le protocole TRAP, c'est-à-dire un résultat comparable à celui observé avec d'autres analogues acridiniques. Ainsi, nos résultats ont confirmé le succès de la synthèse d'un agent pharmacologique potentiel, et les essais basés sur l'évaluation biologique nous ont permis de sélectionner le composé le plus actif, qui a ensuite été utilisé pour l'assemblage des nanosondes multifonctionnelles.

Nous supposons que l'approche alternative à la purification des dérivés 4,5,9-trisubstitués de l'acridine utilisant une résine modifiée en C-8, C-18 pour la chromatographie en phase inverse pourrait être prometteuse, mais d'autres méthodes y compris la purification en mode de refroidissement sont également envisageables. La résolution du problème de la faible stabilité des produits intermédiaires et des dérivés finaux, trisubstitués de l'acridine permettra d'accroître la pureté des produits finaux, ce qui est crucial pour la poursuite des recherches pharmacologiques sur les nouveaux composés. Il est également important de rechercher une classe alternative, plus stable et plus active de composés organiques ayant une activité inhibitrice

élevée envers la télomérase dans les cellules cancéreuses dans le cadre de la conception des nanosondes pharmacologiques.

Le cinquième chapitre décrit la synthèse et l'évaluation biologique des nanosondes comportant des QDs et des dérivés synthétisés de l'acridine. Les nanosondes composées de QDs hydrosolubles et de dérivés d'acridine sous forme de complexes électrostatiques ont été préparées par le mélange direct de deux composants à pH 7.2. Les complexes électrostatiques obtenus ont été purifiés au moyen du SEC. Les nanosondes obtenues ont été purifiées à partir de composés de faible poids moléculaire par chromatographie par perméation de gel et caractérisées par spectrométrie d'absorption. Nous avons constaté que la formation de nanosondes a entraîné une importante extinction de la PL des QD de CdSe/ZnS, causée par le transfert photoinduit d'électrons. Nous avons montré que la structure de la coquille du QD joue un rôle clé dans le développement des nanosondes photoluminescentes. L'utilisation des QDs de type cœur/multicoquille permet de réduire considérablement l'extinction de la fluorescence grâce à un confinement très efficace des porteurs de charge dans la structure de la coquille.

De plus, nous avons estimé de façon préliminaire la toxicité et la plage de concentration opérationnelle des QDs ultrapetits et des dérivés de l'acridine au moyen de l'essai MTT à l'aide de monocytes. Nous avons constaté que la toxicité des QDs ultrapetits était comparable à celle des QDs plus grands de même structure, tandis que la toxicité des dérivés de l'acridine était nettement inférieure à celle des autres analogues et des QDs.

Enfin, la microscopie confocale a été utilisée pour montrer que les QDs ultrapetits pénètrent dans les cellules tout en conservant leur PL brillante et leur stabilité colloïdale. Ainsi, la miniaturisation des QDs assure une pénétration accélérée à travers la membrane cellulaire et rend les QDs ultra petits plus attractifs que les QDs de taille normale.

Ces résultats prouvent l'efficacité de l'approche proposée pour l'ingénierie des nanosondes multifonctionnelles basées sur des QDs avancés. En raison de leur petite taille et de leur PL brillant, les QDs CdSe/ZnS synthétisés sont des étiquettes photoluminescentes pratiques pour une nanosonde théranostique, destinée à l'imagerie et à l'administration rapide de médicaments dans les cellules.

Sachant que les QDs sont engloutis par une culture de monocytes sans perdre leurs propriétés fluorescentes, nous pouvons considérer les QDs CdSe/ZnS core/shell comme un outil utile pour l'imagerie *in vitro/in vivo* des processus cellulaires, la détection des cellules cancéreuses et le développement des systèmes pour la libération des médicaments. L'utilisation des QDs dans les outils d'imagerie pourrait amener le diagnostic du cancer à un autre niveau en raison des propriétés physiques et chimiques uniques et de la petite taille des QDs.

Introduction

The incidence rate of malignant tumours is continuously growing. About six million new cases of cancer are diagnosed annually in the world every year. One of the current strategies for the development of advanced treatment methods focuses on targeted drug delivery to tumor cells, which ensures low concentrations of toxic drugs in healthy tissues. In this case, in addition to the high specific targeting molecule, the drug may be conjugated with a label, usually a magnetic, radioactive, or photoluminescent one. Optical imaging, which is relatively inexpensive and easy to implement, is currently the leading trend in imaging-guided therapy. It relies on the detection of photons transmitted through tissues and provides noninvasive tracking of drug carriers and monitoring of treatment. Linking an imaging (photoluminescent (PL)) agent to a biomarker-recognizing molecule and a pharmacological agent ensures real-time tracking of the delivery of the active substance. Although organic fluorophores (photoluminescent dyes and proteins), traditionally used for engineering diagnostic or therapeutic probes have some advantages, such as a high PL quantum yield (QY) and good compatibility with aqueous media, there are also significant drawbacks that limit their use, notably a low photostability and a narrow absorption spectrum precluding the excitation of the photoluminescence of different organic fluorophores at a single wavelength.

Quantum dots (QDs) are semiconductor nanocrystals (NCs) several nanometers in size capable of photoluminescence in a wide spectral range. Their energy structure and characteristics of light absorption and PL strongly depend on the QD size because of the quantum confinement effect, which accounts for their unique optical characteristics, including size-tunable light emission and a high signal brightness [1]. In particular, using the most common QD type based on cadmium selenide, one can obtain materials with intense PL in the visible region of the spectrum (450–650 nm). At present, the most widespread QDs are those of the core/shell type, where a thin epitaxial shell of a wider-bandgap semiconductor (for example CdS or ZnS) is deposited on the PL CdSe core in order to enhance confinement of charge carriers inside the core and to protect it from the reaction with the ambient medium. In addition, application of this protective shell noticeably simplifies the functionalization of the QD surface with hydrophilic ligands for transfer of the former into aqueous media, as well as with the capture or drug molecules for obtaining multifunctional nanoprobes.

QDs can be used in a wide variety of applications and technologies, which has stimulated efforts towards the development and investigation of QD-based materials and control of their morphology at the nanoscale. A typical biomedical application of QDs is their use as PL labels,

which are advantageous over the routinely used organic dyes due to the unique optical properties.

The use of QDs as PL labels in biology has been limited by the difficulty of solubilizing and low colloidal stability of QDs in an aqueous medium, non-homogeneity of QD ensemble properties, and a strong quenching of PL with polar water molecules. Optimization of QD characteristics includes developments aimed at ensuring particle uniformity, narrow and symmetrical emission bands, a high PL quantum efficiency, and minimal blinking of individual QDs. Computer-aided modeling and theoretical simulations of QD physics and chemistry, for example the study of the influence of the ligand layer and crystal lattice defects of the core/shell system on the optical properties, control of crystal growth, etc., have become a major future concern of the research community. In terms of chemical synthesis, the latest advances have been made in modifying passivated inorganic shells by using novel shell structures, and approaches to the shell growth, that has led to a significant improvement of QD properties. Nevertheless, applications in biomedicine research suffer from the lack of easy, versatile, and reproducible production techniques to prepare highly stable QDs with a quantum efficiency close to 100%.

The uncontrolled growth of cancer cells usually starts due to factors stimulating cell proliferation. Anticancer drugs either kill cancer cells or modify their growth. Inhibitors of the enzymes responsible for DNA replication have become the focus of cancer treatment [2]. Heterocyclic moieties fused with an aromatic system with various heteroatoms, such as N, S, and O, have a wide spectrum of pharmacological effects. Synthesis of bioactive nitrogen-containing heterocyclic compounds has been a subject of great interest due to their important roles in cell biology, including DNA replication, DNA transcription, and segregation of chromosomes during mitosis. Inhibition of enzyme expression by stabilizing both single- and double-stranded DNA can trigger cellular signal transduction pathways leading to cancer cell death. Ensuring targeted delivery of biologically active molecules into the cell is one of the key tasks in the development of anticancer drugs of modern generations. Since cellular membrane defense mechanisms limit intracellular delivery of therapeutic agents [3], intracellular delivery using membrane vectors (molecules with affinity for cell membranes) is a promising method that has been successfully used to transport various functional agents. Properly chosen vector can transport the drug molecule or nanoparticle into the cell or nucleus [4]. Various natural polyamines (putrescine, spermine, spermidine) are convenient vectors for introducing cytotoxic agents into cancer cells. The main way to create probes for targeted drug delivery is to modify the pharmacological agent with the vector residue. The assembly of a pharmacological agent with an imaging fluorescence

agent [5] would ensure both delivery of the active substance into a cancer cell and its spatiotemporal tracking.

The goal and originality of the thesis consist of the synthesis of PL core/shell QDs with optimal optical properties for biomedical applications. For this purpose, the following tasks have been performed: (1) the modeling of QD growth using material physics-based design principles; (2) the synthesis of homogeneous defect-free QD cores; (3) their coating with shells of different chemical compositions; (4) the synthesis of novel DNA ligands capable of conjugating with water-soluble QDs; and (5) the assembling of multifunctional nanoprobe and their biological evaluation *in vitro*.

This research work was carried out as part of a joint international PhD project of the University of Reims Champagne-Ardenne and Moscow State University. The goal of this project, co-supervised by the French research group headed by Prof. Nabiev (EA 4682) and Prof. Sapi (ICMR, UMR CNRS 7312) and the Russian research group headed by Prof. Sidorov (Laboratory of Thermochemistry of Moscow State University) is to develop QDs with advanced colloidal and optical properties for biological applications, such as engineering of compact conjugates of QDs with acridine derivatives, novel potential anticancer agents capable of effectively stabilizing the telomeric G-quadruplex sequences of human DNA.

The **nanotechnological part of this project** was planned to tailor the structure of the PL nanocrystals during their preparation to obtain the following advanced properties: (1) the minimal size of the QDs, which is required for rapid penetration into cells; (2) a PL QY higher than 90%; and (3) a high size homogeneity of QDs in ensembles. Prof. Nabiev's research group has achieved breakthrough results in the colloidal synthesis of QDs, as well as functionalization of the QD surface. Prof. Sidorov's laboratory has much experience in simulation of ideal nanoparticles as well as characterization of bio-molecules on the surface of nanoparticles with mass spectrometry and nuclear magnetic resonance methods. Combining the achievements of the two research groups made it possible to carry out a comprehensive study on modeling ideal QD structures and experimentally validate the resultant models by means of colloidal synthesis of high-quality QDs and subsequent complex characterization.

The **therapeutic part of the project**, related to biomedical applications of advanced QDs, focuses on (1) the design of acridine-derived anticancer agents and their conjugation with specific vehicles ensuring their internalization into tumor cells and (2) the attachment of QDs to the conjugate, which will allow imaging of this nanoprobe. Prof. Sapi's team specializes in the synthesis of nitrogen-containing polyaromatic heterocyclic molecules with a high affinity for telomeric G-quadruplexes of DNA. Synthesis of novel potential anticancer agents, acridine derivatives, and their conjugation with QDs using the approaches developed by Prof. Nabiev's

team allowed obtaining multifunctional nanoprobe. The biological evaluation of the pharmacological agent and imaging probes by Dr. Brassart (Médyc, UMR 7369) and Dr. Baryshnikova (Blokhin Russian Cancer Research Center) has proved the effectiveness of the developed QDs with advanced properties and multifunctional nanoprobe.

The **first chapter** of this thesis is a literature review on the design of multifunctional PL probes. It is divided into three main sections. In the first part, the main types of PL probes carrying a diagnostic or therapeutic agent and imaging agents, such as organic dyes or PL nanocrystals (NCs), are reviewed. The second part of the chapter discusses in detail the general physical and chemical properties of QDs and the strategies for enhancing the quantum confinement, including giant (thick) shell, multishell, and alloyed epitaxial shell growth. The third part of the chapter deals with the stabilization of telomere G-quadruplexes with small molecules. Particular attention is paid to acridine derivatives, including 4,5-disubstituted and 3,6,9-trisubstituted ones, as potential inhibitors of telomerase activity in cancer cells. The main approaches to the biological evaluation of G-quadruplex stabilization effectiveness and selectivity of telomerase inhibition are briefly discussed.

In the **second chapter**, the detailed protocols, as well as characterization methods used throughout this thesis, are presented. First, the methods of colloidal synthesis of CdSe cores and core/shell QDs with different shell compositions obtained using the layer-by-layer approach are described. Briefly, the exact methods for growing an inorganic shell of a specified thickness atop CdSe cores, as well as an organic shell for solubilization of core/shell QDs, is described. Secondly, the multistage protocol of the synthesis of 4,5,9-trisubstituted acridine derivatives is described in detail. In addition, the results of the characterization of the synthesized molecules (nuclear magnetic resonance spectroscopy and mass spectrometry, thin layer chromatography) are given. The protocol of the conjugation of water-soluble QDs and novel acridine-based ligands using carbodiimide chemistry is described. Finally, various techniques for characterization of physical, chemical, and biological properties of the conjugates and their components are described.

In the **third chapter**, the results of colloidal synthesis of CdSe cores and core/shell QDs of different structure are discussed in detail. The influence of the following principal reaction parameters on the homogeneity of the CdSe core ensemble and QD properties are analyzed: the different types of the precursors used, the various type of the organic synthesis medium, the temperature of injection, the reaction duration, and the ratio between the cadmium and selenium precursors. The size-dependent spectral properties of CdSe QDs are analyzed in terms of the synthesis of ultrasmall cores. The necessity and efficiency of gel penetration chromatography for high-performance purification of the ultrasmall cores, as well as the results of precise calculation

of shell precursor amounts, are experimentally confirmed. Size, morphology, crystalline structure and chemical composition of the best QDs samples are analyzed. Finally ultrasmall QDs were solubilized into aqueous media by means of two step ligand exchange approach.

In the **fourth chapter**, the structures of the proposed DNA ligands are reviewed, and the selection of the substituents of the acridine framework are substantiated in detail. The synthetic pathway for obtaining 4,5,9-trisubstituted acridine derivatives is described. The biological evaluation is performed using the fluorescence resonance energy transfer melting assay and telomeric repeat amplification protocol assay.

The **fifth chapter** focuses on the conjugation of water-soluble CdSe/ZnS QDs with 4,5,9-trisubstituted acridine derivatives. The conjugation of the components was performed with the use carbodiimide bond-forming chemistry. The success of the bioconjugation process is estimated and discussed. The cellular toxicities of the conjugates and their components are measured using a colorimetric assay for assessing cell metabolic activity. Cellular uptake is investigated with confocal microscopy.

1. Chapter 1. Review of the literature

1.1. Photoluminescent probes for imaging and drug delivery

Cancer is one of the most serious health threats worldwide. There are expected to be 18.1 million new cancer cases and 9.6 million cancer deaths in 2018, according to the GLOBOCAN estimates [6]. Although increasingly more cancer patients could be diagnosed and treated early due to the progress in cancer screening and control programs [7], the survival rate remains poor, with no significant reduction in mortality over the past several decades, especially in developing countries [8].

Sensitive methods for detection of biomarkers, such as proteins and nucleic acids, are important for diagnosis, making therapeutic decisions, and therapy monitoring (also as part of personalized medicine) [9]. When biomarkers are identified, sensors with high sensitivity, selectivity, and stability are needed. Recent decades have seen an enormous progress in development of luminescent diagnostic probes [10]. Compared to more conventional analytical tools, optical probes have the advantage of being only minimally invasive; in addition, they can be prepared in a variety of forms, including small-molecule probes, analyte-sensitive nanoparticles, and fiber-optic or planar optical sensors [11].

Enzyme-linked immunosorbent assay (ELISA) is an immunoassay used for medical diagnosis, for quality control in different fields of industry, and as an analytical tool in biomedical research [12]. It is intended for the detection and quantification of antigens in a given sample. In the basic setup, an antibody labeled with an enzyme binds to the antigen of interest. The linked enzyme catalyzes a color change through cleavage of a chromogenic substrate. The visible color can then be detected by colorimetric readout and provide quantitative and/or qualitative information about the antigen or antibody present in the sample [13]. In the so-called fluorescence-linked immunosorbent assay (FLISA), fluorescently labeled antibodies or analytes are used for detection. In FLISA, there is no need for addition of a substrate, and the fluorescence can be directly detected in a microplate reader. However, organic fluorescent dyes have several disadvantages: they have to be excited at different wavelengths, have an asymmetrical unsharpened emission peak [14], and suffer from photobleaching [15]. Therefore, quantum dots should be used as fluorescent labels.

Quantum-dot-based FLISA has several advantages over ELISA:

- (i) Due to a higher signal-to-noise ratio and high brightness of quantum dots, the limit of detection can be decreased in FLISA compared to ELISA.
- (ii) The readout is not time-dependent. Since this system is not based on the enzymatic activity to produce substrate, there will be no substrate saturation after a certain time.

Since quantum dots do not suffer from photobleaching, there is no need to perform readout within a definite time period. This also means that the results of different FLISAs are better comparable.

- (iii) FLISA is more robust than ELISA. Because FLISA does not depend on enzyme activity, it is less sensitive to temperature and pH.

Several research groups have used QDs for designing FLISAs. Lv et al. have shown that a quantum-dot-based FLISA is superior over ELISA for detection of C-reactive protein; Zhang et al. have developed a quantum-dot-based FLISA that detects morphine [16], and Yao et al., a FLISA technique for detecting ochratoxin A [17].

In comparison with organic dyes, QDs are about 10–100 times brighter, mainly due to their large absorption cross sections, are 100–1000 times more stable against photobleaching, and have narrower and more symmetric emission spectra. In addition, a single light source can be used to excite QDs with different emission wavelengths, which can be tuned from the ultraviolet to the visible, near-infrared, and even mid-infrared spectral regions [18].

In comparison with small organic fluorophores, QDs have large surfaces that can be modified through versatile chemistry. This makes QDs convenient scaffolds to accommodate therapeutic agents (e.g., anticancer drugs) through chemical linkage or simple physical immobilization. This may enable the development of a nearly limitless library of multifunctional nanostructures for imaging and therapy.

Given the favorable fluorescent properties of QDs as fluorescent labels, especially the narrow symmetrical fluorescent peaks and the possibility to excite them simultaneously at the same wavelength [14,15], multiplexing is only limited by the color separation capacity of the imaging system.

However, QDs are an order of magnitude larger than organic dye macromolecules, which may limit their use in applications in which the size of the fluorescent label should be minimized.

Drug-containing nanoparticles have shown great promise for treating tumors in cell models and even in clinical trials [18]. Both passive and active targetings of QDs have been used to increase the local concentration of chemotherapeutics in the tumor. The size and structure similarities between imaging and therapeutic nanoparticles make it possible to combine their functions in order to directly monitor the drug biodistribution, improve treatment specificity, and reduce side effects. This result has become the principal foundation for the development of multifunctional nanoprobes for combined imaging and cancer treatment.

For example, Farokhzad et al. reported a ternary system composed of a QD, an aptamer, and the small-molecule anticancer drug doxorubicin for *in vitro* imaging, targeted delivery, and

sensing of drug release [19]. The aptamers were conjugated to QDs to serve as targeting units, and doxorubicin was attached to the stem region of the aptamers, taking advantage of the nucleic acid binding ability of doxorubicin [20]. Two donor-quencher pairs of fluorescence resonance energy transfer occurred in this construct, since the QD fluorescence was quenched by doxorubicin, and that of doxorubicin was quenched by the double-stranded RNA aptamers. As a result, gradual release of doxorubicin from the conjugate was found to “switch on” the fluorescence of both QDs and Dox, providing a means to sense the release of the drug. However, it is clear that the current design of this conjugate will not be sufficient for *in vivo* use unless the drug loading capacity can be considerably increased (currently, it is seven to eight Dox molecules per QD).

For oncological and other medical applications, important functions are imaging, therapy (a single drug or a combination of two or more drugs), and targeting (one or more ligands). With each added function, QDs could be designed to have novel properties and applications. For example, binary nanoparticles with two functions could be developed for molecular imaging, targeted therapy, or simultaneous imaging and therapy. Ternary nanoparticles with three functions could be designed for imaging and therapy combined with targeting, targeted dual-modality imaging, or targeted dual-drug therapy.

Most developments are still at the proof-of-concept stage using cultured cancer cells, and they cannot be applied to *in vivo* imaging and treatment of solid tumors at the moment. To date, the use of functionalized QDs as ultrasensitive probes for *in vitro* biodiagnostics seems to be the most important and clinically relevant application of QDs, in particular, because relative toxicity is of no concern in this case [21]. These studies will guide the future design and optimization of multifunctional nanoprobes for *in vitro* imaging and therapy.

1.2. Photoluminescent quantum dots

Quantum dots are semiconductor nanoparticles from 2 to 15 nm in size possessing unique optical properties, including a tunable PL wavelength, high PL QY and molar extinction coefficient, and long-term colloidal stability [22–25]. These and other properties of QDs make them a promising alternative to the traditional luminescent dyes to be used in biomedical technologies [4,26–28], photophysics [29–32], and related areas [33,34].

In the past 30 years, a wide range of methods for obtaining high-quality QDs with controllable physical and chemical characteristics has been suggested [23,35,36]. These achievements are mainly related to the development of novel approaches to coating QDs with a protective passivating shell [37,38], search for new precursors for high-temperature shell growth [24,39], and development of new shell structures [39,40]. Individual QDs may have an ideally

pure color [41], PL QY as high as 100% [25,40], and a monoexponential luminescence decay kinetics [42] and be free of the blinking effect. However, it is difficult to obtain the combination of all these properties in a single type of QD. Moreover, as a rule, all of the abovementioned properties, which may be applicable to a single QD, are substantially compromised in nanoparticle ensembles. Therefore, the selection of the optimal strategy for the synthesis of QDs with improved chemical and physical characteristics requires preliminary detailed analysis of the procedure for the synthesis of PL QDs.

This section reviews the main parameters of QD synthesis affecting the improvement of their main optical properties. These are the type of the reaction mixture, temperature profile, QD energy structure, and the thickness and sequence of shell layers.

1.2.1. Physico-chemical properties of photoluminescent quantum dots

The electronic structure of small nanocrystals is intermediate between the discrete levels of an atomic system and the band structure of a bulk solid, due to the confinement of the electron wave function within the physical dimensions of the particle. This phenomenon is called quantum confinement [23,43,44]. In these particles, the highest occupied atomic levels of the atomic species interact with one another to form the valence band of the nanoparticle. Similarly, the lowest unoccupied levels combine to form the conduction band of the particle. The energy gap between the valence and conduction bands results in the band gap of the nanoparticle (Figure 1).

The simplest example of a multiple electron molecule is that of diatomic hydrogen (H_2). In this molecule, two atomic orbitals (AOs) combine to form two molecular orbitals (MOs) that spread out over both H atoms, namely, a bonding and an anti-bonding MO. The bonding MO is lower in energy compared to the individual AOs, whereas the anti-bonding MO is higher in energy than the individual AOs. The MOs are occupied by electrons in such a manner that the potential energy of the molecule is minimized. The two electrons of the H_2 molecule that are originally in the first AOs of the individual H atoms are accommodated in the bonding MO, thereby leaving the anti-bonding MO unoccupied. The highest occupied and the lowest unoccupied molecular orbitals are referred to as HOMO and LUMO, respectively. The same approach can be extended to larger molecules, clusters, and even bulk materials. In larger molecules, the number of AOs that are combined to form MOs (bonding and anti-bonding) is also larger, which leads to an increasingly larger number of energy levels and a decreased HOMO–LUMO energy gap. Each MO combination has a well-defined energy, but MOs with intermediate energies are more common than those with energies close to the minimum or maximum values (i.e., fully bonding or fully anti-bonding). This means that the density of MO states is the highest at intermediate energy values and the lowest at both minimum and maximum

energies. For a sufficiently large number of combining atoms (i.e., when the bulk limit is reached) the energy levels become so numerous and so closely spaced that a quasi-continuum (i.e., an energy band) is formed, similar to the conduction and valence bands described above. The HOMO level is the top of the VB, whereas the LUMO is the bottom of the CB.

A semiconductor NC can be regarded as a very large molecule or cluster consisting of several dozen to several thousand atomic valence orbitals, forming as many MOs (e.g., a 1.5-nm CdSe QD contains about 50 atoms, while a 10-nm NC consists of 10^4 atoms). Therefore, its electronic structure will be characterized by energy bands with a large density of levels at intermediate energies and discrete energy levels near the band edges, where the density of MO states is small. The HOMO–LUMO energy gap will be larger than in the bulk material and size-dependent, increasing with decreasing NC size (Figure 1). This explains both quantum confinement effects discussed in the previous section on the molecular level.

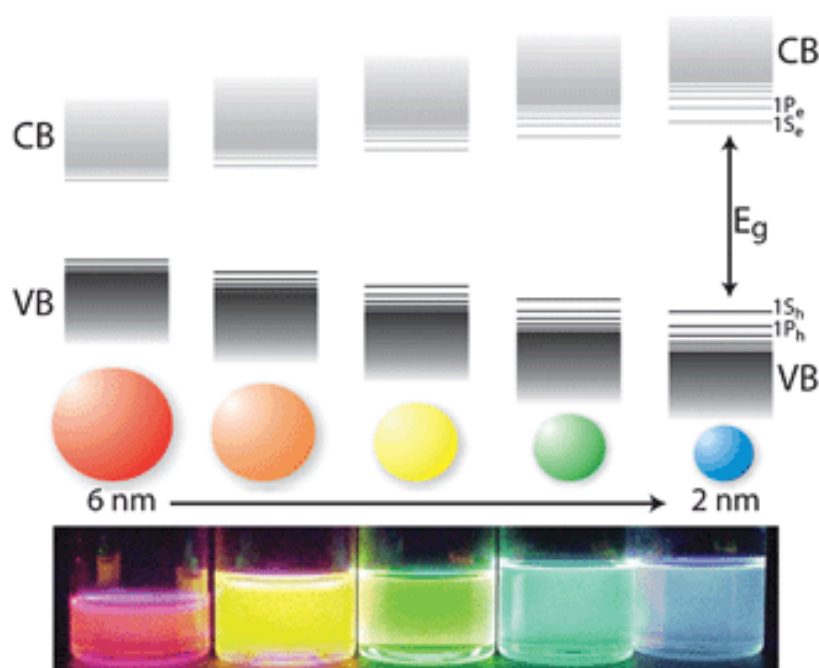


Figure 1: Schematic representation of the quantum confinement effect on the energy level structure of a semiconductor. The lower panel shows colloidal suspensions of CdSe NCs of different sizes under UV excitation [45].

The most striking evidence of quantum confinement in semiconductor QDs is their size-tunable optical properties. In other words, the position of maxima of the optical absorption and emission spectra of QDs is dependent on their size. When a semiconductor absorbs a photon, an electron is promoted from the valence band to the conduction band, creating an exciton

(electron–hole pair) or leaving behind a region of positive charge (hole) in the valence band. During this process, both electron and hole can move around in the bulk material, but because the exciton is composed of an electron and a hole, which have opposite charges, a strong Coulomb attraction causes them to remain relatively localized within a nanometer-sized crystal. This means that, due to the small size of the QDs, the electron–hole separation is confined within a space smaller than the Bohr radius of the semiconductor [43]. Hence, when core nanocrystals are made progressively smaller, more energy is required to confine the exciton and the energy of the emitted photons increases. Therefore, larger nanocrystals absorb and emit in the red region, while smaller nanocrystals absorb and emit in the blue one. By controlling the core size, it is possible to obtain a range of nanocrystals with different emission spectra.

In practice, this means that the optical band gap of QDs can be tuned by simply changing their size. For QDs emitting in the visible range (e.g., CdTe and CdSe QDs), this is distinctly seen from their size-dependent PL colors (Figure 1).

The spectral characteristics of QDs offer other distinctive advantages over those of organic dyes and fluorescent proteins, particularly with regard to the implementation of spectral multiplexed detection schemes (e.g., multicolor imaging). The broad absorption spectra of QDs and the fact that the absorption coefficients increase towards shorter wavelengths facilitates single-wavelength excitation of QD of different sizes and, hence, fluorescence colors. In addition to large molar absorptivity coefficients (10^5 – 10^6 M⁻¹cm⁻¹), the emission spectra of core/shell QDs are narrow, symmetric and can span a broad range of wavelengths by a careful choice of particle size and composition.

QDs also possess high quantum yields due to the large capacity for photon absorption which is propagated into emission of fluorescence photons [40,46]. Another property of QDs is their high photostability when not exposed to extreme conditions. This is because, generally, the core material with a narrow band gap is enclosed within a shell consisting of a different semiconductor material with a higher band gap. This core/shell architecture not only confines excitation and emission of the core, but also enhances the QY and protects the core from photobleaching [47]. These unique properties explain why these nanomaterials of excellence have been used in a variety of biological applications and have allowed researchers to unravel biological functions at the molecular level [27,48]. QDs, despite their many advantages, also have some issues that should be considered before their widespread use, including blinking, biocompatibility issues, larger relative sizes compared to standard fluorophores. However, all these problems have been overcome to some extent and are continually being studied and improved [49–51]. The quality and optical properties of QDs largely depend on the processes taking place at the early stages of nanocrystal nucleation and subsequent growth.

Nucleation of QDs

The formation of QDs is considered to occur in two key steps: (1) nucleation and (2) growth. There is an extremely high energy barrier for spontaneous homogeneous nucleation. Nucleation is not initiated until the nucleation threshold is reached. The LaMer plot (Figure 2) shows how the energy barrier works to induce a “burst of nucleation” [52,53]. At stage I, some nuclei may form under supersaturated conditions of active atomic or molecular species (monomer). But these nuclei are thermodynamically unstable and are readily redissolved. In stage II, a burst nucleation is initiated by abruptly increasing the concentration of the monomer over the threshold. This may be achieved by swiftly injecting the precursor into the solvent at a relatively high temperature, as in the hot injection method. When the monomer pool is depleted owing to the nucleation process, the system moves into the growth stage (nucleation rate = 0, stage III)

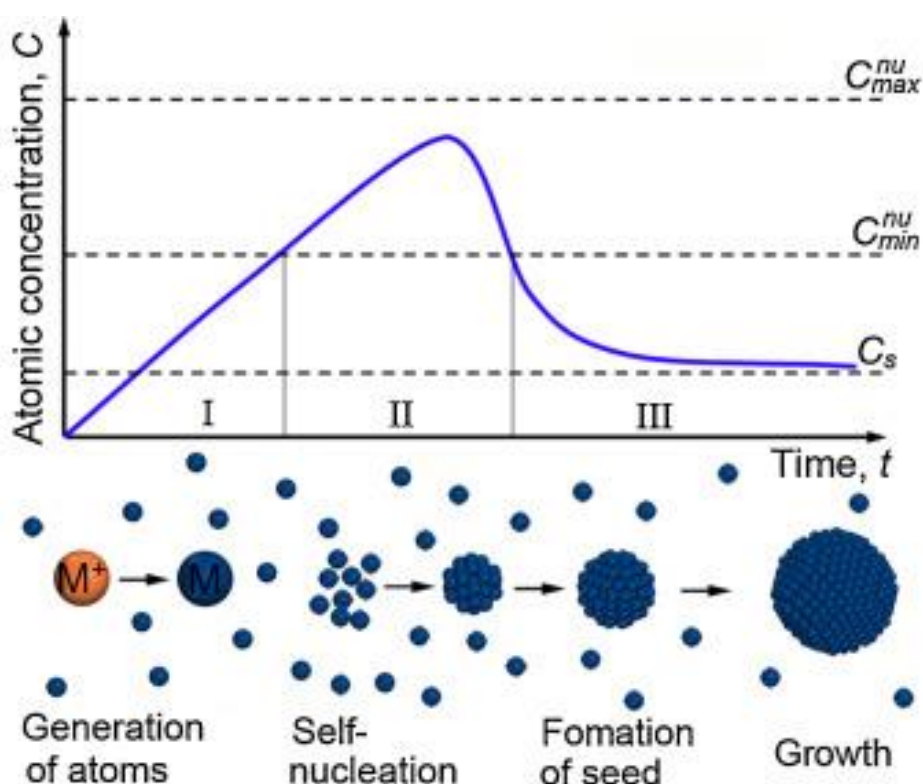


Figure 2: LaMer curve describing three stages of metal nanocrystal formation in a solution. Stage I, atom production; stage II, nucleation; and stage III, seed formation and growth [54].

The growth of nanoparticles can be either “diffusion-controlled” or “kinetically controlled”, and it is strongly dependent on the concentration of the monomer in the reaction mixture. At high monomer concentrations, the critical size, which is the minimum one of a nucleus that can grow spontaneously in the supersaturated solution, is small, so that all the particles grow. According to the “growth by diffusion” model, the growth rate of a particle is

inversely proportional to its radius, which results in the “focusing” effect in the particle size distribution and results in an almost monodisperse product. In contrast, the critical radius is large at low monomer concentrations (Figure 3).

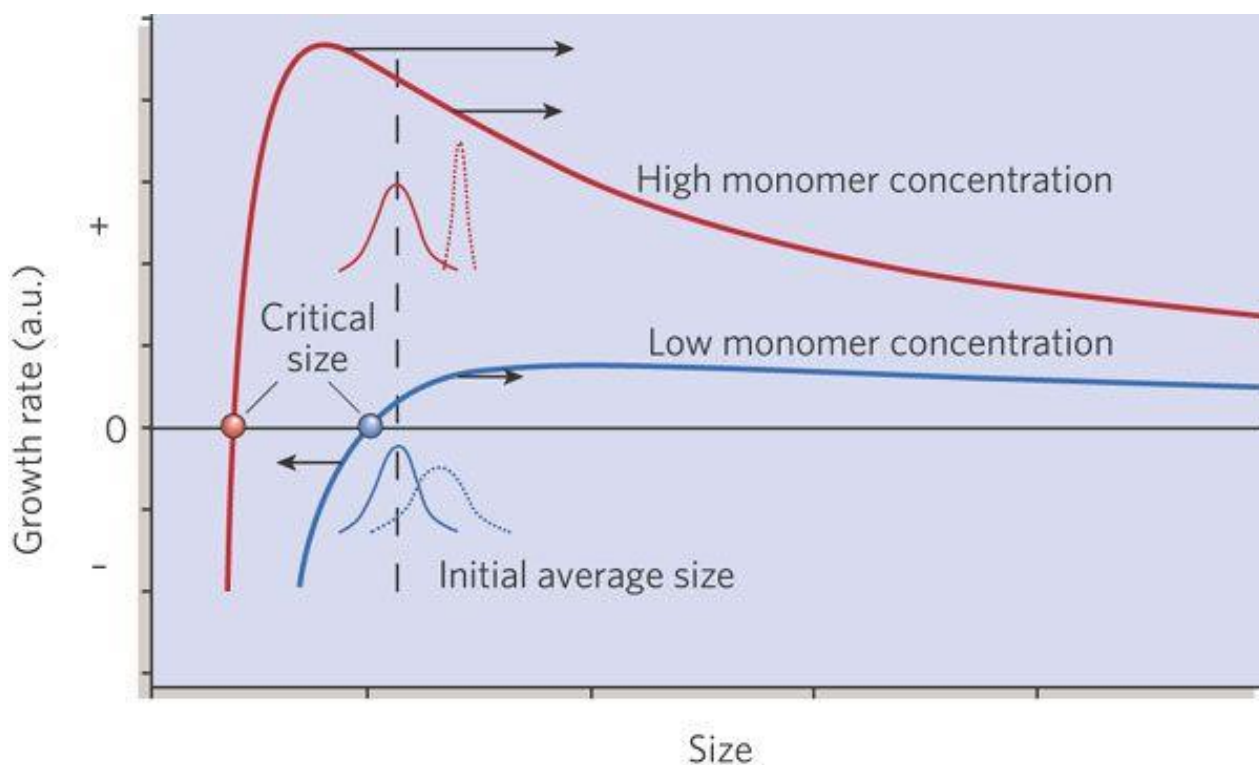


Figure 3: The growth rate as a function of the nanocrystal radius [55].

A critical size exists at any given monomer concentration. At a high monomer concentration, the critical size is small, so that all the particles grow. In this situation, smaller particles grow faster than the larger ones; as a result, the size distribution can be focused down to a nearly monodisperse one. If the monomer concentration is below a critical threshold, small nanocrystals are digested, while larger ones grow and the size distribution broadens or defocuses. Nearly monodisperse spherical particles can be prepared by arresting the reaction while it is still in the focusing regime, with a large concentration of monomer still present.

The geometric shape of colloidal nanocrystals is determined by three critical factors (Figure 4): (1) the crystalline phase of the seed at the nucleation stage; (2) the surface energy effect and (3) the control of the growth regime at the growth stage.

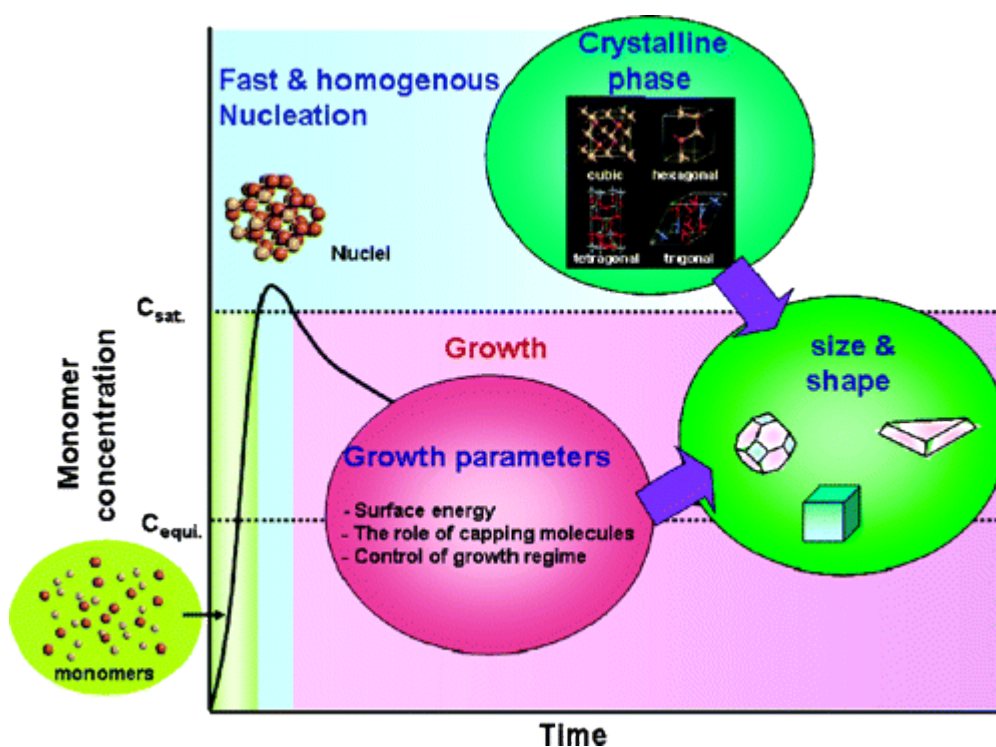


Figure 4: Crystal growth processes and key factors determining the crystal shape [56].

The nanocrystal seed can adopt a variety of potential crystallographic phases, from the isotropic cubic structure to the anisotropic orthorhombic or hexagonal one, but the stable phase strongly depends on the environment conditions, such as temperature and the surfactant. After the nuclei are formed in a preferred crystalline phase, the subsequent growth process governs the final geometry of the NCs. The growth rate in different directions strongly depends on the surface energy of the crystallographic facets of the seed. The growth rate is exponentially proportional to the surface energy. Generally, facets with higher surface energy grow much faster than others. The surface energy of the crystal facet can be tailored by the type and amount of the adsorbed capping molecules. For example, rock-salt PbS crystals usually nucleate as tetradecahedral seeds, exposing six [100] faces and eight [111] faces. The intrinsic surface energy of the [111] faces is higher than that of the [100] faces, hence the relatively fast growth along the eight equivalent [111] directions results in the formation of cubic shaped NCs. When the QDs are synthesized through the thermal decomposition of the $\text{Pb}(\text{S}_2\text{CNET}_2)_2$ organometallic precursors in a hot organic solution in the presence of dodecylamine as a nonselective capping agent, cubic PbS nanocrystals are formed [57]. When dodecanethiol was used as a capping agent to replace dodecylamine, the surface energy of the [111] faces can selectively be lowered relative to that of the [100] faces. The cubic shape of PbS NCs is gradually changed to truncated octahedrons with increasing dodecanethiol concentration [58]. In addition, the shape of the NCs is also determined by the delicate balance between the kinetic and the thermodynamic growth

regimes. Anisotropic growth of NCs normally occurs under kinetic growth regimes, while isotropic growth is predominant under thermodynamic growth regimes. The control of the growth regime between kinetic and thermodynamic growth can be achieved by varying the reaction parameters, such as the monomer concentration and the temperature.

1.2.2. Synthesis of CdSe-based quantum dots

All the available methods of photoluminescent NC synthesis can be classified according to the physical state of the reaction medium: gas-phase, solid-phase, and liquid-phase [59]. However, the gas-phase and solid-phase approaches are often inapplicable for the controlled synthesis of high-quality NCs because of some physical and chemical limitations. In contrast, the liquid-phase synthesis allows the substantial limitations of the other methods to be bypassed [23,60].

Solution-phase synthesis has become a promising approach to the fabrication of high quality QDs with within crystal size range of 2 - 50 nm. The size and shape of the colloidal nanocrystals can be controlled by varying the surfactant. Surfactants (also termed surface ligands) play multiple roles in nanocrystal synthesis: (1) they affect the nucleation and growth speed and consequently control the QD size; (2) they can stabilize the QDs and prevent inter-particle aggregation by increasing the steric barrier; (3) they can improve the nanocrystal solubility in conventional solvents.

In this approach, QDs are synthesized in a solution or, less commonly, at the interface of immiscible liquids [61,62]. There are two main types of liquid reaction media: aqueous and organic. The aqueous synthesis makes it possible to use an environmentally friendly solvent and directly obtain biocompatible QDs [63]. The fact that the stage of post-synthetic replacement of organic molecules (ligands) stabilizing QDs is absent in the case of aqueous synthesis is an important advantage of these QDs in terms of biomedical applications [64–66]. However, because of the mild temperature of the reaction, continuous nucleation and subsequent growth of NCs occurs in the mixture throughout the reaction; therefore, this method does not allow effective control of the nanoparticle morphology and obtaining ensemble of NCs with narrow size distribution. The characteristic PL QY for CdSe QDs synthesized in water is no higher than 50% [66,67]. Cadmium telluride-based QDs are characterized by higher PL QY, reaching 85% [68,69].

The use of hydrothermal synthesis (a sub-type of aqueous synthesis) [70] makes it possible to substantially reduce the growth time and size variation of QDs. However, this method does not yield a considerable improvement of the PL QY; in addition, it requires high pressures in the reactor [70,71].

At present, organometallic synthesis in high-boiling organic solvents is the most commonly adopted method for obtaining QDs. It requires more toxic reagents, but allows more precise control of the characteristics of the resultant NCs [61,60,72]. The characteristic size distribution in the ensemble of QDs obtained by the organometallic method is no more than 10%, what corresponds to a thickness of only one or two monolayers [73]. The other most important advantages of this method are (1) the technological feasibility of the synthesis not requiring expensive equipment and allowing the technique to be scaled to obtain 1 g of pure NCs per synthesis [73,74] and (2) the possibility to precisely control the optical parameters of the NCs, with a PL peak wavelength accuracy of 5 nm and a full width at half maximum (FWHM) less than 30 nm [75,76].

Another advantage of this method of NC synthesis is the possibility to obtain stable and relatively concentrated nanoparticle solutions (>10 g/L), which is important when they are used to make large-area layers of NCs [77,78]. Thus, the aforementioned advantages make organometallic synthesis attractive as a simple and inexpensive method for obtaining high-quality NCs.

The existing methods of organometallic synthesis of QDs can be conventionally divided into two classes: injection [75,79,80] and non-injection [46,81] ones. The non-injection methods are considered less effective in terms of the product crystallinity and the variation of the NC sizes and optical parameters [64,82]. In the non-injection, or “one-pot” method, all components are mixed under normal conditions, and nucleation is initiated chemically, thermally [73], or using another physical factors, such as microwave [65,83] or laser [84] radiation. In this case, the mutually competing formation of new nuclei and NC growth occur in parallel, which leads to an increased size heterogeneity in the NC ensembles being formed and therefore an undesirably wide luminescence band.

The injection methods of synthesis are based on a rapid injection of cold metal or chalcogen precursors into the hot solvent, typically containing another precursor. The injection is typically done at a temperature somewhat higher than the nucleation threshold, and the immediate drop of temperature caused by addition of the cold precursor solution stops nucleation and triggers the slow NC growth mode. Thus, a rapid nucleation and a slow growth limited by ligands (trialkyl phosphine, trialkyl phosphine oxide, fatty acids, and aliphatic amines) allow QD ensembles with a narrow size variation, thus allowing to obtain QD samples with fluorescence peaks having FWHM of about 20 nm [85–88].

The NC size and shape can be controlled by varying the viscosity of the solvent, precursors concentration, and type of the ligands. Hot injection method requires that the formation and growth of the NC nuclei must be controllable. Separation of these stages in time is

crucial for obtaining NCs of the highest quality. Cadmium salts of saturated and unsaturated aliphatic carboxyl acids (hexanoic, oleic, stearic, myristic, and some other acids) and phosphonic acids are commonly used as cadmium precursors. Trioctyl phosphine selenide or a solution of elemental selenium serves as a selenium precursor. The typical solvent for organometallic synthesis is 1-octadecene, trioctylphosphine oxide, or another high-boiling alkane or alkene. Figure 5 shows the mechanism of the chemical reaction yielding CdSe monomers.

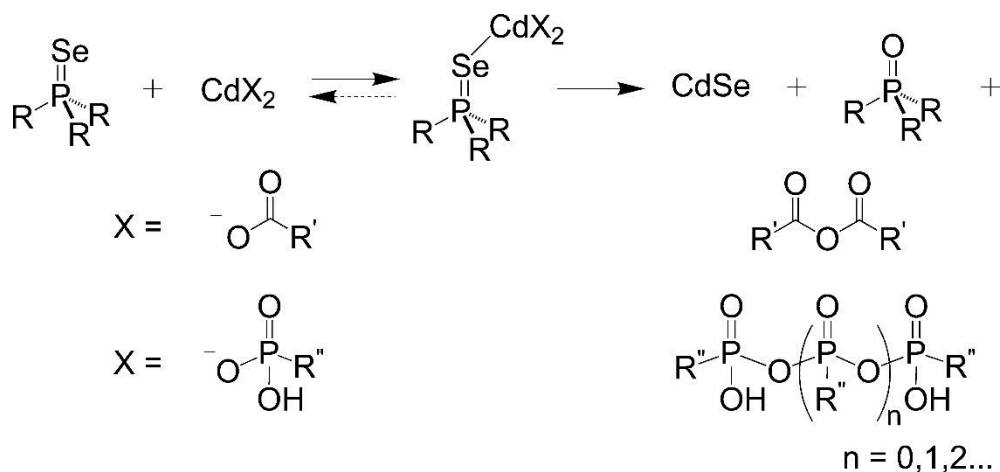


Figure 5: The mechanism of the chemical reaction used to obtain CdSe NCs [89].

1.2.3. Synthesis of core/shell quantum dots

The formation of defectless epitaxial shells of wide band gap semiconductors whose crystal lattice parameters are close to the one of QD's core is increasingly more popular due to the better optical characteristics and higher colloidal stability of the core-shell NCs. A two-stage technique comprising the synthesis QDs cores and growth of the shell with an intermediate core purification stage is usually used to obtain high-quality QDs with a discrete shell-layer structure. This makes it possible to purify the core solution of excess precursors, thereby avoiding the formation of NCs with variable shell composition, and to remove the ligands that could block the homogeneous growth of the shell.

The introduction of an equivalent amount of the shell precursors in the presence of excess ligands ensures the growth of the crystal shell. This process is affected by many factors, including the ratio and reactivities of the precursors, temperature profile of the epitaxial shell growth, and type and parameters of the crystal lattice.

The best effect is achieved if the epitaxial shell is formed from a material with close crystal lattice parameters. NCs with different PL characteristics can be obtained, depending on the type of the semiconductor nanostructure and the relative positions of the electron-hole energy levels

of the core and shell. Table 1 shows the main characteristics of some bulk semiconductor compounds that are taken into account in selecting the material for the shell.

The properties of NCs are also strongly affected by the type of the crystal lattice. The crystallographic and energy parameters of the zinc-blende or sphalerite and wurtzite types characteristic of AIBVI NCs (Table 1) are very close to each other; therefore, small changes in the QD environment may result in surface and bulk defects of the NC crystal structure [80,90,91] and, hence, deterioration of the optical properties.

Table 1: Characteristics of some bulk semiconductor materials [43].

Material	Structure [300K]	Type	E_{gap} [eV]	Lattice parameter [Å]	Density [kg m ⁻³]
ZnS	Zinc blende	II-VI	3.61	5.41	4090
ZnSe	Zinc blende	II-VI	2.69	5.668	5266
ZnTe	Zinc blende	II-VI	2.39	6.104	5636
CdS	Wurtzite	II-VI	2.49	4.136/6.714	4820
CdSe	Wurtzite	II-VI	1.74	4.3/7.01	5810
CdTe	Zinc blende	II-VI	1.43	6.482	5870
GaN	Wurtzite	III-V	3.44	3.188/5.185	6095
GaP	Zinc-blende	III-V	2.27	5.45	4138
GaAs	Zinc blende	III-V	1.42	5.653	5318
GaSb	Zinc blende	III-V	0.75	6.096	5614
InN	Wurtzite	III-V	0.8	3.545/5.703	6810
InP	Zinc blende	III-V	1.35	5.869	4787
InAs	Zinc blende	III-V	0.35	6.058	5667
InSb	Zinc blende	III-V	0.23	6.479	5774
PbS	Rocksalt	IV-VI	0.41	5.936	7597
PbSe	Rocksalt	IV-VI	0.28	6.117	8260
PbTe	Rocksalt	IV-VI	0.31	6.462	8219

Three types of QD energy structure are distinguished according to the arrangement of the core/shell energy levels [23,61,92]. CdSe QDs coated with shells of wide-band-gap materials, such as ZnS and CdS, ensuring that charge carriers (electrons and holes) are retained within the CdSe core are the most commonly used. They are classified as type I QDs [23,61]. This configuration enhances the luminescence efficiency and the chemical and photochemical stabilities. The valence conduction band edges of ZnS are, respectively, ~0.8 eV lower and ~0.5 eV higher than those of the CdSe core, which is sufficient for the reliable confinement of excitons in the core. The CdS valence band is ~0.5 eV lower than that of CdSe, which ensures sufficient shielding of holes inside the core [92]. However, the conduction band edges of CdSe and CdS differ as little as by 0.3 eV, which cannot ensure sufficient charge confinement in the core [24,31]. Delocalization of the electron wave functions into CdS shell should be closely related to the kinetic energy of excitons in the CdSe core [93], which mainly depends on the core

shape and size. This also means that the optical properties of CdSe/CdS NCs are sensitive to the shell size, surface ligands, etc.

The traditional method of shell formation requires the simultaneous introduction of the metal and chalcogen precursors in the presence of excess ligand for passivation of the growing NC surface. However, an incorrectly selected temperature profile may lead to saturation of the reaction mixture with the precursors of the shell components because of the low growth rate. This may result in the formation of a separate phase of nanoparticles of the shell material (ZnS or CdS), as well as inhomogeneous growth of the shell on the core surface because of local oversaturations and temperature oscillations. The method of stepwise injection of the precursors with intermediate steps of annealing the reaction mixture at an enhanced temperature called Successive Ion Layer Adsorption and Reaction (SILAR) solves the problem of the inhomogeneous shell growth [37,38,94]. The essence of the method is the successive addition of precisely calculated amounts of metal (Cd and Zn) and chalcogen (S and Se) precursors to the colloidal solution containing the CdSe cores so that a CdS/ZnS monolayer is formed in each cycle of shell formation. The amounts of the precursors for the formation of each shell monolayer are calculated from the increment in the volume upon application of each monolayer, with the change in the linear sizes and geometry of the NC taken into account. In SILAR, the reaction of each aliquot of the cation precursor introduced into the mixture must be completed before the anion precursor is added.

Metal (cadmium or zinc) oleate and elemental sulfur are usually used as shell precursors. Each of them is dissolved in octadecene/trioctylphosphine and then introduced alternately at temperatures of 240 and 180°C, respectively, and is let to react.

Other compounds, including thiourea [40], octanethiol [39,51], and hexamethyldisilathiane ((TMS)₂S) [38], can serve as sulfur sources. (TMS)₂S efficiently inhibits the formation of the nuclei of new particles consisting of the shell material. In this case, (TMS)₂S is involved in silylation of the ligands [95] and replaces the passivators weakly bound with the metal atoms [87]. Figure 6 shows how the absorbance and PL spectra change as ZnS shells form over CdS cores.

The positive effect of octanethiol as a ligand and sulfur precursor is determined by its low reaction capacity, which requires a temperature above 300°C for the C–S bond to be broken and the shell growth to start. These conditions of the shell growth ensure a narrow QD size distribution (with a FWHM of 20 nm). Thus, the increase in the number of monolayers results in a gradual rise of the PL QY to 100% and prevention of PL blinking [39,51]. The maximum QY is reached at a shell thickness of 2.4 nm, which corresponds to six monolayers. The PL efficiency can also be increased by thermal treatment or UV irradiation of the NCs.

Octanethiol has also been used as a sulfur precursor for a CdS shell applied onto CdSe cores with a wurtzite crystal lattice [24]. Also, a prolonged annealing of the reaction mixture is necessary to obtain a PL QY of 100%. In this case, the PL QY of the CdSe nuclei drops almost to zero, which is related to the highly effective trapping of holes by thiol molecules. After that, however, the PL QY monotonically rises as the shell grows to reach 100% eventually. In addition, the authors have succeeded in suppressing the blinking of individual QDs [24] and achieving the coincidence of the luminescence spectrum of the entire QD ensemble with the PL spectrum of a single QD, which indicates a high homogeneity of the NC shape and size.

It is noteworthy that the high temperatures used in these studies (above 300°C) are close to the boundary of the admissible temperature range; if the temperature varying in the course of the reaction even slightly exceeds this limit, rapid recrystallization and other side reactions may occur, which makes it difficult to reproduce the technique.

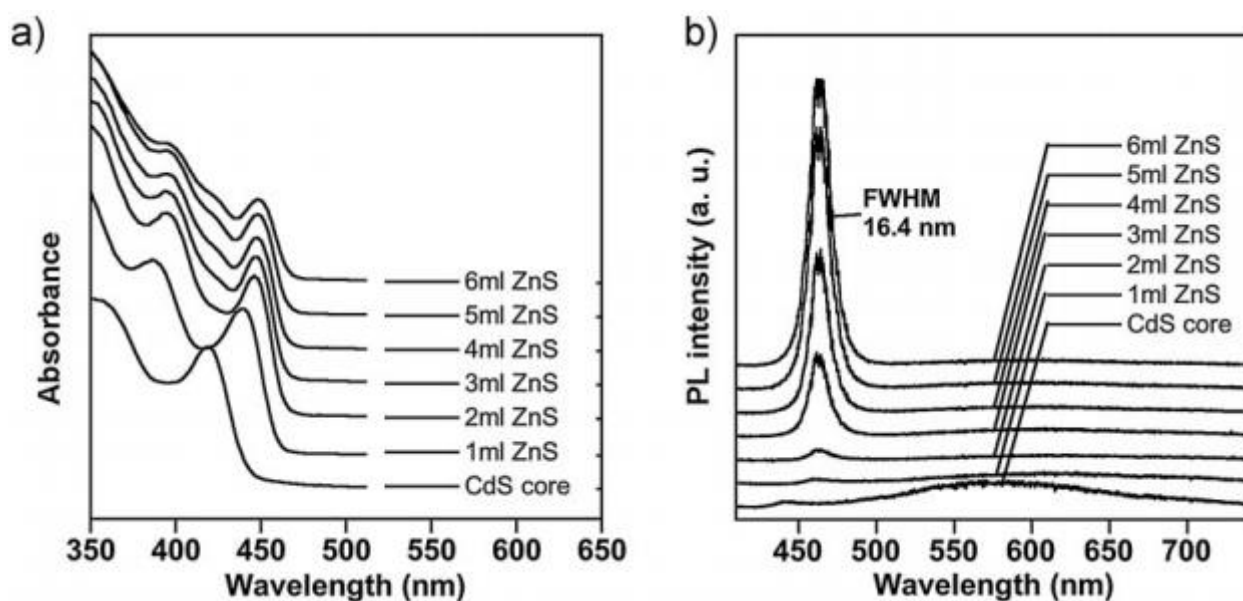


Figure 6: Changes in the typical (a) absorbance and (b) photoluminescence spectra of CdS/ZnS QDs in the course of shell formation. The initial size of the CdS core is 4 nm. The maximum thickness of the ZnS shell after the addition of 6 ml of the precursor solution is approximately five monolayers [96].

It has been reported [97] that the formation of a ZnS crystal shell no thicker than 1.5 monolayers over wurtzite-type CdSe cores leads to an increase in PL QY, but further shell growth results in PL quenching. Zinc-blende-type CdSe NCs cores grow more isotropically than wurtzite-type, which, in turn, ensures a more homogeneous growth of the shell with fewer structural defects [98]. Various one-component protective shells grown on top of these cores also have the zinc-blende structure, which is confirmed by X-ray diffraction analysis [98]. The ZnSe

and CdS shells are characterized by coherent growth, whereas the quality of the ZnS shell is somewhat deteriorated as it grows because of a greater difference between the crystal-lattice parameters of ZnS and CdSe, as mentioned above. However, when the core has the zinc-blende structure, the PL QY monotonically rises with increasing thickness of the shell of any of these materials (ZnS, ZnSe, or CdS) [99].

A detailed study on the conditions for the formation of the epitaxial ZnS shell in the trioctylphosphine/trioctylphosphine oxide medium has shown that the temperature at which the shell is formed strongly affects its quality [97]. At a temperature below a threshold value, the reaction between the sulfur and zinc precursors is not completed, which results in a defective shell. An excessively high temperature leads to recrystallization of the CdSe cores and formation of a separate phase of ZnS nanoparticles, which results in the loss of monodispersity and homogeneity of optical properties. In addition, the dependence of PL QY on the shell thickness is complex and nonmonotonic. For example, the PL QY of CdSe/ZnS NCs is increased to about 90% when the first monolayer of the shell is applied and is gradually decreased with an increase in the number of monolayers, reaching 60% when the shell is three monolayers in thickness and even lower values as the thickness grows to five monolayers [40]. The decrease in PL QY is related to the shearing strains resulting from the substantial difference between the parameters of the elementary cells of CdSe and ZnS (~12%), as well as the large curvature of the core surface at a diameter of 4 nm.

The insignificant mismatch between the parameters of the CdSe and CdS lattices (~4%) compared to the CdSe–ZnS pair favors an almost defect-free growth of the CdS shells over the CdSe cores. Another method for overcoming the mismatch between the crystal lattice parameters is the formation of core/shell/shell structure, e.g., CdSe/ZnSe/ZnS [100] and CdSe/CdS/ZnS [31,73], which ensure a decrease in the structure imperfection at the interface between the core and the first shell. It has been demonstrated that the PL QY of CdSe/ZnSe/ZnS QDs is substantially higher than in the CdSe/ZnS QDs due to the smaller number of pathways for rapid nonradiative recombination related to dangling surface bonds and dislocations at the CdSe/ZnS boundary [101]. However, since the boundaries of the conduction and valence bands of the materials constituting the first shell and the core are close, nonradiative recombination cannot be prevented completely. The ZnS/CdS/ZnS two-component shell makes it possible to eliminate this drawback [102]. Its specific advantage consists of two separate ZnS monolayers ensuring the maximum confinement of charges in the core and a low structure imperfection. This is due to the CdS layer between the two ZnS layers preventing the formation of the aforementioned extended ZnS crystal structure several monolayers in thickness, which would otherwise lead to considerable crystal imperfection at the phase interface. The suggested QD structure,

CdSe/ZnS/CdS/ZnS, has been demonstrated to be efficient for cores of different sizes, with PL QYs as high as 100% [103] throughout the optical spectrum.

"Giant" quantum dots

Despite the excellent PL QY parameters, many QDs are prone to the so-called blinking effect [47,104], when the PL of individual QDs under continuous excitation does not remain permanent but rather switches on and off. This limits the use of QDs as molecular tracking probes or single-photon sources. There are two main strategies for suppressing this effect. The first one is to modify the QD environment by adding anti-blinking agents, which can almost entirely eliminate blinking [105,106]. However, this non-blinking state is temporary, and the QDs may easily revert to the original blinking state [105], which makes these QDs unacceptable for practical use. The second strategy is to grow a thick ("giant") CdS shell to completely insulate the excited charge carriers from the environment [107,108]. This type of NCs is characterized by unique photophysical properties, with blinking [24,47,109], photobleaching [47,110], and nonradiative Auger recombination [111–113] completely suppressed. For example, a duration of the switched-on state of 94% has been obtained for QDs with a seven-monolayer shell [24]. However, this parameter also depends on the irradiation intensity. At high irradiation intensities, some "giant" QDs go into a "gray" state, which is intermediate between the completely switched-off and switched-on PL modes. This effect is the consequence of emitting from higher levels occurring upon intense irradiation of QDs [112,114,115]. The "giant" shells are successfully applied by the SILAR method described above, that allows strict control of the shell thickness and preservation of the high-crystalline structure.

Most studies pay special attention to the effect of the shell thickness on the photophysical properties of "giant" CdSe/CdS QDs, whereas the effects of the core size and other parameters remain poorly studied. One of the few examples of estimation of the core size effect is the study [91] where distinct correlation has been found between the core volume and suppression of blinking: QDs with larger cores required thinner shells for suppressing the blinking compared to QDs with smaller cores, where thicker shells were necessary to reach the same level of blinking suppression. The threshold volume of "giant" QDs at which the blinking was completely suppressed was experimentally estimated to be about 750 nm^3 , the characteristic life time of the NCs of this size being $\sim 65 \text{ ns}$ irrespective of the original core size. Another study [24] reports a complete suppression of blinking at the maximum PL QY for QDs of the same type (CdSe/CdS) that are almost two times smaller ($\sim 390 \text{ nm}^3$) than those used in the previously cited study. This is accompanied by a twofold decrease in the life time, to $\sim 32 \text{ ns}$.

Many authors note that the shell thickness from five to seven monolayers is optimal and ensures the prevention of the maximal PL QY, a high sized homogeneity, and almost complete suppression of blinking [24,116].

However, despite considerable achievements in the synthesis of high-quality "giant" QDs, application of multiple shell layers, even with the use of the SILAR method, deteriorates the NC morphology and increases their size variation, which is hardly acceptable in applications that require precise reproduction of the position of the PL peak. In addition, although the optical properties of single QDs are constantly improved, the proportion of these QDs in ensembles does not reach 100% yet [91].

Alloyed (doped) quantum dots

Alloyed or doped QDs of various compositions have recently become popular due to their excellent optical characteristics and easy tunability of the PL wavelength over the entire visible spectrum without changing the particle size [90,117,118]. These QDs are obtained by introducing an additional cation or anion, or their mixture, into the reaction. This leads to changes in the QD energy structure and the PL spectrum.

It has been found [49] that prolonged annealing of the reaction mixture at a temperature of 310°C during the formation of a shell over the alloyed CdZnS cores results in a gradual increase in the PL QY of the CdZnS/ZnS QDs from ~70 to 98%. The PL QY of the zinc-doped $\text{Cd}_{1-x}\text{Zn}_x\text{Se}$ QDs has been shown [118] to exceed that of the classical CdSe QDs with the same spectral position of the PL peak obtained under similar conditions. In addition, this leads to the suppression of blinking [90,104,118].

A similar approach, with octanethiol as a source of sulfur, has been used to synthesize CdSe/ $\text{Cd}_x\text{Zn}_{1-x}\text{S}$ QDs with a gradient shell structure, which allowed obtaining a PL QY as high as 97% [39]. A PL QY of 100% has been reached in studies where shells with a complex structure were applied onto CdSe cores or CdSe-based alloyed cores. In these studies, a thin ZnS layer was formed on the core surface, and a thick layer with an either gradient or complex multicomponent structure— $\text{Cd}_{1-x}\text{Zn}_x\text{Se}/\text{ZnSe}/\text{ZnS}$ [117] or CdSe/ZnS/ZnS [86,88]—was applied over it.

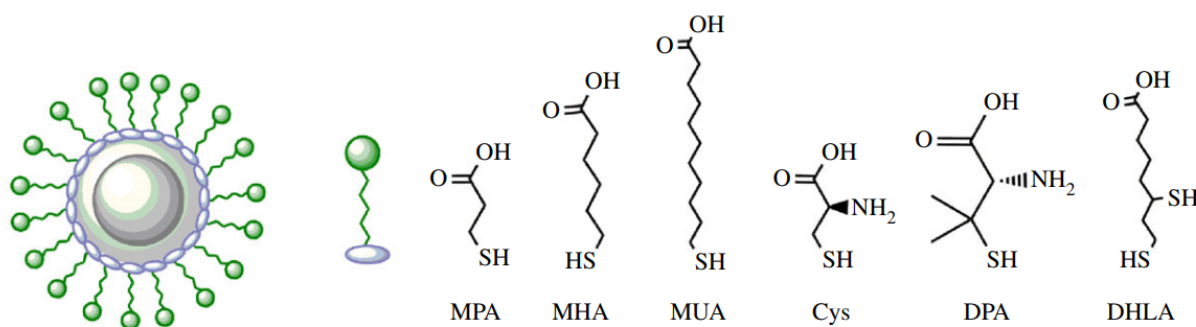
A common characteristic of recent research is considerably complicated procedures for the application of the protective epitaxial shells with the use of multicomponent mixtures or unusual reagents and an increased temperature of the synthesis. This raises the problem of reproducibility of the new techniques, because numerous factors affect the outcome of the reaction.

The two-stage technique of injection synthesis of QD cores followed by application of the epitaxial protective shell by the SILAR method with an intermediate stage of elimination of

excess precursors ensures both the best reproducibility and good optical properties of the QDs. This procedure makes it possible to strictly separate the stages of the core synthesis and the subsequent growth of the epitaxial shell of the desired composition. The precise amounts of the shell precursors to be added at each step can be calculated from the optical characteristics of the cores. This yields QDs characterized by narrow size distribution, high optical qualities, and high colloidal stability.

1.2.4. Quantum dot surface modification

QDs produced in nonpolar solutions using aliphatic coordinating ligands are only soluble in nonpolar organic solvents, making phase transfer an essential and nontrivial step for the QDs to be useful as biological reporters. Alternatively, QD syntheses have been performed directly in aqueous solution, generating QDs ready to use in biological environments [119], but these protocols rarely achieve the level of monodispersity, crystallinity, stability, and fluorescence efficiency as the QDs produced by hot injection method in coordinating solvents. Two general strategies have been developed to render hydrophobic QDs soluble in aqueous solutions: ligand exchange, and encapsulation by an amphiphilic polymer [26]. For ligand exchange, a suspension of hydrophobic QDs is mixed with a solution containing an excess of a bifunctional ligand, which has one functional group that binds to the QD surface, and another functional group that is hydrophilic [18]. Thereby, hydrophobic ligands are displaced from the QD through mass action, as the new bifunctional ligand adsorbs to render water solubility. The direct attachment of thiol-containing molecules to QDs, instead of the bulky hydrophobic coating, yields much smaller nanoparticles. Using this method, CdSe/ZnS QDs have been coated with cysteine, thioglycolic, mercaptoacetic acid or (3-mercaptopropyl) trimethoxysilane, which contain basic thiol groups to covalently bind to the QD surface atoms, yielding QDs displaying carboxylic acids or silane monomers, respectively (Figure 7) [120]. Williams and colleagues [121] have demonstrated that thioglycolic acid capped CdTe QDs with a hydrodynamic diameter of 4 nm can penetrate into the nucleus of THP-1 cell line, making these size-minimized QDs ideal for *in vitro* imaging.



MPA: 3-mercaptopropionic acid
 MHA: 6-mercaptohexanoic acid
 MUA: 11-mercaptoundecanoic acid

Cys: cysteine
 DPA: D-penicillamine
 DHLA: dihydrolipoic acid

Figure 7: Small molecule ligands with affinity towards the surface of QDs. Several small molecular weight thiolated ligands have been used to impart hydrophilicity. Thiols on these ligands bind to the surface of quantum dots and the terminal functional groups (carboxylic acid or amine) impart water solubility [122].

The acid functionalities improve QD hydrophilicity. These methods generate QDs that are useful for biological assays, but ligand exchange procedure is commonly associated with decrease of fluorescence efficiency and a propensity to aggregate and precipitate in biological buffers, especially in the case of using small molecules listed above [123,124]. More recently it has been shown that these problems can be alleviated by retaining the native coordinating ligands on the surface, and covering the hydrophobic QDs with amphiphilic polymers [125,126]. This encapsulation method yields QDs that can be dispersed in aqueous solution and remain stable for long periods of time due to a protective hydrophobic layer surrounding each QD through hydrophobic interactions.

There is also a principally different approach for phase transfer of hydrophobic QDs, which relies on creation of a solid hydrophilic inorganic shell. Inorganic silica is a highly biocompatible material. Encapsulating QDs within silica can provide a hydrophilic surface and facilitate the incorporation of various functional groups such as carboxyl, amine, and thiol groups for further bioconjugation. Furthermore, silica shell can prevent the release of toxic QD components into the biological environment [127,128]. QDs with increased water stability may then be conjugated with specific ligands such as peptides, antibodies or small molecules to impart target specificity. For example, Different length polyethylene glycols (PEGs) can be conjugated to QDs potentially to extend the blood circulation time and reduce nonspecific binding to serum proteins in blood [18].

PEGylated QDs have a nearly neutral surface charge and can maintain colloidal stability through steric repulsion between the PEG chains. The reduced charge of a PEG, as well as its conformational flexibility, provides a stable surface coating that can reduce nonspecific binding in biological environments. Rosenthal and coworkers [129] have shown that PEG chains as short as 550 Da can significantly reduce the nonspecific binding of QDs to cells. As a result, PEGylated QDs have been successfully used for both *in vitro* [21] and *in vivo* [18,21] applications. However, PEG-coated QDs have significantly larger hydrodynamic sizes than those of comparable non-PEGylated nanoparticles, often being twice as large as the latter. This increased size can prevent the probes from accessing biological targets deep in tissue or cellular structures. Kairdolf et al. [21] reported an alternative approach, in which the QD surface is modified with small hydroxyl-containing molecules (such as 1,3-diamino-2-propanol), yielding hydroxylated QDs. These particles have a dramatically reduced surface charge with virtually no nonspecific binding to cells or tissues, while maintaining excellent colloidal stability. Smith and Nie [90] have developed a multifunctional, multidentate polymer ligand for generating highly compact QDs with ultrasmall hydrodynamic sizes of 4 to 6 nm [130], which preserves the excellent optical properties of the nanocrystals. These multidentate polymers can displace the existing ligands on the QD and tightly bind to the nanocrystal surface in a closed “loops-and-trains” conformation. This unique design eliminates the hydrophobic barrier layer and causes the polymer ligand to tightly fit the nanocrystal surface, resulting in an exceptionally thin polymer shell and small overall particle size.

No matter what method is used to suspend the QDs in aqueous buffers, they should be purified from residual ligands and excess amphiphiles before the use in conjugation with biomolecules or biological assays. Ultracentrifugation, dialysis, or filtration is used for this purpose. Furthermore, when choosing a water solubilization method, one should take into account that many biological and physical properties of the QDs may be affected by the surface coating, and the overall physical dimensions of the QDs depend on the coating thickness.

1.2.5. Quantum dot bioconjugation

To make QDs more useful for molecular imaging and other biological applications, QDs need to be conjugated to biological molecules without disturbing the biological function of these molecules. Biomolecules, including peptides, proteins, drugs, and DNA, have been successfully linked to QDs. Several successful approaches have been used for the linkage, including nonspecific adsorption, electrostatic interaction, mercapto (-SH) exchange, and covalent linkage [26].

First, biological molecules containing thiol groups can be conjugated to the QD surface through a mercapto exchange process [131–133]. Unfortunately, the bond between Zn and thiol

is not very strong, so that biomolecules attached to QDs in this way can readily dissociate from the nanoparticle surface, causing QDs to precipitate from the solution. It has also been reported that simple small molecules, such as oligonucleotides [134] and various serum albumins [135], are readily adsorbed to the surface of water-soluble QDs. This adsorption is nonspecific and depends on ionic strength, pH, temperature, and the surface charge of the molecule. Mattoussi et al. presented a method of conjugating proteins to QD surfaces using electrostatic interactions. The protein of interest was engineered with a positively charged domain (polyhistidine), which, in turn, interacted electrostatically with the negatively charged surface of dihydrolipoic acid (DHLLA)-capped QDs [136]. Electrostatic interactions, however, are generally not sufficiently specific, given the complexity of the biological environment. Therefore, conjugates made in this way are not suitable for *in vivo* or *ex vivo* cell labeling due to the possible interference from positively charged proteins. A more stable linkage is obtained by covalently linking biomolecules to the functional groups on the QD surfaces using cross-linker molecules. This method is the most commonly used approach for making bio-functionalized QDs. Most water solubilization methods result in QDs covered with carboxylic acid, amine, or thiol groups. Under these conditions, it is easy to link QDs to biological molecules that also have these functional groups. For example, the cross-linker 1-ethyl-3-(3-dimethylaminopropyl) carbodiimide (EDC) is commonly used to link $-NH_2$ and $-COOH$ groups (Figure 8A), whereas 4-(*N*-maleimidomethyl)-cyclohexanecarboxylic acid *N*-hydroxysuccinimide ester (SMCC) can be used to cross-link $-SH$ and $-NH_2$ groups (Figure 8B). There are numerous reports on using these methods to conjugate QDs with various biological molecules, including oligonucleotides, peptides, and antibodies [26,137].

Another commonly used strategy for functionalization of QDs is through the streptavidin–biotin interaction, which is attractive because of its high affinity and specificity [4,138]. This method relies on either direct binding between streptavidin-functionalized QDs with biotinylated proteins/peptides (Figure 8C), or the use of avidin as a bridge between biotinylated QDs and biomolecules. Metal–histidine binding has also been investigated in terms of surface modification of QDs. In this case, nickel nitrilotriacetic acid (Ni-NTA, a compound widely used for isolation and purification of proteins that contain histidine tags) groups were introduced. For example, QDs can be modified with Ni-NTA groups via EDC coupling, the subsequent metal affinity interactions allowing a stoichiometry-controlled binding of this complex to oligohistidine-tagged proteins (Figure 8D) [18].

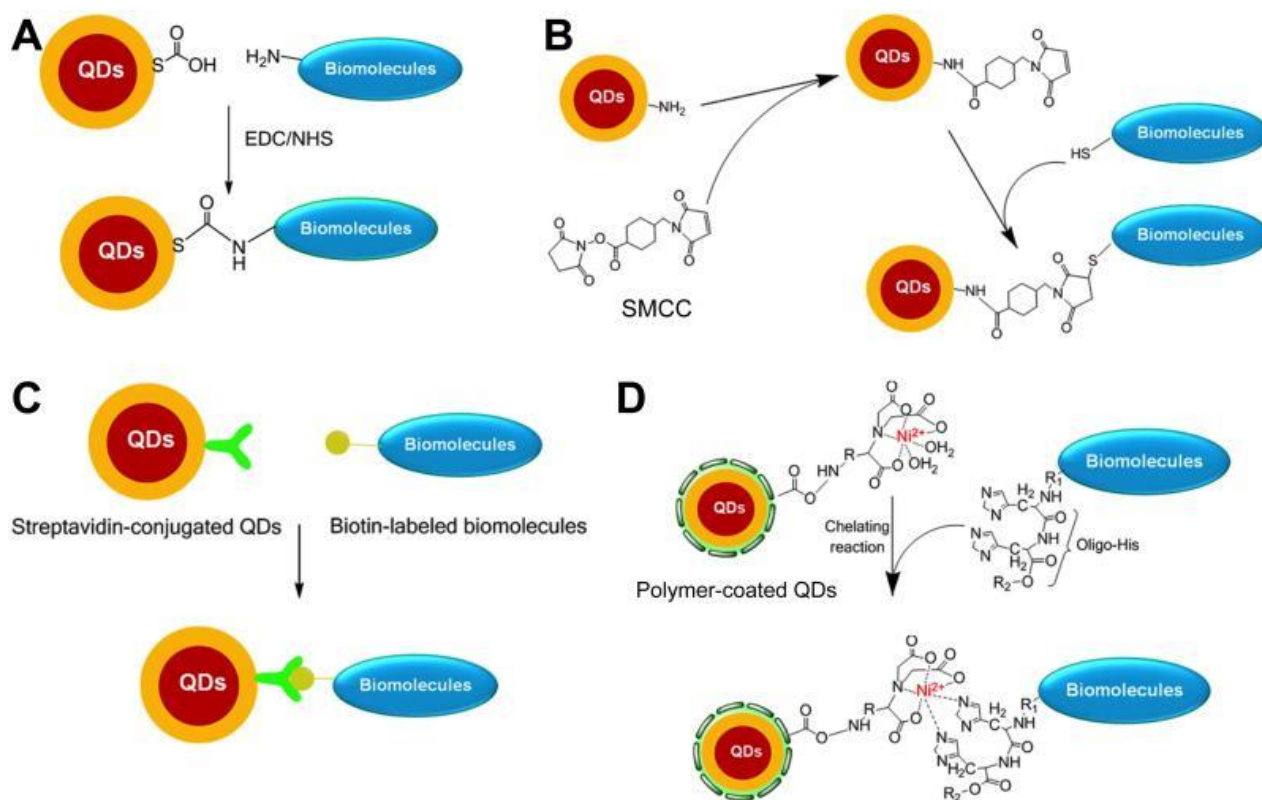


Figure 8: Strategies for bioconjugation of QDs via (A) EDC/NHS coupling, (B) the thiol–maleimide reaction, (C) streptavidin–biotin binding, and (D) interaction between Ni-NTA and histidine [138].

The reactivities of many types of biomolecules have been found to be preserved after conjugation to nanoparticle surfaces, although the binding strength was decreased in some cases. The optimization of surface immobilization of biomolecules is currently an area of intense research [4,139]. The surfaces of QDs may also be modified with biologically inert hydrophilic molecules, such as PEG.

Although there is a wide variety of strategies for conjugating QDs with biomolecules, all of them should meet some general requirements:

(i) Degradation of the natural activity of biomolecules in the process of conjugation should be minimized.

(ii) The obtained conjugates should be stable under physiological conditions and have a long shelf life.

(iii) Conjugation of biomolecules should be highly oriented: the binding sites of the recognition molecules should face outward, so that they could bind their respective antigens contained in the solution. The quantity of the recognition molecules on the surface of a nanoparticle should be controlled [140].

Another challenge is to deliver freely diffusing and monodisperse QD probes into the cell cytoplasm. As discussed above, the large size of conventional QD probes is the main obstacle to their penetration through cell or nucleus membrane pores, which is typically only 10–20 nm wide. Larger QD conjugates have limited access to this region compared with smaller drug–fluorophore conjugates.

Another important problem in using QDs for targeted imaging is the the selection of the targeting ligand. Among different classes of specific ligands, small molecules are preferable over antibodies/proteins, because they can keep the overall size small, are easier to synthesize, are more stable and resistant to harsh reaction conditions, and allow using the full advantage of the multivalency effect, because a larger number of small molecules can be attached to each QD compared to antibodies/proteins. Furthermore, antibodies, proteins, and antibody fragments typically require the use of complicated biological expression systems for their production, and the separation of conjugated QDs from antibodies/proteins can be challenging due to their similar size. Although DNA/RNA aptamers are also easy to produce/synthesize and can have less interactions with proteins *in vitro* than antibodies/proteins, the affinity for an individual target is usually quite low. In theory, QDs are large enough to enable multiple targeting ligands on the surface of a single QD to simultaneously bind to multiple targets. However, this aspect has been virtually unexplored to date. Targeting multiple different but closely related targets by incorporating different targeting ligands on the same QD, with spacers of suitable length, require robust chemistry to minimize batch-to-batch difference and improve reproducibility. In this case, it is more efficient to use a small functional pharmacological molecule.

1.2.6. Quantum dot cytotoxicity

Cytotoxicity of QDs is not relevant for *ex vivo* applications in biosensing, but it is critical for *in vivo* and *in vitro* bioimaging. In some cases, uptake of QDs by cells leads to a number of morphological and biochemical alterations, including the loss of cell functionality, chromosome damage, and eventually cell death [141]. Over the past two decades, the impact of QDs on cells and body has been under thorough investigation, reported in a huge body of literature, with hundreds of papers providing QD cytotoxicity data obtained using a large diversity of experimental designs of biocompatibility studies and a wide range of QD types. However,, there is a lack of a fully comprehensive model for explaining the potential toxic impacts of QDs. Some general conclusions that have been drawn are as follows. (i) The cytotoxicity of QDs is generally attributed to the release of toxic ions, such as heavy metals, into the cytoplasm after the elimination of the ligand shell of QDs in the intracellular environment [136]. Therefore, this parameter is highly dependent on the composition of the QDs. (ii) Due to the high surface-to-

volume ratio, a large number of QD surface atoms with unsaturated bonds are available to form free radicals. (iii) Different localizations of the particles, both intracellularly (in vesicles) and extracellularly (on the cell membrane) may entail different mechanisms of toxicity [142]. However, it has been demonstrated that the cytotoxicity of QDs also depends on a variety of other factors, such as their core composition, size, presence of a protective inorganic shell, nature and even the chirality of capping ligands, surface modification, surface charge and colloidal stability, cell type, and incubation conditions [136,143]. Across the available body of literature, no single study to date has assessed the relationship of toxicity with the combination of all the above conditions/properties. However, there most likely is a complex relationship of the experimental conditions and QD properties in terms of their impact on the observed toxicity; hence, the challenge is how to integrate quantitative/qualitative information from such complex toxicity data to derive generalized relationships and predictable trends from heterogeneous literature-compiled datasets. To address this challenge, mathematical models for literature data-mining, also known as meta-analysis, should be used to provide systematic reviews of the effect of relationships between physicochemical properties and experimental conditions on the toxicity of QDs [141,144]. It has been shown that toxicity is closely correlated with QD surface properties (including shell, ligand, and surface modifications), diameter, assay type, and exposure time. The potential toxicity of QDs *in vivo* determines the health consequences of the use of QDs for organs and is expected to be influenced by many parameters, including the dose, route of administration, absorption, distribution in the body, metabolism, and excretion. Despite the immense potential of QDs in medical applications, the understanding of how nanostructures interact with biological systems is lacking. Common ways to reduce cytotoxicity of QDs are to avoid cytotoxic materials in general and use heavy-metal-free QDs, such as ZnS, ZnSe, and InP-based ones [145], or to prepare a nontoxic protective shell or multiple shells, generally composed of ZnS, silica, or gelatin [144,146].

We expect major advances in both fundamental studies and practical applications of QDs. There is a wide variety of new semiconductor materials available with a diverse range of chemical, electronic, and optical properties for the QD synthesis. The synthesis of new nanocrystals with novel structures and properties will continue to yield unexpected examples such as doped, giant, and strain-tuned QDs. For biomedical applications, it is important to minimize the overall size of bioconjugated nanocrystals, to reduce steric hindrance and nonspecific protein adsorption, and ensure bright and stable PL for super-resolution optical microscopy. Reaching this goal will require innovations in developing not only novel crystalline nanostructures, but also new surface-coating, molecular tagging, and delivery strategies.

1.3. G-quadruplex DNA ligands, based on nitrogen-containing polyaromatic heterocycles

1.3.1. G-quadruplex DNA telomeres

Telomeres are non-coding highly repetitive sequences at the ends of chromosomes protecting them against gene erosion in the course of cell divisions and nuclease attacks [147-149]. Telomeric DNA contains a variable number of guanine (G)-rich, non-coding, 5'-(TTAGGG) n -3' tandem repeats of double-stranded DNA followed by a terminal 3' G-rich single-stranded overhang (150–200 nucleotides long) [150,151] (Figure 9). The approximate total telomere length in humans at birth is 10–15 kilobases.

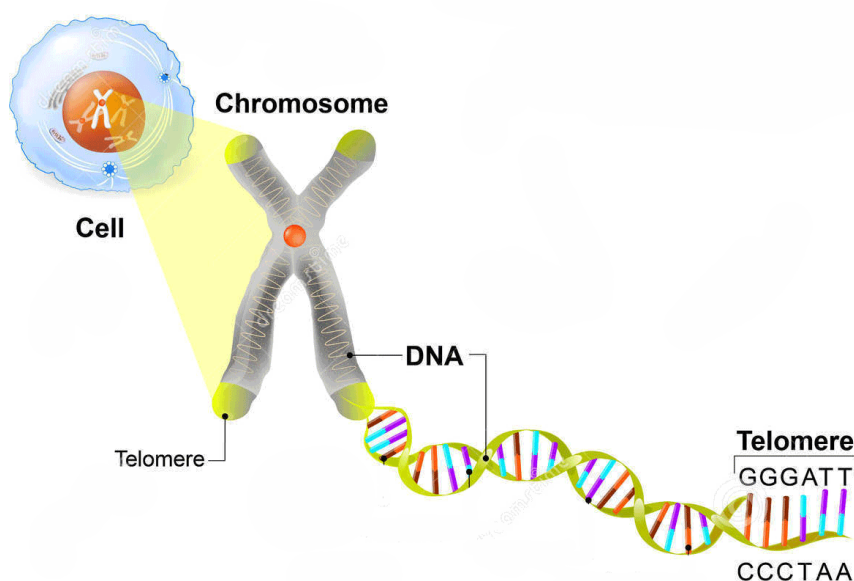


Figure 9: Telomeres in an eukaryote cell.

Telomeres regulate gene expression through transcriptional silencing of genes located close to, or at a distance from, the telomeres, called TPE and TPE-OLD, respectively [152]. In addition, the function of telomeres is strictly regulated and depends on the minimal length of telomeric repeats and the functionality of the associated sheltering protein complexes. Each replication results in a loss of 50–200 base pairs of the telomere, which can be elongated by the enzyme telomerase. After reaching the critical shortening of the telomeric DNA, the cell undergoes apoptosis or programmed cell death [153,154].

The G-rich telomeric sequence can fold into a G-quadruplex [155,156], a DNA secondary structure consisting of stacked G-tetrad planes connected by a network of Hoogsteen hydrogen bonds and stabilized by monovalent cations, such as Na⁺ and K⁺ [155]. Depending on the orientations of the DNA strands and the syn/anti conformations of the guanines, the G-

quadruplex can form different structures (Figure 10) [157,158]. The resulting G-quadruplex structures exhibit a diversity of features [147,149].

The structure and stability of G-quadruplex telomeres are of much research interest because they are closely related to cancer [154,159], aging, [160] and genetic stability [161]. The formation and stabilization of the DNA G-quadruplex in the human telomeric sequence have been shown to inhibit the activity of telomerase, a cancer-specific reverse transcriptase that is activated in 80–90% of tumors [162,163].

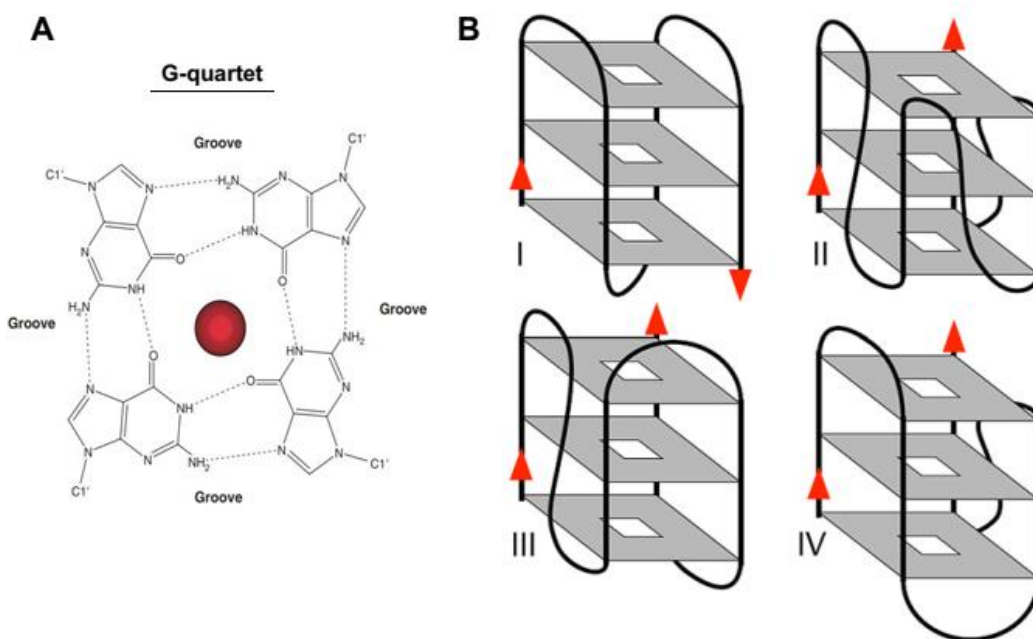


Figure 10: (A) The arrangement of guanine bases in the G-quartet, shown together with a centrally placed metal ion. (B) The possible conformations of the intramolecular G-quadruplex formed by human telomeric DNA [164].

It has recently been suggested that within a cell population there are large variations in telomere length, and, moreover, that the shortest telomeres are the most sensitive and critical for cell viability [165]. This suggests, in turn, that disruption of the delicate balance of telomere maintenance in tumor cells can be readily achieved. Telomeres are currently of considerable interest in view of the finding [166] that tumor cells are fundamentally distinct from normal human somatic cells in their ability to maintain telomere length at a constant level. Telomeres in tumor cells are, on average, significantly shorter than those of normal somatic cells. Thus, inhibition of telomerase can result in telomere truncation to a critically short length (leading to the characteristic senescent state, when cell growth irreversibly ceases, which is a common precursor to apoptosis).

Folding and stabilizing the DNA substrate into a non-single-stranded conformation using a stabilizing ligand results in effective telomerase inhibition. [160,167]. Therefore, ligand-induced stabilization of telomeric G-quadruplexes has become an attractive strategy for the development of anticancer drugs [168-170].

1.3.2. Study of ligand interactions with the G-quadruplex

Detailed studies on drug-quadruplex complexes are essential for understanding the quadruplex recognition and for drug design. There is a wide variety of methods that allow studying this interaction, such as absorption spectroscopy [171], circular dichroism [172], emission spectroscopy [173], calorimetry [174], nuclear magnetic resonance (NMR) [156], surface plasmon resonance [175], mass spectrometry [176], X-ray diffraction [177], and competition dialysis [178]. Particularly noteworthy are two methods. Fluorescence-based melting assays for the study of G-quadruplex ligands have been developed; specifically, fluorescence resonance energy transfer (FRET) assays have been widely used to study the thermal stabilization of preformed G-quadruplex structures upon binding different ligands [179]. If two probes forming a donor-acceptor system are linked at the end of a G-quadruplex-forming sequence, the FRET assay represents a powerful tool for the study of G-quadruplex ligands, because it allows large numbers of simultaneous measurements to be performed under different conditions (including ionic strength and various drug concentrations). Another method, where a polymerase chain reaction step is involved, is the telomeric repeat amplification protocol (TRAP) assay [180]. In this case, the enzymatic activity of telomerase is measured, which is directly proportional to the number of the TTAGGG repeat present. In the PCR, two different primers are used. The first primer acts as a substrate for telomerase-mediated addition of the TTAGGG repeats, and the second primer is used as a reverse primer for PCR. Then, the electrophoretic mobility shift assay is performed with the resultant products.

1.3.3. G-Quadruplex ligands as telomerase inhibitor

The unique structure and topology of G-quadruplexes provide great advantages for a small molecule to specifically target G-quadruplexes against duplex or other nucleic acid secondary structures and even target specific G-quadruplex structures. The modes of interaction of small molecules with a G-quadruplex usually follow three principles [181]:

- Stacking with the G-quartet through π - π interactions. Ligands with an extended planar aromatic system, which are similar to a G-quartet in size and shape, facilitate stacking on the G-quartet. This aromatic system can be a rigid flat or twisted surface.
- Interaction with the loops and grooves of the G-quadruplex. Cationic substituents usually have stronger binding affinities with the anionic phosphate backbone.

- Interaction with the negative electrostatic center of the G-quadruplex by electrostatic interaction with the cationic center of the aromatic core.

The basic binding modes of the G-quadruplex ligand are shown in Figure 11.

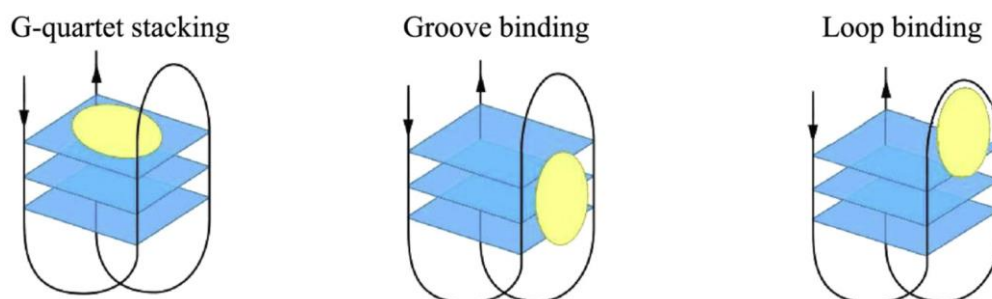


Figure 11: Examples of the binding modes of a small molecule with a G-quadruplex [182].

Four groups among the many G-quadruplex ligands are of special interest [179,183]:

- quinoline derivatives;
- porphyrin derivatives;
- macrocyclic (telomestatin) derivatives;
- acridine derivatives.

Quinoline derivatives

Quinoline (1-azanaphthalene) is a heterocyclic aromatic nitrogen compound characterized by a double-ring structure that contains a benzene ring fused to pyridine at two adjacent carbon atoms. Quinoline compounds are widely used as “parental” compounds to synthesize molecules with medical benefits, especially with anti-malarial, anti-microbial, and anti-cancer activities [184,185]. A large number of structurally diverse quinoline derivatives have recently been examined for their modes of function in G-quadruplex targeting. One of the quinoline compounds for G-quadruplex targeting is cryptolepine (5-methyl indolo[2,3-b]quinoline) (**1**) (Figure 12). This flat tetracyclic compound has provided a potent platform that prefers GC- over AT-rich duplex sequences, but it also recognizes triplex and quadruplex structures [186]. Disubstituted cryptolepine derivatives, with two alkylamino groups at positions C-2 and C-7 or at positions C-2 and C-10 (**2**) and (**3**), have been reported by Neidle *et al.* to have modest G-quadruplex stabilization and telomerase inhibition activity, with IC_{50} values in the range of 6-16 mM [187]. 11-Substituted cryptolepine analogues (**4**) have a significantly enhanced capacity for stabilizing a G-quadruplex [188]. Electron-donating groups at position C-11 can enhance the

basicity of the nitrogen atom in the pyridine ring, thus increasing the electrostatic interaction between the derivatives and the negative electrostatic center of the G-quadruplex. The most active compound, SYUIQ-05, exhibits an improved inhibitory effect on the telomerase activity ($IC_{50} = 0.44 \text{ mM}$) and induces a marked cellular senescence phenotype accompanied by a shortening of the telomeres in cancer cells [189].

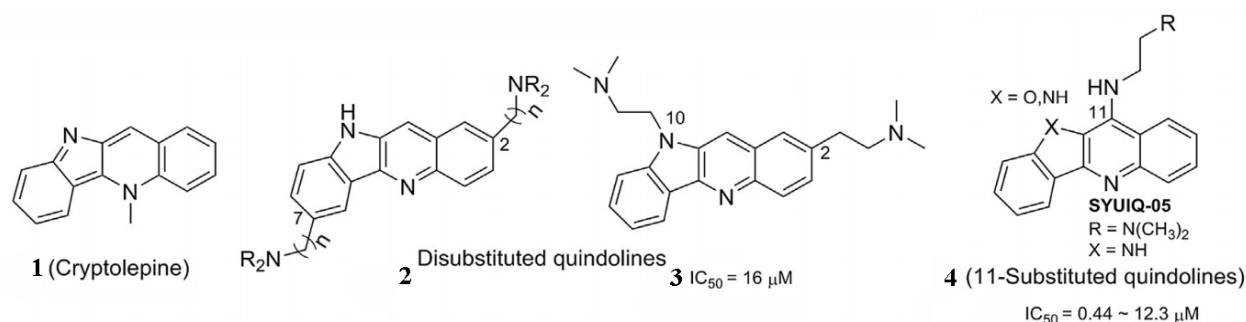


Figure 12: Structures of quindoline derivatives.

Porphyrins and their derivatives

Porphyrins are a group of natural organic compounds, which were initially well known as duplex DNA binding agents. Since then they have been thoroughly investigated for their interactions with G-quadruplex DNA after the pioneering work of the research group headed by Hurley in 1999 [190]. The cationic *meso-tetrakis-(N-methyl-4-pyridyl)porphyrin* TMPyP4 (**5**) (Figure 13) is the most representative example of this family, and it has been extensively investigated for its selectivity, binding mode, and pharmacological effects. The TMPyP4 ring has been assumed to be appropriate to interact with the G-quartet of G-quadruplex structures through π - π stacking interactions. The binding modes, as well as the binding stoichiometry in TMPyP4-G-quadruplex complexes, have remained a controversial issue in recent years. Different binding modes, including intercalation between adjacent G-quartets [191], stacking onto external G-quartets [192], and external stacking on TTA nucleotides without any direct interaction with G-quartets [193], have been discussed. To identify porphyrin derivatives with improved binding selectivity for G-quadruplexes, further studies have been performed with a primary focus on the synthesis of metalporphyrin complexes and modification at the *N*-methylpyridyl positions. TQMP (**6**) exhibits a 30-fold higher selectivity than TMPyP4 due to the efficient groove and loop bindings, which mainly depends on the flexible positively charged ammonium group and the phenolic hydroxyl group of the ligand [194]. Tetramethylpyridinium porphyrazine, TMPyPz (**7**), has a 100-fold higher binding affinity for human telomeric G-quadruplexes and a higher selectivity towards the G-quadruplex over duplex DNA (by a factor of up to 30) [195].

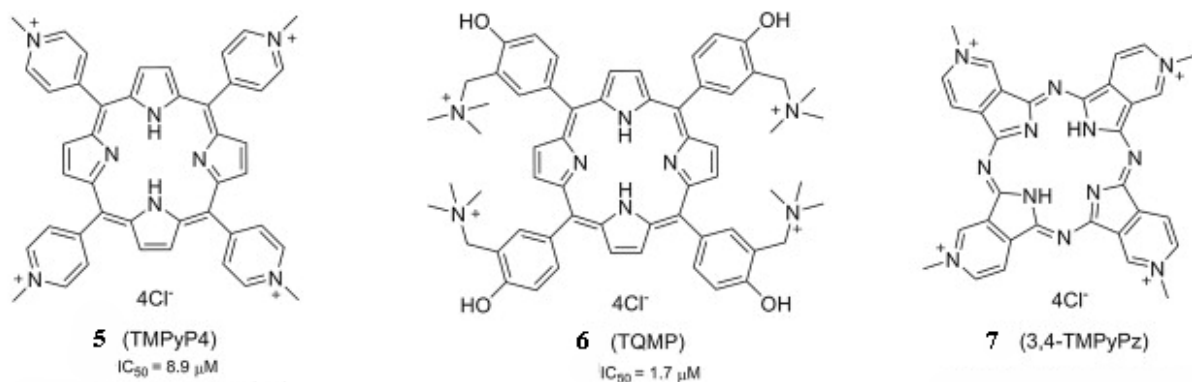


Figure 13: Structures of porphyrin derivatives.

Macrocyclic alkaloids and their derivatives

Telomestatin, a natural macrocyclic compound, is another effective telomeric G-quadruplex stabilizing ligand (**8**) (Figure 14). This molecule is composed of six oxazole rings and one thiazolone ring. The hydrophobicity, almost complete flatness, and the optimal size of telomestatin provide effective overlap with the four guanines when it stacks on top of the G-quartets via π -stacking interactions. One telomestatin molecule stacks at each terminal G-quartet within a G-quadruplex to give a 2:1 complex [170]. Due to its unique structural features, telomestatin exerts a high selectivity towards G-quadruplex over duplex DNA (a >70-fold preference) and the highest *in vitro* telomerase inhibitory activity ($IC_{50} = 5 \text{ nM}$) [196]. Hexa-trioxazole macrocycles (**9**), composed of two symmetric trioxazoles linked by amino acids, have been found to significantly stabilize G-quadruplexes by binding at both external sides of G-quartets [197]. The amino side chain makes them more soluble in water and improves their interaction with the G-quadruplex [198].

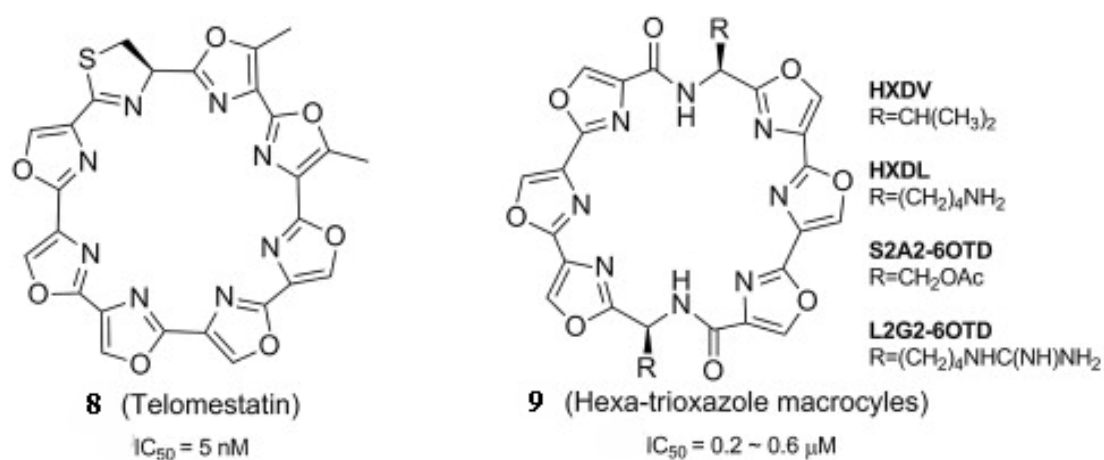


Figure 14: Structures of macrocyclic alkaloids and their derivatives.

Acridone derivatives: Trends in the development of acridine-based drugs.

Acridine alkaloids are the most intensely studied in the G-quadruplex ligand family. Acridine can intercalate between the double-stranded DNA base pairs, thereby distorting the DNA backbone structure and, subsequently, inhibiting the activity of DNA-related enzymes, such as topoisomerases [168]. Most of the shown in Figure 15 structures exhibit a high activity against tumor cell lines, partly due to the planar structure of the tricyclic rings conferring the ability to intercalate in the DNA and interfere with various metabolic processes in both prokaryotic and eukaryotic cells.

Neidle and coworkers first synthesized a series of 3,6-disubstituted acridines to improve the G-quadruplex affinity (**10**) (Figure 15). Introduction of a side chain increases the positive charge of the core and enhances the electrostatic interaction with the negatively polarized G-quartet center. The most potent telomerase inhibitors have IC_{50} values in micromolar concentration range [199]. Neidle et al. also synthesized several series of 2,6-, 2,7-, and 3,6-disubstituted acridone compounds, whose activity patterns are similar to those of their disubstituted acridine counterparts [200]. Particularly, a novel series of 4,5-disubstituted acridone derivatives (**11**) have been found to have a high affinity for telomeric G-quadruplex DNA in classical and competition FRET assays, with an improved selectivity compared to trisubstituted acridine compounds. Some compounds have selective cytotoxicity for cancer cells [201].

Cochard et al. synthesized 4,5-bis-(dialkylaminoalkyl) substituted acridines (**12**) and evaluated them for their telomerase G-quadruplex stabilizing properties using the FRET and TRAP assays. The results showed that the compounds containing a quaternary ammonium function were more active species in both quadruplex stabilization and TRAP assays. Among the 4,5-disubstituted acridine derivatives, the dimethylaminopropyl-substituted one excelled, with its sub-micromolar TRAP inhibitory activity ($IC_{50} = 0.15$ mM) [202].

Through the modification of the acridine structure, acridines can selectively bind to specific DNA configurations and specifically recognize G-quadruplex DNA, with a low affinity for double-stranded DNA, thereby inhibiting the activity of telomerase. The problem of ligand selectivity for G-quadruplex over duplex DNA has been approached using structure-based design methods [203]. In general, quadruplexes have four phosphodiester strands forming four separate grooves in the structure. The results of previous modeling studies have suggested that the two substituents of the bis-amido tricyclic chromophores each reside in a quadruplex groove. A third substituent, an anilino group at the position C-9 on the acridine skeleton, fits into a third groove in this model. The C-9 substituent also enhances the basicity of the acridine central ring nitrogen atom.

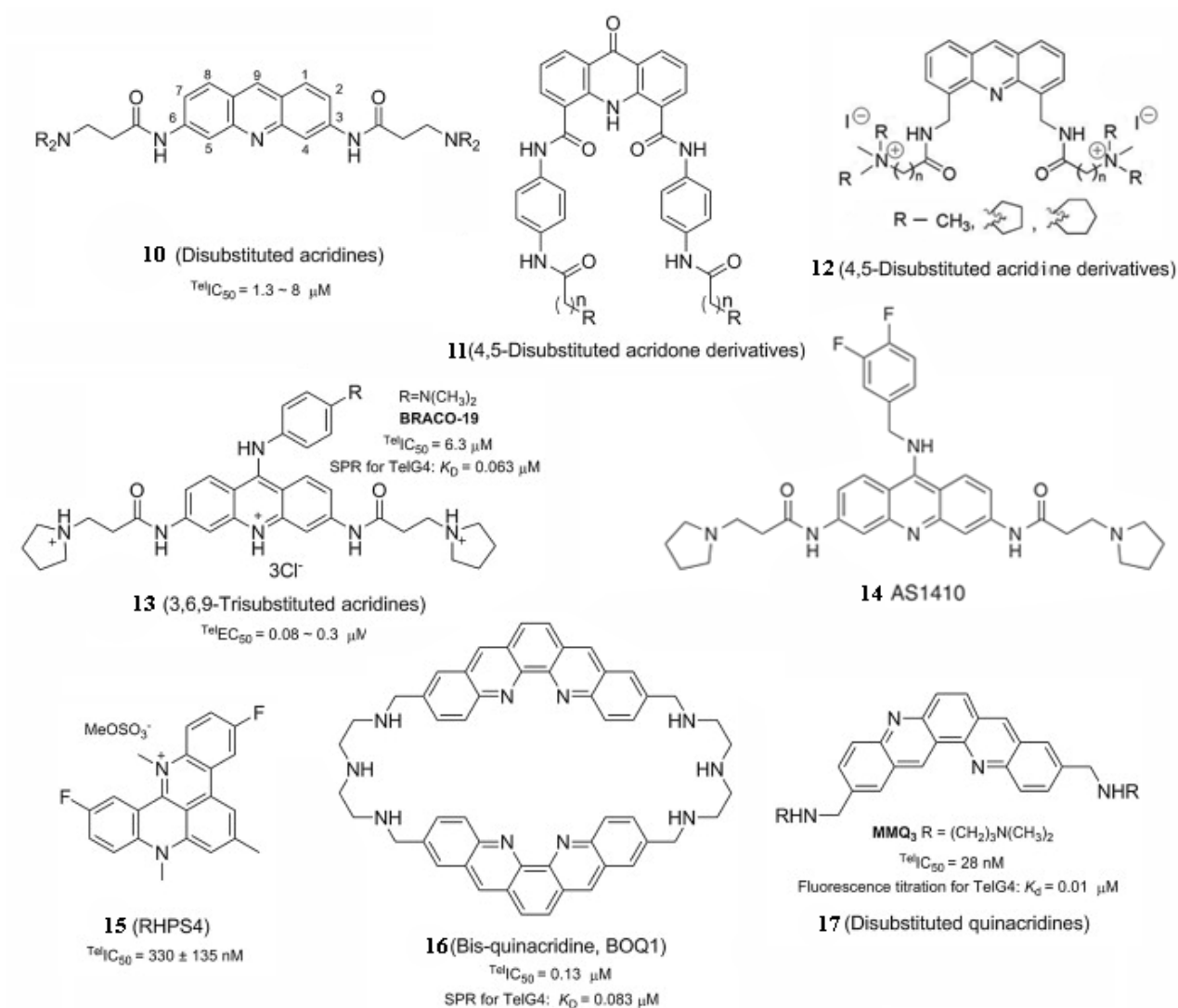


Figure 15: Structures of acridine and acridone derivatives.

One of the most notable compounds in this series BRACO-19 (**13**) – a 3,6,9-trisubstituted acridine have been synthesized [204] via acridone intermediates as shown in Figure 16. The preparation of BRACO-19 was carried out using the commercial starting material diphenylmethane with eight steps.

The increase in telomerase potency for these compounds in the TRAP assay compared to the disubstituted analogues is correlated with an increased quadruplex binding affinity as measured by surface plasmon resonance. The involvement of an anilino group at position C-9 significantly increases the basicity of the pyridine ring nitrogen and allows the ligand core to be protonated at physiological pH values. Moreover, the aniline derivatives at position C-9 provide an additional interaction with the third groove [205]. BRACO-19 has a strong binding affinity for the G-quadruplex structure and a high telomerase inhibitory activity ($IC_{50} = 95 \text{ nM}$). BRACO-19 displays a higher quadruplex binding affinity and improves the telomerase inhibitory

activity compared to the disubstituted acridines. In addition, it was shown that BRACO-19 was selective for G-quadruplex DNA, while the disubstituted acridines can bind both the quadruplex and duplex DNA. Significant tumor growth inhibition by BRACO-19 was observed in early-stage xenograft tumors of nude mice [206].

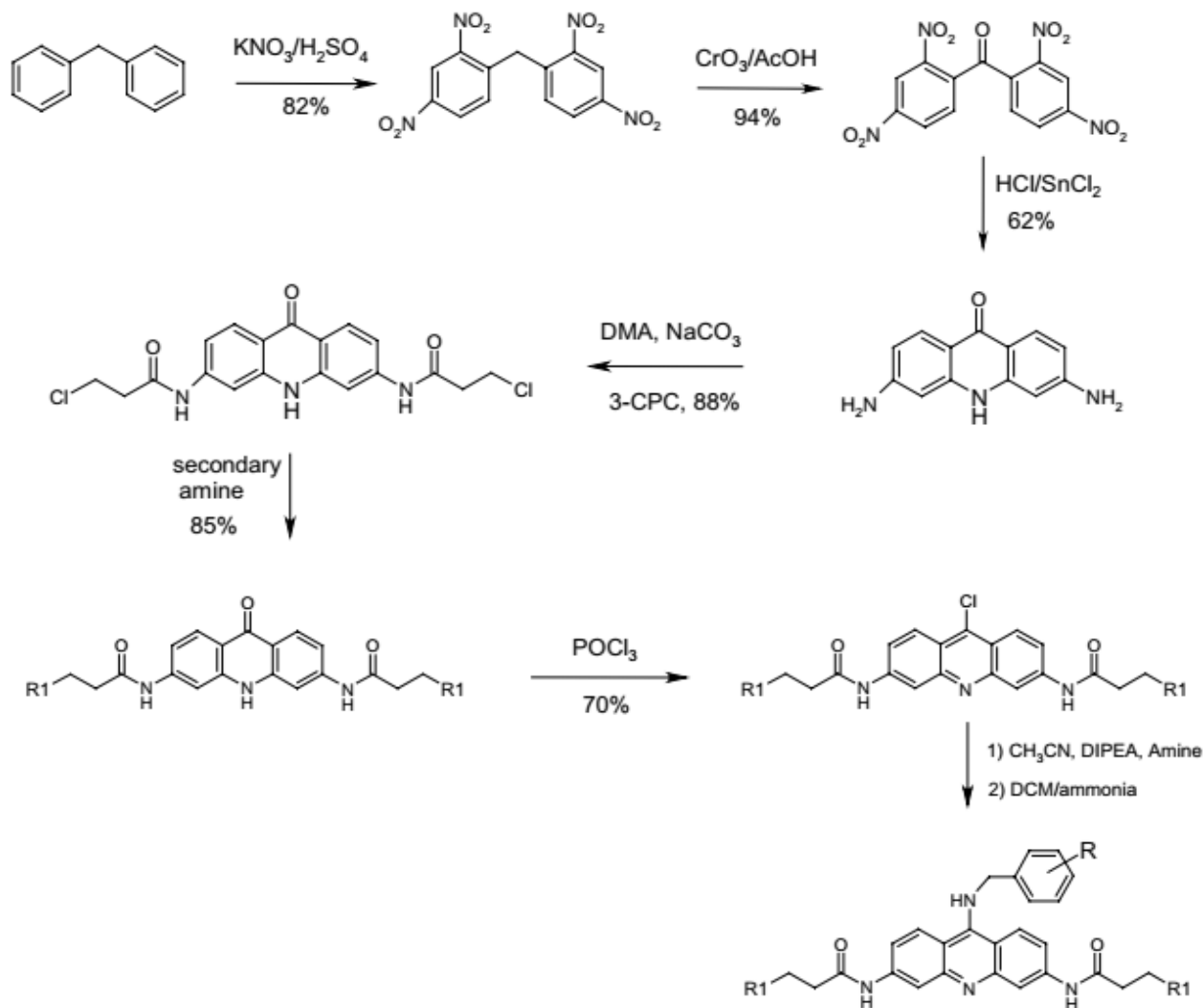


Figure 16: Synthesis route to benzylamino-substituted acridines [204].

In order to estimate the structure-activity relationship, several series of BRACO-19 analogues have been developed. The lengths of the side chains and the sizes of the substituents have a significant effect on the activity. The predictive three-dimensional (3D)-QSAR model was also developed to optimize the trisubstituted acridine derivatives as telomerase inhibitors [207]. When the 4-(*N,N*-dimethylamino)anilino group at position C-9 of BRACO-19 has been replaced by the 3,4-difluorobenzylamino group, the compound AS1410 (**14**) has been derived. Compared with BRACO-19, AS1410 has an increased hydrophobicity. As a result, AS1410 displays a slightly increased quadruplex-binding affinity compared to BRACO-19.

The tricyclic system of acridines has been subsequently modified into a pentacyclic system to enlarge the plane size for π -stacking. One of *N*-methylated pentacyclic acridinium salts, RHPS4 (**15**), has been found to exhibit a considerable telomerase inhibitory activity ($IC_{50TRAP} = 330$ nM). RHPS4 has many pharmacological attributes, which make it an effective telomere-targeting agent to eliminate a panel of cancer cells [208]. Mergny *et al.* introduced another class of pentacyclic ligands containing the crescent-shaped dibenzophenanthroline (quinacridine) and extended amino side chains to maximize the overlap with the G-quartet and electrostatic interaction with the grooves (**16**) [209]. They found that, with more cationic functional groups on the side chains, the binding affinity to intramolecular G-quadruplexes and telomerase inhibitory activity were increased. For example, the most active compounds MMQ3 (**16**) have a telomerase inhibitory value of 28 nM [210]. However, the charged side chains do not help to discriminate between the G-quadruplex and duplex structures. To improve the selectivity of these compounds, a cyclic *bis*-quinacridine (BOQ1) with two quinacridines connected by polyamine linkers has been proposed (**17**) [211,212]. BOQ1 has a better G-quadruplex stabilization activity than that of the monomeric series, most likely because the larger aromatic surface impedes its access to duplex DNA.

For the last 50 years many synthesis methods for acridines have been developed, a variety of functionalized acridines with bioactivity have been continuously synthesized and investigated, some of which have entered clinical or preclinical studies. There are exciting and highly promising developments in the exploration of the unique properties of acridines for dual tumor regulation and DNA binding, DNA adduct-intercalator conjugates, and other therapeutic applications. Despite these advances, there is still much work to be done. DNA and DNA-related enzymes, such as telomerase, are the main targets of acridine derivatives. Inducing DNA damage is one of the main ways of killing cancer cells. Identification and optimization of efficient acridine derivatives are required to fill this gap.

Although considerable progress has been made in the development and exploration of acridine derivatives, more work is needed to further improve the pharmacodynamic and pharmacokinetic properties of acridines, such as target selectivity and bioavailability, and to reduce side effects. Modifying the position and the nature of the substituent on the acridine core opens up broad prospects for the synthesis of novel perspective acridine analogues for inhibition of enzymatic activity in cancer cells.

2. Chapter 2. Materials and methods

2.1. Material preparation

Cadmium oxide (powder, 99.5%), 2-ethyl hexanoic acid (2-EHA, 99%), oleic acid (90%) tri-*n*-octylamine (TOA, 98%), 1-octadecene (ODE, technical grade, 90%), oleylamine (OLA, technical grade, 70%), selenium (powder, 100 mesh, 99.5%), zinc oxide (powder, 99.99% trace metals basis), thiourea ($\geq 99.0\%$) tri-*n*-octylphosphine (TOP, technical grade, 97%), DL-cysteine hydrochloride (98%), methylene glycol dimethyl ether (TEGDME, ReagentPlus, 99%), bromomethylmethylether, trifluoroacetic acid, hydrochloric acid, sulfuric acid, 3,4-difluoroaniline, 4-fluoroaniline, *N,N*-Dimethyl-*p*-phenylenediamine, thionyl chloride, *N,N*-dimethylformamide, sodium hydroxide, potassium permanganate, di-*tert*-butyl dicarbonate (Boc₂O), sodium sulfate, magnesium sulfate, and sodium bicarbonate were purchased from Sigma-Aldrich; *n*-hexadecylphosphonic acid (97%), was purchased from PlasmaChem GmbH; PEG derivatives: HS-(CH₂)₁₁-PEG₆-COOH and HS-(CH₂)₁₁-PEG₆-OH were purchased from ProChimia Surfaces. All chemicals were used as received without any additional purification.

Anhydrous solvents (methanol, chloroform, dichloromethane, hexane, dioxane, acetone, methyl acetate,) were purchased from commercial suppliers (Aldrich, Acros) and used as received or distilled under sodium or CaCl₂ and stored over 4Å molecular sieves. All reactions were carried out in oven-dried glassware and under a nitrogen or argon atmosphere.

2.2. Material characterization

The following techniques and instrumental methods were applied for characterization of physico-chemical and biological properties of the three principal components obtained in this theses, namely QDs, acridine derivatives and conjugates. Transmission electron microscopy (TEM), and the TEM-derived auxiliary techniques were employed to characterize the size, shape, and crystallinity of the QD samples. Ultraviolet–visible (UV-Vis) and photoluminescence spectroscopies were used to measure the optical parameters of the QDs, acridine derivatives and conjugate samples. Nuclear magnetic resonance (NMR) spectroscopy and mass-spectrometry were used to characterize the organic molecules. For biological evaluations of the novel potential pharmacological agent both FRET and TRAP assays were applied. A cell viability assay (MTT assay) was used to evaluate the cytotoxicity of the obtained acridine derivatives, QDs, and conjugates.

2.2.1. Transmission electron microscopy (TEM)

TEM, and the ancillary technique of energy dispersive spectroscopy (EDS) were the primary characterization methods used in this study. The combination of these techniques is a powerful tool for determining a range of material parameters, such as the sample morphology at

high magnification and the crystal structure and composition. HRTEM studies provided detailed information on the structure and crystallographic orientation of the sample. EDS was used to determine the elemental composition of the samples.

Transmission electron microscopy

TEM can provide the information of the sample in the form of an image from which the size, size distribution, and shape of the product can be estimated. TEM offers the unique ability to observe crystal defects at an almost atomic level, because defects scatter electrons differently from their surrounding matrices. At a high magnification of the crystalline sample, the lattice fringes of the material can also be observed, which gives information on the atomic packing of the nanocrystal.

Energy dispersive X-ray spectrometry

EDS is a very important micro-analytical technique that was used in conjunction with TEM. It relies on the characteristic X-rays generated from a sample bombarded with electrons to identify the elemental constituents of the sample. A spectrum corresponding to specific X-ray lines of corresponding elements is collected and can be easily identified. Quantitative data can also be obtained by comparing peak heights or areas for the analyzed and reference materials. Data collection and analysis with EDS is a relatively quick and simple process, because a complete spectrum of energies is acquired simultaneously. Survey analysis is often used in the characterization of the composition of an unknown sample. It can quickly identify the elements which are present in the sample.

HRTEM, EDS were performed using a JEOL JEM-2100F transmission electron microscope with an LaB₆ standard self-biasing thermionic electron source. In the standard mode of operation, the electrons were accelerated by an applied voltage of 200 kV. TEM specimen were prepared by putting a 10- μ l aliquot of a considerably diluted hexane or chloroform solution onto a carbon-coated 200-mesh copper grid (ProScitech) and subsequently dried at room temperature for 1 hour. More than 100 QDs were measured in each sample. After the measurement, all the collected data were analyzed using Origin software.

2.2.2. Steady state optical spectroscopy

UV-Vis spectroscopy

Due to the quantum confinement effect, UV-Vis spectroscopy allows the determination of the size and concentration, as well as the prediction of the size distribution of core QDs. In UV-Vis absorption spectroscopy, the absorption intensity is scanned with a light source with continuously changing wavelength.

Typically, the absorption spectrum of core QDs appears as a series of overlapping peaks that have a larger intensity at shorter wavelengths, and semiconductor-like absorption tail in

short UV range. Owing to the discrete nature of electron energy levels in QDs, each peak corresponds to an energy transition between discrete electron–hole (exciton) energy levels (Figure 17). The QDs absorb light that has a wavelength shorter than that of the first exciton peak. The wavelength of the first exciton peak is a function of the composition and size of the QD. Smaller QDs have the first exciton peak at shorter wavelengths.

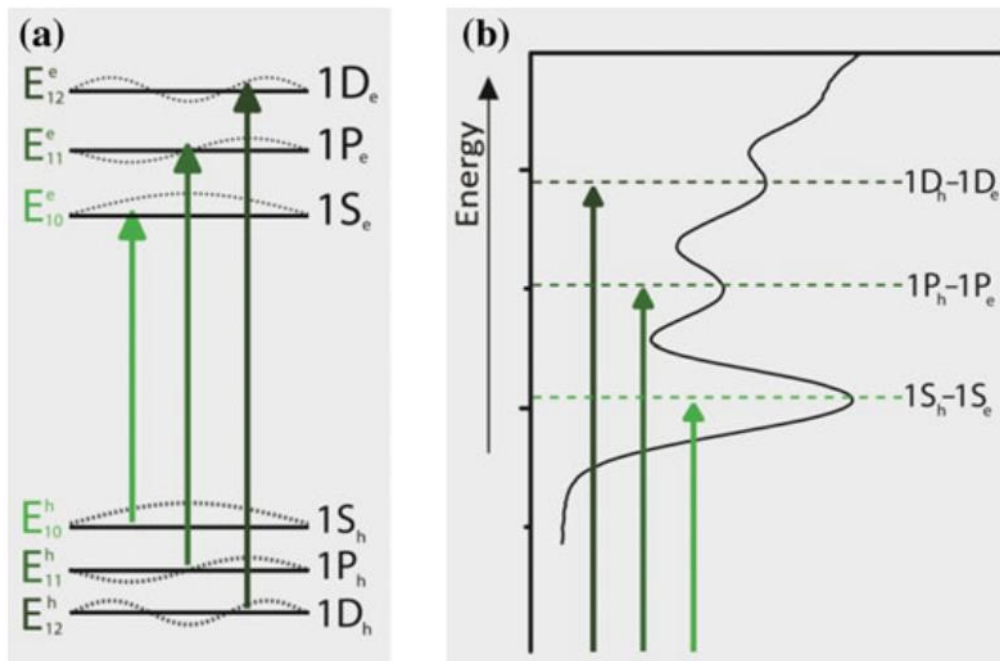


Figure 17: (a) The three lowest electron (E^e) and hole (E^h) energy levels in a semiconductor QD.

The corresponding wavefunctions are represented by dashed lines. Allowed optical transitions are indicated by arrows. (b) Assignment of the transitions in the absorption spectrum of colloidal QDs [213].

UV-Vis spectra were recorded in hexane, chloroform, and aqueous media on a Carry 60 UV-Vis absorption spectrophotometer (Agilent Technology) using quartz cells with optical path lengths of 3 and 10 mm. The measurements were carried out with a data interval of 1 nm and a scan rate of 200 nm/min in the range from 200 to 700 nm. The obtained absorbance values were used to calculate the CdSe core diameters, along with the QD concentrations using molar nanocrystal extinction coefficients given in Ref. [214]. From Lambert-Beer's law one can calculate the molar concentration of the nanoparticles:

$$A = \varepsilon \cdot C \cdot l, \quad (1)$$

In this equation, A is the absorbance of the first exciton absorption peak for a given sample, ε is the extinction coefficient per mole of nanocrystals ($L/(\text{mol cm})$), C is the molar

concentration of the nanocrystals (mol/L), and l is the optical path length used for recording the absorption spectrum (cm). When calculating C from Equation (1), one should take into account the dilution of the measured QD solution.

Photoluminescence spectroscopy

Photoluminescence spectra were recorded using an Agilent Cary Eclipse spectrofluorimeter (Agilent Technology). The solution spectra were recorded on samples with an optical density below 0.1 at the excitation wavelength. This absorption value should assure reabsorption of the emitted light by the sample at a negligible level. The measurements were carried out with a data interval of 1 nm and a scan rate of 200 nm/min.

The typical QD emission peak is Gaussian-shaped and is positioned at a slightly longer wavelength (20-50 nm) than the first exciton peak. This energy separation is referred to as Stoke's shift. An interesting property of QDs is that the emission peak wavelength is practically independent of the wavelength of the excitation light. The bandwidth of the emission spectra, FWHM, is determined by the temperature, natural spectral line width of the QDs, and the size distribution of the population of QDs in a solution. Spectral emission broadening due to size scatter is known as inhomogeneous broadening. Narrower size distributions yield smaller FWHMs.

The PL QYs of the QD samples dissolved in chloroform were determined using different organic dyes with known PL QYs (Table 2). All optical densities at the measurement wavelengths were kept below 0.1 to ensure elimination of emission reabsorption. The PL QY values were determined using the equation

$$QY_{QD} = \frac{tg\alpha_{QD}}{tg\alpha_{dye}} \cdot \frac{n_{dye}^2}{n_{QD}^2} \cdot QY_{dye} , \quad (2)$$

where n is the refractive index of the solvent of sample or reference dye, QY_{dye} is the PL QY of the reference dye from Table 2, and $tg\alpha$ values are determined as the inclination of linear fitting line on the optical density – integrated fluorescence intensity 2D plot, as demonstrated in Figure 18.

Table 2: Optical properties of the reference dyes [215,216].

Spectral region, nm	Dye	PL excitation wavelength, nm	Dye PL QY, % / solvent
<500	Cymerin 102	365	76 / ethanol
500-550	Fluorescein	460	90 / 0.1 M NaOH
550-590	Rhodamine 6G	500	95 / ethanol
570-600	Rhodamine 101	532	95 / Ethanol
600-650	Cresyl violet	580	58 / methanol

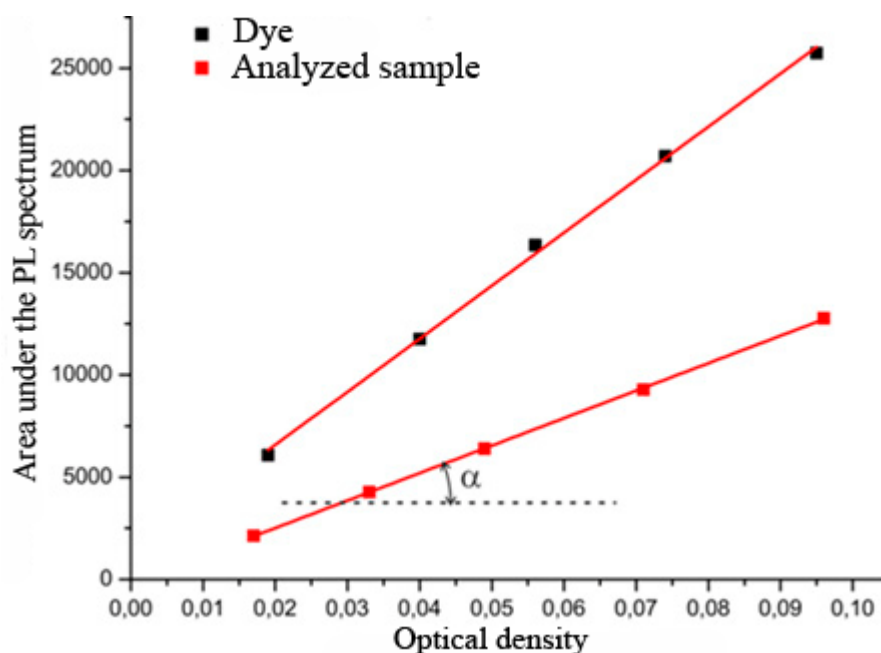


Figure 18: Experimental dependence of the integrated PL intensity from the optical density of the QD solution.

2.2.3. Two-photon spectroscopy

In addition to typical optical characteristics of QDs, two-photon absorption cross section (TPACS) and two-photon emission cross section (TPECS) are important properties in terms of multiphoton imaging. The TPACSs of CdSe/ZnS QDs considerably exceed those of organic dyes [217,218], which allows QDs to be used as photoluminescent markers or bio-nano hybrid photosensitive elements in the two-photon excitation mode [219]. This makes it possible to

engineer highly efficient QD-based two-photon labels that could be excited in the transparency windows of biological tissues in the near infrared spectral range [220]. Furthermore, the spatial resolution in the two-photon imaging mode can be substantially improved through compact localization of the excitation beam by its narrow focusing [221].

The TPECSs of the synthesized QDs were measured according to the method described in refs. [222,223] at equal excitation intensities and calculated using the following equation:

$$\sigma_{TPEQD} = \sigma_{TPEref} \times \frac{C_{ref} \times I_{nQD}}{C_{QD} \times I_{ref}}, \quad (3)$$

where σ_{TPEQD} is the TPECS of QDs, σ_{TPEref} is the TPECS of the reference sample, C_{QD} is the concentration of QDs, C_{ref} is the concentration of the reference sample, I_{QD} is the QD PL intensity, and I_{ref} is the PL intensity of the reference sample. Solutions of rhodamine 6G and rhodamine 101 in methanol were used as the reference samples. Equation (3) was used to calculate the TPECSs of the dyes from the known TPACS values taken from Ref. [224] and the values of PL QYs. The measurements were carried out at an excitation wavelength of 810 nm, which is the center of the transparency window of biological tissues [219]. A Ti:sapphire femtosecond laser system with a pulse repetition rate of 80 MHz, pulse energy of about 20 nJ, and pulse duration of about 50–70 fs was used as an excitation source. The laser beam was focused on the sample with a lens with a focal length of 10 cm. The concentrations of QDs in solutions were estimated using the extinction coefficients at the first exciton maxima for QDs of different diameters taken from [214].

2.2.4. Thin-layer, flash and gel-penetration chromatography.

The organic reactions and products were routinely monitored by thin-layer chromatography (TLC) on silica gel (Kieselgel 60 F254, Merck). Column chromatography purifications were performed using CHROMAGEL Silice 60 ACC 70-160 mm silica gel.

Gel-penetration chromatography (GPC) of nonpolar solutions of QDs was performed using Bio-Beads SX-1 cross-linked polystyrene granules (BIO-RAD) swollen in toluene. GPC of water-soluble QDs was performed using Sephadex G25, G100, G200 (GE Healthcare) with medium size beads swollen in phosphate or MES buffer.

2.2.5. Nuclear magnetic resonance (^1H NMR) spectroscopy

Nuclear magnetic resonance (NMR) spectroscopy is an analytical chemistry technique used in quality control and research for determining the composition and purity of a sample, as well as its molecular structure. NMR spectroscopy detects the energy absorbed by changes in the nuclear spin state. In addition, NMR can also provide atomic-level structural information.

The ^1H NMR (300 MHz) spectra were recorded by means of a Bruker AC 300 spectrometer using tetramethylsilane as an internal reference. The chemical shifts (δ) were measured in ppm.

The structures and chemical compositions of acridine derivatives were analyzed by comparing the chemical shifts of the synthesized molecules, literature data, and predicted NMR spectra.

2.2.6. Mass spectrometry

Mass spectrometry is an analytical technique where chemical species are ionized and the ions are sorted according to their mass-to-charge ratio. In simpler terms, a mass spectrum measures the masses within a sample. Mass spectrometry is used in various fields and is applied to pure samples as well as complex mixtures.

The mass spectra were recorded by means of an MSQ ThermoFinnigan apparatus using electrospray ionization (ESI) or a GCT Waters apparatus using the electron impact (EI) ionization method.

2.2.7. Dynamic light scattering (DLS) and zeta-potential measurements

DLS is an optical method for measuring the size variation of a colloidal suspension of QDs and other micro/nanomaterials. A coherent light source is directed through the suspension, and the autocorrelation of the time-resolved intensity of light scattered by the QDs reveals characteristic time scales related to the Brownian motion of small particles in solution. This correlation decays exponentially due to the diffusion of the particles. The accuracy which DLS affords can be enhanced by working at low nanoparticle concentrations and neutral pH; inter-particle collisions and electrostatic interactions are not accounted for and can be avoided in diluted samples.

DLS measurements were performed by means of a Malvern Zetasizer Nano ZS in a diluted aqueous solution with a low ionic strength using quartz cells with a path length of 3 mm. Every sample was analyzed in triplicate, 20 runs in each replication. Zeta potential measurements were performed in Zeta cells. Every sample was analyzed in triplicate, 100 runs in each replication.

2.2.8. Fluorescence resonance energy transfer (FRET) melting assay

Initial screening experiments were performed by means of a LightCycler real-time PCR device (Roche, Basel, Switzerland) as described previously [225] using the fluorescent oligonucleotide F21D (50-FAMGGGTTAGGGTTAGGGTTAGGG-DabCyl-30), alone or in the presence of the tested compound. Assays were performed in a buffer solution containing 0.2 mM F21D, 10 mM cacodylate, (pH 8.0), 0.1 M LiCl, and 5 mM KCl. The excitation wavelength was 470 nm, and the emission of fluorescein was recorded at 530 nm.

2.2.9. Telomeric repeat amplification protocol (TRAP) assay

The TRAP reaction was performed as described earlier [226]. PCR was performed in a total reaction volume of 50 μ l, including 45 μ l of the RM containing 20 mM Tris-HCl (pH 8.0), 50 mM dNTPs, 1.5 mM MgCl₂, 63 mM KCl, 1 mM EGTA, 0.005% Tween 20, 20 mg/mL bovine serum albumin, 0.1 μ g of the TS primer (5'-AATCCGTCGAGCAGAGTT-3'), 0.1 mg of the CXext primer (5'-GTGCCCTTACCCTTACCCTTACCCTAA-3'), 0.1 μ g of the NT pM primer (5'-ATCGCTTCTCGGCCTTTT-3'), 0.01 aM TSNT internal control (5'-ATTCCGTCGAGCAGAGTTAAAAGGCCGAGAAGCGAT-3'), 2.5 U of Taq DNA polymerase (DyNAzyme II DNA polymerase, Ozyme), and 200 ng of HT1080 cell CHAPS extract, as well as 5 μ L of distilled water. PCR was performed in an Eppendorf Mastercycler system equipped with a hot lid and incubated for 15 min at 30°C and 1 min at 92°C, which was followed by 30 cycles of 30 s at 92°C, 30 s at 52°C, and 30 s at 72°C each. After amplification, 8 mL of the loading buffer containing 20% sucrose, 5 \times TBE, 0.2% bromophenol blue, and 0.2% xylene-cyanol were added to the reaction mixture. The amplified products were resolved on a 12% nondenaturing polyacrylamide gel in 1 \times TBE and stained with SYBR Green I (Roche). Fluorescence was analyzed using a Typhoon 9210 PhosphorImager (GE Healthcare, Chalfont St. Giles, Buckinghamshire, UK). HT1080 human lung carcinoma cells were obtained from the American Type Culture Collection (Manassas, VA, USA). The cells were grown in Dulbecco's modified Eagle's medium containing GlutaMAX (Invitrogen) supplemented with 10% fetal calf serum and antibiotics.

2.2.10. Cell viability assay (colorimetric MTT assay)

Measurement of cell viability and proliferation forms the basis for numerous *in vitro* assays of a cell population's response to external factors. The reduction of tetrazolium salts is now widely accepted as a reliable way to examine cell proliferation. The yellow 3-(4, 5-dimethylthiazol-2-yl)-2,5-diphenyltetrazolium bromide (MTT) is reduced by metabolically active cells, in part by the action of dehydrogenase enzymes, to generate reducing equivalents such as nicotinamide adenine dinucleotide and nicotinamide adenine dinucleotide phosphate. The resulting intracellular purple formazan can be solubilized and quantified by spectrophotometric means [227,228].

The MTT reduction assay was used to estimate the cell viability. The toxicity of the QDs was evaluated *in vitro* using human monocytes. Monocytes were cultured in 96-well plates (Costar, USA) containing a final volume of 180 μ l/well of Roswell Park Memorial Institute medium at 37°C in an atmosphere of 5% CO₂. The QDs were added to the cells at different concentrations. Every concentration of QDs was analyzed in triplicate. After incubation of the

cells in the presence of QDs at 37°C in an atmosphere of 5% CO₂, the cells were washed with phosphate buffer (pH 7.4). A solution of MTT was then added to the wells, and cells were incubated for 4 hours at 37°C in an atmosphere of 5% CO₂. After formazan formation, the supernatant was removed and the solubilization solution (dimethylsulfoxide) was added to each well to dissolve formazan crystals. The solubilization solution was then thoroughly mixed to ensure complete solubilization. The absorbance of the solution was measured on using a Multiskan EX microplate reader (Thermo Fisher, USA) at a wavelength of 540 nm. The cell viability (CV) was determined as follows: $CV = A_i/A_0 \times 100\%$, where A_i is the optical density of the wells containing microcapsule suspension and A_0 is the optical density of the control.

2.2.11. Confocal microscopy

Confocal microscopy offers several advantages over conventional widefield optical microscopy, including the possibility to control the depth of field, elimination or reduction of background information away from the focal plane (that leads to image degradation), and the possibility to collect serial optical sections from thick specimens. The key to the confocal approach is the use of spatial filtering techniques to eliminate out-of-focus light or glare in specimens whose thickness exceeds the immediate plane of focus. There has been a tremendous explosion in the popularity of confocal microscopy in recent years, partly due to the relative ease with which extremely high-quality images can be obtained from specimens prepared for conventional fluorescence microscopy, and the growing number of applications in cell biology that rely on imaging both fixed and live cells and tissues. Confocal microscopy measurements of QD accumulation in cells have been performed using an LSM-710-NLO laser scanning confocal microscope (Carl Zeiss Microscopy, Germany) with a 20× Plan-Apochromat objective lens (NA = 0.8). The samples were placed onto a Petri dish with a glass bottom 0.16 mm thick. The spectral-resolved fluorescence emission was detected by a GaAsP 32-channel detector in the visible spectral range (400–700 nm).

The QD fluorescence excitation was performed by a laser at wavelengths of 488 and 561 nm. Fluorescence was recorded in the wavelength range of 500–720 nm.

An image in transmitted light was obtained by recording the signal of the excitation laser beam after passing through the sample by a separate T-PMT detector. Thereby the imposition of the fluorescence image and images in the transmitted light mode was obtained.

2.3. Synthesis of CdSe quantum dots

CdSe-core QDs were prepared using a modified procedure described in the literature [40]. CdSe cores of different sizes were synthesized by the hot-injection method in the low-polar high-boiling organic solvent 1-octadecene. The CdSe cores were obtained from cadmium *n*-

hexadecylphosphonate and selenium tri-*n*-octylphosphine complex as precursors and tri-*n*-octylamine as a co-surfactant. The cadmium precursor was obtained in two steps, since one-stage synthesis of cadmium *n*-hexadecylphosphonate is more difficult due to a low reactivity between cadmium oxide and HDPA. In the first step, a solution of cadmium 2-ethyl hexanoate (Cd-EHA) was obtained in three neck flask by dissolving 1 mmol (128 mg) of cadmium oxide (II) and 2.5 mmol (400 μ L) of 2-ethylhexanoic acid in 2 mL of ODE under fast heating to 300°C. The reaction apparatus is shown in Figure 19. After complete dissolution of CdO, the reaction mixture was cooled to room temperature. In the second step, the residue of 2-ethylhexanoic acid was replaced with *n*-hexadecylphosphonate residue; to this end, 150 mg of *n*-hexadecylphosphonic acid (HDPA), 2 mL of trioctylamine (TOA) as a co-surfactant, and 6 mL of 1-octadecene were placed into the solution in the flask cooled to room temperature. The flask was heated to 100°C and evacuated at 10 mbar for 30 min to remove residual water. Then the solution was slowly heated to 240°C and kept at this temperature for 1 h under an argon atmosphere to assure complete transformation of Cd 2-ethylhexanoate to Cd hexadecyl phosphonate.

The selenium precursor was prepared by dissolving 2 mmol (158 mg) of selenium powder in 2 mL of tri-*n*-octylphosphine (TOP) and 0.5 mL of 1-octadecene under an argon flow under mild heating.

For QD nucleation (Schematic of chemical synthesis is shown in Figure 20), the selenium precursor was rapidly injected into the cadmium precursor solution at a specified temperature (240, 270, or 300°C) and kept in an argon atmosphere under vigorous stirring at 950 rpm. The reaction was monitored by UV-Vis spectroscopy and was stopped on reaching the required size of the NCs by intense cooling with air flow or transfusion of the reaction mixture into liquid nitrogen.

Purification of the core CdSe QDs was carried out to remove excess surfactants, solvent, impurities, and by-products to facilitate further shell coating. The obtained QDs were isolated from the crude solution by precipitation with methyl acetate. For this purpose, a twofold volume of methyl acetate was added to the QD solution, and then the solution was stirred until precipitation of most QDs and discoloration of the supernatant was clearly visible, which was followed by centrifugation (5000 rpm, 5 min) and removal of the supernatant. The QD pellet was dissolved in 4 mL of toluene. The as-synthesized nanomaterials were then characterized using a variety of techniques.

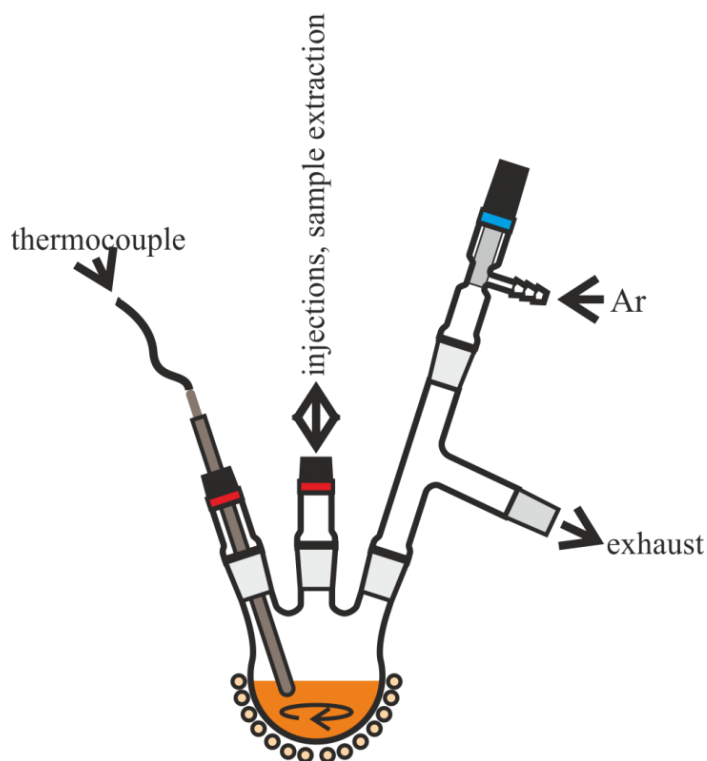


Figure 19: Reaction apparatus of CdSe core and core/shell QD synthesis.

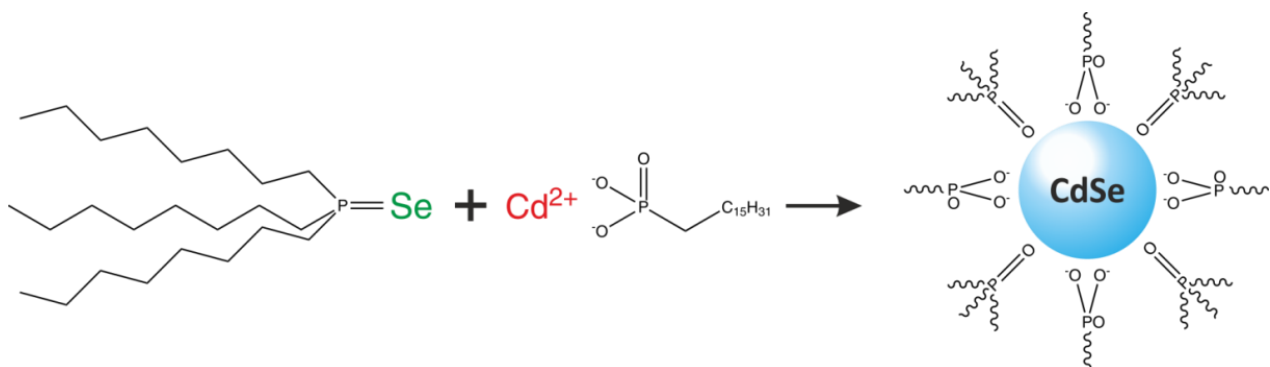


Figure 20: Schematic of chemical synthesis.

2.4. Synthesis of core/shell quantum dots

CdSe core purification.

As-prepared CdSe QDs were isolated from the crude solution by precipitation with methyl acetate. Then, for purification of the reaction mixture from remaining precursors that were captured during precipitation, and preparation of the QD surface for the shell growth, the following manipulations were performed. A QD solution in toluene was successively filtered through a PET syringe filter with a pore diameter of 450 nm and purified by gel permeation chromatography (GPC) using SX-1 cross-linked polystyrene beads (BIO-RAD) as the stationary carrier phase. In this method, QD cores rapidly migrate along the stationary phase, while the

low-molecular-weight unreacted precursors are slowed down as a result of retention in the pores of the carrier [229]. When the chromatographic column was filled as shown in Figure 21, the toluene solution of QDs was applied to it. Intensely colored fractions of purified QDs obtained by elution were collected into a glass beaker.

After the GPC procedure, HDPA residues on the surface of the cores were replaced with oleylamine in the presence of sodium borohydride [230]. This manipulation was performed twice using fresh portions of oleylamine and NaBH_4 , followed by coagulation of QDs and redispersion of them in toluene. After the second step, core solution in toluene was filtered through a glass filter (25-50 μm) and then QDs were precipitated with excess methyl acetate. After centrifugation and removal of the supernatant, purified core solution was filtered through a PTFE syringe filter with a pore diameter of 220 nm. After that 6 mL of ODE was added to the solution and toluene was distilled on a rotary evaporator under vacuum. Further on, core solution in ODE was transferred into reaction vessel, to which 6 ml of OLA was added. After additional degassing at 100°C , under argon atmosphere 1 mmol of TOP was injected into the flask, and the core solution was allowed to settle for 10 min prior to the beginning of shell growth followed by measurement of PL QY by the method described in Chapter 2.2.2.

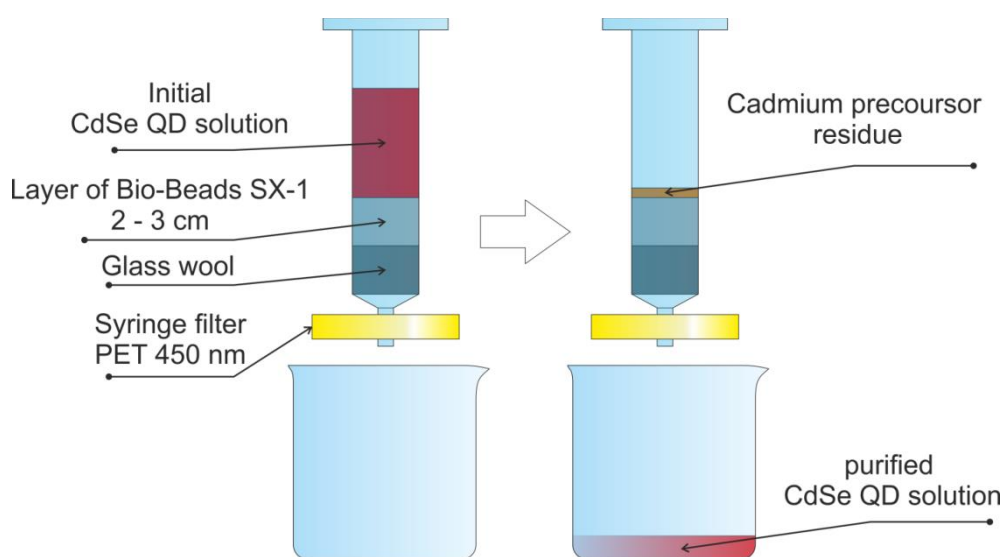


Figure 21: Scheme of gel filtration of CdSe cored using Bio-Beads SX-1 (Bio-RAD) as a stationary phase.

Preparation of stock solutions of the precursors.

The zinc and cadmium stock solutions with concentrations of 0.61 and 0.44 M, respectively, were prepared by dissolving the corresponding metal oxides in a 2.05-fold excess of 2-EHA in ODE while heating and under vigorous stirring and argon atmosphere. The sulfur

stock solution was prepared by dissolving 34 mmol of thiourea in 40 mL of methylene glycol dimethyl ether (TEGDME) under sonication. All solutions were levelled with TEGDME to obtain final precursor concentrations of 0.85 M.

ZnS shell coating.

Determination of the QD core size and concentration in stock shell coating solution for quantification of precursors needed for shell deposition was performed by UV-Vis spectroscopy using the dependences of the first excitonic absorption peak position on the QD size and corresponding QD extinction coefficients presented in [214]. For the smallest (1.5 nm) QDs, which are off the valid range of data presented in Ref. [214], the molar extinction coefficient of $130000 \text{ l}\cdot\text{mol}^{-1}\cdot\text{cm}^{-1}$ was used as a result of linear extrapolation of the known dependence. After performing the calculations discussed in Chapter 3.1.2, known amounts of precursors were loaded into syringes and the injection of zinc and sulfur precursors was started in parallel with two syringe pumps under slow heating to 170°C for 30 min. After the shell growth completion, the obtained core/shell QDs were isolated from the crude solution in a similar manner as was described earlier for the case of CdSe core QDs.

ZnS/CdS/ZnS multishell coating.

Multishell (MS) coating was done according to the SILAR procedure in the thermocycling mode, with the quantities of reagents calculated using our QD growth model (see Chapter 3.1.2) to avoid excess precursor accumulation in the reaction mixture. All precursor injections were made at 100°C; then, the temperature of the reaction mixture was raised to 175°C for the ZnS shell and 165°C for the CdS shell within 5 min, and the solution was kept at this temperature for another 5 min to complete the adsorption and reaction. The first cycle was started with zinc injection, and 0.5 mmol of TOP was added to the reaction mixture prior to each injection of the sulfur precursor to stabilize QDs obtained in the following cycle when thiourea is injected. The shell growth was finalized with additional injection of the amount of the zinc precursor sufficient for the formation of $\frac{1}{2}$ shell ML calculated according to the model. This ensured complete coating of the QD surface with zinc atoms, which was necessary for further phase transfer and better passivation with organic ligands. The shell growth was monitored using UV-Vis and PL spectrophotometry and PL QY measurements.

After completion of the shell growth, the resulting QDs were isolated from the crude solution by the procedure described earlier.

2.5. Preparation of water-soluble quantum dots

The preparation of water-soluble QDs was performed according to Ref. [121] with some principal modifications, including exact calculation of the necessary equivalents of the ligands

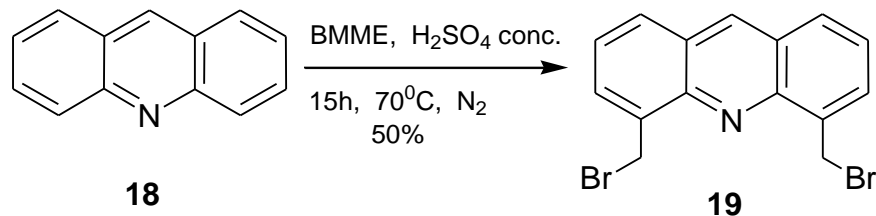
required for complete passivation of zinc atoms on the QD surface. The number of surface zinc atoms was calculated using the growth model CdSe NCs, as was used in the calculation of the quantities of shell precursors during shell coating. For example, for complete surface passivation of a single ultrasmall QD with 3 ML of ZnS plus $\frac{1}{2}$ terminal ML of Zn, 264 molecules of ligands are necessary. Solubilization of QDs was performed by the two-stage ligand exchange approach. At the first stage, original hydrophobic ligands were exchanged for DL-cysteine; at the second stage, DL-cysteine was exchanged for a chosen mixture of two PEG derivatives terminated with different functional groups. For this purpose, 5 mg of initial QDs was once purified from the excess of ligands by the dispersion/coagulation procedure with hexane/methyl acetate, respectively, and subsequent centrifugation of the suspension at 5000 rpm for 5 min. After that, the QD solution in chloroform was titrated with 15 mg/mL DL-cysteine solution in methanol until the calculated amount of new ligand was reached, and then stirred during 5 min. After centrifugation, the precipitate was twice washed with 2 mL of methanol with short sonication in an ultrasonic bath followed by centrifugation. To make the cys-QDs soluble in aqueous media, the precipitate was first suspended in several drops of methanol with short sonication, and then 0.6 mL of an alkaline water solution (60 μ L 0.1 M NaOH in 540 μ L of deionized water (pH 12-13) was added to the suspension to obtain a transparent QD solution. This QD solution was sonicated for 10 min until total dissolution of QDs was observed. After a short-term distillation of methanol in a vacuum concentrator, the QD solution was centrifuged at 14000 RPM to remove residual undissolved QDs.

At the second stage, DL-cysteine was replaced with an excess of PEG derivatives with terminal hydroxyl or carboxyl groups (HS-(CH₂)₁₁-PEG₆-COOH; -OH) at a ratio of 9:1, respectively. Hydroxyl derivatives provide chemical inertness in biological media, and carboxyl derivatives provide a small zeta-potential, better colloidal stability of the QD solution, and the possibility for their conjugation with biomolecules and enhancement of cellular uptake. For this purpose, the amount of ligands four times higher than the calculated value was added to the solution of the QDs.

The PEGylated QDs were incubated overnight and roughly purified of excess PEG derivatives by centrifugation using Amicon Ultra-15 filter units with a 10 kDa cut-off (Millipore) in phosphate buffer (pH 8.0, 50 mM) at 3500 rpm. The QD solution was concentrated to 100 μ L and then purified by means of GPC using Sephadex G100 as the stationary carrier for fine purification from residual free PEG derivatives. After the chromatographic column was filled with Sephadex G100 granules preliminarily soaked in phosphate buffer (pH 8.0), a concentrated QD solution was applied onto the column. Intensely colored fractions of purified QDs obtained by elution were collected into an Eppendorf test tube.

2.6. Synthesis of 4,5,9-trisubstituted acridine derivatives

2.6.1. Synthesis of 4,5-bis(bromomethyl)acridine (**19**)



The reaction was adapted from Ref. [231,232].

Bromomethylmethylether (BMME) (25 ml, 180 mmol, 4 eq.) was gradually added into the solution of 8.0 g (45 mmol, 1 eq.) of acridine (**18**) in 120 mL of concentrated sulfuric acid. The solution was heated to 70°C and stirred at this temperature for 15 h under the nitrogen atmosphere, which was accompanied by the evolution of ether and hydrogenbromide gas. After completion of the reaction detected by TLC (petroleum ether /CH₂Cl₂ 4 mL / 1 mL), the reaction mixture (RM) was poured into a glass in an ice bath and stirred at 0°C for 1 h to give a yellow suspension. After filtration of the suspension, the filtrate was dried by air flow and then dissolved in 1 L of dichloromethane, and then neutralized with potassium carbonate to pH 10-11. The combined organic layer after fivefold extraction was dried with MgSO₄, filtrated, and partly concentrated under reduced pressure. The crude product was recrystallized diethyl ether. The precipitate was collected and washed with diethyl ether to obtain 8.19 g of (**19**) as a pale yellow powder.

Form: pale yellow powder.

Yield: 50 %

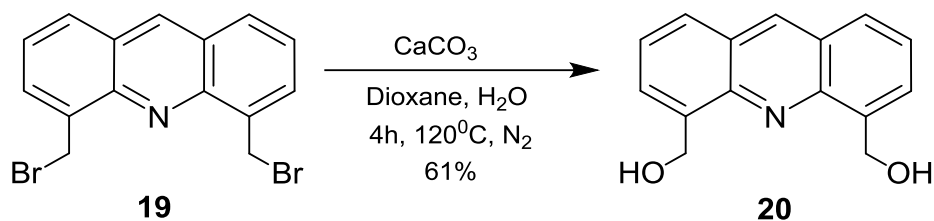
Formula: C₁₅H₁₁Br₂N

MW: 362.93

R_f (CH₂Cl₂/cyclohexane, 5 mL / 5 mL): 0.5

¹H NMR (300 MHz, DMSO-d₆): δ = 9.09 (s, 1H), 8.04 (d, 2H), 7.84 (d, 2H), 7.59 (dd, 2H), 4.47 (s, 4H).

2.6.2. Synthesis of acridine-4,5-(dihydroxymethyl)acridine (**20**)



The reaction was adapted from Ref. [231,232].

Dibrominated acridine (**19**) (4.0 g, 11 mmol, 1 eq.) was dissolved in 120 mL of mixture dioxane/H₂O (1:1), and excess of CaCO₃ (6.6 g, 55 mmol, 5 eq.) was added to the RM, which was refluxed at 120°C for 4 h under inert atmosphere. After completion of the reaction, followed by TLC (CH₂Cl₂/AcOEt, 5 mL / 5 mL), the RM was filtrated, the filtrate was concentrated, obtained crude product was dissolved in 300 mL of CH₂Cl₂. The organic phase was washed with 50 mL of water and 1×100 mL of brine. The organic phase was dried over Na₂SO₄ and concentrated to obtain a dark red-brown crude product. Purification provided by column chromatography with gradually increasing polarity (with a CH₂Cl₂/AcOEt ratio of 5 mL / 5 mL) to obtain 1.6 g (61%) of (**20**).

Form: pale yellow powder.

Yield: 61 %

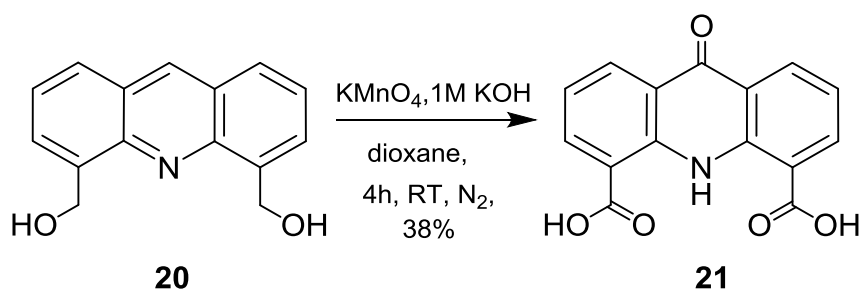
Formula: C₁₅H₁₃NO₂

MW: 239.09

R_f (CH₂Cl₂/AcOEt, 5 mL / 5 mL): 0.4

¹H NMR (300 MHz, DMSO-*d*₆): δ = 9.09 (s, 1H), 8.03 (d, 2H), 7.88 (dd, 2H), 7.62 (dd, 2H), 5.38–5.27 (m, 6H).

2.6.3. Synthesis of 9-oxo-9,10-dihydroacridine-4,5-dicarboxylic acid (**21**)



The diol (**20**) (1.0 g, 4.2 mmol, 1 eq.) was dissolved in 1 mL of dioxane, which was followed by adding 7 mL of 1 M potassium hydroxide. After a 5-min sonication, 2.0 g (12.5 mmol, 3 eq.) of potassium permanganate was added to the RM at 0°C. The suspension was

vigorously stirred for 4 h under natural heating to room temperature. The reaction was stopped by addition of a small amount of acetone in order to transform residual potassium permanganate into manganese oxide (IV) and to avoid problems during further filtration. The residue was filtrated and thrice washed with water (3×100 mL) and 50 mL of acetone; the water phase was concentrated under the reduced pressure to eliminate acetone and dioxane. The remaining aqueous solution was acidified with 2 mL of concentrated (6 M) hydrochloric acid to pH 1-2, with the precipitate color changing from yellow to brown. The precipitate was filtrated, and the solution was concentrated to 100 mL and cooled to 4°C into a fridge overnight and filtrated on the next day. The combined filtrate was washed by water (2×10 mL) and methanol (10 mL). The solid phase was dried with phosphorus pentoxide at 80°C under reduced pressure for 5 h to a brown solid compound, with a yield of 0.45 g (38%) of (**21**).

Form: brown powder.

Yield: 38 %

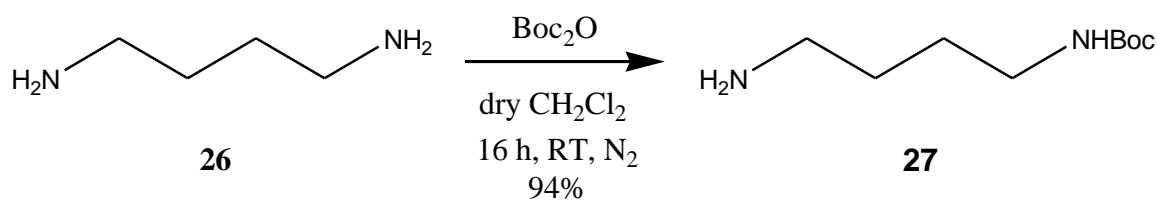
MW: 283.24

Formula: $\text{C}_{15}\text{H}_9\text{NO}_5$

R_f ($\text{CH}_2\text{Cl}_2/\text{MeOH}$, 5 mL / 5 mL): 0.4

^1H NMR (300 MHz, $\text{DMSO}-d_6$): $\delta = 13.95$ (s, 1H), 8.51 (dd, 2H), 8.46 (dd, 2H), 7.40 (t, 2H).

2.6.4. Synthesis of *tert*-butyl 4-aminobutylcarbamate (**27**)



The reaction was adapted from Ref. [233–235].

A preliminarily prepared solution of di-*tert*-butyl dicarbonate (Boc_2O) (0.95 g, 4.36 mmol, 1 eq.) in 9 mL of dry dichloromethane was added dropwise during 2 h to a solution of putrescine (butane-1,4-diamine) (**26**) obtained by dissolving 2.0 g (22.7 mmol, 5 eq.) of the substance in 20 mL of dry dichloromethane. The RM was then stirred for 14 h. The resulting precipitate was diluted with dichloromethane and then twice washed with 10% NaHCO_3 (20 mL). The organic layer was dried with Na_2SO_4 , filtrated, and concentrated under a reduced pressure to obtain 0.77 g (94%) of (**27**) as a clean colorless oil.

Form: colourless oil.

Yield: 94%

Formula: C₉H₂₀N₂O₂

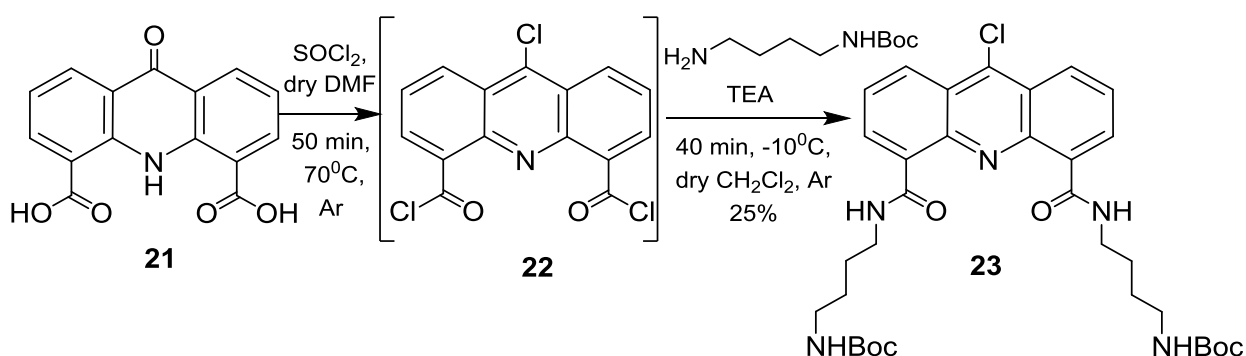
MW: 188.27

R_f (CH₂Cl₂/MeOH, 9 mL / 1 mL): 0.1

¹H NMR (300 MHz, CDCl₃): 4.78 (s 2H), 3.13 (q 4H), 2.72 (t 4H), 1.64-1.55 (m, 1H), 1.44 (s, 4H).

¹H NMR (300 MHz, CD₃OD): 3.04 (m 2H), 2.67 (m 2H), 1.55-1.47 4H 4H, 1.43 s 9H).

2.6.5. Synthesis of 9-chloroacridine-4,5-dicarbonyl dichloride (**23**)



Two drops of *N,N*-dimethylformamide were added to 200 mg (0.71 mmol, 1 eq.) of (**21**) in dry thionylchloride (3 mL), and RM was heated to refluxing (70°C) for 50 min under an inert atmosphere. Then, the remaining thionylchloride was evaporated, and residual traces were removed with the addition of volatile dry dichloromethane (3 × 10 mL) under reduced pressure. The freshly prepared 9-chloro 4,5-diacyl chloride derivative (**22**) was dissolved in dry dichloromethane and treated with an excess of the desired amine (276 mg, 2.1 eq.) in 4 mL of dry dichloromethane and in the presence of 280 μL (2.1 mmol, 3 eq.) of triethylamine at -10 to -5°C for 40 min. The reaction was monitored with TLC CH₂Cl₂/MeOH/NH₃·H₂O 95/5/10 drops. After completion, the crude product was washed with 10 mL of saturated NaHCO₃, 10 mL of water and 10 mL of brine. The organic layer was dried with MgSO₄, and concentrated under a reduced pressure to obtain a dark-brown solid mixture, which was purified by column chromatography with elution of CH₂Cl₂/MeOH/NH₃·H₂O, 9.8 mL / 0.2 mL / 7 drops, to obtain 112 mg of (**23**). The mass spectrum of (**23**) is shown in Annex 1.

Form: brown powder

Yield: 25% (from **21**)

Formula: C₃₃H₄₄ClN₅O₆

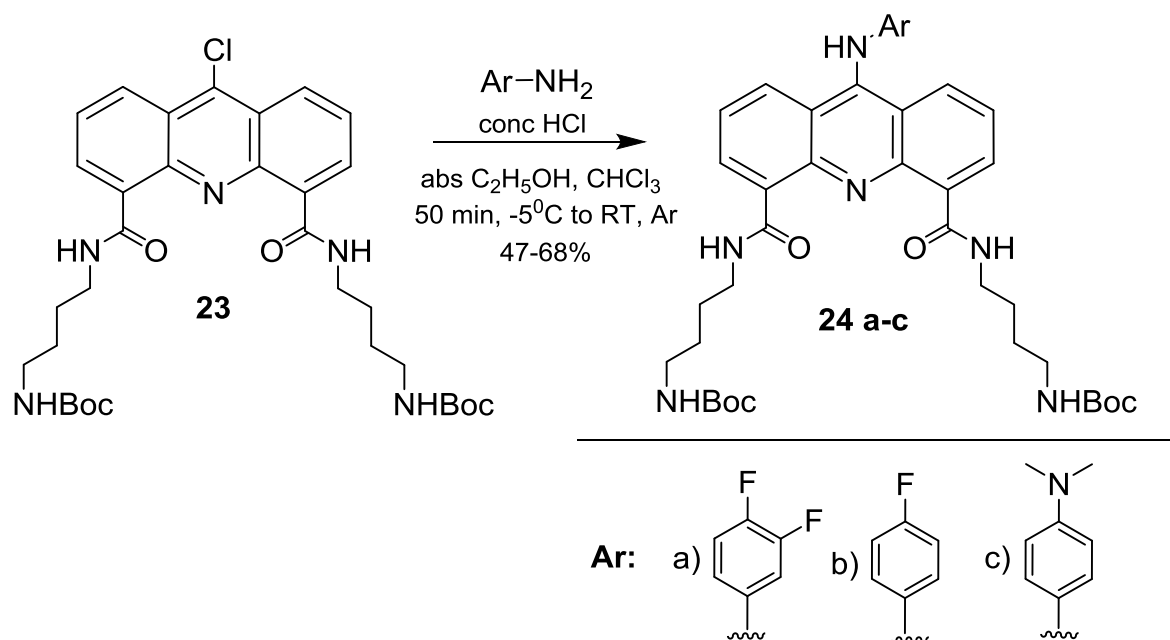
MW: 642.19

TOF mass-spectrometry (ESI+) m/z: 642.6 (Annex 1).

R_f (CH₂Cl₂/MeOH/NH₃·H₂O, 9.5 mL / 0.5 mL / 3 drops): 0.4

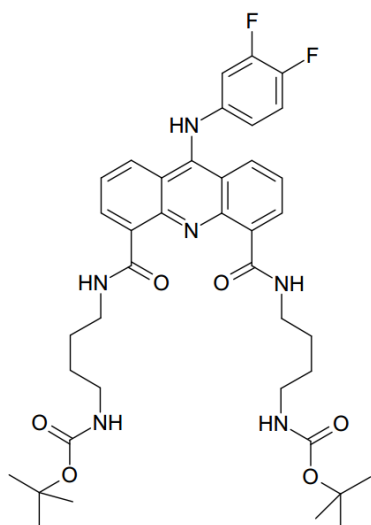
¹H NMR (300 MHz, DMSO-d₆): δ 10.02 (s, 2H), 8.73-8.42 (m, 4H), 7.91 (dd, 1H), 6.80 (t, 2H), 3.44 (q, 3H), 2.96 (q, 4H), 1.61 (q, 4H), 1.48 (t, 5H), 1.35 (s, 18H).

2.6.6. Synthesis of 9-substituted acridines with substituted anilines (**24a-c**)



To the solution of (**23**) (54 mg, 0.084 mmol; purity, 90%) in 1 mL of dry CHCl₃, 11.9 mg of aniline ArNH₂ (3,4-difluoroaniline (**26**), 4-fluoroaniline (**27**), *N,N*-Dimethyl-*p*-phenylenediamine (**28**)) in 1.2 mL of abs. EtOH and 3 drops of concentrated hydrochloric acid were added at -5 C. The RM was stirred for 50 min under natural heating until it reached naturally to the room temperature. The reaction was controlled via TLC (CH₂Cl₂/MeOH/NH₃·H₂O, 9.5 mL / 0.5 mL / 10 drops). The RM was concentrated under reduced pressure and purified with column chromatography with elution of CH₂Cl₂/MeOH/NH₃·H₂O, 9.6 mL / 4 mL / 3 drops.

N4,N5-bis(tert-butyl-4-aminobutylcarbamate)-9-(3,4-difluorophenylamino)acridine-4,5-dicarboxamide (24a)



Form: brown power

Yield: 68 %

Formula: C₃₉H₄₈F₂N₆O₆

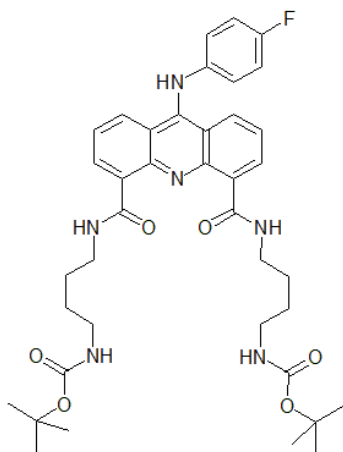
MW: 734.83

TOF mass-spectrometry (ESI+) m/z: 735.7 (Annex 2).

R_f (CH₂Cl₂/MeOH/NH₃·H₂O, 9.0 mL / 1.0 mL / 3 drops): 0.15

¹H NMR (300 MHz, CD₃OD) δ 8.41–8.25 (dd, 2H), 7.82 (m, 1H), 7.54 (dd, 1H), 7.29–7.04 (m, 1H), 6.66 (s, 2H), 3.66–3.43 (t, 4H), 3.13 (t, 4H), 1.82–1.55 (m, 2H), 1.42 (d, 18H).

N4,N5-bis(tert-butyl-4-aminobutylcarbamate)-9-(4-fluorophenylamino)acridine-4,5-dicarboxamide (24b)



Form: brown power

Yield: 60%

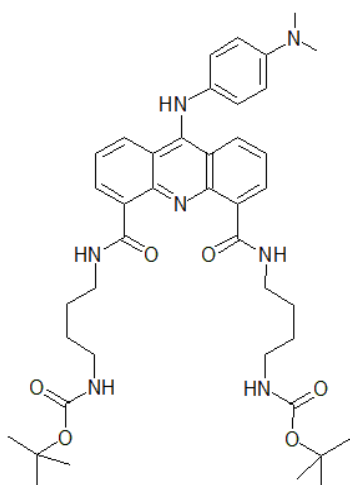
Formula: C₃₉H₄₉N₆O₆

MW: 716.84

R_f (CH₂Cl₂/MeOH/NH₃·H₂O, 9.0 mL / 1.0 mL / 6 drops): 0.1

¹H NMR (300 MHz, CD₃OD): δ 8.40 (m, 5H), 7.58-7.56 (q, 2H), 7.49 (d, 2H), 7.30 (t, 2H), 3.55 (t, 5H), 3.35 (s, 4H), 3.17 - 3.04 (t, 4H), 1.85 (6H).

N4,N5-bis(tert-butyl-4-aminobutylcarbamate)-9-(4-(dimethylamino)phenylamino)acridine-4,5-dicarboxamide (24c)



Form: black powder.

Yield: 47%

Formula: C₄₁H₅₅N₇O₆

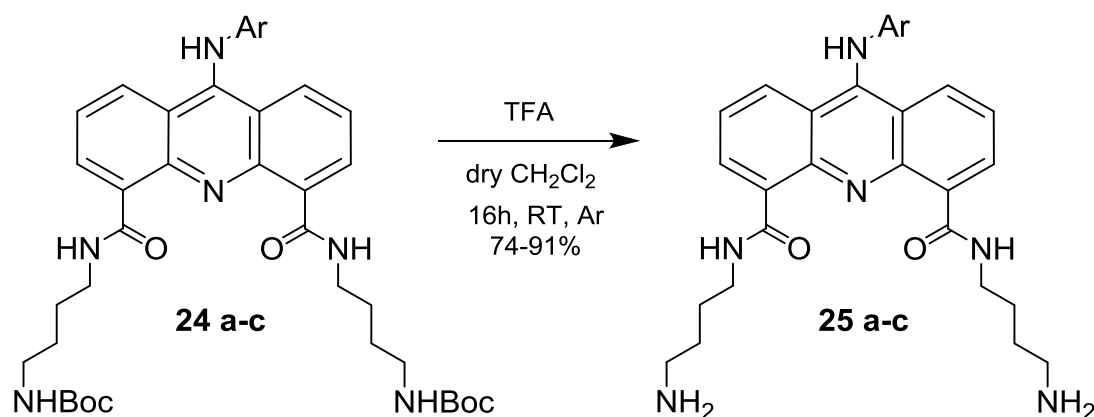
MW: 741.92

HRMS (APCI+) m/z: Found: 742.4282, calcd [M+H]⁺ 742.4292 (Annex 3).

R_f (CH₂Cl₂/MeOH/NH₃·H₂O, 9.0 mL / 1.0 mL / 5 drops): 0.1

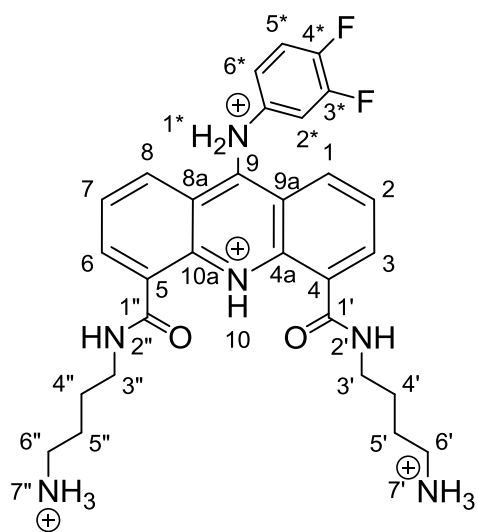
¹H NMR (300 MHz, CD₃OD) δ 8.45 - 8.26 (m, 3H), 7.62 (d, 1H), 7.56 - 7.54 (m, 1H), 7.53 (d, 1H), 7.51 (m, 3H), 7.46 (t, 1H), 7.44 (t, 1H), 3.74 (s, 1H), 3.69 (s, 1H), 3.58 - 3.47 (m, 4H), 3.35 (s, 2H), 3.16 - 3.04 (m, 4H), 1.84 (d, 4H), 1.59 (s, 2H), 1.42 (d, 7H).

2.6.7. Synthesis of 4,5,9-trisubstituted acridines derivatives (**25a-c**)



To a suspension of (**24 a-c**) (0.1 mmol, 1 eq.) in 5 ml of dry CH_2Cl_2 , 500 μL of trifluoroacetic acid (TFA) (6.5 mmol, 65 eq.) was added in portions for 2 h. The RM was stirred for 16 h at room temperature under an inert atmosphere. The RM was concentrated under reduced pressure and purified by column chromatography with elution of $\text{CH}_2\text{Cl}_2/\text{MeOH}/\text{NH}_3 \cdot \text{H}_2\text{O}$, 9 mL / 1 mL / 6 drops.

N4,N5-bis(4-aminobutyl)-9-(3,4-difluorophenylamino)acridine-4,5-dicarboxamide (25 a)



Form: brown powder.

Yield: 91%

Formula: $\text{C}_{29}\text{H}_{32}\text{F}_2\text{N}_6\text{O}_2$

MW: 534.6

HRMS (APCI+) m/z : Found: 535.2640, calcd $[\text{M}+\text{H}]^+$ 535.2633 (Annex 4).

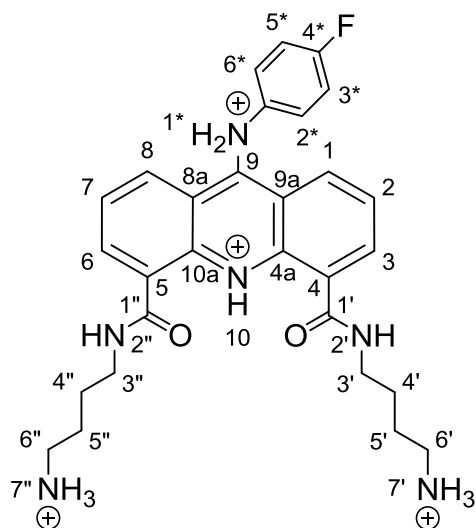
Solubility¹ (pH 7 buffer): 102 g/L (0.150 mol/L).

R_f (CH₂Cl₂/MeOH/NH₃·H₂O, 8.5 mL / 1.5 mL / 6 drops): 0.15

¹H NMR (600 MHz, CD₃OD) δ 8.43 – 8.46 (m, 2H, H-3, H-6), 8.39 – 8.43 (m, 2H, H-1, H-8), 7.55 – 7.60 (m, 2H, H-2, H-7), 7.48 – 7.54 (m, 2H, H-2* and H-6* or H-3* and H-5*), 7.30 – 7.36 (m, 2H, H-2* and H-6* or H-3* and H-5*), 3.59 – 3.66 (m, 4H, 2 × H-3', 2 × H-3''), 3.06 – 3.14 (m, 4H, 2 × H-7', 2 × H-7''), 1.80 – 1.90 (m, 8H, 2 × H-4', 2 × H-5', 2 × H-4'', 2 × H-5'').

¹³C NMR (151 MHz, CD₃OD) δ 167.38 (2 × CO), 160.79 (C-F), 157.17 (C-9), 138.71 (C-4a, C-10a), 136.59, 135.23 (CH-3, CH-6), 129.04 (CH-2, CH-7), 126.70 (CH-2* and CH-6* or CH-3* and CH-5*), 123.09 (CH-2, CH-7), 122.03 (C-4 and C-5 or C-8a and C-9a), 117.11 (CH-2* and CH-6* or CH-3* and CH-5*), 114.23 (C-4 and C-5 or C-8a and C-9a), 39.01 (CH₂-6', CH₂-6''), 38.71 (CH₂-3', CH₂-3''), 25.95 (CH₂-5', CH₂-5''), 24.53 (CH₂-4', CH₂-4'').

N4,N5-bis(4-aminobutyl)-9-(4-fluorophenylamino)acridine-4,5-dicarboxamide (25b)



Form: brown powder.

Yield: 84%

Formula: C₂₉H₃₃FN₆O₂

MW: 516.61

HRMS (APCI+) m/z: Found: 517.27190, calcd [M+H]⁺ 517.2727 (Annex 5).

Solubility² (pH 7 buffer): 32.5 g/L (0.049 mol/L).

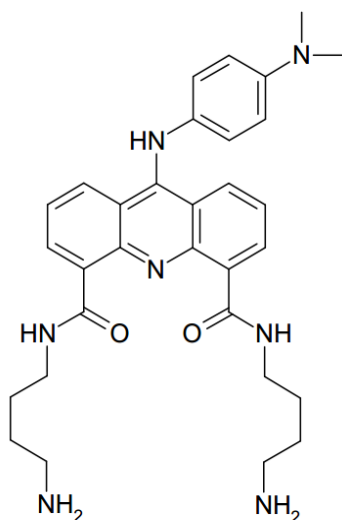
¹ solubilities of the hydrochloric salt of the compound at pH 7 are given taken into account a moderate heating the mixture in a water bath to 40°C.

R_f(CH₂Cl₂/MeOH/NH₃·H₂O, 8.5 mL / 1.5 mL / 6 drops): 0.15

¹H NMR (600 MHz, CD₃OD) δ 8.43 – 8.46 (m, 2H, H-3, H-6), 8.39 – 8.43 (m, 2H, H-1, H-8), 7.55 – 7.60 (m, 2H, H-2, H-7), 7.48 – 7.54 (m, 2H, H-2* and H-6* or H-3* and H-5*), 7.30 – 7.36 (m, 2H, H-2* and H-6* or H-3* and H-5*), 3.59 – 3.66 (m, 4H, 2 × H-3', 2 × H-3''), 3.06 – 3.14 (m, 4H, 2 × H-7', 2 × H-7''), 1.80 – 1.90 (m, 8H, 2 × H-4', 2 × H-5', 2 × H-4'', 2 × H-5'').

¹³C NMR (151 MHz, CD₃OD) δ 167.38 (2 × CO), 160.79 (C-F), 157.17 (C-9), 138.71 (C-4a, C-10a), 136.59, 135.23 (CH-3, CH-6), 129.04 (CH-2, CH-7), 126.70 (CH-2* and CH-6* or CH-3* and CH-5*), 123.09 (CH-2, CH-7), 122.03 (C-4 and C-5 or C-8a and C-9a), 117.11 (CH-2* and CH-6* or CH-3* and CH-5*), 114.23 (C-4 and C-5 or C-8a and C-9a), 39.01 (CH₂-6', CH₂-6''), 38.71 (CH₂-3', CH₂-3''), 25.95 (CH₂-5', CH₂-5''), 24.53 (CH₂-4', CH₂-4'').

N4,N5-bis(4-aminobutyl)-9-(4-(dimethylamino)phenylamino)acridine-4,5-dicarboxamide
(25c)



Form: black powder.

Yield: 74%

Formula: C₃₁H₃₉N₇O₂

MW: 541.69

R_f(CH₂Cl₂/MeOH/NH₃·H₂O, 8.5 mL / 1.5 mL / 6 drops): 0.15

¹H NMR (300 MHz, CD₃OD) δ 8.54 - 8.37 (m, 4H), 7.68 - 7.51 (m, 5H), 3.58 (m or t, 6 or 4 H), 3.35 (s, 1H), 3.24 (s, 1H), 3.14 (t, 4H), 2.15 (s, 1H), 1.42 (s, 15H), 1.42 (d, 4H), 1.25 (d, 5H), 1.17 (t, 2H).

2.7. Assembling of multifunctional nanoprobes

The assembling of the nanoprobes was performed in two ways: (i) covalent immobilization by means of carbodiimide coupling, (ii) electrostatic immobilization by means of direct mixing of the stock solution.

The covalent conjugation of the QDs and the acridine ligand (AL) was performed in accordance with the adopted procedure for two-step coupling using EDC and NHS [236,237]. The stock solution of the water soluble blue emitting CdSe/ZnS QDs with maximum PL band at 476 nm and proportion of hydroxyl /carboxyl PEG surface ligands 9:1 were desalted using a Sephadex G25 column and equilibrated with MES buffer (pH 5.2, 0.1M). Equivalent volume of 4 mg QD was activated with freshly prepared 50 mM stock solutions of EDC and NHS in MES buffer in molar excess of 800 to QDs. After activation for 15 min, the RM was purified on a desalting column Sephadex G25, equilibrated with phosphate buffer (pH 7.2, 50mM) for the elimination of the excess of the activating agents. After measuring of QD concentration, an equivalent volume of 3 mg QD and the required excess of AL was immediately mixed. After 2 hours of incubation, the RM was purified from the inactivated crosslinker and other low-molecular-weight molecules by passing of the reaction mixture through Sephagex G100 column, and equilibrated with phosphate buffer (pH 7.2, 50 mM).

The electrostatic immobilization of the QDs and the AL was performed by mixing of 3 mg of 0.05M solution of CdSe/ZnS QDs in phosphate buffer (pH 7.2, 50 mM) with the required excess of AL. Then the RM was purified on Sephagex G100 equilibrated with phosphate buffer (pH 7.2, 50 mM) from low-molecular-weight molecules.

Two prepared nanoprobe solutions were characterized and subsequently used for following experiments.

2.8. Cellular uptake of CdSe/ZnS QDs

Human monocytes were isolated using the ficoll reagent. Ficoll was added to the test tube, and fresh human whole blood was added to the top layer of it. The tube was centrifuged at 1500 rpm for 25 min. The layer of mononuclear cells was removed into a separate tube. The cells were washed with PBS containing heparin at a concentration of 5000 U/mL, and the tube was centrifuged for 15 min at 1500 rpm. The top layer was collected with a pipette. The precipitate was shaken and washed in 10 ml of RPMI-1640 medium at 1000 rpm for 8 min. The cells were counted, and 5×10^6 cells per Petri dish were seeded in 1% RPMI-1640 medium supplemented with 2% of human serum. The Petri dishes were placed into an incubator for 1.5 h. Unattached cells were removed with a pipette, and the Petri dish containing monocytes was gently washed

with PBS. Afterwards, 20 mL of 1% RPMI-1640 medium (containing 2% of human serum) was placed into the Petri dish.

To analyze the interaction of water-soluble QDs-PEG-OH with monocytes, the QDs were added to the cell medium to a final concentration of 1 mg/mL. After incubation at 37°C for 10 min, the uptake of the QDs by human monocytes was studied using an LSM-710-NLO laser scanning confocal microscope.

3. Chapter 3. High quality CdSe-based quantum dots

This chapter is devoted to the methods of colloidal synthesis and surface modification of high-quality CdSe-based core/shell QDs for biological applications. This chapter is sectioned into three principal parts: synthesis of high quality CdSe-cores, engineering of bright core/shell QDs and development of water-soluble QDs with enhanced colloidal stability.

The section devoted to the synthesis of high-quality CdSe –core QDs includes:

- Development of the method of colloidal hot-injection QD synthesis via investigation and optimisation of critical reaction parameters.
- Synthesis of ultrasmall 1.5 nm CdSe QD cores with narrow size distribution for biological applications achieved via fast termination of QD growth and further multistep purification.
- Development of the CdSe QD growth model for accurate prediction of structural and optical properties, planning of the quantitative shell growth process and increasing the reproducibility of the QD synthesis.

The section about developing of bright core/shell QDs includes:

- Synthesis of compact CdSe/ZnS QDs based on the ultrasmall 1.5 nm QD cores using the developed QD growth model.
- Development of the novel ZnS/CdS/ZnS multishell QD structure with optimised charge carrier localisation for maximum PL efficiency and subsequent surface functionalization.

The section on the engineering of water-soluble core/shell QDs describes functionalization of developed core-shell QDs with organic ligands via two-stage ligand exchange approach.

3.1. Hot-injection synthesis of colloidal CdSe nanocrystals.

3.1.1. Development and optimisation of hot injection method for QD synthesis.

The hot-injection technique was used for the synthesis of CdSe cores. The essence of the technique is that the high-temperature reaction of NC synthesis is carried out by injecting one of the precursors (the "cold" precursor) into a solution of the other precursor (the "hot" one), which has been heated to a high temperature and is vigorously stirred. At the moment of injection, a limited number of QD cores are rapidly formed, the reaction mixture being simultaneously drastically cooled due to the difference between the temperatures of the "cold" and "hot"

precursors. This allows to stop the nucleation process and to trigger the stage of growth of the cores formed. The latter stage is characterized by a gradual increase in the mean size of the NCs in the ensemble without an increase in the size distribution. The duration of the first stage ranges from 1 to 15 min, depending on the amounts and reactivities of the precursors. Then, the oversaturation of the reaction mixture with the precursors considerably decreases, and the transition to the Ostwald ripening occurs, with the NC size slightly increased and polydispersity becoming considerably higher.

The following main parameters of the reaction were analyzed:

- the types of "hot" and "cold" precursors;
- the type of organic solvent;
- the type of the cadmium salt;
- the temperature of injection;
- the reaction duration;
- the ratio between the cadmium and selenium precursors.

The first step was aimed at studying how the type of the injected precursor affected the course of the reaction. If CdSe cores are to be synthesized, it is more suitable to inject the selenium precursor into the hot cadmium precursor for two reasons. First, the selenium precursor always remains liquid at room temperature, whereas cadmium salts are prone to solidification and precipitation at a temperature under 50°C (see below). Second, cadmium precursors are more stable and are not oxidized readily, whereas trioctylphosphine selenium (TOPSe) is oxidized to form trioctylphosphine oxide (TOPO) and selenium, and it is better to prepare this precursor shortly before the injection. Therefore, we used this variant of the procedure in subsequent experiments.

The organic solvent for the core synthesis was selected on the basis of its boiling temperature, viscosity, and convenient purification method. We compared three solvents: 1-octadecene (ODE), cetane (*n*-hexadecane), and paraffin oil. ODE is most commonly used for the synthesis of CdSe QDs. This solvent is relatively inexpensive, has a boiling temperature of 315°C, and is liquid at room temperature. Paraffin oil is even more inexpensive analogs of ODE. Apart from the boiling temperatures, these solvents differ in viscosity, which grows in the order cetane → ODE → paraffin oil. The viscosity may affect the rate of precursor diffusion in the solvent, thereby influencing the growth of QDs. Table 3 shows the characteristics of the solvents.

Table 3: Properties of solvents used in the synthesis of QDs.

Solvent	Boiling temperature, °C	Viscosity under normal conditions, mm ² /s
Cetane	287	3.45
1-ODE	315	3.6
Paraffin oil	-	>35

In the experiments with different types of solvents, cadmium hexadecyl phosphonate was used as a cadmium precursor, and TOPSe dissolved in a TOP-ODE mixture, as a selenium precursor. TOPSe was injected into the cadmium precursor solution at 240°C, and the reaction was stopped at the 50 min. Figure 22 shows the absorption spectra of the NCs obtained.

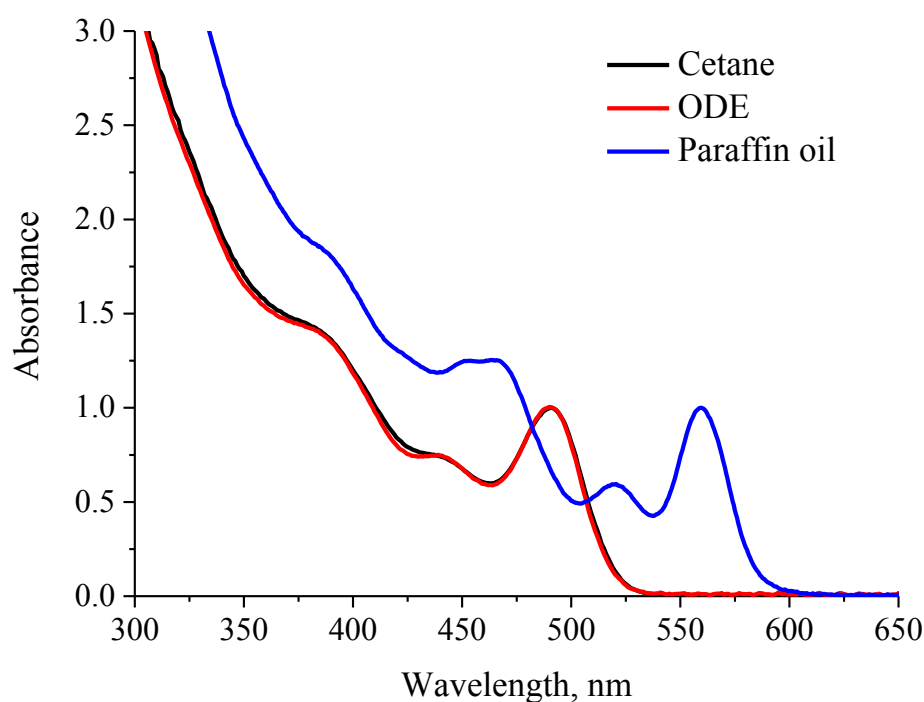


Figure 22: Absorption spectra of CdSe QDs in different solvents.

As seen from Figure 22, the reactions in cetane and ODE yield almost identical CdSe cores. If the more viscous paraffin oil is used, the cores grow to larger sizes, as evidenced by the

red shift of the first exciton absorption peak. In this case, it is also evidenced that more monodisperse CdSe cores are formed, because a greater number of optical transitions are distinctly seen in the spectrum. These effects can be explained by the slower reaction kinetics due to higher viscosity of the medium compared to ODE and cetane. The slower course of reaction favors a more homogeneous growth of NCs, which makes the QD ensembles more monodisperse. However, although the QDs synthesized in paraffin oil are of better quality, the isolation of the QDs from the reaction mixture is much more difficult, because the components of this medium, being nonpolar and of greater molecular weight, deposit together with QDs to form a practically insoluble pellet. The QD quality synthesized in ODE and cetane is similar, however cetane is significantly more expensive than ODE. Thus, ODE is the best reaction medium due to its relatively low cost and a good quality of the QDs obtained.

At the next stage of the study, different cadmium salts were tested as the cadmium source. For synthesis in an organic medium, salts of cadmium and organic acids that have an aliphatic fragment stabilizing the salt in the nonpolar solution are commonly used. The length and structure of this fragment mainly determine the stability of the salt solution and the mobility of the salt molecules in the solution. Acids with a linear aliphatic chain C14–C18 in length are most frequently used. The type of the acid moiety determines the strength of the acid residue–cadmium bond and, hence, the reactivity of the precursor. QD synthesis typically employs carboxylic (-COOH) and phosphonic (-P(O)(OH)₂) acids, examples of the use of thiols (-SH) or other Cd complexes are rare. In our experiments on selecting the type of cadmium salt to be used as a precursor, 2-ethylhexanoic (2-EHA), myristic (MA), stearic (SA), oleic (OA), and *n*-hexadecylphosphonic (HDPa) acids were tested. Table 4 shows the temperatures of obtaining these salts and their stabilities.

Table 4: Properties of cadmium salt precursors.

Acid	Metal : acid ratio	Dissolution temperature, °C	Approx. crystallization temperature in ODE, °C
2-EHA	1:2	200	stable
MA	1:2	280	>50
SA	1:2	280	>50
OA	1:2	250	metastable
HDPa	1:1	300	>100

The synthesis of CdSe QDs using these cadmium precursors was performed as follows. The ODE solution of the cadmium precursor was heated to 240°C, and 2 mmol of TOPSe (0.4 M solution) was injected, after which the reaction was traced for 5 min. Figures 23, 24 show the absorption and PL spectra of CdSe QDs obtained using different salts as cadmium precursors.

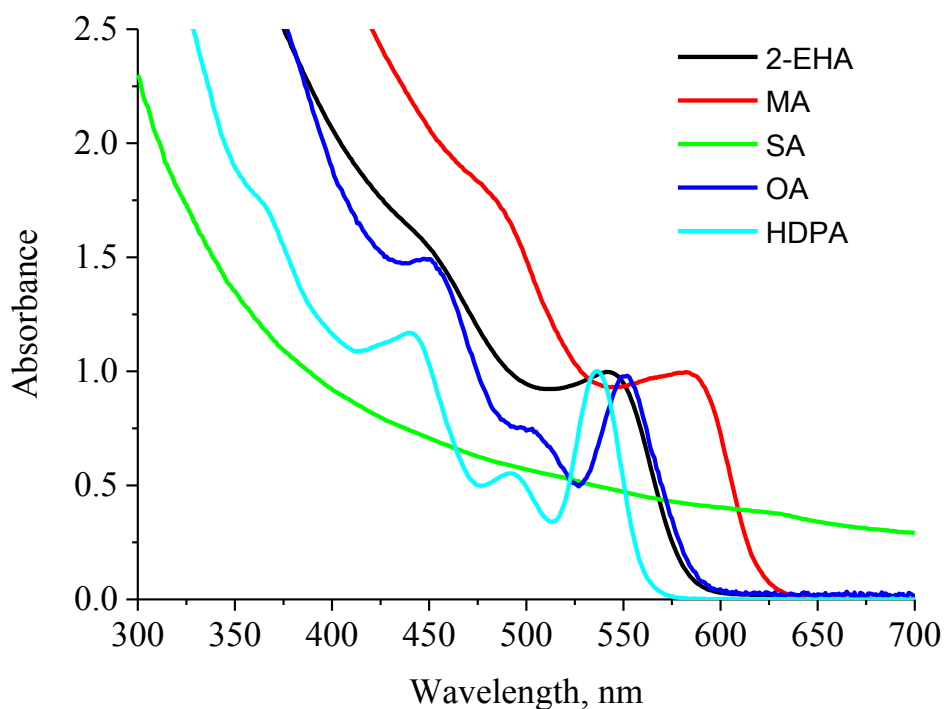


Figure 23: Absorption spectra of CdSe QDs obtained from various precursors.

The absorption spectra can be used to evaluate the size monodispersity of the synthesized QDs by estimating how pronounced the excitonic transitions are, and the PL spectra allow both the evaluation of the monodispersity (by estimating the width and symmetry of the PL peak) and the detection of admixtures based on additional PL lines. If cadmium 2-ethylhexanoate (black line) is used, there are a slightly pronounced excitonic transition in the absorption spectrum and two distinct peaks with different band widths in the PL spectrum. Thus, the use of this precursor type does not allow obtaining CdSe QD ensembles of acceptable quality, because they clearly contain two fractions of QDs. The possible reason is too high mobility of molecules in the reaction solution and their too high reactivity, with the consequence that the reaction of core formation and core growth occur in parallel.

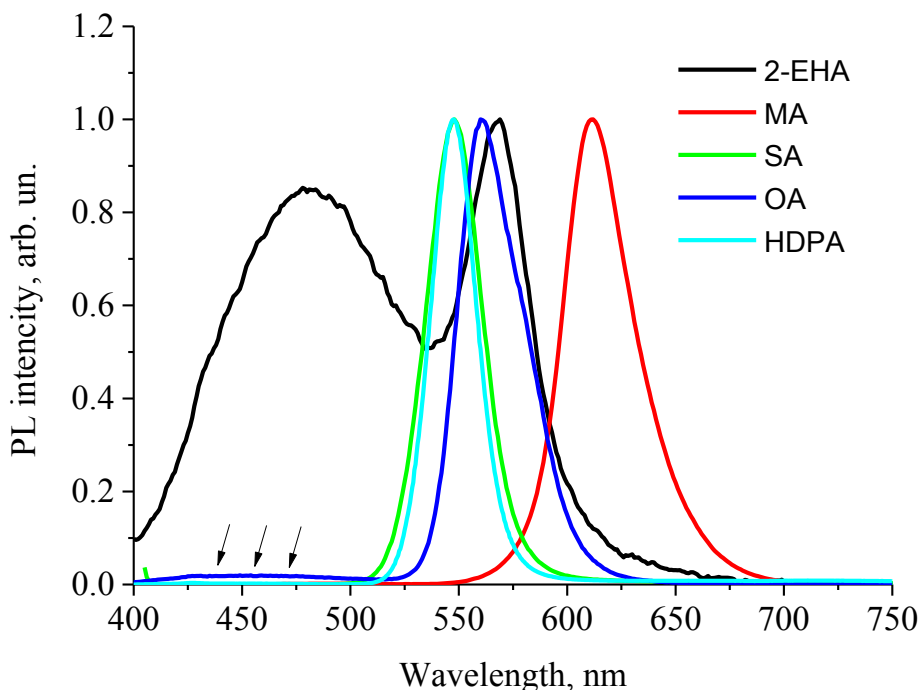


Figure 24: Photoluminescence spectra of CdSe QDs obtained from various precursors.

If cadmium myristate (red line) is used, it is obvious from the absorption spectrum that the CdSe ensemble is polydisperse, and the PL spectrum is distinctly asymmetric. The spectral patterns allow us to conclude that the quality of CdSe QDs obtained using cadmium myristate is acceptable but worse than that obtained with other precursors.

If cadmium stearate (green line) serves as a precursor, the PL spectra correspond to a single QD ensemble with a low polydispersity. In the absorption spectrum, however, the baseline is considerably elevated throughout the range studied, which indicates a greater scattering of the sample. In this case, a low solubility of the precursor in the reaction medium leads to its precipitation accompanied by capturing and encapsulating part of QDs. Further experiments have shown that the isolation of CdSe QDs from the reaction mixture is extremely difficult if cadmium stearate has been used as a precursor. Thus, despite the good quality of the NCs obtained, the use of cadmium stearate as a precursor is inadvisable.

With cadmium oleate (blue line) as a precursor, the absorption spectrum of the resultant CdSe QDs reflects the formation of a monodisperse QD ensemble with distinct excitonic transitions, which indicates a good quality of the sample. A slight asymmetry is seen in the PL spectrum, but there is also a wide, low-intensity band (marked with arrows) in the blue spectral region (400–500 nm), which shows that the sample contains a small proportion of smaller CdSe NCs.

The use of cadmium hexadecylphosphonate (cyan line) as a precursor yields NC ensembles of excellent quality, as evidenced by numerous distinct excitonic transitions in the absorption spectrum and a narrow symmetric band in the PL spectrum.

Thus, Cd-HDPA was selected as a basic cadmium precursor with optimal reactivity. In fact, Cd-EHA was used as the initial cadmium precursor for preparation of cadmium solution from cadmium oxide powder. The complex formed by Cd^{2+} and two 2-ethyl hexanoate anions was transformed to cadmium hexadecylphosphonate by heating of the reaction mixture in presence of TOA for an hour at 240°C. The conversion could be evidenced by the change in the colour of the reaction mixture from colorless to yellowish within about 30 min.

After that, we performed experiments with different temperatures of the "hot" precursor at the moment of injection. The injection temperature affected both main factors determining the properties of the obtained CdSe QDs, the rate of cores formation and the rate of core growth. With an increase in temperature, both the rate of molecule diffusion in the reaction mixture and the rates of chemical reactions between the precursors were increased. The cadmium precursor was rapidly heated to the specified temperature, and then the selenium precursor was injected. In this series, we carried out three syntheses with injection temperatures of 240 (the lowest temperature at which the rate and reproducibility of the reaction are acceptable), 270, and 300°C. Figure 25 shows the results of these experiments in the form of the absorption spectra of the end product and the time course of the mean QD size.

It can be concluded from the absorption spectra shown in Figure 25a that CdSe cores of good quality are obtained at temperatures of 240 and 270°C, because numerous well-resolved excitonic transitions can be seen. At 300°C, the NC quality is lower, and the reproducibility of the reaction is also decreased. Figure 25b shows how the course of the reaction changes with increasing temperature. It is obvious that the rate of the increase in the mean size of QDs considerably grows with increasing temperature. In this case, the reaction is extremely difficult to control, because small variations of the synthesis conditions may cause large differences in the optical characteristics of the resultant QDs. Thus, CdSe QDs should be synthesized at a temperature between 240 and 270°C, depending on their desirable final diameter.

At the last stage, the ratio of Cd-HDPA to TOPSe during the injection was varied at a constant amount of the cadmium precursor (1 mmol). The initial Cd to Se precursor ratio is an important parameter for determining the size of the resulting QDs. This parameter can influence the nucleation of QDs since the number of cores formed at the initial moment of the reaction, and the maximum size of QDs depend on the amount of the selenium precursor. We empirically found that TOP-Se was more active than Cd-HDPA. As a result, the more selenium precursor

there was at the initial stage, the faster the nucleation was. A series of experiments showed that optimal initial precursor ratio Cd to Se was 1 : 2, which was used for further synthesis.

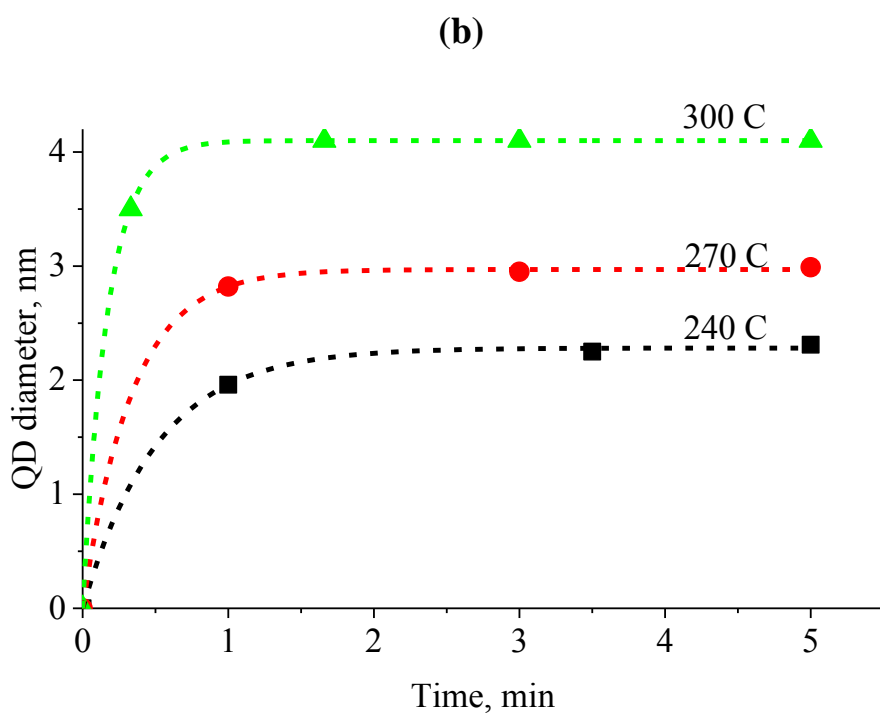
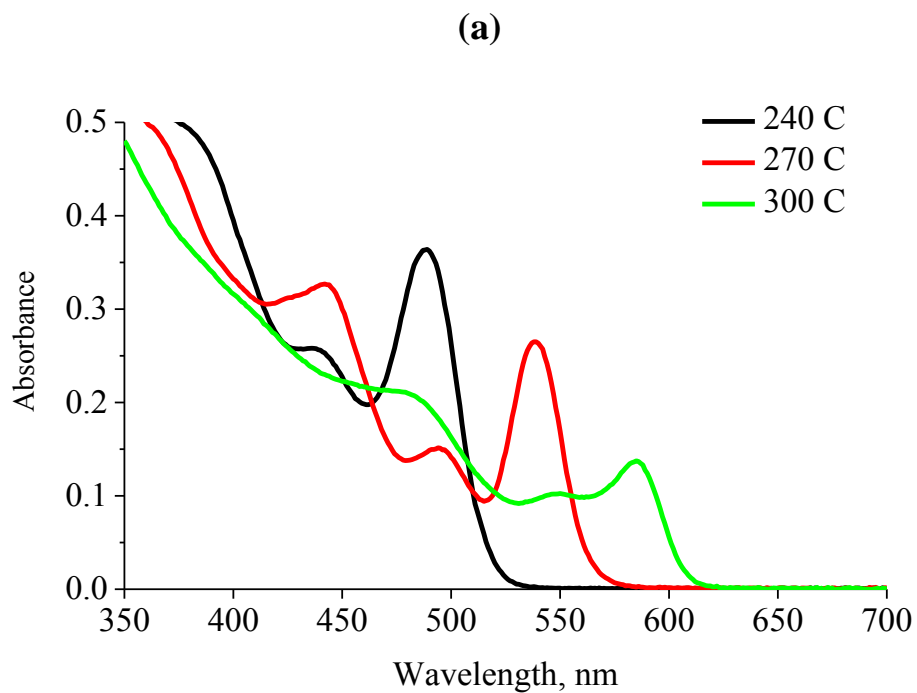


Figure 25: (a) Absorption spectra after 5 min of QD growth and (b) changes in the average size of CdSe QDs obtained at different injection temperatures.

Summarizing the results, we found the optimal condition for the hot-injection synthesis of high-quality CdSe QDs. The essential advantage of the hot-injection method is the simultaneous formation of seeds and retention of uniform morphology during the QD ensemble growth. The optimal QD formation conditions are those where the reaction system should form a relatively small amount of cores within a short period, and these cores do not noticeably consume the remaining monomers, because they grow quickly to the desired size. For this purpose, relatively less reactive precursors would be helpful. High-quality cores were synthesized according to the protocol adapted from [238] using Cd-HDPA in the presence of TOA to stabilize the growing QDs and restrict their rapid growth in the ODE solution. After the injection of a cold TOP-Se solution into this hot cadmium precursor solution, the reaction mixture colour changed from yellowish to rich yellow, then darkened to orange, and ultimately to red over a period of 15 min. Manipulation only with injection temperature, growth duration, and ligand quantity allows obtaining defect-free QDs of the specified size in the interval from 1.8 to 5 nm with a narrow size distribution and tunable emission band (Figure 26). The obtained QDs were isolated from the crude solution by precipitation with methyl acetate and then were dispersed in chloroform for further characterization.



Figure 26: Photoluminescence of the solutions of CdSe QDs with the size varying from 1.8 (blue line) to 5 nm (red line).

For detailed characterization, we chose relatively small CdSe cores with the first excitonic transition at 495 nm, because, in this case, the quality of the shell and its confinement potential should have the highest possible effect on the photoluminescent properties of the resulting QDs due to the large band gap and the maximum deviation of the band levels from their bulk values.

The absorbance and PL spectra of CdSe QDs cores as well as STEM images are presented in Figure 27 and respectively.

First, we studied the optical properties of the core solution. In the absorption spectrum, pronounced well-resolved first excitonic transition at 495 nm is seen; in the PL spectrum, there is a single emission band with FWHM = 30 nm, which indicates the presence of one size-homogeneous ensemble. The PL QY was determined to be 33%. The PL QY of the initial CdSe cores significantly depended on the size of QDs: an increase in the core size resulted in an increase in their PL QYs up to 40%. QYs of 30-40% were typical of medium-sized cores. The PL efficiency of small CdSe QDs was typically less than 10%. The large difference in the PL efficiency can be explained by the higher sensitivity of small QDs to the environment and, hence, higher probability of PL quenching.

Then, we studied the shape and morphology of QDs. The average diameter of the cores and its standard deviation, as determined by STEM, are shown in Figure 28.

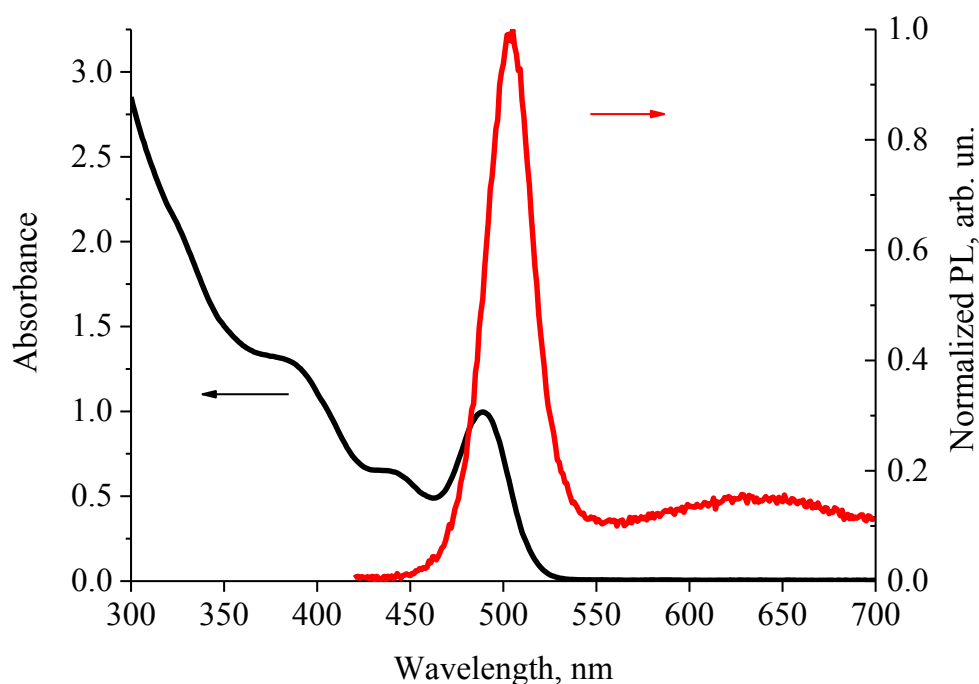


Figure 27: Absorption and PL spectra of CdSe core QDs [40].

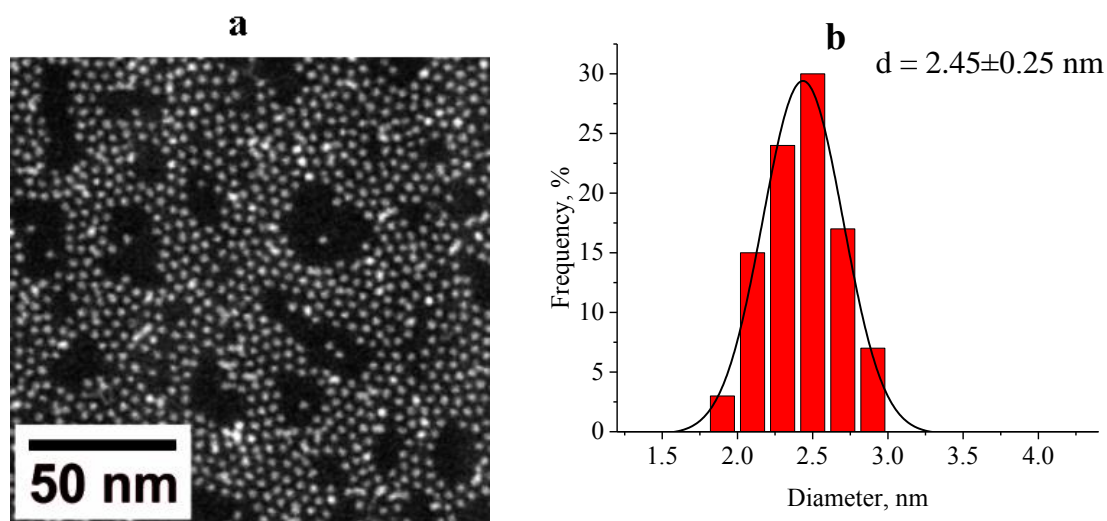


Figure 28: (a) A STEM image of CdSe core QDs. (b) Histogram of size distribution [40].

The STEM images of the CdSe QDs showed that these QDs had a uniform morphology. The exact sizes of QDs based on STEM images were determined to be 2.45 ± 0.25 nm, the size distribution is close to the normal distribution, which confirms ensemble homogeneity. The measured size was close to the model particle size from a calibrating curve from Ref. [214] (2.3 nm) calculated from the position of the first excitonic transition of the absorption spectrum.

Thus, the experimental results confirmed the efficiency of our procedure of colloidal hot-injection synthesis. Combination of the hot-injection approach with correctly selected cadmium and selenium precursors, as well as ligands and solvent allowed obtaining size-homogeneous QD ensembles with a narrow PL emission band. The main ways to control the reaction kinetic (injection temperature, reaction duration, etc.) provide convenient and easy tuning of the QD size and position of the PL band.

3.1.2. Synthesis of ultrasmall CdSe QDs.

The use of ultrasmall QDs as components of nanoprobes extends the possibilities of bioimaging owing to their enhanced capacity for penetrating through cell membranes. However, the typical procedure of CdSe QD synthesis by hot injection method involves the rapid growth of nanocrystals in a colloidal medium, which prevents obtaining sufficiently small QDs. High-quality CdSe QDs synthesized by the method described above are larger than 2.4 nm, which is not small enough.

For evaluating the applicability of the standard QD synthesis procedure to the synthesis of ultrasmall QDs, we measured the kinetics of QD growth (Figure 29) and plotted an approximated calibration curve of the core QD diameter dependence on growth time, using the data on the position of the first excitonic transition of the absorption spectrum [214] (Figure 29, inset). The

figure shows the evolution of the absorbance spectra of colloidal CdSe QDs, displaying a fluent red shift of the first excitonic transition with time. Following the growth time, the formation of the distinguishable narrow excitonic transition subsequently perfecting its shape was observed. Rapid formation of a single QD ensemble and sharpening of size distribution during the growth are conditioned by a combination of well-selected synthesis conditions and good passivation of the QD surface with a mixture of organic ligands.

From the calibration curve in the inset of Figure 29, one can see that, for the formation of QDs with a diameter smaller than 1.5 nm, the reaction had to be terminated within approximately 30 seconds after the injection. However, the commonly used method of terminating the synthesis by cooling the reaction flask with an air flow or injection of cool solvent into the reactor takes significant time for the reaction termination, during which the crystal growth gradually slows down, which prevents the synthesis of compact CdSe QDs of strictly controllable size and results in deterioration of the ensemble homogeneity [239]. Batch synthesis of ultras-small QDs by the hot-injection method is limited by the fact that growth of QD at early stages is so rapid that QDs with a diameter of more than 2 nm are formed almost instantaneously. In addition, rapid termination of QD synthesis at the early stages left considerable amounts of unreacted precursors in the mixture. Cadmium precursors, in the form of cadmium alkyl phosphonates and carboxylates, cannot be completely removed by the dispersion/coagulation procedure, because they are partly adsorbed on the QD surface [229]. The process is further facilitated by the small size of QDs and, hence, the large relative surface area of the nanocrystals. Moreover, these remaining precursors react with one another during the subsequent shell growth, either causing the additional growth of the core or being included in the shell and disturbing its designed stoichiometry with formation of alloyed CdZnS shells, or, in some cases, the formation of an additional fraction of CdS/ZnS QDs with PL in the blue region of the spectrum (see an example in Figure 30).

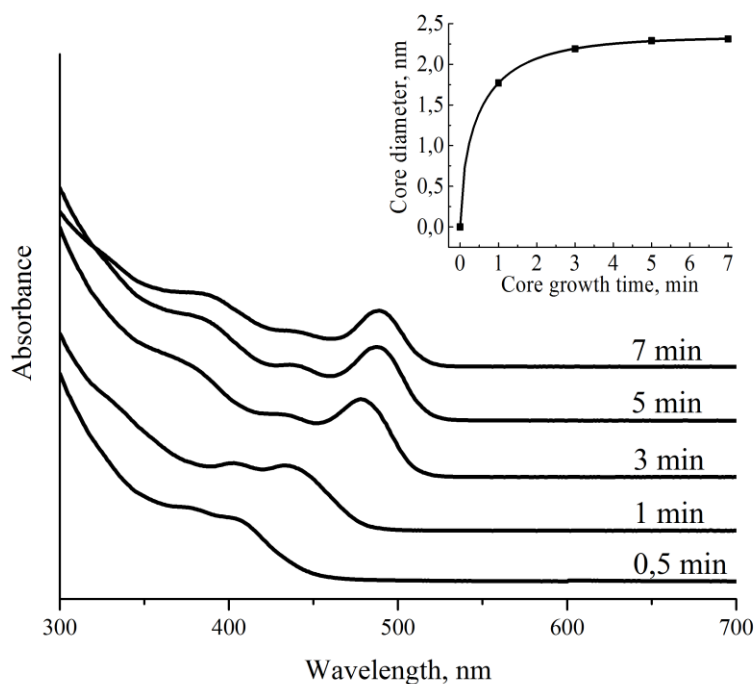


Figure 29: Evolution of the absorption spectra during CdSe QD growth; the inset shows the calibration curve of the QD diameter versus the CdSe-core growth time.

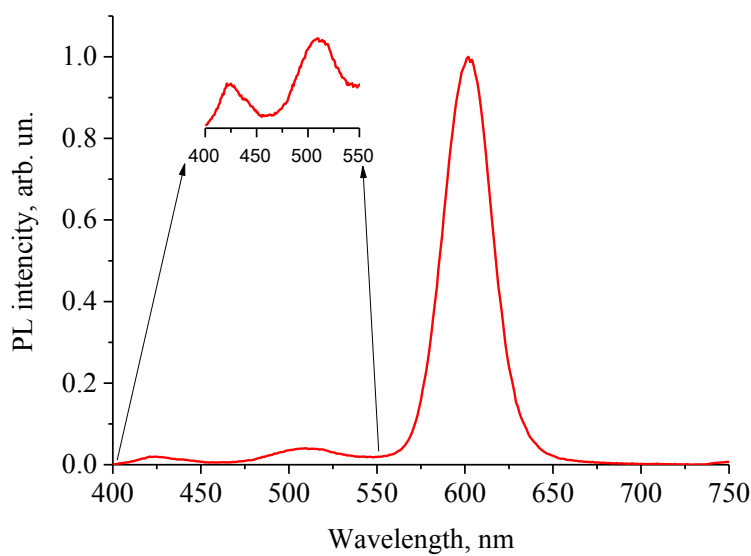


Figure 30: The PL spectra of the CdSe/ZnS QD synthesis reaction mixture, with the shell grown in situ in the presence of a residual amount of the cadmium precursor.

An advanced procedure for the synthesis of ultrasmall monodisperse CdSe QD core has been developed. This procedure relies on a combination of fast termination of core formation and growth by cooling of the reaction mixture with liquid nitrogen and multistep high-performance

core purification using gel penetration chromatography. For ultrafast stopping of the reaction, we transferred the reaction mixture into liquid nitrogen after 15 seconds after injection. After evaporation of liquid nitrogen, and subsequent melting of the reaction mixture at room temperature, we obtained a stable colloidal solution of ultras-small CdSe QDs containing a large amount of unreacted precursors. Then, the cores were separated from the nonpolar reaction solution by precipitation using methyl acetate as a coagulant. However, this method has a disadvantage: the efficiency of the purification from the precursor varies depending on the size of the CdSe cores being isolated. This is because smaller cores have a relatively high resistance to coagulation, even in the presence of a large excess of the polar precipitant. On the other hand, the low polar cadmium precursor can precipitate from the solution with a large excess of coagulant. Thus, during isolation of small CdSe cores, simultaneous precipitation of both CdSe NCs and cadmium precursors takes place.

To achieve complete removal of unreacted cadmium precursor from CdSe core solution, an additional purification stage was introduced to the synthesis routine. Namely, we applied GPC using Bio-Beads SX-1 cross-linked polystyrene granules (BIO-RAD) as the stationary carrier and toluene as eluent. This method, in which QDs rapidly migrate along the stationary phase, while the low-molecular-weight precursors are removed as a result of retention in the pores of the carrier, has been proven for efficient removal of excess surface ligands or unreacted Cd precursors on relatively large CdSe nanocrystal ensembles [229].

After GPC, we obtained a toluene solution of QDs containing purified CdSe cores whose surface was covered with the HDPAs anions passivating it. This type of ligands forms a strong bond with the NC surface [240], which ensures sufficient stabilization of colloidal solutions of QD cores but, on the other hand, may decrease the homogeneity of shell growth on their surface. The growth of shells on the QD cores consists of two main stages: adsorption of the metal and chalcogen precursors on the surface and their subsequent reaction yielding the shell material. The phosphonate anions on the core surface can effectively prevent the adsorption of the shell precursors [241]. Thus, to improve the quality of the passivating shell, phosphonate anions on the CdSe core surface should be preliminarily replaced with ligands that have a lower affinity for the surface and higher mobility. In this study, oleylamine (OLA) molecules were used as such ligands. The ligand exchange was performed through addition of an excess of OLA to the solution of CdSe cores in toluene, treatment for 15 min under ambient conditions and mild stirring, and subsequent purification by coagulation and centrifugation. This procedure was further improved by conduction of ligand exchange in presence of a reducing agent (sodium borohydride), which intensely reduces anions on the QD surface, thereby facilitating their desorption and replacement with OLA molecules [230]. The use of this procedure leads to a

substantial increase in the intensity of the PL of the CdSe core solution and ultimately improves the optical properties of the core/shell QDs.

In order to estimate how this additional GPC purification improved the quality of the resultant QDs, we compared the optical characteristics of CdSe core QDs purified by the dispersion/coagulation method alone and QDs purified by the dispersion/coagulation method followed by GPC (Figure 31).

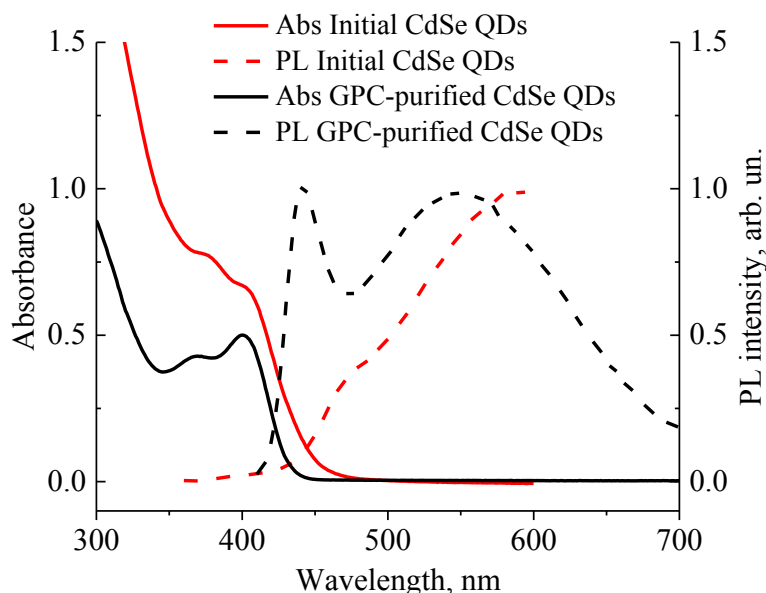


Figure 31: The absorption (Abs) and photoluminescence (PL) spectra of CdSe quantum dots prepared using different procedures.

As a result of a GPC purification, the position of the first excitonic transition in the absorption spectra did not change (Figure 31); however, both the first excitonic transition and a decrease in the absorbance in the blue region of the spectrum were distinct after the core solution was purified from excess organic molecules. In addition, the low density of electron and hole states, which was a distinctive feature of small-sized QDs, took the form of a clear first absorption band. The first excitonic transition of CdSe cores at 401 nm corresponded to a core diameter of 1.5 nm according to Ref. [214]. The result of purification was also clearly seen in the PL spectra. In the PL spectra of the original QDs, the PL excitonic band was poorly distinguishable, and the main contribution to the PL spectrum was made by the defect PL. After GPC purification, the intensity of defect PL was significantly decreased, the PL band with a maximum at 441 nm was well-distinguishable, had a symmetrical shape and the distribution spectrum close to Gaussian, and the FWHM was about 45 nm. Precise measurement of the FWHM of the main band was limited by an intense surface defect luminescence, which was

typical of the PL spectra of the smallest QDs. The PL QY of the ultrasmall QDs was 4%. The low value of the PL QY was related to the high sensitivity of the small QDs to the environment and the resultant suppression of PL, which agrees with literature data [242,243].

Thus, we propose an effective method of ultrafast reaction termination by freezing the reaction mixture with liquid nitrogen, which allows obtaining QDs that are formed at the earliest growth stages in bulk quantities. Effective purification of these small QDs from the cadmium precursor and excess adsorbed ligands was achieved only by combining the traditional dispersion/precipitation method and GPC. We have used this method to obtain CdSe core QDs with the first excitonic absorption peak at 401 nm, which corresponds to the QD diameter of 1.5 nm. As a result of the multistep purification, we were able to isolate highly uniform ultrasmall CdSe QDs from ligands and unreacted precursors. The isolated samples were of minimal size with a narrow size distribution, the QD surface was ready for subsequent shell growth.

3.1.3. Development of CdSe nanocrystals growth model

As seen from the previous results, QD cores with specified optical properties are easy to obtain by controlling the reaction kinetics through variation of the reaction temperature, precursor and ligand concentrations. It is more difficult to predict the optical and morphological characteristics of core/shell QDs, because the additional phase (shell) alters the energy structure of the QD, a phase interface appears, and defective structure can form due to the difference between the crystallographic parameters of the core and shell materials. The structural properties of core/shell QDs can be predicted by using a correct model that would follow the growth process of a QD shell and allow a strict control over the shell growth process.

To date, a number of QDs growth models exist, mainly based on well-established physical and chemical principles [244-246]. As an example, in the widely used SILAR approach for controllable shell growth [74], in which the anionic and cationic precursors are added into the reaction in an alternating way, only a simple spherical NC model is used for calculation of reagent quantities. The determination of the shell thickness is based on the change in the radius of the initial and final QDs (Figure 32a). A common drawback of the spherical models is the fact that they do not allow to predict the shape and faceting of QDs. This is important since such small nanocrystals are much close to molecular species where each added atom has an effect on the electronic structure of QDs. In practice, small sized QDs have a non-spherical shape, which is confirmed by TEM images (Figure 32b). For example, in the case CdSe cores synthesized with HDPA, QDs have the wurtzite crystal structure with hexagonal bipyramid shape (Figure 32c). As a result it was found relatively large differences in the precursor quantity (about 10-20%) between the spherical (classical) model and a model that takes into account geometry and

faceting of the real QDs [247]. It follows that the calculation of the number of precursors in the SILAR model is based on an incorrect geometric model of QD and, hence, contains a sufficient systematic error, which results in the formation of non-uniform shells or nucleation of shell material. Also, in the case of a spherical NC model, it is impossible to determine the cation to anion surface atom ratio, what is essential to know when calculating the required quantity of ligands or functional biomolecules.

Taking into account the abovementioned shortcomings of the model of QD growth, we proposed an alternative approach for modelling QD growth, based on the crystallographic characteristics of the bulk QD material and morphology relevant to that is observed in microscopy images of real QD samples. Our model allows a more accurate description of the process of QD growth on the atomistic level, regardless of the chemical system used for the synthesis and reaction kinetics. This model is based on four principles:

- the model is based on experimentally determined crystal faceting and crystallographic data of the QD material;
- QD formation and growth occur upon the sequential addition of Cd-Se monomers, i.e. nanocrystal is stoichiometric on each growth stage (Figure 32d) [89];
- a single CdSe monomer is the starting point of the growth process;
- in each stage of QD growth the coordination spheres of the surface atoms is maximally saturated in accordance with the coordination number of the selected atoms, and thus growth occurs layer-by-layer (Figure 32d,e).

The following text is an example of how a structural growth model of wurtzite CdSe QD is obtained from raw crystallographic data. Modelling can be done using commercial crystallographic software like Diamond (Crystal Impact), but we have developed specifically designed software for automated construction of nanocrystal growth models. Crystallography Open Database entry #9011664 [248] was used as a source of crystallographic data. The first step of NC growth modeling is the selection of starting geometry. A single Cd-Se monomer, a chain of atoms or more complex clusters could serve as a starting point, yielding either quasi-spherical, nanorod or other nanocrystal geometries. For the purpose of this work, a Cd-Se monomer is the best choice of starting QD geometry, since it allows to obtain nanocrystal morphology close to the one observed in TEM (Figure 32b). In the following steps of modeling, the coordinating sphere of each atom in the existing structure is filled with “free” atoms from crystallographic space (i.e. all the bonds of the existing atoms are saturated). The new atoms attached to the existing structure are labeled as belonging to the next layer. This procedure is repeated iteratively until the desired size of the nanocrystal (including the layers of the shell

being planned to be grown atop CdSe core), measured as the maximum interatomic distance is achieved. This way, the geometry and stoichiometry of the NC, as well as the number of metal and chalcogen atoms in each layer, is known at each growth stage. These data are sufficient for the precise calculation of the quantities of precursors necessary for the layer-by-layer expansion of the NC core, if assumed that the shell will grow epitaxially (Figure 32e). Table 5 summarizes the obtained data of wurtzite-CdSe QD growth at different stages, starting from a CdSe monomer and ending with 4.3 nm nanocrystal.

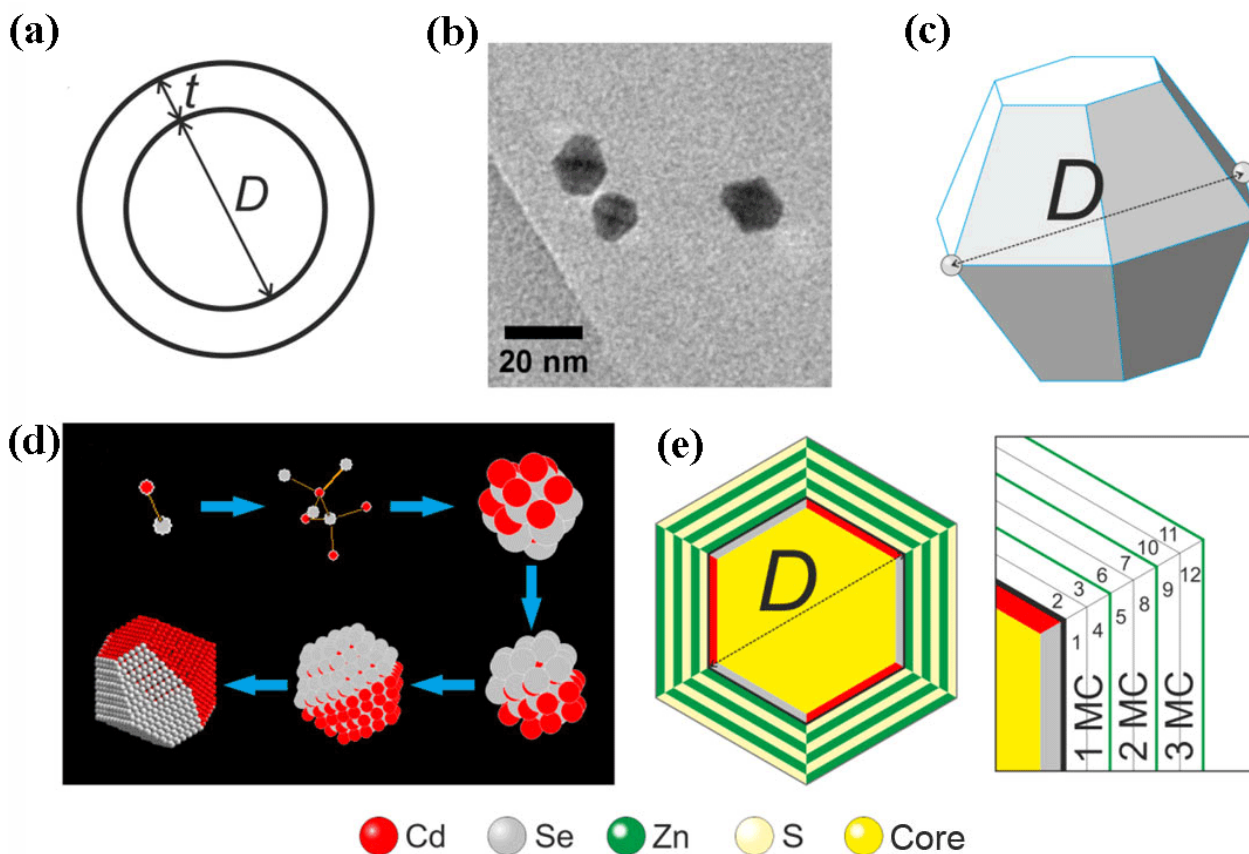


Figure 32: Key elements of the QD growth model: (a) spherical model of a QDs; (b) TEM images of synthesized CdSe QDs; (c) geometrical model of a QD, a hexagonal bipyramid; (d) step-by-step growth of a CdSe QD, starting from the monomer; (e) model layer-by-layer shell growth.

Table 5: Atomic composition and basic properties of CdSe QDs at different stages of growth.

# iter	Cd atoms	Se atoms	total atoms	diameter, nm	abs λ_{\max} , nm
1	1	1	2		
2	3	3	8		
3	9	9	26		
4	16	16	58	1,51	404
5	28	28	114	1,84	441
6	39	39	192	2,3	489
7	57	57	306	2,66	518
8	73	73	452	3,12	546
9	97	97	646	3,48	563
10	117	117	880	3,94	580
11	147	147	1174	4,3	591
12	172	172	1518	4,76	603
13	208	208	1934	5,12	611
14	237	237	2408	5,58	621
15	279	279	2966	5,95	628
16	313	313	3592	6,41	636
17	361	361	4314	6,77	641
18	399	399	5112	7,23	648

To verify the proposed model, we have used the results of modeling for an experiment with overgrowth of small CdSe nanocrystals. First, we have made a correlation between the calculated diameters of CdSe NCs on each stage starting from 4 and the corresponding position of the first excitonic absorption peak in the absorbance spectra using calibration curve from Ref. [248]. This, in turn, allowed us to select the appropriate stage of the model as the starting stage for overgrowth of obtained sample of CdSe nanocrystals. In this case, we have obtained CdSe cores with the first excitonic transition at 486 nm (Figure 33a), what corresponds to stage 6 of the proposed model. After purification and isolation of the cores, they were transferred to a fresh ODE:OLA solution and the overgrowth was performed in a thermocycling regime, using the data from Table 5 scaled according to the quantity of CdSe NCs in the reaction solution. Figure 33a shows the absorption spectra at different stages of CdSe core overgrowth, and Figure 33b presents the comparison of the dynamics of changes in the position of the exciton absorption maximum in experiments and those calculated using the proposed growth model. As can be seen, for all overgrowth stages, the deviations of the wavelength absorbance maxima obtained in the simulation and experiment are small. Based on these results, it can be stated that the proposed model corresponds well to the real CdSe QD growth process. Thus, it can be concluded that the

proposed QD growth model allows predicting the size and composition of QDs at any stage of QD formation and can be harnessed to the calculation of exact quantities of the precursors required for deposition of successive shell layers. For the latter process, if shell growth is assumed to be epitaxial, i.e. without distortion of NC crystal structure, all that is needed is to virtually replace Cd and Se atoms with Zn and S atoms (or any other for the selected shell composition) and perform calculations and precursor injection sequence in a SILAR-like manner.

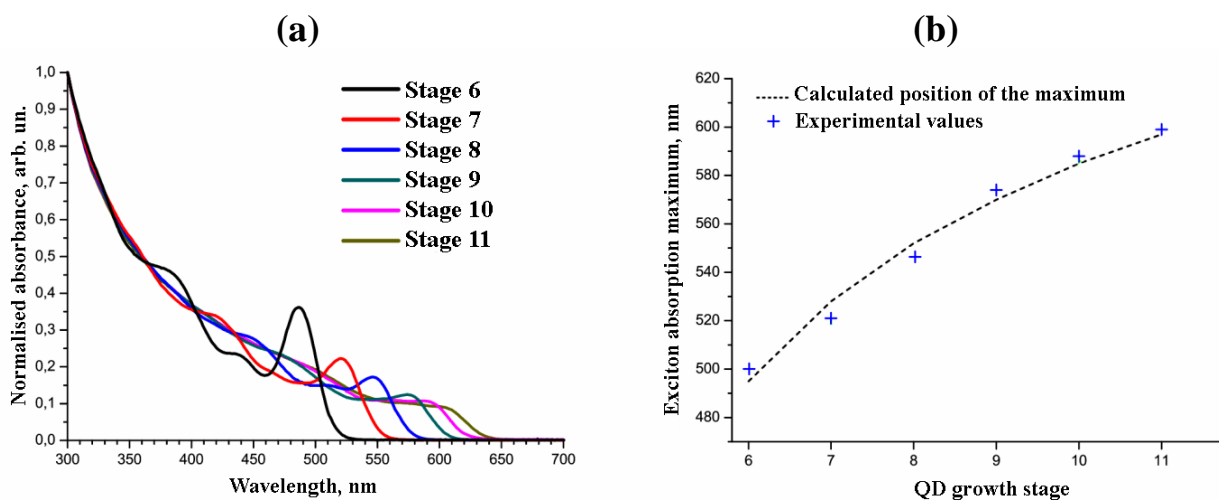


Figure 33: (a) Evolution of the extinction spectra at different stages of wurtzite-CdSe QD growth. (b) Comparison of the exciton absorption maximum wavelengths calculated using the QD growth model and the experimental data for different stages of growth.

To conclude, taking into account the shortcomings of the classical spherical model of QD growth, we proposed an optimized QD growth model, based on the crystallographic characteristics of the bulk material and prevailing typical morphology of real wurtzite- CdSe nanocrystals. The model allows a more accurate description of the QD growth and to calculate precise quantities of precursors necessary for layer-by-layer deposition of the shell.

3.2. Synthesis of CdSe-based core/shell QDs.

3.2.1. Synthesis of CdSe/ZnS core/shell QDs

It is well known that the size distribution of the core/shell QDs is typically significantly worse than that of the original core QDs, even in the case if shell growth is conducted carefully by dropwise addition of the shell precursors. The layer-by-layer shell growth method allows an increased accuracy of core-shell QDs size distribution in comparison with the classical one-solution approach, yet, even the SILAR approach can result in the formation of non-uniform and irregular shells [249]. Two critical issues for maintaining the size distribution of QDs during the

growth of the shell are (1) elimination of homogeneous nucleation of the shell materials and (2) homogeneous monolayer growth of shell precursors on all core QDs in the solution, yielding shell layers with nearly the same thickness. In principle, the reactivity of the precursors should be weak enough to prevent independent nucleation but sufficiently strong to promote the epitaxial growth around the cores. Therefore, relatively reactive and thermodynamically stable precursors are required for the growth of high-quality core/shell NCs.

In this work, epitaxial shell growth was carried out using the SILAR-like approach, based on the sequential injection of small discrete portions of metal and chalcogen precursors starting from metal (in the order metal→chalcogen→metal etc.) into the reaction mixture. This approach, compared to the classical method of continuous injection of two precursors or their mixture using a syringe pump, allows to synthesize QDs with well-controlled structure and shell thickness. Specifically, only one-half of a monolayer grows in each injection cycle of either the cationic or the anionic precursors. Because the two precursors do not coexist in the reactor, homogenous nucleation of the shell phase NCs is avoided. This approach allows to obtain high-quality shells, to significantly increase PL QY and to manipulate both the composition and the shell thickness over a wide range in a controllable manner.

The CdSe QD growth model was used to calculate the precursor quantities necessary for the growth of a protective epitaxial shell of zinc sulfide with high accuracy. Accurate calculation of the necessary precursor quantities takes into account the 3-ML shell thickness, known precursor concentrations, and the quantity of CdSe cores in solution determined by absorption spectroscopy. Quantification of the surface layer plays a key role in the calculation of the necessary amount of ligands or biomolecules for further solubilization or functionalization. The exact quantity of CdSe cores in the reaction solution was measured shortly before the shell growth using the known calibration curves [214].

Four types of candidate sulfur precursors were tested for the formation of the ZnS and CdS shells: elemental sulfur dissolved in ODE, thiourea ((NH₂)C=S) dissolved in TEGDME, trioctylphosphine sulfide (TOPS), and two alkanethiols, octanethiol and dodecanethiol. Alkanethiols are widely used for fabricating CdSe/CdS QDs with giant shells. Although this method yields QDs with good optical properties, including very narrow PL bands, high PL QDs, and an almost completely suppressed blinking effect [24,50], it suffers from a low reproducibility of results and exceedingly slow reaction kinetics. The ODE solution of sulfur is hardly acceptable as a sulfur precursor for layer-by-layer shell formation, because this solution is unstable at room temperature. Another drawback is that different forms of sulfur considerably differ in reactivity, and their ratio in the precursor strongly depends on the conditions of preparation (the temperature and the rate and duration of heating). TOPS, obtained by dissolving

elemental sulfur in TOP, is convenient for forming shells in various modes, but is unstable when stored in the air because of oxidation. The sulfur precursor in the form of a TEGDME solution of thiourea (0.85 M) was obtained by dissolving thiourea under sonication or stirring with a mild heating to 45°C. This precursor remains stable in the air in the absence of intense illumination for more than half a year. If it is heated to more than 100°C in the presence of oxygen-containing compounds, it is decomposed into reactive elemental sulfur and urea. Thus, the use of this precursor provides a solution of elemental sulfur in the reaction medium, and then sulfur reacts with the zinc and cadmium precursors *in situ*. This type of precursor is very convenient for growing the shell in both layer-by-layer mode and in the mode of continuous infusion of the precursors.

Thus, the combination of the quality of the shells grown and the convenience of the procedure indicates that 0.85 M TEGDME solution of thiourea is the best sulfur precursor for the synthesis of PL QDs.

The temperature conditions of the shell growth reaction were varied to find the optimal temperature interval in which the shell monolayers grow at an acceptable rate while the shell material does not form nanocrystals as byproducts. Experiments at temperatures ranging from 160 to 200°C showed that the optimal temperature was 165°C in the case of a CdS shell and 175°C in the case of a ZnS shell. At temperatures higher than 180°C, the formation of new core fraction of the shell material as byproducts was observed, that can be seen in the micrograph in Figure 34. Here, in addition to the main product, core/shell QDs, small NCs of the shell material are seen. At lower than 160°C temperatures, conversely, chemical reactions and the growth of shell monolayers are decelerated.

Analysis of the possible ways to optimize the conditions showed that the introduction of additional portions of TOP before each injection of the sulfur precursor further increases the PL QY of the resultant QDs. Apparently, this effect of TOP is accounted for by a more reliable stabilization of QDs in the reaction medium at the moment when their surface is terminated with sulfur atoms, because the OLA molecules and carboxylate anions contained in the medium cannot serve as effective surface ligands at this stage.

Thus, to enhance the QD quality, it is preferable to form the shell layer-by-layer from zinc or cadmium 2-ethylhexanoate and thiourea as precursors, at temperatures from 165 to 175°C, by means SILAR-like injection routine and thermocycling, with TOP added both before the start of the shell growth and before each addition of the sulfur precursor to the reaction medium.

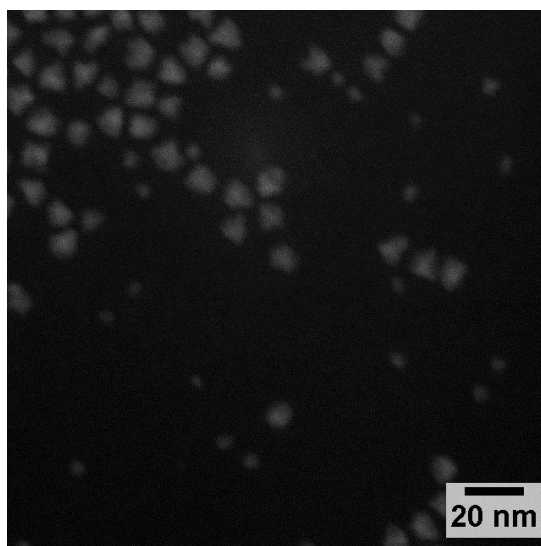


Figure 34: A STEM image of the CdSe/ZnS QD sample in which shell growth was performed at 200°C.

After the optimization of all synthetic processes, we compared the optical characteristics of the QDs with GPC-purified and nonpurified cores to estimate how this additional purification improves the quality of the resultant QDs. The CdSe cores purified by the dispersion/coagulation method alone (Sample 1 in Table 6) or dispersion/coagulation followed by GPC (Sample 2) were coated with three monolayers of ZnS. The optical spectra of two products are shown in Figure 35 and Table 6.

As can be seen from Figure 35 and Table 6, Sample #1 has a "blurred" excitonic transition due to the formation of QDs with non-uniform shell thickness throughout the ensemble, which is expressed in a wide FWHM. It is also characterized by a 56-nm red shift of the PL peak. The incomplete removal of cadmium precursors from the solution of CdSe cores leads to the formation of an inner CdS layer or a layer of a more complex and varying composition ($\text{Cd}_x\text{Zn}_{1-x}\text{S}$) in the shells of some QDs in Sample #1. Sample #2 of CdSe/ZnS QDs is considerably more homogeneous, as evidenced by its more than 1.5-fold narrower PL band. In addition, the red shift of the PL peak is also smaller (37 nm). Thus, the additional GPC purification of CdSe cores has substantially improved the optical parameters of the resultant QDs. The PL QY of ultrasmall QDs was calculated to be 68%. This PL QY value is far from the maximum possible one, which is typical of such small QDs because of the high probability of PL quenching via various mechanisms [47].

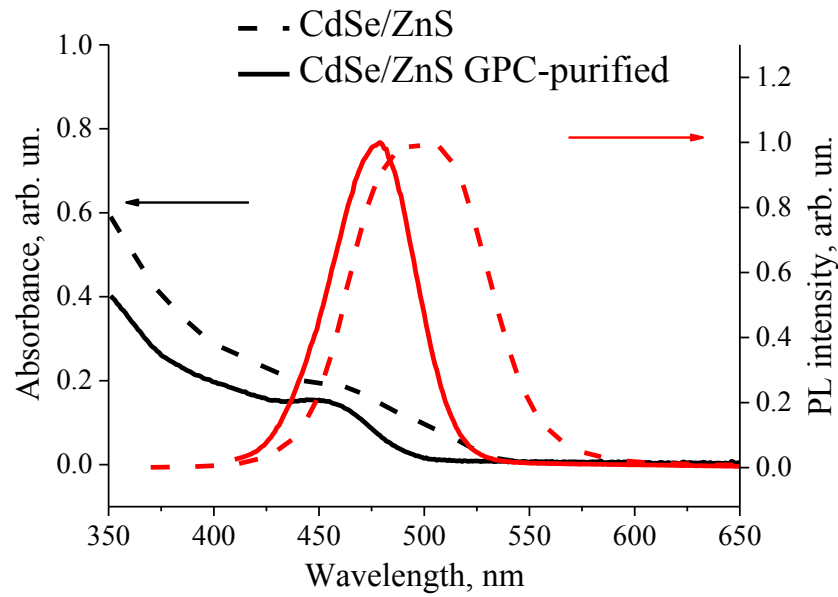


Figure 35: Absorption and fluorescence spectra of CdSe/ZnS QDs based on the cores purified using different procedures.

Table 6: Main optical properties of CdSe/ZnS QDs with cores purified using different procedures.

Sample #	Sample	Absorbance peak, nm / PL peak, nm / FWHM, nm	PL QY, %
1	CdSe/ZnS	- / 498 / 73	63 (relative to Coumarin 102)
2	CdSe/ZnS with GPC-purified cores	449 / 479 / 46	68 (relative to Coumarin 102)

In HRTEM images of Sample #2 (Figure 36a), one can see that the QD morphology was nearly spherical. The existence of lattice fringes and no visible crystal lattice defects in the HRTEM image further confirmed the high crystallinity of CdSe QDs. The average diameter of the QDs estimated from HRTEM images was determined to be 3.7 ± 0.5 nm. The size distribution is also close to normal. The histogram of the size distribution of QDs of the HRTEM images is shown in the inset of Figure 37a. The STEM images of Sample #2 (Figure 37b) showed that these NCs had similar morphologies in the ensemble. Measurement of the exact sizes of QDs based on STEM images yielded a value of 4.2 ± 1.1 nm.

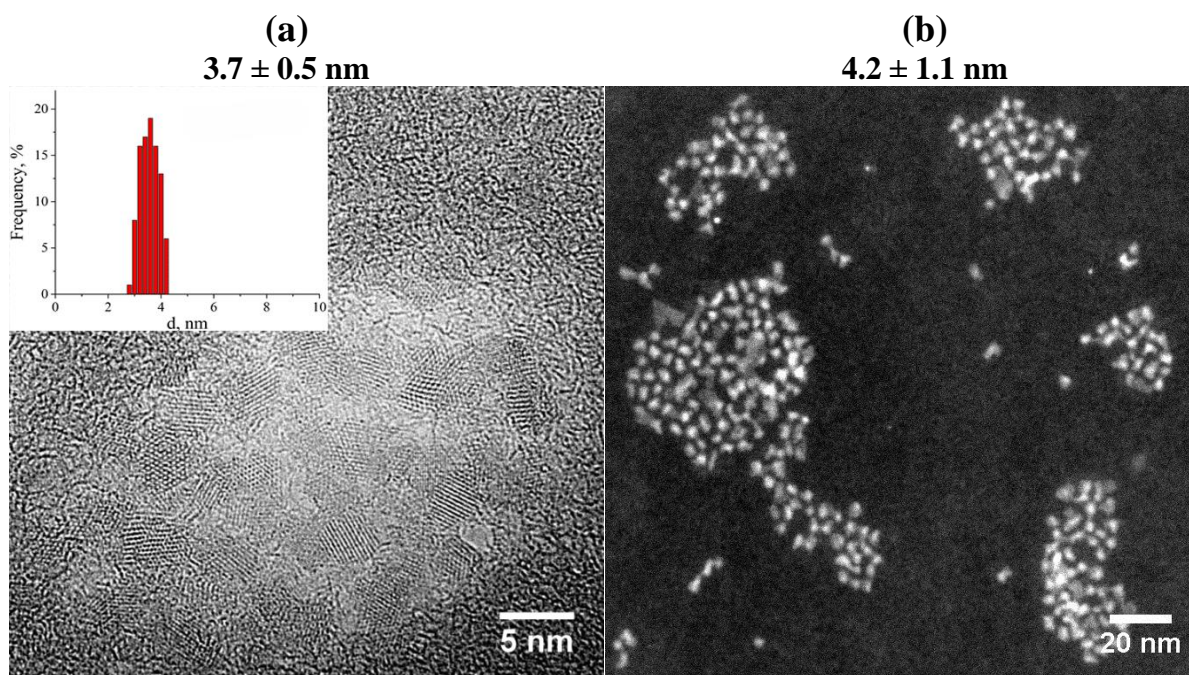


Figure 36: (a) an HRTEM image of CdSe/ZnS QDs; the inset shows the histogram of the size distribution based on the analysis of HRTEM images. (b), a STEM image of CdSe/ZnS QDs.

EDS analysis was used to characterize qualitatively the components in the sample by detecting characteristic X-rays. Analysis of the spectrum of CdSe/ZnS QD (Sample # 2) sample allowed us to find the atomic composition of the analyzed area (Figure 37). EDS analysis of the prepared nanoparticles, which confirmed the presence of Cd, Se, Zn, and S atoms and the absence of impurity elements. Two unmarked most intensive bands are the signals of C and Cu from carbon coated copper grid. EDS analysis also gives quantitative data of each component in the sample, to relatively small QDs however it is too difficult to apply this function.

To conclude, Ultrasmall CdSe QDs with a diameter of 1.5 nm were obtained by optimized colloidal hot injection synthesis modified with the fast termination of QD growth using liquid nitrogen. The use of size exclusion chromatography for high-performance purification of the QDs cores made it possible to avoid non uniform growing growth of the protective epitaxial shells with a nonstoichiometric composition, and had a positive effect on the homogeneity of the QD ensemble and optical characteristics of the QDs. The subsequent deposition of the ZnS shell on the obtained cores provided growth increase of the PL QY from 4 to 69%. The obtained compact QDs are suitable for further solubilisation in aqueous media and are promising photoluminescent labels for developing nanoprobe for intracellular imaging.

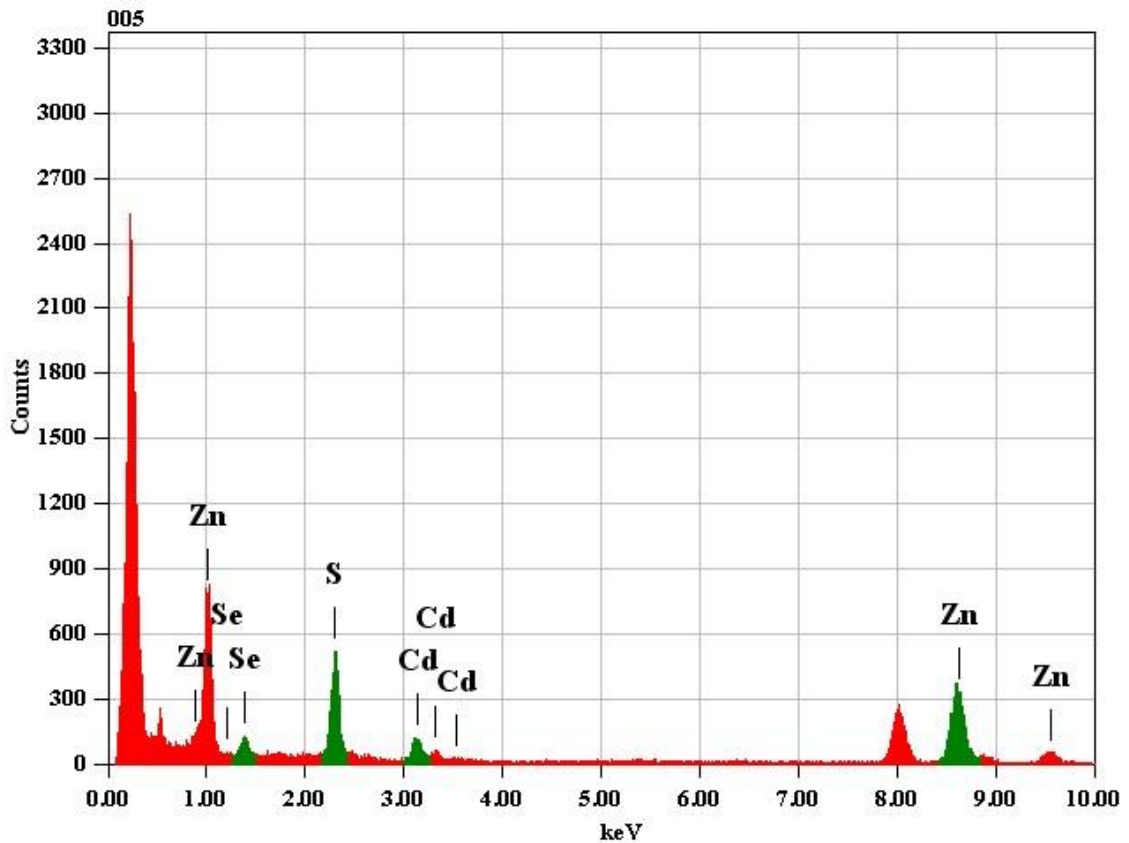


Figure 37: EDS spectrum of a CdSe/ZnS QDs.

3.2.2. Synthesis of multishell QDs

As it was shown above, a wide-bandgap epitaxial shell increases the PL QY of core/shell QDs and provides sufficient protection of the core from the environment. It is generally accepted that a ZnS shell provides a better passivation of CdSe cores. Despite the high precision of the proposed shell growth method, the PL QY of the obtained CdSe/ZnS core/shell QDs is limited by the magnitude of the potential barrier for excited charge carriers created by the shell (Figure 38). Growing a 1 ML thick ZnS shell ensures substantial enhancement of the PL of core-shell QD relative to core QD, but further thickening of the shell leads to degradation of PL QY because of formation of strain-induced defects and decrease of potential barrier of the shell, for which quantum confinement effect is also applicable. The band gap of CdS, also used as a shell material, is not high enough in the thin shell QD geometry to provide an effective potential barrier that would block charge carriers inside the CdSe core and, hence, increase radiative recombination. CdSe/CdS QDs can have a PL QY as high as 100% in organic solvents for the “giant” shell nanostructure, but the large size of these QDs precludes a high PL QY in an aqueous medium. The combination of ZnS and CdS shell layers allows to partially compensate

the lacks of each structure. Therefore, synthesis of small QDs with a high PL QY is an attractive goal at the moment. Schematic structure and the energy-level diagrams of different core/shell QDs are shown in Figure 38.

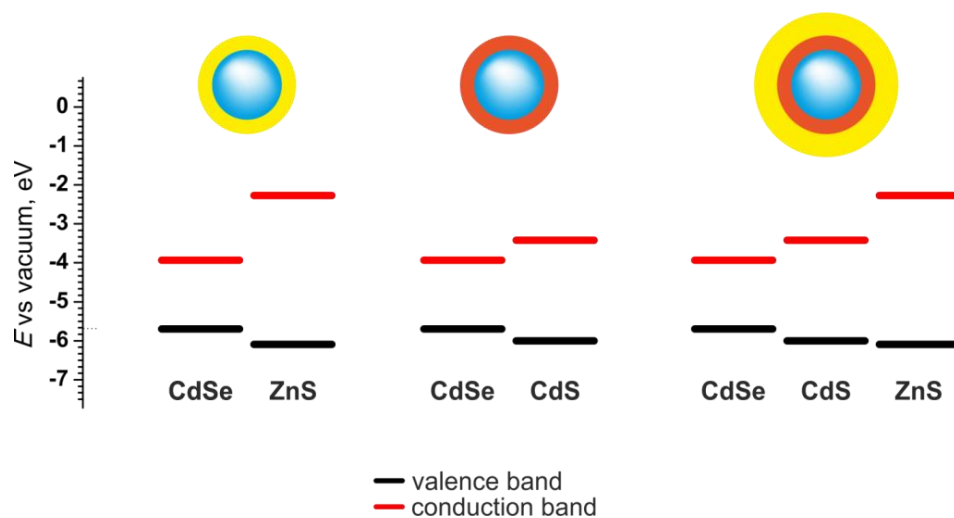


Figure 38: Schematic structure and energy-level diagrams of different core/shell QDs.

We suggest another approach, which ensures strong confinement of the electron-hole pair in the luminescent CdSe core. The shell itself undergoes a strong quantum confinement effect, and the smallest possible shell thickness should create the maximum potential barrier for photoexcited charge carriers. These high barriers should considerably increase the probability of radiative recombination of the exciton and hinder any charge transfer processes. On the other hand, the shell should be sufficiently thick to protect the luminescent QD core from the environment. Therefore, an increase in the shell thickness will not be enough to preserve the initially high confinement potential. A solution to this problem may be found in introducing a compatible thin interlayer between the first shell monolayer and its residual external part in order to break the high-bandgap shell crystal continuity. This interlayer will create a high and abrupt potential barrier at the core-shell interface and also serve as a “padding” for further thick shell growth. Experimentally, this novel nanostructure may be engineered in the form of a CdSe/ZnS/CdS/ZnS core/multishell (MS) QD, whose energy level diagram and schematic structure is shown in Figure 39.

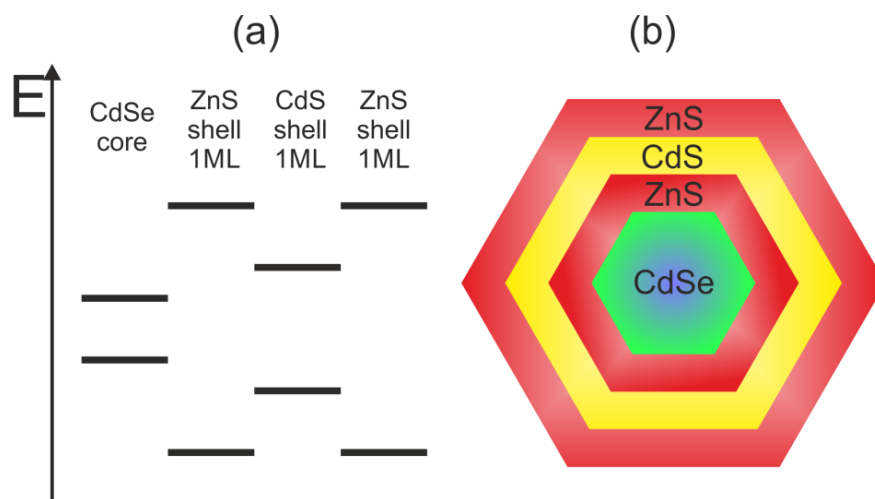


Figure 39: (a) The energy-level diagram of the novel core/multishell CdSe/ZnS/CdS/ZnS quantum dot; (b) the schematic structure of the core/multishell colloidal QD.

To test the efficiency of the proposed structure, we synthesized a series of core/shell QDs from one batch of previously synthesized 2.45-nm CdSe cores with the first excitonic transition at 495 nm (Chapter 3.1.1). Employing the SILAR procedure, we have synthesized core/shell QDs with three different shell types: CdSe/ZnS (3 ML), CdSe/CdS (1 ML)/ZnS (2 ML), and CdSe/ZnS (1 ML)/CdS (1 ML)/ZnS (1 ML). Since all samples have the same shell monolayer number grown under the same synthesis conditions, the shell structure and its confinement potential are the key parameters determining the optical properties of the QDs. The absorption and emission spectra of the three obtained samples are shown in Figure 40a,b. The samples containing a CdS layer in the shell exhibit a large spectral shift of both the PL and first excitonic absorption peaks towards the red region as compared to the CdSe/ZnS samples. Interestingly, when the first shell monolayer is CdS, the excitonic transition in the absorption spectrum becomes smeared. We assume that the weak barrier potential created by cadmium sulfide is the reason for this effect, because, in both samples having ZnS as the first monolayer of the shell, the excitonic transitions are clearly resolved. Therefore, the application of a CdS interlayer inside the ZnS shell may be used as a method of tuning the PL wavelength range of fixed-sized CdSe cores without degradation of the spectral purity.

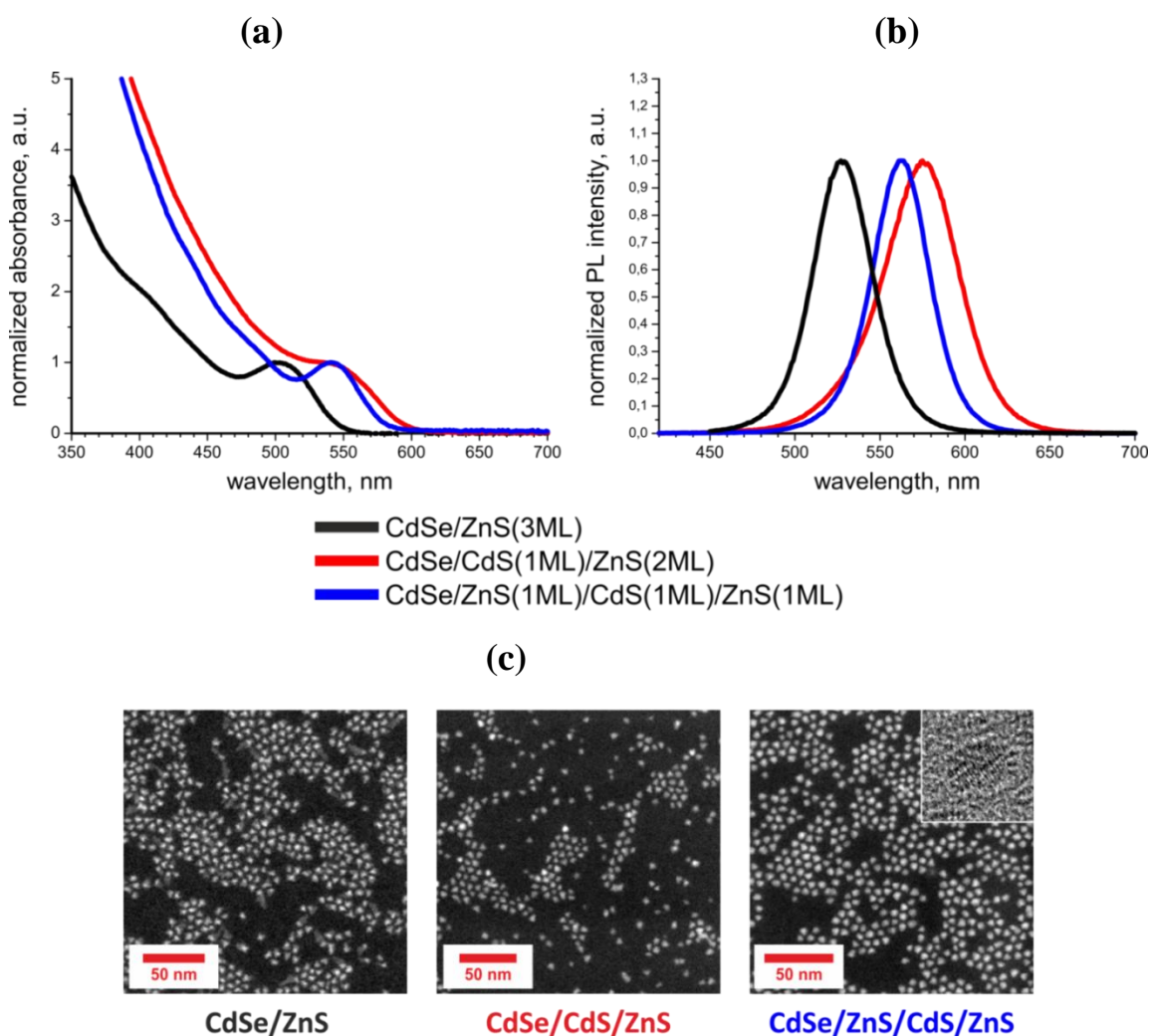


Figure 40: The (a) absorption and (b) emission spectra of QDs with different shells. (c) A DF-STEM image of different shell structure QDs; an HRTEM image of a single quantum dot is given in the inset.

A dark-field STEM image of QDs with different shell structures is presented in Figure 40c. The diameters of CdSe/ZnS, CdSe/CdS/ZnS and CdSe/ZnS/CdS/ZnS QDs were 4.7 ± 0.5 , 4.7 ± 0.7 and 4.6 ± 0.4 nm, respectively. The high size uniformity in one ensemble and the series of three QD structures proves the applicability of the QD growth model to the synthesis of QDs with different shell structures. The shell thickness of MS QDs can be estimated as 1.15 nm, which is close to the predicted 0.95 nm, the sum of wurtzite-phase single CdS and double ZnS monolayers. The MS QDs have no pronounced regular shape, but their local arrangement in a hexagonal lattice pattern gives evidence for a high size uniformity. An inset in Figure 40c shows an HRTEM image of a single CdSe/MS QD. The visible lattice fringes give evidence for the conformal growth of the complex shell, despite the expected high strains caused by the combination of the materials used.

Figure 41 shows the evolution of the PL QY during the shell growth of three different samples. As expected, the CdSe/ZnS QDs exhibited a slow degradation of the initially high PL QY with an increase in the shell thickness. In contrast, the PL QYs of the CdSe/CdS/ZnS and CdSe/MS samples did not fall during shell growth; however, the difference in the type of the first shell monolayer and its band levels leads to quite a different PL QY of the obtained core/shell QDs. PL QY of CdSe/CdS/ZnS QDs does not increase 70%, while PL QY of CdSe/MS QDs reaches 97%. Furthermore, the FWHM of CdSe/MS QDs is minimal among all the types of QDs studied. The main optical characteristics are summarized in Table 7.

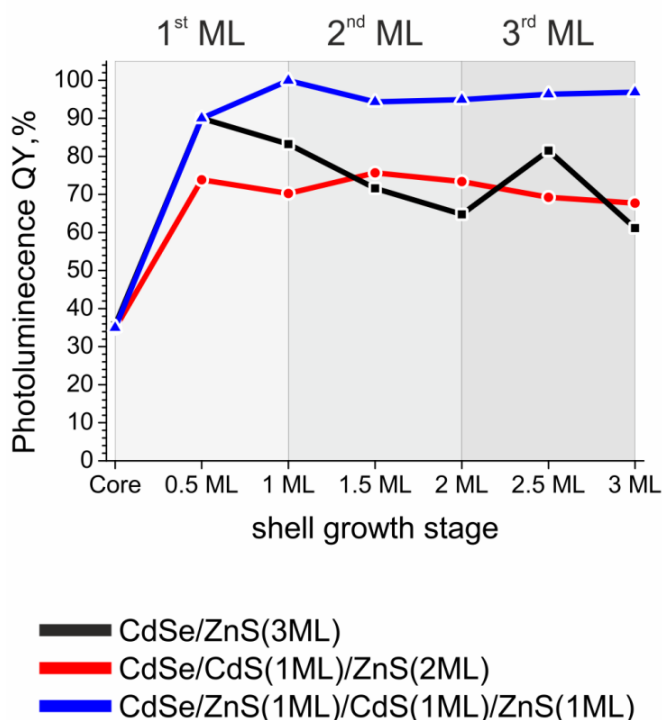


Figure 41: Evolution of the PL QY during shell growth of the three samples studied.

In order to demonstrate the effectiveness of the MS structure for QDs of other sizes, we synthesized and compared a series of core/shell QDs QD-540, QD-570, QD-610 with different sizes of the CdSe cores with diameters of 1.8, 2.45, and 2.7 nm, respectively.

The photoluminescence and absorption spectra of the obtained core/MS samples are shown in Figure 42a, the evolution of the PL QY during the shell growth is shown in Figure 42b. During the alternating shell precursor injection, we observed a significant red shift (55–65 nm) in the absorption spectra of all QDs relative to the cores, which indicated the formation of the CdSe/MS QD structure. The formation of the shell atop CdSe cores resulted in a drastic improvement of the PL efficiency. The PL QY of the first ZnS shell was increased to 100% for QD-570 sample and remained practically unchanged during the growth of the next shell layers.

The PL QY of the QD-540 and QD-610 samples increased to the maximum value, but then it slightly decreased to 80% during the deposition of the CdS shell and did not change considerably until the end of the shell growth. This decrease in PL QY was probably due to the accumulation of lattice strains at the shell border because of the large area of the core/shell interface in QD-610.

Table 7: The main optical characteristics of the different core/shell structure QD samples.

Sample type	Abs. _{max} , nm / PL _{max} , nm / FWHM, nm	PL QY, %
CdSe/ZnS	502 / 527 / 41	60
CdSe/CdS/ZnS	540 / 575 / 52	68
CdSe/ZnS/CdS/ZnS	541 / 563 / 39	97

We suppose that these advanced optical properties, including ultimate values of PL QY, result from the combination of a high band gap of the first ZnS layer, second CdS interlayer, and an external potential barrier created by the third ZnS layer, which also makes the inorganic QD surface compatible with the surfactant complexation and common ligand exchange procedures.

In addition to typical optical characteristics of QDs, multiphoton optical properties were studied. We measured two-photon absorption cross sections (TPACSs) of three core/MS QD solutions in chloroform. The values of σ_{TPE} measured for these samples were found to be 1100, 16000, and 13000 GM (1 GM = 10^{50} cm³ s/photon) for QD-540, QD-570, and QD-610, respectively. The values of σ_{TPE} for our samples are an order of magnitude higher than those for CdSe QDs [223] and comparable with those for the best samples of CdSe/ZnS QDs of the same size found in the literature [217]. Thus, the TPACS of CdSe/MS QDs considerably exceeds those of organic dyes [4,250]. This allows one to engineer highly efficient QD-based two-photon labels that could be excited in the transparency windows of biological tissues in the near infrared spectral range [219]. Furthermore, the spatial resolution in the two-photon imaging mode can be substantially improved due to the possibility of compact localization of the excitation beam by its narrow focusing [220].

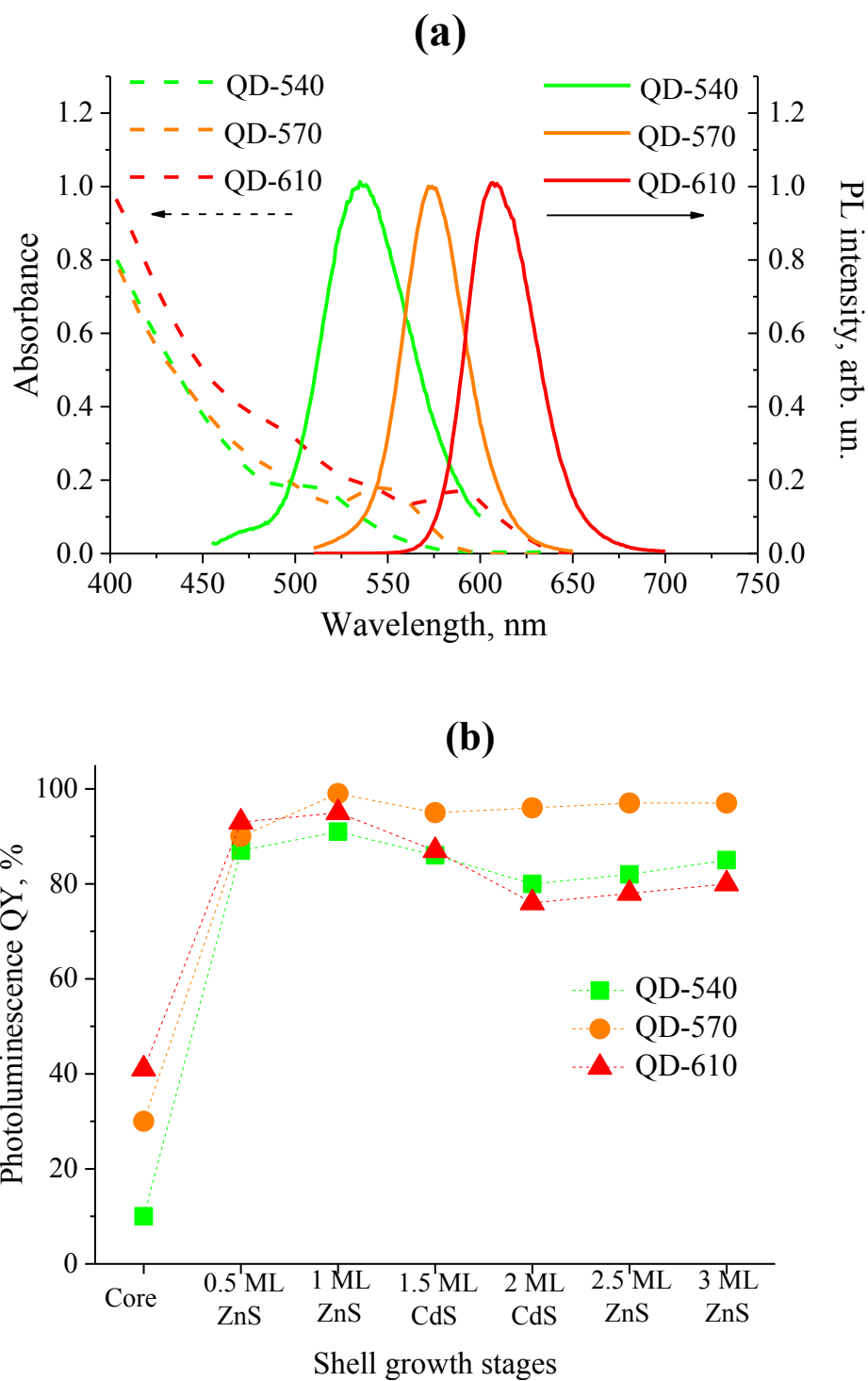


Figure 42: (a) Absorption and PL spectra of CdSe/ZnS/CdS/ZnS QD-540, QD-570, and QD-610. (b) Evolution of PL QY during shell growth.

It should be noted that after optimization of all synthetic processes the obtained core/MS QDs are characterized by a high reproducibility of their optical properties. Figure 43 shows the absorbance and PL spectra of the three QD samples fabricated from different lots of CdSe cores

using different reactor loadings and different lots of shell precursors. As seen from the spectra, all the three lots have almost identical optical characteristics.

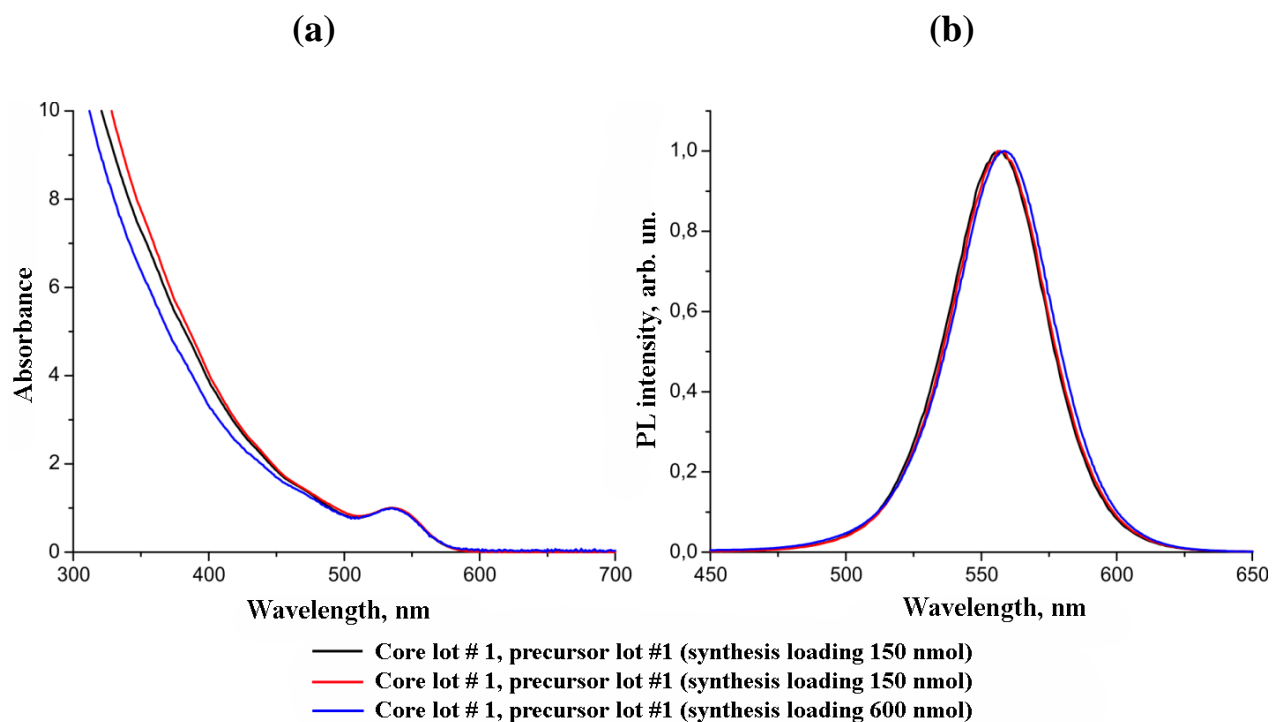


Figure 43: The (a) absorption and (b) PL spectra of three CdSe/MS lots with different reactor loadings (150 and 600 mmol) fabricated from different lots of CdSe cores and different lots of shell precursors.

The proposed new structure of core/MS QDs has a highly efficient charge carrier confinement in the PL cores due to the specific energy structure of the multicomponent shell. The first, 1-ML ZnS shell provides the highest potential barrier for electron–hole pairs, thus ensuring the maximal PL outcome. The second, CdS shell separates two monolayers of ZnS, thus increasing the shell thickness. The last, ZnS shell creates an additional potential barrier and is perfectly compatible with common surface ligand exchange protocols for QD solubilization and functionalization for biomedical applications. Core/MS QDs of different sizes exhibit a PL QY close to 100% and TPECS values considerably exceeding those of CdSe QDs [222] and are comparable with the best known CdSe/ZnS samples [217]. Furthermore, these multishell QDs allows one to obtain small-sized QDs with an emission outcome comparable with those of thick-shell analogues. Thus, the obtained QDs can serve as excellent materials for designing small-sized PL nanoprobe employed in two-photon studies.

3.3. Water-solubilization of ultrasmall QDs

The method of phase transfer of organically-soluble QDs was developed based on the procedure reported in Refs. [251,252] with some modifications, including exact calculation of the necessary equivalents of hydrophilic ligands and more soft solubilization conditions to avoid aggregation of ultrasmall QDs. Solubilization of QDs was performed using the two-stage ligand exchange approach. At the first stage, hydrophobic ligands were exchanged for DL-cysteine; at the second stage, DL-cysteines were exchanged for a mixture of two PEG derivatives. It was found that the published protocols, developed for solubilisation of QDs with sizes of more than 5 nm, is not readily applicable for ultrasmall QDs, because of occasional etching the QD's surface by excess cysteine hydrochloride or occasional spontaneous aggregation of the too much saturated QD solution. The main disadvantage of the original solubilization procedure is that it does not take into account the alteration of the specific surface area depending on the QD size. The lack of ligands led to poor passivation of the surface and accelerated aggregation of QDs. On the other hand, the use of cysteine hydrochloride as cysteine source leads to release of hydrochloric acid into the aqueous solution during exchange procedure, and chemical etching of the QD surface in case of large excess of cysteine. This leads to changes in the shell structure, size distribution, and PL shift to the blue region of the spectrum.

We performed an adaptation of the method via precise calculation of necessary ligand quantities using the data on the composition of final shell layer obtained using QD growth model, and applying soft solubilization conditions to avoid QD aggregation. Therefore, we estimated the necessary quantity of cysteine for complete passivation of the surface of the ultrasmall core/shell QDs. In the given case, this amount was found to be 264 molecules of the ligand per single QD. The value was calculated as the sum of zinc atoms of stages 10 and 11 (117 and 147 atoms, respectively) of the QD growth model (Chapter 3.1.2). The minimum diameter and narrow size distribution of water-soluble Cys-QDs were achieved with a twofold excess of cysteine over the calculated quantity, which is explained by the necessity of ligand excess in the competitive replacement of the ligands on the QD surface.

At the second stage, DL-cysteine was replaced with an excess of PEG derivatives (HS-(CH₂)₁₁-PEG₆-COOH; -OH) with terminal hydroxyl or carboxyl groups at a ratio of 9:1, respectively. Hydroxyl derivatives provide chemical inertness in biological media, and carboxyl derivatives provide a small ζ -potential, better colloidal stability of the QD solution, and the possibility for their conjugation with biomolecules and enhancement of cellular uptake. The PEGylated QDs were incubated overnight and pre-cleaned by centrifugation using Amicon Ultra-15 filter units (Millipore) with a cut-off of 10 kDa in a phosphate buffer (pH 8.0, 50 mM) at 3500 rpm. Since surface molecules of the QDs were similar to the free ligands in the solution,

it was difficult to remove the excess of free capping molecules by affinity or ion exchange chromatography. Therefore, we decided to use the size difference between the free ligands and QDs, what is implemented by means of SEC. Sephadex - cross-linked dextran gel beads with different porosities are the most popular stationary carrier phases used in SEC. However, the choice of the porosity is difficult because the manufacturer's recommendations on the separating ability are given for globular proteins but not for nanoparticles.

We investigated the resolution ability of medium-size Sephadex beads with different porosities (Sephadex G25, Sephadex G100, and Sephadex G200). Sephadex G25 exhibited a low efficiency of separation of QDs and free PEG, while Sephadex G200 had the best separation efficiency but required too much eluent volume. The separation quality of G100 was similar to that of G 200, and its relatively low porosity provided rapid elution. Thus, it had the best balance of separation efficiency and elution time; therefore, it was used for purification of QDs from free PEG and, afterwards, free AL.

Characterization of the aqueous QD solution followed by SEC.

The main characteristics (size distribution and zeta (ζ)-potential) of the ultrasmall QD solution were estimated using DLS (Figures 44, 45).

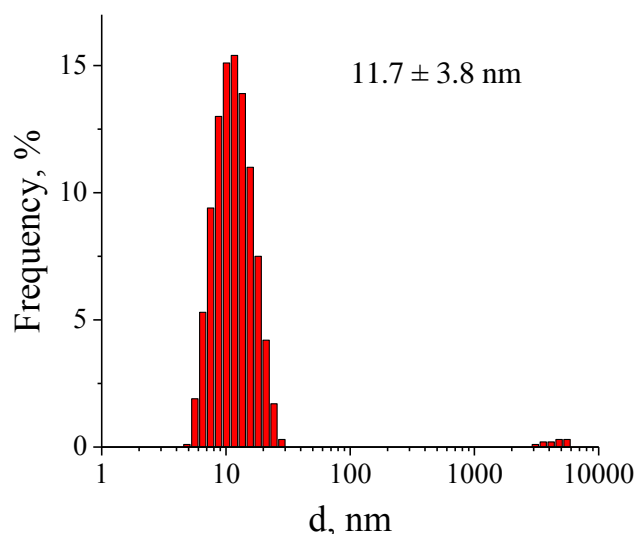


Figure 44: Size distribution of PEG-stabilized CdSe/ZnS QDs in a phosphate buffer (pH 8, 0.1 M) after GPC from the excess of the PEG derivatives.

	Mean (mV)	Area (%)	Width (mV)
Zeta Potential (mV): -12,6	Peak 1: -12,0	100,0	6,24
Zeta Deviation (mV): 13,3	Peak 2: 0,00	0,0	0,00
Conductivity (mS/cm): 0,160	Peak 3: 0,00	0,0	0,00

Result quality : Good

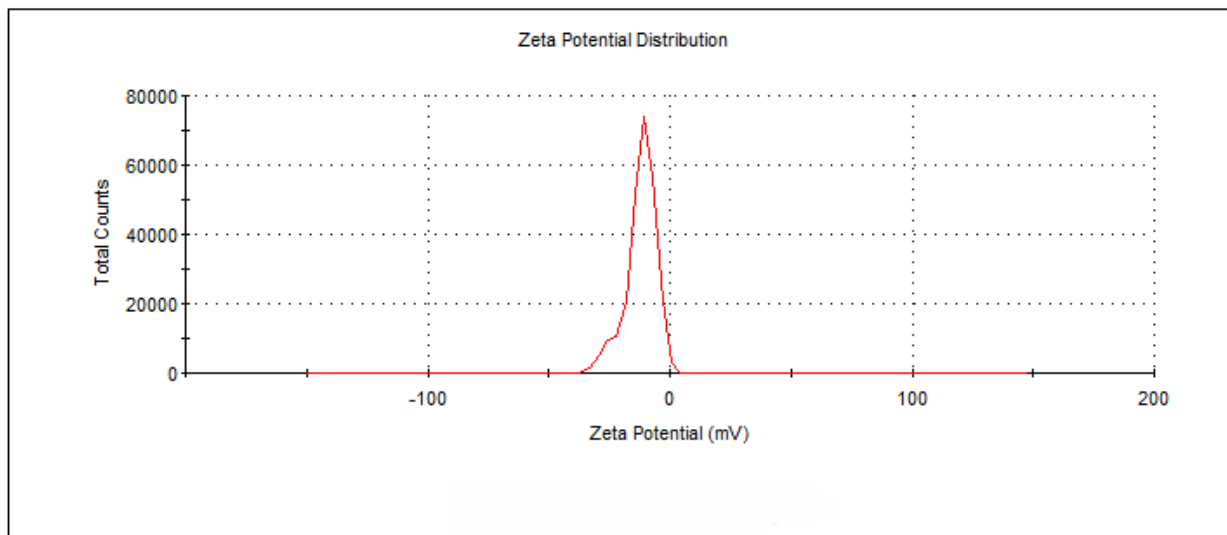


Figure 45: Zeta-potential distribution of PEG-QDs.

Thus, using the adapted approach, we were able to obtain water-soluble QDs with an average hydrodynamic diameter of 11.7 ± 3.8 nm. The zeta-potential was close to neutral and was determined to be -12.6 ± 6.2 mV, which demonstrated an insignificant charge due to a small amount of negatively charged carboxylic derivatives of PEG. The combination of a stable ligand shell and a slight negative surface charge provides high colloidal stability for more than 6 months.

Summary

Engineering of ultrasmall and bright QDs for biological application included three stages: the hot-injection colloidal synthesis of uniform and highly crystalline CdSe cores, development of bright core/shell QDs, and engineering of water-soluble QDs suitable for further functionalization.

The high-quality CdSe cores were obtained using the hot-injection approach with the optimized main reaction parameters: the types of the "hot" and "cold" precursors, type of organic solvent, type of cadmium salt, type of selenium precursor, injection temperature, reaction time, and ratio between the precursors of cadmium and selenium. CdSe QDs were successfully synthesised according to a modified literature procedure involving the reaction of Cd-HDPA and

TOP-Se at 240-270°C in ODE solution in the presence of TOA as a ligand. Distinct evolutions of the absorption and emission spectra of the CdSe QDs, as well as the size, were observed with increasing reaction time. The average diameter of CdSe QDs produced by the reaction immediately after nucleation was more than 1.8 nm and increased to 5.0 nm. The increase in the average diameter was correlated with the progressive red shift of the optical absorption and emission spectra, towards those of the bulk material. Synthesis of minimal-size CdSe QDs was performed under selected synthesis conditions via fast termination of QD growth with liquid nitrogen after 30 s of QD growth. Further high-performance purification, including SEC, allowed the isolation of ultrasmall (1.5-nm) QD cores. On the basis of CdSe-wurtzite crystallographic data and analysis of the morphology and optical properties of CdSe cores, we proposed a QD growth model that accurately simulated the NC formation process and predicted their optical properties. The effectiveness of the model was experimentally confirmed by synthesis of different size wurtzite-CdSe QDs.

In order to improve the optical and colloidal properties of CdSe QDs, the cores were capped with an epitaxial wide-bandgap shell. For the optimization of the synthesis conditions, the following parameters were investigated: the types of the cation and anion precursors, shell growth temperature regime, shell structure, and coating method. The CdSe QD growth model was used to calculate the precursor quantities necessary for the growth of an epitaxial shell with high accuracy. An epitaxial shell 3 ML in thickness was formed using Zn-EHA and thiourea as precursors in ODE / OLA as solvent / ligand mixture at 175°C. The highly crystalline core/shell structure allowed a significant increase in the colloidal stability and PL QY of ultrasmall QDs (the latter, up to 69%).

To achieve the maximum PL QY, we developed a new structure of highly luminescent QDs based on charge carrier confinement engineering. Specifically, we have synthesized novel CdSe/ZnS/CdS/ZnS core/multishell QDs, which benefit from both a high barrier potential of the first ZnS ML enhanced by a strong quantum confinement effect in the shell and a moderate total shell thickness (3 ML), which is, however, sufficient for reliable protection of excited carriers from the environment.

We have synthesized three batches of CdSe/ZnS/CdS/ZnS QDs with different core sizes and emission at different wavelengths and analyzed their one- and two-photon photoluminescence properties. The results showed that core/multishell QDs of different sizes exhibited a PL QY close to 100% in the one-photon mode significantly surpassing the QDs with classical shell structures as well as in two-photon mode TPECS values considerably exceeding those of CdSe QDs and are comparable with the best known CdSe/ZnS samples.

For biological applications, these QDs were transferred from the organic medium into the aqueous solution. Solubilization of QDs was performed using a two-stage ligand exchange approach taking into account the peculiarities of ultrasmall QDs. At the first stage, hydrophobic ligands were exchanged for DL-cysteine; at the second stage, DL-cysteines were exchanged for a mixture of two PEG derivatives. In order to achieve a complete QD surface passivation with water-soluble ligands, we calculated the necessary ligand quantity with the use of the proposed QD growth model. This approach allowed calculating and obtaining a dense organic shell on the QD surface, which ensured high colloidal stability for more than 6 months and prevented quenching of PL in aqueous media. The terminal carboxyl groups of the ligand shell made QDs suitable for further functionalization with the AL.

4. Chapter 4. Synthesis and structural and biological functional characterization of 4,5,9-trisubstituted acridine derivatives

4.1. Synthesis of 4,5,9-trisubstituted acridine derivatives

The purpose of this chapter was to synthesize a pharmacological agent that could effectively stabilize DNA G-quadruplexes and would be suitable for conjugation with water-soluble QDs. To do this, it was necessary to synthesize a series of compounds with a potential to stabilize the G-quadruplex DNA structure, compare the biological activities of molecules with different substitutes, and find the most active one for further conjugation with QDs.

As it was shown previously, polyaromatic nitrogen-containing derivatives, with their planar structure and partial positive charge of the heteroatom, are effective agents for interaction with G-quadruplexes. The synthesis of acridine and its analogues has attracted considerable attention from organic and medicinal chemists for many years, after some natural sources were reported to have an acridine-based skeleton. Acridine and its homologues are stable, weakly basic compounds. Acridine has a pKa of 5.6. The chemistry of acridine is very diverse and well studied. Acridine exhibits variable regioselectivity towards nucleophiles. Usually, substituents are introduced into acridine scaffolds by selection of appropriate precursors during the ring formation or already formed scaffolds. Acridines substituted at position C-9 are easy to obtain through aromatic nucleophilic substitutions. The acridine derivative is obtained by direct reaction of a nucleophile with activated acridine or reaction of a strong nucleophile with C-9 unsubstituted acridine in the presence or absence of a hydride ion scavenger. Substituent introduction at positions C-3,6 and C-4,5 are also well studied. For example, the 3,6,9-trisubstituted acridine compound BRACO-19 is one of the reference compounds used to search for optimal structures and characterized by both a high affinity and a high selectivity for the G-quadruplex. In addition, there is a wide variety of BRACO-19 analogues, such as AS1410 (14), with different side chain substituents (primary and secondary amines, benzylamines, acylamines, and others).

Special attention is being paid to unbranched polyamines. Polyamines are positively charged at physiological pH, with amino groups separated by 3 or 4 carbon atoms. They are found ubiquitously in all living cells; the most common naturally occurring polyamines are putrescine, spermidine, and spermine [235]. These polyamines are biosynthesized in most cell types, where they are necessary for optimal growth and replication of all cells by influencing the transcriptional and translational stages of protein synthesis and by altering the intracellular levels of free calcium, which suggests their roles as intracellular messengers and stabilizers of conformations of nucleic acids [253]. Cellular polyamines originate mainly from intracellular

biosynthesis or uptake from the extracellular environment via transporters. In addition, the terminal amine group of the ligand is an effective site for conjugation with QD by means of carbodiimide chemistry. This approach provides a high selectivity of coupling and reliability due to the formation of a peptide bond. This approach has already been developed with several cytotoxic substances. Among the three naturally occurring polyamines, putrescine has the smallest size and high biocompatibility.

Thus, the target molecule comprises three parts: a heterocyclic acridine framework, functionalized with one of the three anilines (4-fluoroaniline, 3,4-difluoroaniline, *N,N*-dimethyl-*p*-phenylenediamine) at position C-9, and two symmetrical putrescine side chains at positions C-4,5. The proposed structure of the AL is shown in Figure 46. It was expected that the planar structure of the acridine would interact with DNA base pairs, while the aniline would bind to the negatively charged phosphate DNA backbone and also to bind DNA bases for better stabilization of the DNA G-quadruplex, and putrescine would increase the solubility of the agent in water and ensure conjugation with the carboxyl-functionalized QDs.

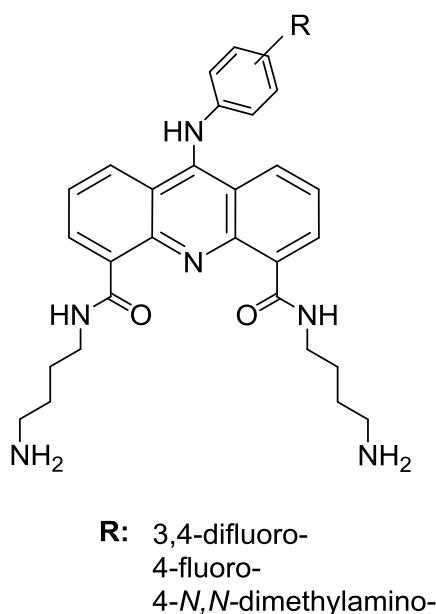


Figure 46: Proposed structure of the acridine ligand.

The synthetic pathway (Figure 47) included some steps and approaches that had been developed in the Institute of Molecular Chemistry at Reims, France, and had already been described in the literature. Similarly, the biological evaluations of acridines derivatives by the FRET and TRAP assays had already been developed [202]. The synthesis was carried out in seven consecutive reactions, starting from acridine. The key stage was the synthesis of the 4,5-disubstituted acridone intermediate. It was followed by substitution of C-4,5 with two putrescine chains, which had one terminal *tert*-butyloxycarbonyl protecting (Boc) group, and C-9

functionalization with one of the three anilines. The precursor for C-4,5 functionalization, Boc-protected putrescine, was obtained by adding di-tert-butyl dicarbonate (Boc_2O) to the primary amine in an alkaline aqueous medium.

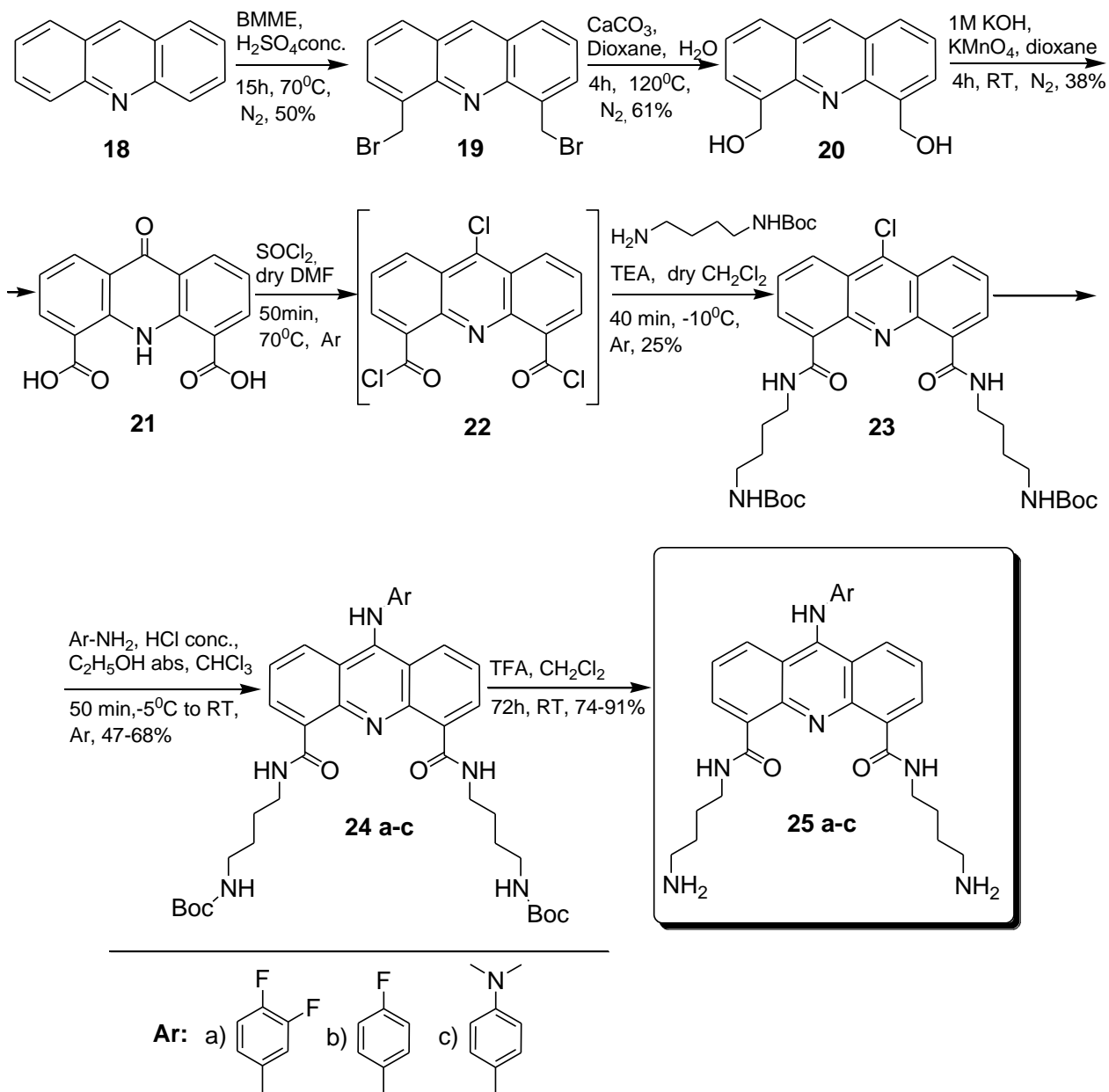


Figure 47: Synthetic pathway of 4,5,9-trisubstituted acridine derivatives.

In the first reaction, the electrophilic substitution at C-4,5 of the acridine ring of the original acridine (**18**) is performed under Tscherniac-Einhorn conditions using brommethylmethyl ether (BMME) in concentrated sulfuric acid [231,232]. This reaction yielded 4,5-bis(methylbromo)-substituted acridine (**19**) as the major product and monomethylbromo-

substituted acridine as the minor product. The dibrominated crude product was not well soluble in organic solvents and was recrystallized in diethyl ether without any additional purification. The presence of **(19)** was confirmed only by ^1H NMR spectroscopy using DMSO-d_6 . This reaction had a yield of 56 %.

The next step of the synthesis involves the well-described SN_2 aliphatic substitution of two bromine atoms by hydroxyl groups under refluxing in aqueous/dioxane mixture for better solubility of the reagent and the product. Side products and impurities were eliminated by column chromatography. NMR spectra provided clear evidence for the anticipated product. Signals of **(20)** in the aromatic region remained almost the same as for the dibrominated product **(19)**. A multiplet of overlapping signals from two hydroxyl groups was observed at 5.38–5.27 ppm. After purification, the anticipated product was collected in 60% yield.

Then, the dihydroxylated compound **(20)** was oxidized under basic conditions in the presence of the excess of potassium permanganate. Not only hydroxyl groups were oxidized to acid functional groups, but also the whole acridine ring at position C-9 was oxidized to acridone. In the TLC assay, acridone is well distinguished because of intense fluorescence under UV irradiation. As the reaction proceeded, a brown precipitate of MnO_2 started to appear, which indicated an oxidation–reduction process. The solubility of the diacid product **(21)** is not very good in organic solvents but rather good in water. The formation of the desired product **(21)** was confirmed by ^1H NMR. The signal from acidic hydrogen atoms was seen as a broad singlet at 13.95 ppm. This reaction had an average yield of 36%.

In parallel, one of the two amine groups of putrescine **(26)** was protected with the *tert*-butyl group under mild conditions and in the presence of less than 1 eq. of Boc_2O [233–235]. This reaction had an average yield of 94%. The presence of the desired product **(27)** was confirmed by ^1H NMR. The signal from nine *tert*-butyl protons was seen as an intense peak at 1.43 ppm.

The next reactions of chlorination by SOCl_2 and further amidification are very sensitive to the condition and require strict compliance with the following protocol. The diacid compound **(21)** was allowed to react with thionyl chloride acting as a solvent under dry conditions with the formation of 9-chlorinated diacylchloride **(22)**. This compound is unstable and very sensitive to water traces leading by hydrolysis of **(22)** to the corresponding 9-chloro-acridine-4,5-dicarboxylic acid. For this reason, **(22)** was used for the next reaction without any purification or characterization. To a solution of **(22)** in dry dichloromethane in the presence of TEA at -10°C , Boc-putrescine **(27)** was added to obtain 9-chlorinated acridine with symmetrical putrescine substitutions at side chains at positions C-4 and C-5 **(23)**. This product was found to be relatively stable, but, during the reaction, a certain amount of 9-oxo substituted diamide was always

detected by TLC. The structure of the desired compound (**23**) was also confirmed by ^1H NMR spectroscopy in $\text{DMSO-}d_6$. The aromatic region consisted of triplet signals, which correspond to two amidic hydrogen atoms in the 6.86–6.75 ppm region. The aliphatic area was occupied by two quartets of pairs of methylene groups at 3.44 and 2.96 ppm. This anticipated structure was also confirmed by mass spectrometry analysis, the calculated and experimentally determined values being 642.19 and 642.6, respectively (Annex 1). Product (**23**) was obtained with a maximum overyield of 25% (from **21**) as a dark powder. A very low conversion or decomposition of the intermediate was always observed.

9-Chlorinated diamide (**23**) was subjected to nucleophilic aromatic substitution reaction with variously substituted anilines ((3,4-difluoroaniline (**26**), 4-fluoroaniline (**27**), and *N,N*-dimethyl-*p*-phenylenediamine (**28**)) in a mixture of chloroform and absolute ethanol with a catalytic amount of hydrochloric acid at a low temperature (-10°C). Side products and impurities were eliminated by column chromatography. Even after column chromatography, the analysis of NMR spectra was difficult due to the presence of side-product signals. Signals of aromatic aniline protons were observed in the aromatic region. The composition of (**24a-c**) was also confirmed by mass spectrometry analysis (Annexes 2,3). After purification, the anticipated product was collected with a yield of 47-68%, depending on the substituent.

Finally, the Boc protection groups of (**24a-c**) were cleaved with a 50-fold excess of TFA in dichloromethane. Side products and impurities were eliminated by column chromatography with $\text{CH}_2\text{Cl}_2/\text{MeOH}/\text{NH}_3\cdot\text{H}_2\text{O}$. The observed low yields in some cases were probably due to purification difficulties. The final products were unstable on silica gel during column chromatography in the alkaline medium of an aqueous solution of ammonia, which led to its partial decomposition. This resulted in a reduced reaction yield. In the case of high purity of the starting material, for example, (**24a**), the reaction mixture consisted of pure (**25a**) with a small residual of volatile TFA, which did not require additional column purification. Products (**25a-c**) were obtained with an average yield of 74-91%. The composition of (**25a-c**) was also confirmed by mass spectrometry analysis (Annexes 4,5).

Some NMR spectra of acridine derivatives with substitutions at positions 4,5 and 9 were poorly resolved in both CD_3OD and $\text{DMSO-}d_6$. The signals were often broad without splitting and hardly recognizable. Purification was carried out by column chromatography with a multicomponent eluent of composition $\text{CH}_2\text{Cl}_2/\text{MeOH}/\text{NH}_3\cdot\text{H}_2\text{O}$. In fact, the presence of several nitrogen atoms with different basicity required a careful elution with basic eluting solvent. In ^1H NMR spectra some signals in both aromatic and aliphatic region were multiplied, probably due to the presence of protonated and non-protonated forms. For this reason, all final compounds

(**25a-c**) were transferred to the hydrochloric acid salt form and in further experiments were used in this form. This manipulation also solved the problem of low stability and allowed to isolate the compounds in a more pure form, which was extremely important for biological evaluation.

4.2. Biochemical evaluation of 4,5,9-trisubstituted acridine derivatives

The screening of potential G-quadruplex ligands needs an inexpensive, reproducible, and quick assay to test G-quadruplex binding. The main methods used for this are presented above in the Chapter 1.3.2. To identify the interaction between a ligand and the quadruplex structure we need to measure the increase in the melting temperature of the G-quadruplex induced by the ligand by means of the FRET assay. The telomeric repeat amplification protocol is also commonly used to evaluate the telomerase activity in tissues or cell extracts, as well as to determine the telomerase inhibitory capacity of small molecules. The main advantage of these two tests over others is a low material consumption. The results of the two tests usually don't exhibited a simple correlation between G-quadruplex stabilization data. Therefore, in this research the study of the affinity of ligands to G-quadruplexes required two independent experiments.

Biochemical evaluation of the synthesized 4,5,9-trisubstituted acridine derivatives (**25a-c**) was carried out by using both assays. First, their G-quadruplex stabilization potential was determined by FRET melting experiments with telomeric sequence (F21D) using four ligand concentrations: 20, 10, 5, and 1 μM .

Changes in the FRET signal upon melting of a DNA probe (the telomeric sequence d[GGG(TTAGGG)₃] were observed under the following conditions (10 mM cacodylate buffer (pH 8.0), 0.1 M LiCl, and 5 mM KCl) [225]. All the three compounds had significant effects on the ΔT_m of the telomeric sequences at micromolar concentrations, which indicates a significant G-quadruplex complexing potential. We didn't observe significant difference in the stabilizing capacity in the ligand series; the ΔT_m value of the nucleotide was in the range of 10-12°C for compounds (**25a-c**) at a concentration of 1 μM and 37-38°C for 5 μM for (**25a,b**). Moreover, it was impossible to perform the FRET assay at higher ligand concentrations (10 and 20 μM) for all compounds of the series and for (**25c**) even at a concentration of 5 μM due to the limitation of the methods caused by strong staining of the solution. These values were rather low compared to the reference compound BRACO 19, which had $\Delta T_m = 29.1^\circ\text{C}$ at a concentration of 1 μM .

It should be noted that the results and efficiency of the FRET assay depend on the conformation structure of the G-quadruplex. Hence, cation-dependent FRET melting assays

revealed that the ligands are comparatively less effective in the case of the antiparallel G4 conformation.

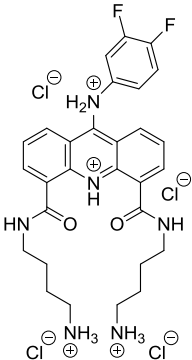
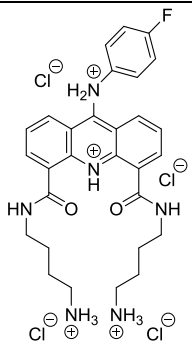
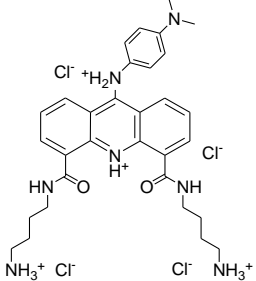
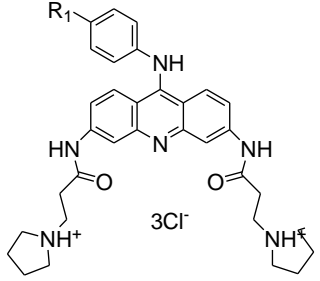
The second biological test used for the study of the ligands was the TRAP assay, measuring the ability of a ligand to block polymerase extension of telomeric sequences. This test allowed us to estimate the capacity of the acridine derivatives for inhibiting the telomerase enzyme activity. In this case, the enzymatic activity of telomerase was measured, which was directly proportional to the amount of the TTAGGG repeat. At the PCR step, two different primers were used. The first primer acted as a substrate for telomerase-mediated addition of the TTAGGG repeats, and the second primer was used as a reverse primer. G-quadruplex-interacting agents block telomerase extension through the stabilization of the G-quadruplex structure, which then inhibits the translocation step of the enzyme functioning. Because the formation of an intramolecular G-quadruplex requires at least four TTAGGG repeats in the portion of the primer that is not base-paired to the hTR RNA template, inhibition of the telomerase extension would be detectable after the synthesis of four TTAGGG repeats.

Acridine derivatives at a concentration of 5 mM were subjected to the assay. The summarized results of two experiments are shown in Table 8. All acridine derivatives displayed micromolar TRAP inhibitory potency. Two other acridine derivatives did not differ significantly in the telomerase inhibition activity. The IC_{50} values for **(25b)** and **(25c)** were 4.2 and 3.88 μ M, respectively. This result indicated that the type of aniline substituent at position C-9 of the acridine framework had no significant effect despite the different nature and hydrophilicity of the substituents of the aniline ring. BRACO 19 was included to serve as a reference. The best IC_{50} value of **(25c)**, 3.88 μ M, was lower than that of the reference product BRACO 19 (IC_{50} 0.09 μ M).

After that, the polyacrylamide gel retardation assay was performed with a mixture of the repeated guanine-rich G-quadruplex sequence and the potential inhibitor - synthesized ALs. Each compound were left at four different concentrations (1, 5, 10 and 20 μ M).

Lanes (1) and (2) correspond to control samples. The well (1) is blank, containing no telomerase or potential inhibitor; only the Taq polymerase enzyme required for the PCR has been introduced into the first well, as well as into all others. In well (2), there are Taq polymerase and the telomeric sequence. The following twelve lanes contain the tested compound (potential inhibitor) at a specified concentration, added to the mixture of lane (2): Taq polymerase and the telomeric sequence. The index **(25a-c)** corresponds to the designation of the synthesized ligand, below the numerical index corresponds to the ligand concentration (1, 5, 10, or 20 μ M). The image of the polyacrylamide gel is shown in Figure 48.

Table 8: Telomeric G-quadruplex stabilization measured by FRET and TRAP inhibition. “-“ colored solution.

Compound	FRET, ΔT_m				TRAP
	20 μM	10 μM	5 μM	1 μM	IC_{50} , μM
(25a)					-
(25b)					4.20
(25c)					3.88
BRACO 19					0.09

In two control lanes, no thin ladder bars are observed. In lane (1), there is only a large one, which corresponds to Taq polymerase. Lane (2) shows telomerase activity. Two spots, a large spot corresponding to the Taq polymerase activity and a small one corresponding to the telomere sequences, are seen. The following twelve lanes contain potential inhibitors added at a specified

concentration. Depending on the concentration and the inhibiting capacity of the ligand, more or fewer ladder bars can be observed. The thin ladders correspond to the formation of TTAGG nucleotides of different lengths that have migrated over different distances into the electrophoresis gel. The large ladder bar corresponding to the Taq polymerase activity is also observed.

Interpretation of the results is based on the assumption that the more active the compound is, the smaller the number of bars is; i.e., if a compound is active, the number of bars is decreased. For example, the ladder bars in all four lanes of **(25a)** indicate a low efficiency of telomerase inhibition in the given concentration range. For two other compounds, **(25b)** and **(25c)**, there are almost no ladder bars at concentrations of 5 μM and higher. This result clearly demonstrates the substantially higher inhibitory capacity of **(25b)** and **(25c)** compared to **(25a)**. Comparison of these differences and absolute values of IC_{50} shows that the gel retardation assay has a high sensitivity.

These results agree with those obtained using the FRET assay, where these three acridines exhibited high affinities for the telomeric G-quadruplex DNA sequences at a concentration of 1 μM , except for compound **(25a)**, which had a G-quadruplex affinity similar to those of **(25b)** and **(25c)** but **(25a)** did not inhibit the telomerase activity. This can be explained by the fluorescence of **(25a)**, which may have interfered with the ΔT_m measurement.

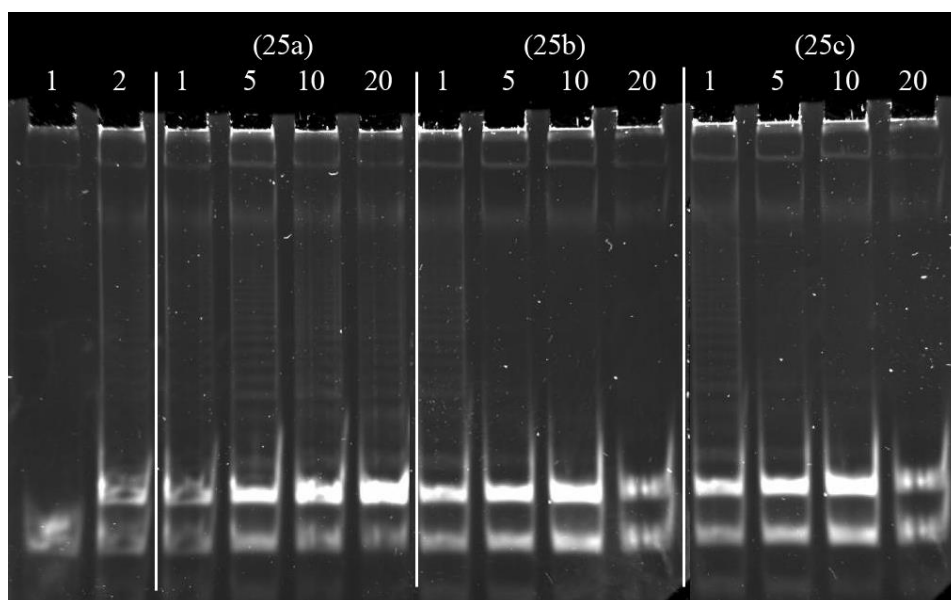


Figure 48: Gel retardation analysis of the binding of the potential inhibitors with the telomere nucleotide sequence. 1, Taq polymerase; 2, initial telomeric sequence with Taq polymerase; the remaining lanes contain the potential inhibitor at different concentrations and a mixture of the telomeric sequence with Taq polymerase.

Into all wells, Taq polymerase enzyme, required for PCR, has been introduced. Numerous thin ladder bars are observed, corresponding to the formation of TTAGG nucleotides of different lengths (depending on the number of sequences that the telomerase could add to the starting/initial sequence) that migrate over different distances into the electrophoresis gel. The following eight lanes contain the tested compound (potential inhibitor) added at a specified concentration.

The results of the FRET assay have confirmed those presented above: a strong inhibition of the telomerase activity by a compound observed using the TRAP assay requires its high affinity (high ΔT_m at a low concentration of the tested compound) for the telomeric-like sequence in G-quadruplexes observed in the FRET assay.

Summary

We have designed and synthesized three novel 4,5,9-trisubstituted acridine derivatives as potential telomerase inhibitors, by means of a seven-step synthesis starting from acridine. The synthesized structures have two symmetrical putrescine substitutions at positions C-4 and C-5 and one of three different anilines at position C-9. The putrescine residues provide better solubility in aqueous media and the possibility of conjugation with quantum dots. Also, we assume that putrescine provides vectorization and simplify penetration of the nanoprobe through the cell membrane. The aniline residues provide better interaction with G-quadruplexes by stacking with the G-quadruplexes. The synthetic procedure provides an overall yield from 1 - 2% (from acridine) of the final trisubstituted compounds (**25a-c**). The structure of the anticipated products was confirmed by ^1H NMR and high-resolution mass spectrometry.

The effectiveness of the interaction with the telomere G-quadruplex and the selectivity of telomerase inhibition have been confirmed by both FRET and TRAP assays, respectively. In the FRET assay, the ΔT_m of the duplex telomeres was 10-12°C for all ligands at a concentration of 1 μM . The telomerase inhibition capacities of the ligands have been estimated using the human telomeric DNA sequence. Among the three acridine derivatives, *N4,N5*-bis(4-aminobutyl)-9-(4-(dimethylamino)phenylamino)acridine-4,5-dicarboxamide (**25c**) has been found to have the highest sub-micromolar TRAP inhibitory activity ($\text{IC}_{50} = 3.88 \text{ mM}$). The results demonstrate that the synthesis procedure developed here afforded a G-quadruplex ligand suitable for conjugation with quantum dots.

5. Chapter 5. Engineering, properties and application of the PL nanoprobes.

5.1. Engineering of multifunctional nanoprobes

To make biomolecule useful for intracellular imaging the synthesised molecule need to be conjugated to PL QD without disturbing the biological function of this molecule. The water-soluble QDs stabilized with PEG-COOH were originally planned to be covalently bound with AL containing terminal amino groups using carbodiimide coupling, because this is one of the extensively used strategies for oriented molecule–molecule or molecule-QD conjugation. Covalent methods of conjugation involve the use of commercially available linkers, such as EDC and NHS, to conjugate carboxylic functional groups of ligands to the amine group of QDs or vice versa. The structure of AL was so designed as to provide conjugation with QDs.

However, we found that two QDs and acridine derivatives can form complexes even without a crosslinker in a neutral medium (phosphate buffer, 0.1 M, pH 7–8), which was detected due to an instantaneous change in QD PL intensity when the two components were mixed. The spontaneous formation of electrostatic complexes occurred instantaneously, whereas carbodiimide coupling with the EDC or NHS zero-length crosslinker took 2 h by the coupling methodology. Hence, although the covalent coupling may be thermodynamically favourable than electrostatic one, there is no reason to use it for the conjugation, because the difference between the reaction rates is too large.

The obtained electrostatic complexes were purified using GPC using the Sephadex G100 as the stationary carrier from unbound AL molecules. We found that Sephadex G100 had optimal molecular weight cut-off limits for the QDs than Sephadex G25 and Sephadex G200. The chromatogram of GPC purification of AL–QD electrostatic complexes using Sephadex G100 as the stationary carrier is shown in Figure 49. The figure shows that the original QDs and electrostatic complexes are eluted similarly to pure QDs as a narrow band, while AL is not eluted. In order to estimate the efficiency of AL–QD binding, we compared the absorption spectra of the electrostatic complexes before and after GPC purification. The results showed that the ratio between the characteristic absorption maxima of AL and QD in the spectrum of the complex was not changed in the course of purification. Thus, the binding resulted in the formation of stable electrostatic complexes.

After that, the colloidal properties of the conjugates were analyzed using DLS. The formation of complexes resulted in a slight increase in the hydrodynamic size, from 11.2 to 14.7 nm. The size distribution pattern remained the same, which indicated the absence of aggregation

and a highly homogeneous distribution of the ligand molecules over the QD ensemble. The size distribution of the original QDs and the AL–QD complexes is shown in Figure 50. The zeta-potential of the QDs increased from -12.6 to -8.6 mV after AL binding. This could be explained by the change in the ligand composition on the QD surface. In addition to the carboxyl groups imparting a weak negative charge to the QD, acridine molecules appeared on the surface. They contain seven nitrogen atoms each, three of which are readily protonated (the primary amine groups of putrescine and the heteroatom in the acridine backbone). This led to a decrease in the negative surface charge of QDs because the positive charges of the amine groups compensated for it. The zeta-potential distribution of AL–QD complexes is shown in Figure 51.

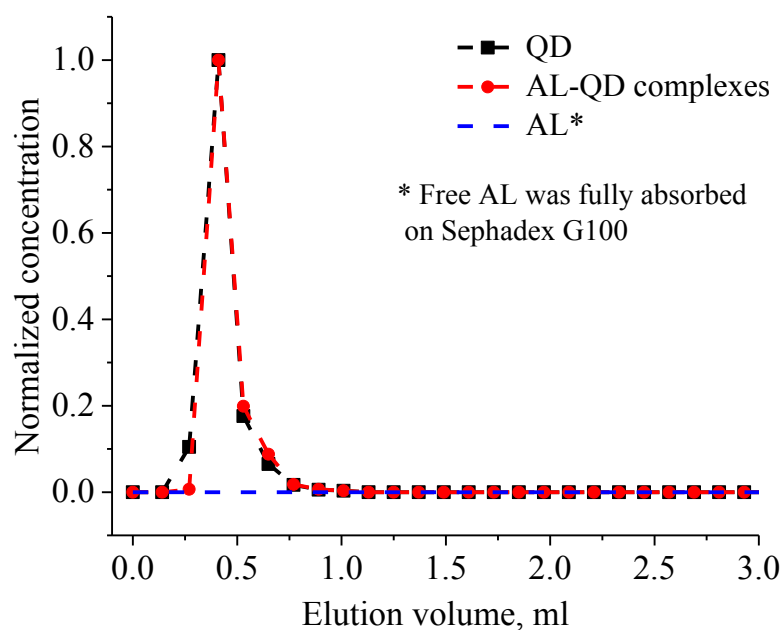


Figure 49: Elution chromatogram of acridine ligand (AL)–QD and their components. A GPC column with Sephadex G100 as a stationary phase.

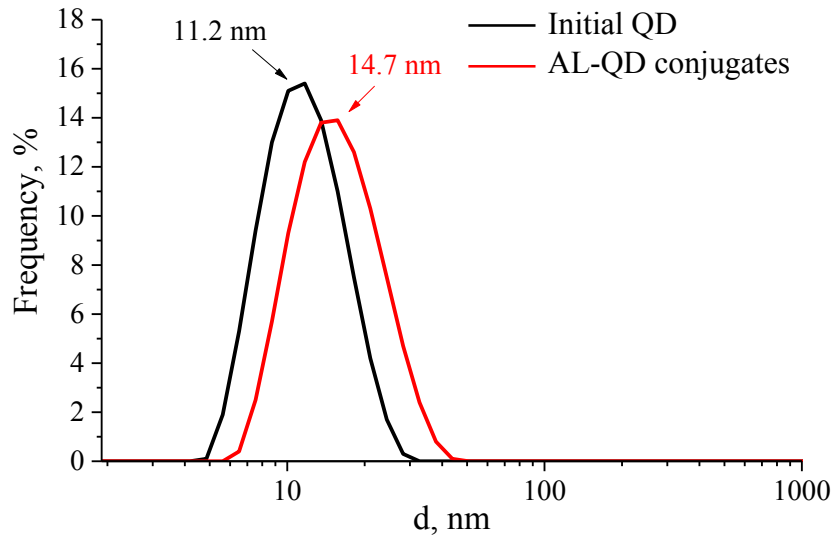


Figure 50: Size distribution of the original CdSe/ZnS QDs and AL-QD complexes in phosphate buffer (pH 8, 0.1 M).

	Mean (mV)	Area (%)	Width (mV)
Zeta Potential (mV): -8,56	Peak 1: -8,56	100,0	8,43
Zeta Deviation (mV): 8,43	Peak 2: 0,00	0,0	0,00
Conductivity (mS/cm): 0,206	Peak 3: 0,00	0,0	0,00

Result quality : Good

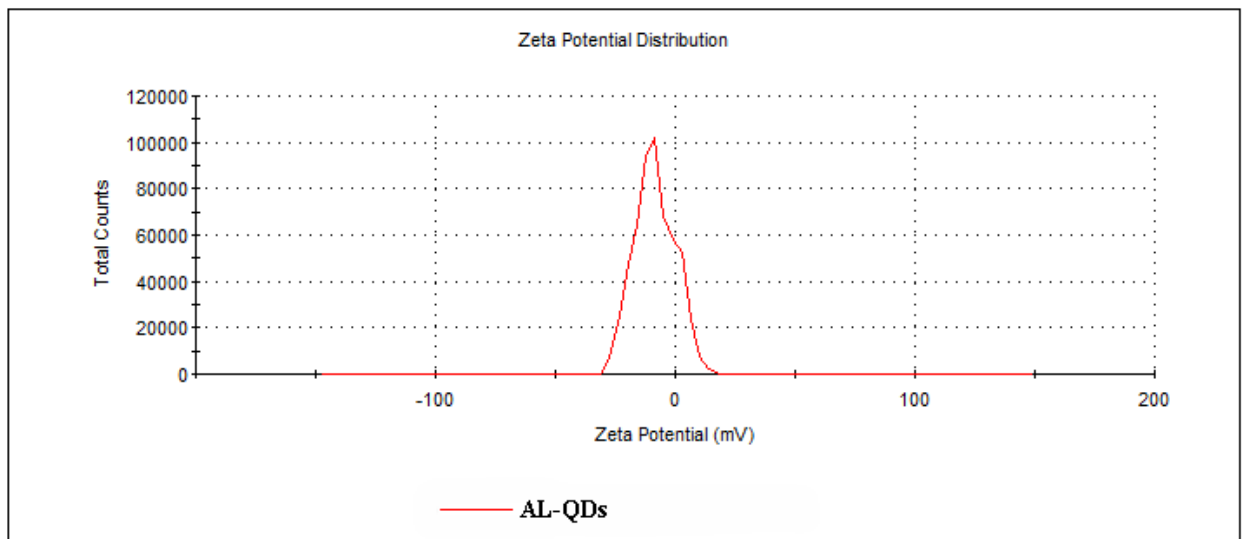


Figure 51: Zeta-potential distribution of AL-QD complexes.

5.2. Optical properties of nanoprobes

The molar ratio of the conjugate components was analyzed using absorption spectrometry. When the electrostatic complexes were formed, the absorption spectra of their components added up in proportion to the component concentrations in the mixture. The molar ratio between the ligand and QDs was determined from the change in the conjugate absorbance at the wavelength of the AL absorption peak (417 nm), given the molar attenuation coefficient of AL of $46000 \text{ M}^{-1}\cdot\text{cm}^{-1}$. As a result, we obtained a series of conjugates with the molecular excess of acridine over QDs ranging from 1 to 10.

The PL properties of the conjugates play an important role in their biological applications. Acridine-based ligands constitute an effective charge carrier transfer system because of their polyaromatic structure. The HOMO and LUMO energy levels of 4,5-acridine derivatives are comparable to those of semiconductor nanocrystals [254–256], which makes it possible to use these derivatives as hole-transporting materials in designing perovskite solar cells [254] and light-emitting diodes [257]. On the other hand, this charge transfer leads to the problem of QD fluorescence quenching [258,259] by photo-induced electron transfer (PET) [76]. This hampers the use of acridine derivatives as targeting agents in designing QD-based nanoprobes.

We studied the conjugation of AL to QDs from the viewpoint of the effects of inorganic shell structure and shell thickness of the CdSe-based core/shell QDs on the degree of fluorescence quenching. For investigation of this phenomenon, we used series of CdSe-based QDs coated with shells of different compositions (CdS and ZnS) and thicknesses in experiments on QD PL quenching by an excess of AL.

Specifically, we used CdSe-core QDs with a three-monolayer (3-ML) ZnS shell, a “giant” 5-ML ZnS shell, and a 3-ML ZnS/CdS/ZnS “multishell” (MS). The first type is a “classical” one-component wide-band-gap shell. The thickness of 3 ML provides sufficient protection of the charge carriers in CdSe cores in polar media. The “giant” shell makes it possible to suppress Auger recombination, and thereby to escape large nonradiative losses and to minimize the intermittency (“blinking”) of fluorescence from individual nanocrystals [50,107]. The MS, as we have shown previously, provides high localization of charges inside the fluorescent cores at a relatively low shell thickness [40]. The absorption and emission spectra of the phosphate buffer dispersions of the QDs used in the experiment are shown in Figure 52.

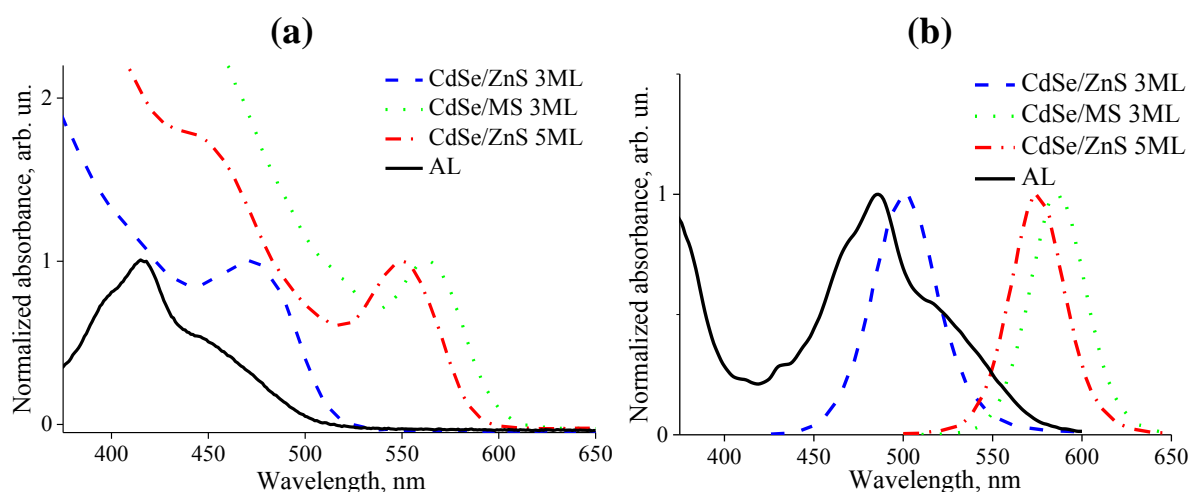


Figure 52: The (a) absorbance and (b) photoluminescence spectra of the acridine ligand (AL) and QDs with different shell structures and numbers of shell monolayers.

In our experiments, the solution of each type of QDs containing ~ 1 nmol ($1 \mu\text{M}$) of nanoparticles was titrated with 1 mg/ml stock solution of AL (**25a**) in 0.05 M phosphate buffer solution (pH 8.0). An example of the dependence of CdSe/ZnS/CdS/ZnS QDs fluorescence quenching on the amounts of excess AL is shown in Figure 53. Changes in quenching of PL of different QDs with an increase in the amount of excess AL is shown in Figure 54.

The light absorption by AL in the wavelength region between 300 and 450 nm is considered to be determined by the π - π transitions of the complex π -conjugated system of acridine [258]. The PL and absorption maxima of AL in an aqueous solution were observed at 417 and 487 nm, respectively, with a large Stokes shift of 60 nm. The aqueous solutions of the obtained QDs exhibited PL/absorbance maxima at 503/472 nm for CdSe/ZnS (3 ML), 572/551 nm for CdSe/ZnS (5 ML), and 584/563 nm for CdSe/MS. As can be seen from these spectra, the PL FWHM was close to 40 nm, which indicates size homogeneity of the QD ensembles studied. The small quantity of carboxyl groups on the surface of QDs provides a small negative surface charge (from -10 to -15 mV), which prevents aggregation of QDs. The hydrodynamic size of the QDs was found to be ~ 10 – 12 nm, which confirms monodispersity of the QDs in the solution. The physical diameters of the inorganic part of QDs were 4.3, 7, and 5 nm for CdSe/ZnS (3 ML), CdSe/ZnS (5 ML), and CdSe/MS, respectively, as calculated from the size of the core and the projected shell thickness using crystallographic data and detailed structural models of QDs. The diameter of the CdSe core was determined from an empirical calibration curve describing the relationship between the position of the first exciton transition in the optical absorption spectrum and the size of QDs [214].

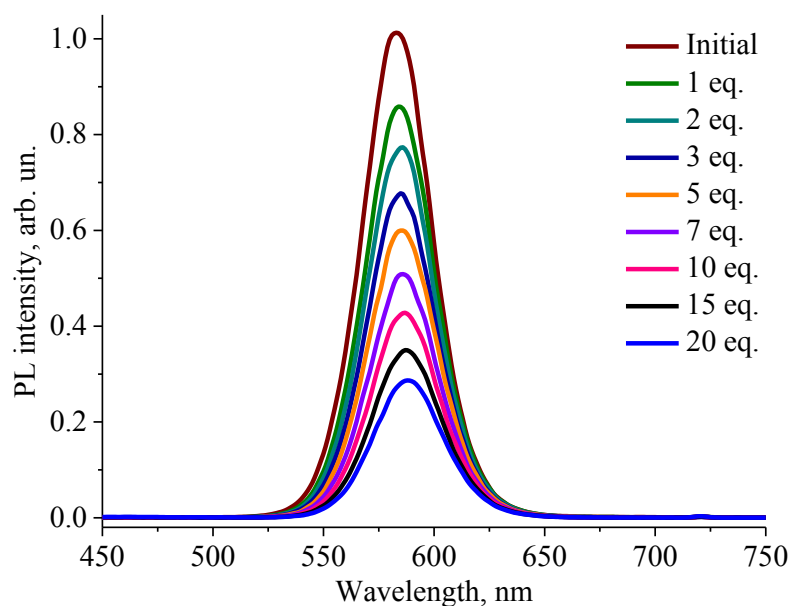


Figure 53: Dependence of CdSe/ZnS/CdS/ZnS QDs fluorescence quenching on the amounts of excess AL.

Titration of the QD solution with AL leads to quenching of the PL of all QDs studied. It can be seen that typical CdSe/ZnS QDs ($d \approx 4.3$ nm) with a 3-ML shell were completely quenched by addition of only 5 molar equivalents of acridine, whereas QDs with a “giant” (5-ML) ZnS shell ($d \approx 7$ nm) and QDs with a ZnS/CdS/ZnS MS with a total shell thickness of 3 ML ($d \approx 5$ nm) exhibited a smaller degree of fluorescence quenching even when the QD-to-acridine ratio reached 35. Thus, both MS and “giant” shell types provide more efficient protection of excited charge carriers in QDs from the quencher ligands than the “classic” thin ZnS shells. However, MS QDs are considerably smaller in physical size, which makes them more preferable as components of nanoprobe, because they could ensure better tissue and cell penetration.

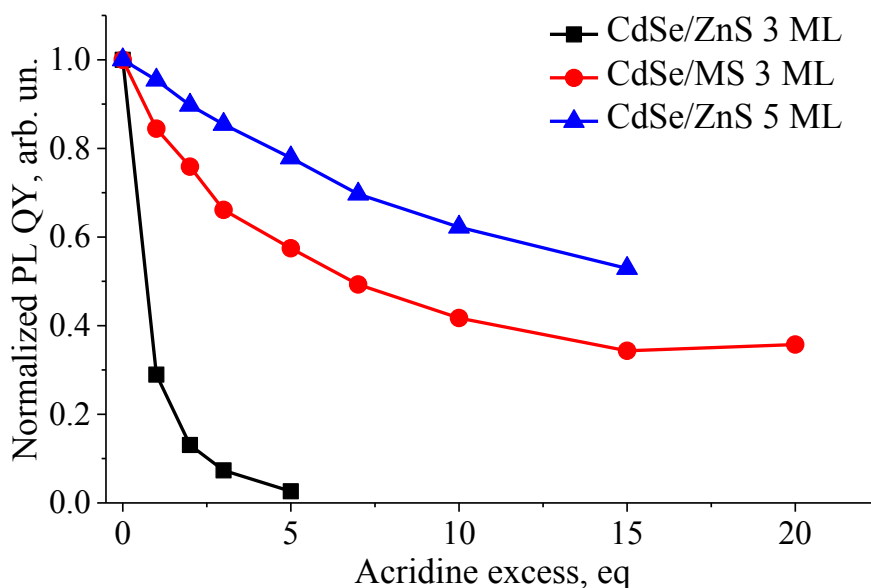


Figure 54: Changes in quenching of PL of different QDs with an increase in the amount of excess AL.

Charge transfer from QDs to ligand molecules leads to positive or negative charging of QDs and, as a consequence, quenching of QD PL. We suppose that in the system studied, quenching is caused by electron transfer from QD to AL because of the proximity of LUMO energy levels of both components. Schematic illustration of the photoinduced electron transfer (PET) mechanism from the core/shell QD to the AL is shown in Figure 55. The LUMO level of AL is slightly lower than that of the CdSe core, which indicates that AL has favourable energetics for electron extraction from the QD, which leads to charging of the QD and quenching of PL. However, the probability of PET varies for different shell structures, because every type of shell used in our experiments has its own barrier potential and length. In the case of the “classical” 3-ML ZnS shell, the barrier potential is sufficiently high to protect CdSe cores from the environment but fails to prevent PET when it is favourable, as in our case.

In a “giant” 5-ML ZnS shell, the value of the barrier can be considered to be the same, but the tunnelling length for the electron is higher. Thus, PET is much less effective in QDs shelled with 5 ML of ZnS. Regarding the MS QDs, the quantum confinement effect comes into place when the inner ZnS layer (as well the other two layers) is sufficiently thin, leading to an increase in the confinement potential compared to the thick ZnS shell. As can be seen, our approach to creating the confinement potential by engineering an MS structure allows us to suppress PET with high efficiency.

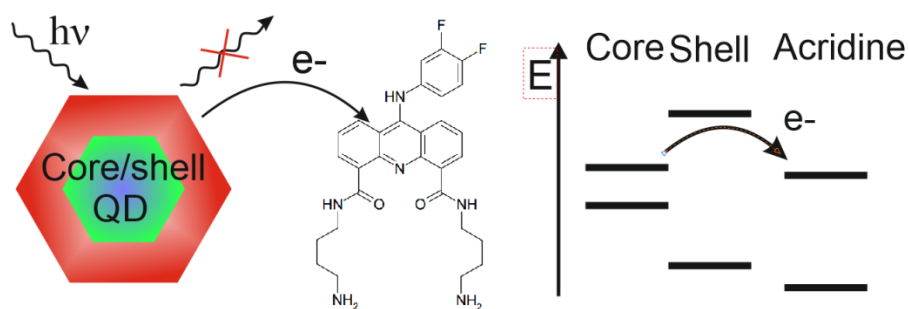


Figure 55: Schematic illustration of the photoinduced electron transfer mechanism from a core/shell QD to the acridine ligand.

We have studied the optical characteristics of the QD–AL electrostatic complex and found that the absorption spectra of their two components are additive. The molar absorption coefficient of AL in the aqueous medium has been determined, which has allowed us to calculate the precise molar ratio between the components in the complex.

We have found that the QD shell structure plays the decisive role in photoinduced electron transfer from the QD to the acridine ligand, which leads to quenching of QD PL. The ZnS/CdS/ZnS MS structure has been shown to provide the minimal reduction of the PL QY at the minimal shell thickness compared to the classical thin ZnS and “giant” shells. Thus, the CdSe/ZnS/CdS/ZnS core/MS QDs could be an optimal choice for engineering small-sized acridine-based fluorescent labels for tumor diagnosis and treatment systems.

It has been found that the formation of conjugates is accompanied by fluorescence quenching of QDs. The degree of quenching is mainly determined by the shell structure, the effect of the QD size being negligible. MS QDs with a highly efficient charge carrier confinement are significantly less susceptible to a decrease in PL QY as compared to QDs with both the classical ZnS thin shells and “giant” ZnS shells. Based on the analysis of QD band edge positions, we assume that the photoinduced charge transfer from the QD to the AL is responsible for the observed fluorescence quenching.

5.3. Toxicity and cellular uptake of nanoprobes and components

5.3.1. Assessment of cytotoxicity by cell viability assay

It is critical to understand the QD toxicity and its mechanisms for the development of the practical biological and biomedical applications of QDs in imaging, diagnosis, and therapy. However, it is difficult to compare the available studies and draw unambiguous conclusions from them, because they use different QDs, cell lines, and analytic methods. The synthetic methods and surface modifications of QDs also strongly affect their physicochemical characteristic, interaction with the cell membrane, and subsequent uptake into the cells.

Before the functional evaluation of QDs, the half maximal inhibitory concentration (IC_{50}) of both components and the electrostatic conjugates were determined in order to evaluate the differences in cytotoxicity and estimate the operating QD concentration range. This analysis was performed *in vitro* using the cell viability assay (MTT assay) with monocytes. A human monocyte cell line was used because the cells have a high ability to uptake foreign objects, including nanoparticles and QDs, which also makes the cells a convenient model for investigation of the penetration of water-soluble QDs and biological imaging. The monocytes were incubated in the presence of QDs, AL, and conjugates at concentrations ranging from 10^{-3} to 10^{-11} M. The monocyte viability was determined after 24 h of incubation. As shown in Figure 56, the cell viability was decreased in a concentration-dependent manner. The graphically found IC_{50} values for AL, CdSe/ZnS QDs, and nanoprobes are shown in Table 9.

This has permitted us to identify the highest CdSe/ZnS QD concentration at which they can be regarded as reasonably safe, low toxic agents for cell culture applications. As seen from Figure 56 and Table 9, the QD toxicity is four orders of magnitude higher than that of AL; therefore, the concentrations of QDs as the most toxic component were used to set the working concentration limits in the subsequent experiments on cells.

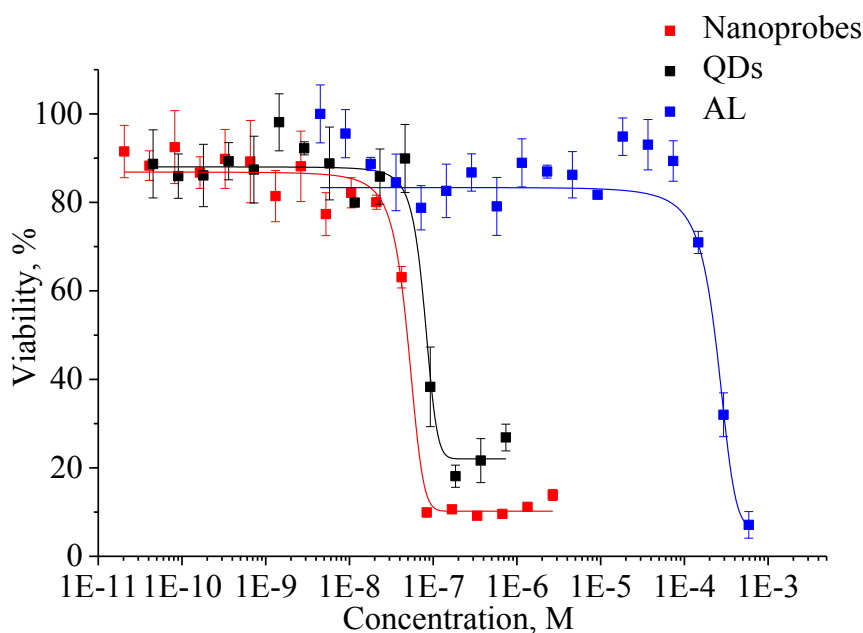


Figure 56: Cell viability in the presence of the conjugate and its components.

Table 9: Human monocyte viability

	AL	QD	Nanoprobe
IC₅₀, M*	$(2 \pm 0.11) \cdot 10^{-4}$	$(5 \pm 0.27) \cdot 10^{-8}$	$(8 \pm 0.15) \cdot 10^{-8}$

* The data represent the concentration of QD required to cause 50% reduction in cell viability (IC₅₀).

IC₅₀ of ultrasmall QDs was comparable to this value for structurally similar but larger QDs [260]. It is noteworthy that the toxic concentration of AL was lower than those reported earlier for most of other acridine derivatives (1-50 μM) [261-263]. The positive results of the biological evaluation of (25c) described in Chapter 4.2, as well as the low toxicity, compared to most analogues, make this compound a promising inhibitor of telomerase in cancer cells. However, this issue requires further biochemical studies.

5.3.2. Uptake analysis of ultrasmall CdSe/ZnS QDs *in vitro*

The obtained results on QD toxicity in a monocyte culture allow us to investigate CdSe/ZnS core/shell QDs *in vitro* by means of the localization assay using confocal laser microscopy. Analysis of the uptake of ultrasmall CdSe/ZnS QDs was performed to examine the capacity of the PEGelated water-soluble QDs for penetrating into cells while retaining their PL. Uptake experiments were carried on cells seeded on glass Petri dishes (as described above). Confocal fluorescence microscopy images (Figure 57) detected PL from the cells that was more

intense than the background PL of the extracellular medium. The results showed that QDs at a concentration of 0.5 μM were detectable inside the monocytes after 10 min of incubation.

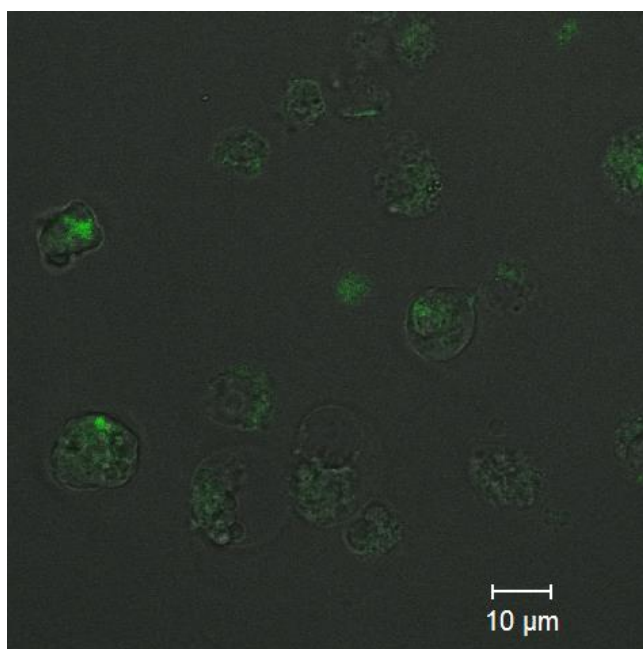


Figure 57: Confocal fluorescence microscopy images.

Summary

The nanoprobe of water-soluble QDs and acridine derivatives in the form of electrostatic complexes were prepared by directly mixing the two components at pH 7.2. Irreversible complex formation under neutral conditions was proved. The obtained electrostatic complexes were purified from low-molecular-weight compounds using gel-penetration chromatography and characterized by means of absorption spectrometry. We found that the formation of electrostatic complexes resulted in a significant quenching of the PL of CdSe/ZnS QDs caused by photoinduced electron transfer. We showed that the structure of the QD shell plays the key role in the characteristics of PL nanoprobe. The use of core/multishell QDs allows the fluorescence quenching to be considerably decreased due to highly efficient charge carrier confinement in the multishell structure.

We also preliminarily estimated the toxicity and the operating concentration ranges of ultrasmall QDs and acridine derivatives and electrostatic complexes by means of the MTT assay using human monocytes. We have found that the toxicity of the complexes is determined by the toxicity of QDs as the most toxic component of the system. It should be noted that the toxic concentration of AL is lower than those reported earlier for most of other acridine derivatives with apparent pharmacological activity. The positive results of the biological evaluation of (25c),

as well as the low toxicity, compared to most analogues, make this compound a promising inhibitor of telomerase in cancer cells.

Fluorescent cell imaging experiments have shown that ultrasmall (3.7-nm) QDs could rapidly penetrate into the cells after 10 min of incubation, with intense PL preserved. Thus, ultrasmall core/shell QDs can be used as fluorescent agents of compact probes for the development of systems for targeted delivery of antitumor acridine derivatives and diagnosis of cancer.

The development of these drug-delivery and diagnostic systems requires further comprehensive study of the behavior of the nanoprobe and their components *in vitro*.

The finding that QDs can penetrate into cultured monocytes without losing their fluorescent properties allows us to consider CdSe/ZnS core/shell QDs to be a useful tool for *in vitro* imaging of cellular processes, cancer cells detection, and development of drug delivery systems. Using QDs in imaging tools could bring cancer diagnosis to a new level due to the unique physico-chemical properties and the small size of QDs.

Conclusions and prospects

The results presented in this study demonstrate the feasibility of a new approach for the synthesis of ultrasmall QDs with the maximal PL QY, and high colloidal stability for engineering of PL pharmacological nanoprobe, based on QDs and novel acridine derivatives, displaying as potential inhibitors of telomerase activity in cancer cells.

The **first chapter** presents the literature overview, including the state-of-the-art engineering of PL probes based on organic dyes and QDs. The synthesis of core/shell QDs for biological applications and strategy of achieving the maximal PL QY by optimizing the shell structure are considered in detail. The main classes of nitrogen-containing polyaromatic organic compounds, including di- and trisubstituted acridine derivatives as the most promising G-quadruplex ligands are reviewed in detail. There is also a brief outlook on engineering conjugates of QDs and biomolecules and the problems of their colloidal stability and toxicity.

In the **second chapter**, detailed protocols and characterization methods used throughout this thesis are presented. A detailed description of the pathway of colloidal synthesis of high-quality core/shell QDs, the synthesis of 4,5,9-trisubstituted acridine derivatives, as well as the assembling of PL nanoprobe are described.

The **third chapter** deals with the synthesis of QDs. Ideal QDs for biological applications should be compact and have a bright PL and high colloidal stability. We have developed an advanced method for the synthesis of QDs smaller than 2 nm, which includes termination of the QD growth at the earliest stages by ultrafast freezing of the reaction mixture with liquid nitrogen followed by gel penetration chromatography for high-performance purification of the cores. An increase in the PL QY of these small QDs was achieved by growing an epitaxial shell. The traditional layer-by-layer shell growth model assuming a spherical geometry of QDs has significant drawbacks and does not allow precise control of QD growth. We have developed an advanced model of QD growth, which takes into account the crystallographic parameters of the material and the real geometry of QDs. The model is consistent with both literature and our own data, and it accurately predicts the optical properties of QDs and makes it possible to calculate the amounts of the precursors required for QD growth. The accuracy of the proposed model was experimentally confirmed by synthesis of a series of QDs to several successive growth stages in the size interval of 2.3–4.3 nm whose PL spectra overlap to encompass the entire visible range. The applicability of this model has been confirmed in experiments with epitaxial ZnS shell growth. Coating the minimal-sized cores with precisely three-monolayer-thick shells has yielded a highly uniform ultrasmall QDs with a PL QY of 70%. The high reproducibility of this method opens new horizons for the use of ultrasmall core/shell CdSe-based QDs in engineering compact PL nanoprobe for intercellular imaging.

The achieved PL efficiency of CdSe/ZnS QDs is not the maximum possible, which indicates that there are some drawbacks of the energy structure of the core/shell QDs. To solve this problem, we have developed the novel CdSe/ZnS/CdS/ZnS core/multishell structure with a highly efficient charge-carrier confinement. In this structure, the first one-monolayer ZnS shell provides the highest potential barrier for electron-hole pairs, thus ensuring the maximal photoluminescence emission outcome. The second, CdS shell with a significant potential barrier separates two ZnS monolayer shells and increases the shell thickness, thereby reducing the probability of charge-carrier tunnelling. The last ZnS shell creates an additional potential barrier and, in addition, is perfectly compatible with the common surface ligand exchange protocols for QD solubilization and functionalization for biomedical applications. The novel multishell structure has made it possible to increase the PL QY to more than 90% for all series of QDs of different sizes, which confirms the effectiveness of the new shell structure. The results presented in this chapter prove the effectiveness of the proposed novel approaches to the synthesis of bright ultrasmall QDs for biomedical applications.

The synthesis of small QDs at a low nucleation rate is inextricably related to the problem of the low yield of the reaction. The hot-injection synthesis procedure could be suitable for batch synthesis of QDs if not for the low reproducibility, which is the critical shortcoming of the approach. In addition, optimized reaction conditions can simplify the synthesis procedure, excluding the long and complex stages of nanoparticle treatment and isolation. This would ultimately increase the reproducibility of the techniques and reduce the time and cost of their preparation. For future work, combinations of different types of solvents, precursors, and surfactants can be tested in order to develop simple and reproducible methods of synthesis of high-quality QDs in batch quantities.

Also, the problems of blinking and quenching of PL caused by charge transfer inside QDs or by an external donor or acceptor as a pharmacological agent are significant disadvantages of all semiconductor QDs. Investigation of QD charging mechanisms and the search for new ways of their suppression will increase the stability of the PL of individual QDs, which, at the practical level, opens new prospects for systems of early diagnosis using the detection of signals from single QDs.

The **forth chapter** deals with the synthesis of 4,5,9-trisubstituted acridine derivatives that may have a high affinity for the DNA G-quadruplexes and inhibitory activity against telomerase enzyme, which is an important target of antitumor therapy. This potential biologically active component of the nanoprobe should meet the following basic requirements: (i) a high affinity for stabilized structures of telomeric DNA, the so-called G-quadruplexes, which is prerequisite for inhibiting the telomerase activity; (ii) the possibility of conjugation with the organic shell of QDs

through direct covalent binding with them. The hydrophilicity of the molecule, which provides solubility in an aqueous medium and does not lead to disturbance of the colloidal stability of the nanoprobe, is also an important requirement for the ligand.

The potential inhibitors were synthesized starting from the acridine framework, which was successively functionalized at positions 4 and 5 with putrescine chains and at position C-9 with an aniline moiety required for better stabilization of DNA G-quadruplexes. The two primary polyamine chains are supposed to increase the biocompatibility and to provide the possibility of conjugation with carboxyl-functionalized QDs. To increase the stability of the synthesized 4,5,9-trisubstituted acridine derivatives, we performed crystallization of the initial compounds under hydrochloride salts, which ensured the isolation of final compounds in a purer form, as well as increased their solubility in aqueous media. As a result, three 4,5,9-trisubstituted acridine derivatives were successfully synthesized and characterized.

We also investigated the synthesized acridine derivatives using the two most popular *in vitro* tests: (i) measurement of the affinity of the synthesized acridine derivatives for the telomeric G-quadruplex DNA sequence (FRET assay) and (ii) evaluation of the capacity of the acridine derivatives for inhibiting the telomerase enzyme activity (TRAP assay). The results of the biological evaluation showed high affinities of all synthesized molecules (25a-c) for the telomeric G-quadruplex DNA sequences at micromolar concentrations. In the second test, the telomerase inhibition capacities of the ligands were estimated using the human telomeric DNA sequence. Among the three acridine derivatives, compound (25c) has been found to have the highest micromolar TRAP inhibitory activity ($IC_{50} = 3.88$ mM), that is competitiveness result among modern acridine based analogs. Thus, our results have confirmed the successful synthesis of a potential pharmacological agent, and the assays based on biological evaluation allowed us to select the most active compound, which was subsequently used for the assembly of multifunctional nanoprobe.

We suppose that the alternative approach to the purification of the 4,5,9-trisubstituted acridine derivatives using C-8, C-18-modified resin for reverse phase chromatography is promising for purifying the final product, including purification in the cool-down mode. Solving the problem of the low stability of the intermediates and final trisubstituted acridine derivatives will provide an increase in the purity of the final products, which is crucial for further pharmacological investigation of the novel compounds. It is also important to search for an alternative, more stable and active class of organic compounds with high inhibitory activity towards telomerase in cancer cells as part of pharmacological nanoprobe.

The **fifth chapter** describes the synthesis and study of the PL nanoprobes of QDs and the synthesized acridine derivatives. The nanoprobes of water-soluble QDs and acridine derivatives in the form of electrostatic complexes were prepared by direct mixing of two components at pH 7.2. Irreversible complex formation under neutral conditions was proved. The obtained electrostatic complexes were purified from low-molecular-weight compounds using gel-penetration chromatography and characterized by means of absorption spectrometry. We found that the formation of electrostatic complexes resulted in a significant quenching of the PL of CdSe/ZnS QDs caused by photoinduced electron transfer. We showed that the structure of the QD shell plays the key role in the development of PL nanoprobes. The use of core/multishell QDs allows the fluorescence quenching to be considerably decreased due to highly efficient charge carrier confinement in the multishell structure.

Also, we preliminarily estimated the toxicity and the operating concentration range of ultrasmall QDs and acridine derivatives by means of the MTT assay using monocytes. We have found that the toxicity of ultrasmall QDs was comparable with the toxicity of larger QDs of the same structure, while the toxicity of acridine derivatives was substantially lower than those of other analogues and QDs.

Finally, confocal microscopy has been used to show that ultrasmall QDs penetrate into monocyte cells more rapidly than larger (6-nm) QDs while retaining their bright PL and colloidal stability.

Thus, miniaturization of QDs ensured accelerated penetration through the cell membrane and made ultrasmall QDs more attractive imaging agents than regular-sized QDs.

These results prove the effectiveness of the proposed approach to engineering multifunctional nanoprobes based on advanced QDs. Due to their small size and bright PL, the synthesized CdSe/ZnS QDs are convenient PL labels for a theranostics nanoprobe intended for imaging and rapid drug delivery into cells. Knowing that QDs are engulfed by a monocyte culture without losing their fluorescent properties allow us to consider CdSe/ZnS core/shell QDs to be a useful tool for *in vitro* imaging of cellular processes, cancer cells detection, and development of drug delivery systems. Using QDs in imaging tools could bring cancer diagnosis to another level due to the unique physical and chemical properties and small size of QDs.

Bibliography

1. Murray C.B., Kagan C.R., Bawendi M.G. Haracterization of monodisperse nanocrystals and close -packed nanocrystal assemblies // *Annu. Rev. Mater. Sci.* 2000. Vol. 30, № 1. P. 545–610.
2. Arcidiacono B., Iiritano S., Nocera A., Possidente K., Nevolo M.T., Ventura V., Foti D., Chiefari E., Brunetti A. Insulin resistance and cancer risk: An overview of the pathogenetic mechanisms // *Experimental Diabetes Research.* 2012. Vol. 2012. P. 789174.
3. Torchilin V. Intracellular delivery of protein and peptide therapeutics // *Drug Discov. Today Technol.* 2009. Vol. 5, № 2–3. P. e95–e103.
4. Hafian H., Sukhanova A., Turini M., Chames P., Baty D., Pluot M., Cohen J.H.M., Nabiev I., Millot J.-M. Multiphoton imaging of tumor biomarkers with conjugates of single-domain antibodies and quantum dots. // *Nanomedicine.* 2014. Vol. 10, № 8. P. 1701–1709.
5. Palmer A.J., Wallace H.M. The polyamine transport system as a target for anticancer drug development // *Amino Acids.* 2010. Vol. 38, № 2. P. 415–422.
6. Bray F., Ferlay J., Soerjomataram I., Siegel R.L., Torre L.A., Jemal A. Global cancer statistics 2018: GLOBOCAN estimates of incidence and mortality worldwide for 36 cancers in 185 countries // *CA. Cancer J. Clin.* 2018.
7. Hermann E.A., Ashburner J.M., Atlas S.J., Chang Y., Percac-Lima S. Satisfaction With Health Care Among Patients Navigated for Preventive Cancer Screening // *J. Patient Exp.* 2018. Vol. 5, № 3. P. 225–230.
8. Chen C., Peng J., Sun S.-R., Peng C.-W., Li Y., Pang D.-W. Tapping the potential of quantum dots for personalized oncology: current status and future perspectives // *Nanomedicine.* 2012. Vol. 7, № 3. P. 411–428.
9. Biju V., Mundayoor S., Omkumar R. V., Anas A., Ishikawa M. Bioconjugated quantum dots for cancer research: Present status, prospects and remaining issues // *Biotechnol. Adv.* 2010. Vol. 28, № 2. P. 199–213.
10. Prabhakar B., Shende P., Augustine S. Current trends and emerging diagnostic techniques for lung cancer // *Biomed. Pharmacother.* 2018. Vol. 106. P. 1586–1599.
11. Jacob L.J., Deigner H.-P. Nanoparticles and Nanosized Structures in Diagnostics and Therapy // *Precision Medicine.* Elsevier, 2018. P. 229–252.
12. Grigore A., Albulescu A., Albulescu R. Current methods for tumor-associated macrophages investigation // *J. Immunoass. Immunochem.* 2018. Vol. 39, № 2. P. 119–135.
13. Gan S.D., Patel K.R. Enzyme Immunoassay and Enzyme-Linked Immunosorbent Assay //

- J. Invest. Dermatol. 2013. Vol. 133, № 9. P. 1–3.
14. Resch-Genger U., Grabolle M., Cavaliere-Jaricot S., Nitschke R., Nann T. Quantum dots versus organic dyes as fluorescent labels // *Nat. Methods*. 2008. Vol. 5, № 9. P. 763–775.
 15. Beloglazova N.V., Speranskaya E.S., Wu A., Wang Z., Sanders M., Gofman V.V., Zhang D., Goryacheva I.Y., De Saeger S. Novel multiplex fluorescent immunoassays based on quantum dot nanolabels for mycotoxins determination // *Biosens. Bioelectron.* 2014. Vol. 62. P. 59–65.
 16. Zhang C., Han Y., Lin L., Deng N., Chen B., Liu Y. Development of Quantum Dots-Labeled Antibody Fluorescence Immunoassays for the Detection of Morphine // *J. Agric. Food Chem.* 2017. Vol. 65, № 6. P. 1290–1295.
 17. Yao J., Xing G., Han J., Sun Y., Wang F., Deng R., Hu X., Zhang G. Novel fluoroimmunoassays for detecting ochratoxin A using CdTe quantum dots // *J. Biophotonics*. 2017. Vol. 10, № 5. P. 657–663.
 18. SMITH A., DUAN H., MOHS A., NIE S. Bioconjugated quantum dots for in vivo molecular and cellular imaging // *Adv. Drug Deliv. Rev.* 2008. Vol. 60, № 11. P. 1226–1240.
 19. Xiao Z., Farokhzad O.C. Aptamer-Functionalized Nanoparticles for Medical Applications: Challenges and Opportunities // *ACS Nano*. 2012. Vol. 6, № 5. P. 3670–3676.
 20. Wang A.Z., Gu F., Zhang L., Chan J.M., Radovic-Moreno A., Shaikh M.R., Farokhzad O.C. Biofunctionalized targeted nanoparticles for therapeutic applications // *Expert Opin. Biol. Ther.* 2008. Vol. 8, № 8. P. 1063–1070.
 21. Kairdolf B.A., Smith A.M., Stokes T.H., Wang M.D., Young A.N., Nie S. Semiconductor Quantum Dots for Bioimaging and Biodiagnostic Applications // *Annu. Rev. Anal. Chem.* 2013. Vol. 6, № 1. P. 143–162.
 22. Chang J., Waclawik E.R. Colloidal semiconductor nanocrystals: controlled synthesis and surface chemistry in organic media // *RSC Adv.* 2014. Vol. 4, № 45. P. 23505–23527.
 23. Samokhvalov P., Artemyev M., Nabiev I. Basic Principles and Current Trends in Colloidal Synthesis of Highly Luminescent Semiconductor Nanocrystals // *Chem. - A Eur. J.* 2013. Vol. 19, № 5. P. 1534–1546.
 24. Chen O., Zhao J., Chauhan V.P., Cui J., Wong C., Harris D.K., Wei H., Han H.-S., Fukumura D., Jain R.K., Bawendi M.G. Compact high-quality CdSe-CdS core-shell nanocrystals with narrow emission linewidths and suppressed blinking. // *Nat. Mater.* 2013. Vol. 12, № 5. P. 445–451.
 25. Gao Y., Peng X. Photogenerated Excitons in Plain Core CdSe Nanocrystals with Unity

- Radiative Decay in Single Channel: The Effects of Surface and Ligands // *J. Am. Chem. Soc.* 2015. Vol. 137, № 12. P. 4230–4235.
26. Bilan R., Fleury F., Nabiev I., Sukhanova A. Quantum Dot Surface Chemistry and Functionalization for Cell Targeting and Imaging // *Bioconjug. Chem.* 2015. Vol. 26, № 4. P. 609–624.
 27. Brazhnik K., Sokolova Z., Baryshnikova M., Bilan R., Efimov A., Nabiev I., Sukhanova A. Quantum dot-based lab-on-a-bead system for multiplexed detection of free and total prostate-specific antigens in clinical human serum samples // *Nanomedicine Nanotechnology, Biol. Med.* 2015. Vol. 11, № 5. P. 1065–1075.
 28. Conroy E.M., Li J.J., Kim H., Algar W.R. Self-Quenching, Dimerization, and Homo-FRET in Hetero-FRET Assemblies with Quantum Dot Donors and Multiple Dye Acceptors // *J. Phys. Chem. C.* 2016. Vol. 120, № 31. P. 17817–17828.
 29. Chilvery A.K., Batra A.K., Yang B., Xiao K., Guggilla P., Aggarwal M.D., Surabhi R., Lal R.B., Currie J.R., Penn B.G. Perovskites: transforming photovoltaics, a mini-review // *J. Photonics Energy.* 2015. Vol. 5, № 1. P. 57402.
 30. Anikeeva P.O., Halpert J.E., Bawendi M.G., Bulović V. Quantum dot light-emitting devices with electroluminescence tunable over the entire visible spectrum. // *Nano Lett.* 2009. Vol. 9, № 7. P. 2532–2536.
 31. Dovzhenko D., Osipov E., Martynov I., Linkov P., Chistyakov A. Enhancement of Spontaneous Emission from CdSe/CdS/ZnS Quantum Dots at the Edge of the Photonic Band Gap in a Porous Silicon Bragg Mirror // *Phys. Procedia.* 2015. Vol. 73. P. 126–130.
 32. Adinolfi V., Sargent E.H. Photovoltage field-effect transistors // *Nature.* 2017. Vol. 542, № 7641. P. 324–327.
 33. Sousa A.A., Hohmann-Marriott M., Aronova M.A., Zhang G., Leapman R.D. Determination of quantitative distributions of heavy-metal stain in biological specimens by annular dark-field STEM. // *J. Struct. Biol.*, 2008. Vol. 162, № 1. P. 14–28.
 34. Grainger D.W., Castner D.G. Nanobiomaterials and Nanoanalysis: Opportunities for Improving the Science to Benefit Biomedical Technologies // *Adv. Mater.* 2008. Vol. 20, № 5. P. 867–877.
 35. Pu C., Qin H., Gao Y., Zhou J., Wang P., Peng X. Synthetic Control of Exciton Behavior in Colloidal Quantum Dots // *J. Am. Chem. Soc.* 2017. Vol. 139, № 9. P. 3302–3311.
 36. Boles M.A., Ling D., Hyeon T., Talapin D. V. The surface science of nanocrystals // *Nat. Mater.* 2016. Vol. 15, № 2. P. 141–153.
 37. Dubal D.P., Holze R. A successive ionic layer adsorption and reaction (SILAR) method to induce Mn₃O₄ nanopots on CNTs for supercapacitors // *New J. Chem.* 2013. Vol. 37, №

2. P. 403.
38. Sci C., Greytak A.B., Allen P.M., Liu W., Zhao J., Young E.R., Popovi Z., Walker B.J., Nocera D.G., Bawendi M.G., Popović Z., Walker B.J., Nocera D.G., Bawendi M.G. Alternating layer addition approach to CdSe / CdS core / shell quantum dots with near-unity quantum yield and high on-time fractions // *Chem. Sci.* 2012. Vol. 3, № 6. P. 2028–2034.
 39. Boldt K., Kirkwood N., Beane G.A., Mulvaney P. Synthesis of Highly Luminescent and Photo-Stable, Graded Shell CdSe/Cd_xZn_{1-x}S Nanoparticles by In Situ Alloying // *Chem. Mater.* 2013. Vol. 25, № 23. P. 4731–4738.
 40. Samokhvalov P., Linkov P., Michel J., Molinari M., Nabiev I. Photoluminescence quantum yield of CdSe-ZnS/CdS/ZnS core-multishell quantum dots approaches 100% due to enhancement of charge carrier confinement // *Colloid. Nanopart. Biomed. Appl.* IX. *Proceed. SPIE* / ed. Parak W.J., Osinski M., Yamamoto K.I. 2014. Vol. 8955. P. 89550S.
 41. Zhou J., Pu C., Jiao T., Hou X., Peng X. A Two-Step Synthetic Strategy toward Monodisperse Colloidal CdSe and CdSe/CdS Core/Shell Nanocrystals // *J. Am. Chem. Soc.* 2016. Vol. 138, № 20. P. 6475–6483.
 42. Wuister S.F., de Mello Donegá C., Meijerink A. Influence of Thiol Capping on the Exciton Luminescence and Decay Kinetics of CdTe and CdSe Quantum Dots // *J. Phys. Chem. B.* 2004. Vol. 108, № 45. P. 17393–17397.
 43. Jasprit Singh. *Physics of semiconductors and their heterostructures*. New York: McGraw-Hill, 1993.
 44. Lim S.J., Kim W., Jung S., Seo J., Shin S.K. Anisotropic Etching of Semiconductor Nanocrystals // *Chem. Mater.* 2011. Vol. 23, № 22. P. 5029–5036.
 45. Donegá C. de M. Synthesis and properties of colloidal heteronanocrystals // *Chem. Soc. Rev.* 2011. Vol. 40, № 3. P. 1512–1546.
 46. Lim S.J., Zahid M.U., Le P., Ma L., Entenberg D., Harney A.S., Condeelis J., Smith A.M. Brightness-equalized quantum dots // *Nat. Commun.* 2015. Vol. 6. P. 8210.
 47. Lee S.F., Osborne M.A. Brightening, Blinking, Bluing and Bleaching in the Life of a Quantum Dot: Friend or Foe? // *ChemPhysChem*. WILEY-VCH Verlag, 2009. Vol. 10, № 13. P. 2174–2191.
 48. Sukhanova A., Even-Desrumeaux K., Kisserli A., Tabary T., Reveil B., Millot J.-M., Chames P., Baty D., Artemyev M., Oleinikov V., Pluot M., Cohen J.H.M., Nabiev I. Oriented conjugates of single-domain antibodies and quantum dots: toward a new generation of ultrasmall diagnostic nanoprobe. // *Nanomedicine*. 2012. Vol. 8, № 4. P. 516–525.

49. Talapin D. V, Rogach A.L., Kornowski A., Haase M., Weller H. Highly Luminescent Monodisperse CdSe and CdSe/ZnS Nanocrystals Synthesized in a Hexadecylamine–Trioctylphosphine Oxide–Trioctylphosphine Mixture // *Nano Lett.* 2001. Vol. 1, № 4. P. 207–211.
50. Chen Y., Vela J., Htoon H., Casson J.L., Werder D.J., Bussian D.A., Klimov V.I., Hollingsworth J.A. ‘Giant’ multishell CdSe nanocrystal quantum dots with suppressed blinking. // *J. Am. Chem. Soc.* 2008. Vol. 130, № 15. P. 5026–5027.
51. Chen O., Zhao J., Chauhan V.P., Cui J., Wong C., Harris D.K., Wei H., Han H.-S., Fukumura D., Jain R.K., Bawendi M.G. Compact high-quality CdSe–CdS core–shell nanocrystals with narrow emission linewidths and suppressed blinking // *Nat. Mater.* Nature Research, 2013. Vol. 12, № 5. P. 445–451.
52. Peng Z.A., Peng X. Nearly Monodisperse and Shape-Controlled CdSe Nanocrystals via Alternative Routes: Nucleation and Growth // *J. Am. Chem. Soc.* 2002. Vol. 124, № 13. P. 3343–3353.
53. Park J., Joo J., Kwon S.G., Jang Y., Hyeon T. Synthesis of Monodisperse Spherical Nanocrystals // *Angew. Chemie Int. Ed.* 2007. Vol. 46, № 25. P. 4630–4660.
54. You H., Fang J. Particle-mediated nucleation and growth of solution-synthesized metal nanocrystals: A new story beyond the LaMer curve // *Nano Today.* 2016. Vol. 11, № 2. P. 145–167.
55. Yin Y., Alivisatos A.P. Colloidal nanocrystal synthesis and the organic–inorganic interface // *Nature.* 2005. Vol. 437, № 7059. P. 664–670.
56. Jun Y.-W., Lee J.-H., Choi J.-S., Cheon J. Symmetry-Controlled Colloidal Nanocrystals: Nonhydrolytic Chemical Synthesis and Shape Determining Parameters. 2005.
57. Wang F., Dong A., Buhro W.E. Solution–Liquid–Solid Synthesis, Properties, and Applications of One-Dimensional Colloidal Semiconductor Nanorods and Nanowires. 2016.
58. Alivisatos A.P., Peng X., Manna L., Yang W., Wickham J., Scher E., Kadavanich A. Shape control of CdSe nanocrystals // *Nature.* 2000. Vol. 404, № 6773. P. 59–61.
59. Rogach A.L. *Semiconductor Nanocrystal Quantum Dots* / ed. Rogach A.L. Vienna: Springer Vienna, 2008.
60. Peng X., Peng Z., Qu L. Synthesis of colloidal nanocrystals: pat. US6872249 B2 USA. US, 2000.
61. Donegá C. de M. Synthesis and properties of colloidal heteronanocrystals // *Chem. Soc. Rev.* 2011. Vol. 40, № 3. P. 1512–1546.
62. Page R.C., Espinobarro-Velazquez D., Leontiadou M.A., Smith C., Lewis E.A., Haigh

- S.J., Li C., Radtke H., Pengpad A., Bondino F., Magnano E., Pis I., Flavell W.R., O'Brien P., Binks D.J. Photoluminescence: Near-Unity Quantum Yields from Chloride Treated CdTe Colloidal Quantum Dots // *Small*. 2015. Vol. 11, № 13. P. 1482–1482.
63. Jing L., Kershaw S. V., Li Y., Huang X., Li Y., Rogach A.L., Gao M. Aqueous Based Semiconductor Nanocrystals // *Chem. Rev.* 2016. Vol. 116, № 18. P. 10623–10730.
64. Rakgalakane B.P., Moloto M.J. Aqueous Synthesis and Characterization of CdSe/ZnO Core-Shell Nanoparticles // *J. Nanomater.* 2011. Vol. 2011. P. 1–6.
65. Zhan H.J., Zhou P.J., He Z.Y., Tian Y. Microwave-assisted aqueous synthesis of small-sized, highly luminescent CdSeS/ZnS core/shell quantum dots for live cell imaging // *Eur. J. Inorg. Chem.* 2012. № 15. P. 2487–2493.
66. Kalasad M.N., Rabinal M.K., Mulimani B.G. Ambient Synthesis and Characterization of High-Quality CdSe Quantum Dots by an Aqueous Route // *Langmuir*. 2009. Vol. 25, № 21. P. 12729–12735.
67. Silva A.C.A., da Silva S.W., Morais P.C., Dantas N.O. Shell Thickness Modulation in Ultrasmall CdSe/CdS x Se $1-x$ /CdS Core/Shell Quantum Dots via 1-Thioglycerol // *ACS Nano*. 2014. Vol. 8, № 2. P. 1913–1922.
68. He Y., Lu H.-T., Sai L.-M., Lai W.-Y., Fan Q.-L., Wang L.-H., Huang W. Microwave-Assisted Growth and Characterization of Water-Dispersed CdTe/CdS Core-Shell Nanocrystals with High Photoluminescence // *J. Phys. Chem. B*. 2006. Vol. 110, № 27. P. 13370–13374.
69. Bao H., Gong Y., Li Z., Gao M. Enhancement Effect of Illumination on the Photoluminescence of Water-Soluble CdTe Nanocrystals: Toward Highly Fluorescent CdTe/CdS Core-Shell Structure // *Chem. Mater.* 2004. Vol. 16, № 20. P. 3853–3859.
70. Sobhani A., Salavati-Niasari M. CdSe nanoparticles: facile hydrothermal synthesis, characterization and optical properties // *J. Mater. Sci. Mater. Electron.* 2015. Vol. 26, № 9. P. 6831–6836.
71. Han H., Francesco G. Di, Maye M.M. Size Control and Photophysical Properties of Quantum Dots Prepared via a Novel Tunable Hydrothermal Route // *J. Phys. Chem. C*. 2010. Vol. 114, № 45. P. 19270–19277.
72. Jeong B.G., Park Y.-S.S., Chang J.H., Cho I., Kim J.K., Kim H., Char K., Cho J., Klimov V.I., Park P., Lee D.C., Bae W.K. Colloidal Spherical Quantum Wells with Near-Unity Photoluminescence Quantum Yield and Suppressed Blinking // *ACS Nano*. 2016. Vol. 10, № 10. P. 9297–9305.
73. Protière M., Nerambourg N., Renard O., Reiss P. Rational design of the gram-scale synthesis of nearly monodisperse semiconductor nanocrystals. // *Nanoscale Res. Lett.*

2011. Vol. 6, № 1. P. 472.
74. Li J.J., Wang Y.A., Guo W., Keay J.C., Mishima T.D., Johnson M.B., Peng X. Large-scale synthesis of nearly monodisperse CdSe/CdS core/shell nanocrystals using air-stable reagents via successive ion layer adsorption and reaction. // *J. Am. Chem. Soc.* 2003. Vol. 125, № 41. P. 12567–12575.
 75. Conde J., Dias J.T., Grazú V., Moros M., Baptista P. V, de la Fuente J.M. Revisiting 30 years of biofunctionalization and surface chemistry of inorganic nanoparticles for nanomedicine. // *Front. Chem.* 2014. Vol. 2, № July. P. 48.
 76. Bang J., Park J., Velu R., Yoon E., Lee K., Cho S., Cha S., Chae G., Joo T., Kim S. Photoswitchable quantum dots by controlling the photoinduced electron transfers // *Chem. Commun.* 2012. Vol. 48, № 73. P. 9174.
 77. Lee K.-H., Lee J.-H., Song W.-S., Ko H., Lee C., Lee J.-H., Yang H. Highly efficient, color-pure, color-stable blue quantum dot light-emitting devices. // *ACS Nano.* 2013. Vol. 7, № 8. P. 7295–7302.
 78. Asami H., Abe Y., Ohtsu T., Kamiya I., Hara M. Surface State Analysis of Photobrightening in CdSe Nanocrystal Thin Films // *J. Phys. Chem. B.* 2003. Vol. 107, № 46. P. 12566–12568.
 79. Ren C., Hao J., Chen H., Wang K., Wu D. Prepare core–multishell CdSe/ZnS nanocrystals with pure color and controlled emission by tri-n-octylphosphine-assisted method // *Appl. Surf. Sci.* 2015. Vol. 353. P. 480–488.
 80. Gao Y., Peng X. Crystal Structure Control of CdSe Nanocrystals in Growth and Nucleation: Dominating Effects of Surface versus Interior Structure // *J. Am. Chem. Soc.* 2014. Vol. 136, № 18. P. 6724–6732.
 81. Linkov P., Artemyev M., Efimov A.E., Nabiev I. Comparative advantages and limitations of the basic metrology methods applied to the characterization of nanomaterials // *Nanoscale.* 2013. Vol. 5, № 19. P. 8781.
 82. Xu S., Wang C., Xu Q., Zhang H., Li R., Shao H., Lei W., Cui Y. Key Roles of Solution pH and Ligands in the Synthesis of Aqueous ZnTe Nanoparticles // *Chem. Mater.* 2010. Vol. 22, № 21. P. 5838–5844.
 83. Luo J., Wei H., Li F., Huang Q., Li D., Luo Y., Meng Q. Microwave Assisted Aqueous Synthesis of Core–Shell CdSexTe1-x –CdS Quantum Dots for High Performance Sensitized Solar Cells // *Chem. Commun.* 2014. Vol. 50, № 26. P. 3464–3466.
 84. Lin Y.-W., Hsieh M.-M., Liu C.-P., Chang H.-T. Photoassisted Synthesis of CdSe and Core–Shell CdSe/CdS Quantum Dots // *Langmuir.* 2005. Vol. 21, № 2. P. 728–734.
 85. Peng X., Li J., Battaglia D., Wang Y.A., Wang Y. Monodisperse core/shell and other

- complex structured nanocrystals and methods of preparing the same: pat. US8900481 B2 USA. 2010.
86. Fu Y., Kim D., Jiang W., Yin W., Ahn T.K., Chae H. Excellent stability of thicker shell CdSe@ZnS/ZnS quantum dots // RSC Adv. 2017. Vol. 7, № 65. P. 40866–40872.
 87. Caldwell M.A., Albers A.E., Levy S.C., Pick T.E., Cohen B.E., Helms B.A., Milliron D.J. Driving oxygen coordinated ligand exchange at nanocrystal surfaces using trialkylsilylated chalcogenides // Chem. Commun. 2011. Vol. 47, № 1. P. 556–558.
 88. Lee K.-H., Lee J.-H., Kang H.-D., Park B., Kwon Y., Ko H., Lee C., Lee J., Yang H. Over 40 cd/A Efficient Green Quantum Dot Electroluminescent Device Comprising Uniquely Large-Sized Quantum Dots // ACS Nano. 2014. Vol. 8, № 5. P. 4893–4901.
 89. Liu H., Owen J.S., Alivisatos A.P. Mechanistic Study of Precursor Evolution in Colloidal Group II–VI Semiconductor Nanocrystal Synthesis // J. Am. Chem. Soc. 2007. Vol. 129, № 2. P. 305–312.
 90. Smith A.M., Nie S. Next-generation quantum dots // Nat. Biotechnol. 2009. Vol. 27, № 8. P. 732–733.
 91. Ghosh Y., Mangum B.D., Casson J.L., Williams D.J., Htoon H., Hollingsworth J.A. New Insights into the Complexities of Shell Growth and the Strong Influence of Particle Volume in Nonblinking ‘Giant’ Core/Shell Nanocrystal Quantum Dots // J. Am. Chem. Soc. 2012. Vol. 134, № 23. P. 9634–9643.
 92. Reiss P., Protière M., Li L. Core/Shell Semiconductor Nanocrystals // Small. Wiley Online Library, 2009. Vol. 5, № 2. P. 154–168.
 93. Zhou J., Zhu M., Meng R., Qin H., Peng X. Ideal CdSe/CdS Core/Shell Nanocrystals Enabled by Entropic Ligands and Their Core Size-, Shell Thickness-, and Ligand-Dependent Photoluminescence Properties // J. Am. Chem. Soc. 2017. Vol. 139, № 46. P. 16556–16567.
 94. Zeng Q., Kong X., Sun Y., Zhang Y., Tu L., Zhao J., Zhang H. Synthesis and Optical Properties of Type II CdTe/CdS Core/Shell Quantum Dots in Aqueous Solution via Successive Ion Layer Adsorption and Reaction // J. Phys. Chem. C. 2008. Vol. 112, № 23. P. 8587–8593.
 95. Allen P.M., Walker B.J., Bawendi M.G. Mechanistic Insights into the Formation of InP Quantum Dots // Angew. Chemie Int. Ed. 2010. Vol. 49, № 4. P. 760–762.
 96. Protière M., Reiss P. Facile synthesis of monodisperse ZnS capped CdS nanocrystals exhibiting efficient blue emission // Nanoscale Res. Lett. 2006. Vol. 1, № 1. P. 62–67.
 97. Dabbousi B.O., Rodriguez-Viejo J., Mikulec F. V., Heine J.R., Mattoussi H., Ober R., Jensen K.F., Bawendi M.G. (CdSe)ZnS Core–Shell Quantum Dots: Synthesis and

- Characterization of a Size Series of Highly Luminescent Nanocrystallites // *J. Phys. Chem. B.* 1997. Vol. 101, № 46. P. 9463–9475.
98. Lim S.J., Chon B., Joo T., Shin S.K. Synthesis and Characterization of Zinc-Blende CdSe-Based Core/Shell Nanocrystals and Their Luminescence in Water // *J. Phys. Chem. C.* 2008. Vol. 112, № 6. P. 1744–1747.
 99. Smith A.M., Nie S. Bright and Compact Alloyed Quantum Dots with Broadly Tunable Near-Infrared Absorption and Fluorescence Spectra through Mercury Cation Exchange // *J. Am. Chem. Soc.* 2011. Vol. 133, № 1. P. 24–26.
 100. Reiss P., Carayon S., Bleuse J., Pron A. Low polydispersity core/shell nanocrystals of CdSe/ZnSe and CdSe/ZnSe/ZnS type: preparation and optical studies // *Synth. Met.* 2003. Vol. 139, № 3. P. 649–652.
 101. Fitzmorris B.C., Cooper J.K., Edberg J., Gul S., Guo J., Zhang J.Z. Synthesis and Structural, Optical, and Dynamic Properties of Core/Shell/Shell CdSe/ZnSe/ZnS Quantum Dots // *J. Phys. Chem. C.* 2012. Vol. 116, № 47. P. 25065–25073.
 102. Linkov P., Krivenkov V., Nabiev I., Samokhvalov P. High Quantum Yield CdSe/ZnS/CdS/ZnS Multishell Quantum Dots for Biosensing and Optoelectronic Applications // *Mater. Today Proc.* 2016. Vol. 3, № 2. P. 104–108.
 103. Linkov P., Laronze-Cochard M., Sapi J., Sidorov L.N., Nabiev I. Multifunctional Nanoprobes for Cancer Cell Targeting, Imaging and Anticancer Drug Delivery // *Phys. Procedia.* 2015. Vol. 73. P. 216–220.
 104. Wang X., Ren X., Kahen K., Hahn M.A., Rajeswaran M., Maccagnano-Zacher S., Silcox J., Cragg G.E., Efros A.L., Krauss T.D. Non-blinking semiconductor nanocrystals // *Nature.* 2009. Vol. 459, № 7247. P. 686–689.
 105. Fomenko V., Nesbitt D.J. Solution Control of Radiative and Nonradiative Lifetimes: A Novel Contribution to Quantum Dot Blinking Suppression // *Nano Lett.* 2008. Vol. 8, № 1. P. 287–293.
 106. Hammer N.I., Early K.T., Sill K., Odoi M.Y., Emrick T., Barnes M.D. Coverage-mediated suppression of blinking in solid state quantum dot conjugated organic composite nanostructures // *J. Phys. Chem. B.* 2006. Vol. 110, № 29. P. 14167–14171.
 107. Razgoniaeva N., Moroz P., Yang M., Budkina D.S., Eckard H., Augspurger M., Khon D., Tarnovsky A.N., Zamkov M. One-Dimensional Carrier Confinement in ‘Giant’ CdS/CdSe Excitonic Nanoshells // *J. Am. Chem. Soc.* 2017. Vol. 139, № 23. P. 7815–7822.
 108. Vela J., Htoon H., Chen Y., Park Y.-S., Ghosh Y., Goodwin P.M., Werner J.H., Wells N.P., Casson J.L., Hollingsworth J.A. Effect of shell thickness and composition on blinking suppression and the blinking mechanism in ‘giant’ CdSe/CdS nanocrystal

- quantum dots. // *J. Biophotonics*. 2010. Vol. 3, № 10–11. P. 706–717.
109. Mahler B., Lequeux N., Dubertret B. Ligand-controlled polytypism of thick-shell CdSe/CdS nanocrystals. // *J. Am. Chem. Soc.* 2010. Vol. 132, № 3. P. 953–959.
 110. Rinehart J.D., Schimpf A.M., Weaver A.L., Cohn A.W., Gamelin D.R. Photochemical electronic doping of colloidal CdSe nanocrystals. // *J. Am. Chem. Soc.* 2013. Vol. 135, № 50. P. 18782–18785.
 111. García-Santamaría F., Chen Y., Vela J., Schaller R.D., Hollingsworth J.A., Klimov V.I. Suppressed Auger Recombination in ‘Giant’ Nanocrystals Boosts Optical Gain Performance // *Nano Lett.* 2009. Vol. 9, № 10. P. 3482–3488.
 112. Malko A. V, Park Y., Sampat S., Galland C., Vela J., Chen Y., Hollingsworth J.A., Klimov V.I., Htoon H. Pump-Intensity- and Shell-Thickness-Dependent Evolution of Photoluminescence Blinking in Individual Core/Shell CdSe/CdS Nanocrystals. 2011. P. 5213–5218.
 113. García-Santamaría F., Brovelli S., Viswanatha R., Hollingsworth J.A., Htoon H., Crooker S.A., Klimov V.I. Breakdown of Volume Scaling in Auger Recombination in CdSe/CdS Heteronanocrystals: The Role of the Core–Shell Interface // *Nano Lett.* 2011. Vol. 11, № 2. P. 687–693.
 114. Guo Y., Marchuk K., Sampat S., Abraham R., Fang N., Malko A. V., Vela J. Unique Challenges Accompany Thick-Shell CdSe/nCdS ($n > 10$) Nanocrystal Synthesis // *J. Phys. Chem. C*. 2012. Vol. 116, № 4. P. 2791–2800.
 115. Todescato F., Minotto A., Signorini R., Jasieniak J.J., Bozio R. Investigation into the Heterostructure Interface of CdSe-Based Core–Shell Quantum Dots Using Surface-Enhanced Raman Spectroscopy // *ACS Nano*. 2013. Vol. 7, № 8. P. 6649–6657.
 116. Mahler B., Spinicelli P., Buil S., Quelin X., Hermier J.-P., Dubertret B. Towards non-blinking colloidal quantum dots. // *Nat. Mater.* 2008. Vol. 7, № 8. P. 659–664.
 117. Fitzmorris B.C., Pu Y.-C., Cooper J.K., Lin Y.-F., Hsu Y.-J., Li Y., Zhang J.Z. Optical Properties and Exciton Dynamics of Alloyed Core/Shell/Shell Cd $1-x$ Zn x Se/ZnSe/ZnS Quantum Dots // *ACS Appl. Mater. Interfaces*. 2013. Vol. 5, № 8. P. 2893–2900.
 118. Regulacio M.D., Han M.-Y. Composition-Tunable Alloyed Semiconductor Nanocrystals // *Acc. Chem. Res.* 2010. Vol. 43, № 5. P. 621–630.
 119. Gaponik N., Talapin D. V., Rogach A.L., Hoppe K., Shevchenko E. V., Kornowski A., Eychmüller A., Weller H. Thiol-Capping of CdTe Nanocrystals: An Alternative to Organometallic Synthetic Routes // *J. Phys. Chem. B*. 2002. Vol. 106, № 29. P. 7177–7185.
 120. Chan W.C., Nie S. Quantum dot bioconjugates for ultrasensitive nonisotopic detection. //

- Science. 1998. Vol. 281, № 5385. P. 2016–2018.
121. Williams Y., Sukhanova A., Nowostawska M., Davies A.M., Mitchell S., Oleinikov V., Gun'ko Y., Nabiev I., Kelleher D., Volkov Y. Probing Cell-Type-Specific Intracellular Nanoscale Barriers Using Size-Tuned Quantum Dots // *Small*. 2009. Vol. 5, № 22. P. 2581–2588.
 122. Dubertret B., Banerjee A., Pons T., Lequeux N. Quantum dots-DNA bioconjugates: synthesis to applications // *Interface Focus*. 2016. Vol. 6, № 6. P. 20160064.
 123. Gerion D., Pinaud F., Williams S.C., Parak W.J., Zanchet D., Weiss S., Alivisatos A.P. Synthesis and Properties of Biocompatible Water-Soluble Silica-Coated CdSe/ZnS Semiconductor Quantum Dots // *J. Phys. Chem. B*. 2001. Vol. 105, № 37. P. 8861–8871.
 124. Deng Z., Lie F.L., Shen S., Ghosh I., Mansuripur M., Muscat A.J. Water-Based Route to Ligand-Selective Synthesis of ZnSe and Cd-Doped ZnSe Quantum Dots with Tunable Ultraviolet A to Blue Photoluminescence // *Langmuir*. 2009. Vol. 25, № 1. P. 434–442.
 125. Wu X., Liu H., Liu J., Haley K.N., Treadway J.A., Larson J.P., Ge N., Peale F., Bruchez M.P. Erratum: Immunofluorescent labeling of cancer marker Her2 and other cellular targets with semiconductor quantum dots // *Nat. Biotechnol.* 2003. Vol. 21, № 1. P. 41–46.
 126. Dubertret B. In Vivo Imaging of Quantum Dots Encapsulated in Phospholipid Micelles // *Science* (80-.). 2002. Vol. 298, № 5599. P. 1759–1762.
 127. Wegner K.D., Hildebrandt N. Quantum dots: bright and versatile in vitro and in vivo fluorescence imaging biosensors // *Chem. Soc. Rev.* 2015. Vol. 44, № 14. P. 4792–4834.
 128. Krug H.F., Wick P. Nanotoxicology: an interdisciplinary challenge. // *Angew. Chem. Int.* 2011. Vol. 50, № 6. P. 1260–1278.
 129. Bentzen E.L., Tomlinson I.D., Mason J., Gresch P., Warnement M.R., Wright D., Sanders-Bush E., Blakely R., Rosenthal S.J. Surface Modification To Reduce Nonspecific Binding of Quantum Dots in Live Cell Assays // *Bioconjug. Chem.* 2005. Vol. 16, № 6. P. 1488–1494.
 130. Smith A.M., Nie S. Minimizing the Hydrodynamic Size of Quantum Dots with Multifunctional Multidentate Polymer Ligands // *J. Am. Chem. Soc.* 2008. Vol. 130, № 34. P. 11278–11279.
 131. Parungo C.P., Ohnishi S., Kim S.-W., Kim S., Laurence R.G., Soltesz E.G., Chen F.Y., Colson Y.L., Cohn L.H., Bawendi M.G., Frangioni J. V. Intraoperative identification of esophageal sentinel lymph nodes with near-infrared fluorescence imaging // *J. Thorac. Cardiovasc. Surg.* 2005. Vol. 129, № 4. P. 844–850.
 132. Borse V., Kashikar A., Srivastava R. Fluorescence Stability of Mercaptopropionic Acid

- Capped Cadmium Telluride Quantum Dots in Various Biochemical Buffers // *J. Nanosci. Nanotechnol.* 2018. Vol. 18, № 4. P. 2582–2591.
133. Ensafi A.A., Nasr-Esfahani P., Rezaei B. Quenching-recovery fluorescent biosensor for DNA detection based on mercaptopropionic acid-capped cadmium telluride quantum dots aggregation // *Sensors Actuators B Chem.* 2017. Vol. 249. P. 149–155.
 134. Qi L., Gao X. Quantum Dot–Amphipol Nanocomplex for Intracellular Delivery and Real-Time Imaging of siRNA // *ACS Nano.* 2008. Vol. 2, № 7. P. 1403–1410.
 135. Sen D., Deerinck T.J., Ellisman M.H., Parker I., Cahalan M.D. Quantum Dots for Tracking Dendritic Cells and Priming an Immune Response In Vitro and In Vivo // *PLoS One.* 2008. Vol. 3, № 9. P. e3290.
 136. Derfus A.M., Chan W.C.W., Bhatia S.N. Probing the Cytotoxicity of Semiconductor Quantum Dots // *Nano Lett.* 2004. Vol. 4, № 1. P. 11–18.
 137. Xing Y., Chaudry Q., Shen C., Kong K.Y., Zhau H.E., Chung L.W., Petros J.A., O'Regan R.M., Yezhelyev M. V, Simons J.W., Wang M.D., Nie S. Bioconjugated quantum dots for multiplexed and quantitative immunohistochemistry // *Nat. Protoc.* 2007. Vol. 2, № 5. P. 1152–1165.
 138. Zhu Y., Hong H., Xu Z.P., Li Z., Cai W. Quantum dot-based nanoprobe for in vivo targeted imaging. // *Curr. Mol. Med.* 2013. Vol. 13, № 10. P. 1549–1567.
 139. Ag D., Bongartz R., Dogan L.E., Selecı M., Walter J.-G., Demirkol D.O., Stahl F., Ozcelik S., Timur S., Scheper T. Biofunctional quantum dots as fluorescence probe for cell-specific targeting. // *Colloids Surf. B. Biointerfaces.* 2014. Vol. 114. P. 96–103.
 140. Huo Q. A perspective on bioconjugated nanoparticles and quantum dots // *Colloids Surfaces B Biointerfaces.* 2007. Vol. 59, № 1. P. 1–10.
 141. Gladkovskaya O., Greaney P., Gun'ko Y.K., O'Connor G.M., Meere M., Rochev Y. An experimental and theoretical assessment of quantum dot cytotoxicity // *Toxicol. Res.* 2015. Vol. 4, № 5. P. 1409–1415.
 142. Rejman J., Nazarenus M., Jimenez de Aberasturi D., Said A.H., Feliu N., Parak W.J. Some thoughts about the intracellular location of nanoparticles and the resulting consequences // *J. Colloid Interface Sci.* 2016. Vol. 482. P. 260–266.
 143. Soenen S.J., Demeester J., De Smedt S.C., Braeckmans K. The cytotoxic effects of polymer-coated quantum dots and restrictions for live cell applications // *Biomaterials.* 2012. Vol. 33, № 19. P. 4882–4888.
 144. Martynenko I. V., Litvin A.P., Purcell-Milton F., Baranov A. V., Fedorov A. V., Gun'ko Y.K. Application of semiconductor quantum dots in bioimaging and biosensing // *J. Mater. Chem. B.* 2017. Vol. 5, № 33. P. 6701–6727.

145. Soenen S.J., Manshian B.B., Aubert T., Himmelreich U., Demeester J., De Smedt S.C., Hens Z., Braeckmans K. Cytotoxicity of Cadmium-Free Quantum Dots and Their Use in Cell Bioimaging // *Chem. Res. Toxicol.* 2014. Vol. 27, № 6. P. 1050–1059.
146. Štefančíková L., Porcel E., Eustache P., Li S., Salado D., Marco S., Guerquin-Kern J.-L., Réfrégiers M., Tillement O., Lux F., Lacombe S. Cell localisation of gadolinium-based nanoparticles and related radiosensitising efficacy in glioblastoma cells // *Cancer Nanotechnol.* 2014. Vol. 5, № 1. P. 6.
147. Mergny J.-L., Riou J.-F., Mailliet P., Teulade-Fichou M.-P., Gilson E. Natural and pharmacological regulation of telomerase. // *Nucleic Acids Res.* 2002. Vol. 30, № 4. P. 839–865.
148. Gomez D., Aouali N., Renaud A., Douarre C., Shin-Ya K., Tazi J., Martinez S., Trentesaux C., Morjani H., Riou J.-F. Resistance to senescence induction and telomere shortening by a G-quadruplex ligand inhibitor of telomerase. // *Cancer Res.* 2003. Vol. 63, № 19. P. 6149–6153.
149. White L.K., Wright W.E., Shay J.W. Telomerase inhibitors. // *Trends Biotechnol.* 2001. Vol. 19, № 3. P. 114–120.
150. Rocco L., Costagliola D., Stingo V. (TTAGGG)_n telomeric sequence in selachian chromosomes // *Heredity (Edinb).* 2001. Vol. 87, № 5. P. 583–588.
151. Artese A., Costa G., Distinto S., Moraca F., Ortuso F., Parrotta L., Alcaro S. Toward the design of new DNA G-quadruplex ligands through rational analysis of polymorphism and binding data // *Eur. J. Med. Chem.* 2013. Vol. 68. P. 139–149.
152. Robin J.D., Ludlow A.T., Batten K., Magdinier F., Stadler G., Wagner K.R., Shay J.W., Wright W.E. Telomere position effect: regulation of gene expression with progressive telomere shortening over long distances // *Genes Dev.* 2014. Vol. 28, № 22. P. 2464–2476.
153. Binz N., Shalaby T., Rivera P., Shin-ya K., Grotzer M.A. Telomerase inhibition, telomere shortening, cell growth suppression and induction of apoptosis by telomestatin in childhood neuroblastoma cells // *Eur. J. Cancer.* 2005. Vol. 41, № 18. P. 2873–2881.
154. Ivancich M., Schrank Z., Wojdyla L., Leviskas B., Kuckovic A., Sanjali A., Puri N. Treating Cancer by Targeting Telomeres and Telomerase // *Antioxidants.* 2017. Vol. 6, № 1. P. 15.
155. Luu K.N., Phan A.T., Kuryavyi V., Lacroix L., Patel D.J. Structure of the Human Telomere in K⁺ Solution: An Intramolecular (3 + 1) G-Quadruplex Scaffold // *J. Am. Chem. Soc.* 2006. Vol. 128, № 30. P. 9963–9970.
156. Franceschin M. G-quadruplex DNA structures and organic chemistry: More than one

- connection // *European J. Org. Chem.* 2009. № 14. P. 2225–2238.
157. Seenisamy J., Bashyam S., Gokhale V., Vankayalapati H., Sun D., Siddiqui-Jain A., Streiner N., Shin-ya K., White E., Wilson W.D., Hurley L.H. Design and Synthesis of an Expanded Porphyrin That Has Selectivity for the c-MYC G-Quadruplex Structure // *J. Am. Chem. Soc.* 2005. Vol. 127, № 9. P. 2944–2959.
 158. Campbell N.H., Parkinson G.N., Reszka A.P., Neidle S. Structural basis of DNA quadruplex recognition by an acridine drug // *J. Am. Chem. Soc.* 2008. Vol. 130, № 21. P. 6722–6724.
 159. Gellert G.C., Jackson S.R., Dikmen Z.G., Wright W.E., Shay J.W. Telomerase as a therapeutic target in cancer // *Drug Discov. Today* 2005. Vol. 2, № 2. P. 159–164.
 160. Shay J.W. Aging and cancer: are telomeres and telomerase the connection? // *Mol. Med. Today*. 1995. Vol. 1, № 8. P. 378–384.
 161. O’Sullivan R.J., Karlseder J. Telomeres: protecting chromosomes against genome instability // *Nat. Rev. Mol. Cell Biol.* 2010. Vol. 11, № 3. P. 171–181.
 162. Shamma M.A., Shmookler Reis R.J., Li C., Koley H., Hurley L.H., Anderson K.C., Munshi N.C. Telomerase inhibition and cell growth arrest after telomestatin treatment in multiple myeloma. // *Clin. Cancer Res.* 2004. Vol. 10, № 2. P. 770–776.
 163. Huang H.-S., Chou C.-L., Guo C.-L., Yuan C.-L., Lu Y.-C., Shieh F.-Y., Lin J.-J. Human telomerase inhibition and cytotoxicity of regioisomeric disubstituted amidoanthraquinones and aminoanthraquinones // *Bioorg. Med. Chem.* 2005. Vol. 13, № 5. P. 1435–1444.
 164. Burge S., Parkinson G.N., Hazel P., Todd A.K., Neidle S. Quadruplex DNA: Sequence, topology and structure // *Nucleic Acids Res.* 2006. Vol. 34, № 19. P. 5402–5415.
 165. Nersisyan L. Integration of Telomere Length Dynamics into Systems Biology Framework: A Review // *Gene Regul. Syst. Bio.* 2016. Vol. 10. P. GRSB.S39836.
 166. Monaghan P. Telomeres and life histories: the long and the short of it // *Ann. N. Y. Acad. Sci.* 2010. Vol. 1206, № 1. P. 130–142.
 167. Cuesta J., Read M., Neidle S. The Design of G-quadruplex Ligands as Telomerase Inhibitors // *Mini-Reviews Med. Chem.* 2003. Vol. 3, № 1. P. 11–21.
 168. Temime-Smaali N., Guittat L., Sidibe A., Shin-ya K., Trentesaux C., Riou J.-F. The G-Quadruplex Ligand Telomestatin Impairs Binding of Topoisomerase III α to G-Quadruplex-Forming Oligonucleotides and Uncaps Telomeres in ALT Cells // *PLoS One*. 2009. Vol. 4, № 9. P. e6919.
 169. Wang C., Carter-Cooper B., Du Y., Zhou J., Saeed M.A., Liu J., Guo M., Roembke B., Mikek C., Lewis E.A., Lapidus R.G., Sintim H.O. Alkyne-substituted diminazene as G-quadruplex binders with anticancer activities // *Eur. J. Med. Chem.* 2016. Vol. 118. P.

- 266–275.
170. Kim M.-Y., Vankayalapati H., Shin-ya K., Wierzba K., Hurley L.H. Telomestatin, a Potent Telomerase Inhibitor That Interacts Quite Specifically with the Human Telomeric Intramolecular G-Quadruplex // *J. Am. Chem. Soc.* 2002. Vol. 124, № 10. P. 2098–2099.
 171. Wei C., Jia G., Yuan J., Feng Z., Li C. A Spectroscopic Study on the Interactions of Porphyrin with G-Quadruplex DNAs // *Biochemistry*. 2006. Vol. 45, № 21. P. 6681–6691.
 172. Paramasivan S., Rujan I., Bolton P.H. Circular dichroism of quadruplex DNAs: Applications to structure, cation effects and ligand binding // *Methods*. 2007. Vol. 43, № 4. P. 324–331.
 173. Keating L.R., Szalai V.A. Parallel-Stranded Guanine Quadruplex Interactions with a Copper Cationic Porphyrin † // *Biochemistry*. 2004. Vol. 43, № 50. P. 15891–15900.
 174. Erra E., Petraccone L., Esposito V., Randazzo A., Mayol L., Ladbury J., Barone G., Giancola C. Interaction of porphyrin with G-quadruplex structures. // *Nucleosides. Nucleotides Nucleic Acids*. 2005. Vol. 24, № 5–7. P. 753–756.
 175. Redman J.E. Surface plasmon resonance for probing quadruplex folding and interactions with proteins and small molecules // *Methods*. 2007. Vol. 43, № 4. P. 302–312.
 176. Mazzitelli C.L., Brodbelt J.S., Kern J.T., Rodriguez M., Kerwin S.M. Evaluation of binding of perylene diimide and benzannulated perylene diimide ligands to dna by electrospray ionization mass spectrometry // *J. Am. Soc. Mass Spectrom.* 2006. Vol. 17, № 4. P. 593–604.
 177. Campbell N.H., Parkinson G.N. Crystallographic studies of quadruplex nucleic acids // *Methods*. 2007. Vol. 43, № 4. P. 252–263.
 178. Ragazzon P., Chaires J.B. Use of competition dialysis in the discovery of G-quadruplex selective ligands // *Methods*. 2007. Vol. 43, № 4. P. 313–323.
 179. De Cian A., Guittat L., Kaiser M., Saccà B., Amrane S., Bourdoncle A., Alberti P., Teulade-Fichou M.P., Lacroix L., Mergny J.L. Fluorescence-based melting assays for studying quadruplex ligands // *Methods*. 2007. Vol. 42, № 2. P. 183–195.
 180. Evison B.J., Phillips D.R., Cutts S.M. In vitro Transcription Assay for Resolution of Drug-DNA Interactions at Defined DNA Sequences // *Drug-DNA Interaction Protocols*. 2010. P. 207–222.
 181. Yan Y., Tan J., Ou T., Huang Z., Gu L. DNA G-quadruplex binders: a patent review // *Expert Opin. Ther. Pat.* 2013. Vol. 23, № 11. P. 1495–1509.
 182. Xiong Y.X., Huang Z.S., Tan J.H. Targeting G-quadruplex nucleic acids with heterocyclic alkaloids and their derivatives // *Eur. J. Med. Chem.* 2015. Vol. 97, № 1. P. 538–551.

183. Zhang S., Wu Y., Zhang W. G-Quadruplex Structures and Their Interaction Diversity with Ligands // *ChemMedChem*. 2014. Vol. 9, № 5. P. 899–911.
184. Kumar S., Bawa S., Gupta H. Biological Activities of Quinoline Derivatives // *Mini-Reviews Med. Chem.* 2009. Vol. 9, № 14. P. 1648–1654.
185. R. Solomon V., Lee H. Quinoline as a Privileged Scaffold in Cancer Drug Discovery // *Curr. Med. Chem.* 2011. Vol. 18, № 10. P. 1488–1508.
186. Guittat L., Alberti P., Rosu F., Van Miert S., Thetiot E., Pieters L., Gabelica V., De Pauw E., Ottaviani A., Riou J.-F., Mergny J.-L. Interactions of cryptolepine and neocryptolepine with unusual DNA structures // *Biochimie*. 2003. Vol. 85, № 5. P. 535–547.
187. Guyen B., Schultes C.M., Hazel P., Mann J., Neidle S. Synthesis and evaluation of analogues of 10H-indolo[3,2-b]quinoline as G-quadruplex stabilising ligands and potential inhibitors of the enzyme telomerase // *Org. Biomol. Chem.* 2004. Vol. 2, № 7. P. 981.
188. Zhou J.-L., Lu Y.-J., Ou T.-M., Zhou J.-M., Huang Z.-S., Zhu X.-F., Du C.-J., Bu X.-Z., Ma L., Gu L.-Q., Li Y.-M., Chan A.S.-C. Synthesis and Evaluation of Quindoline Derivatives as G-Quadruplex Inducing and Stabilizing Ligands and Potential Inhibitors of Telomerase // *J. Med. Chem.* 2005. Vol. 48, № 23. P. 7315–7321.
189. Zhou J.-M., Zhu X.-F., Lu Y.-J., Deng R., Huang Z.-S., Mei Y.-P., Wang Y., Huang W.-L., Liu Z.-C., Gu L.-Q., Zeng Y.-X. Senescence and telomere shortening induced by novel potent G-quadruplex interactive agents, quindoline derivatives, in human cancer cell lines // *Oncogene*. 2006. Vol. 25, № 4. P. 503–511.
190. Izbicka E., Wheelhouse R.T., Raymond E., Davidson K.K., Lawrence R.A., Sun D., Windle B.E., Hurley L.H., Von Hoff D.D. Effects of cationic porphyrins as G-quadruplex interactive agents in human tumor cells. // *Cancer Res.* 1999. Vol. 59, № 3. P. 639–644.
191. Lubitz I., Borovok N., Kotlyar A. Interaction of Monomolecular G4-DNA Nanowires with TMPyP: Evidence for Intercalation † // *Biochemistry*. 2007. Vol. 46, № 45. P. 12925–12929.
192. Han H., Langley D.R., Rangan A., Hurley L.H. Selective Interactions of Cationic Porphyrins with G-Quadruplex Structures // *J. Am. Chem. Soc.* 2001. Vol. 123, № 37. P. 8902–8913.
193. Parkinson G.N., Ghosh R., Neidle S. Structural Basis for Binding of Porphyrin to Human Telomeres †, ‡ // *Biochemistry*. 2007. Vol. 46, № 9. P. 2390–2397.
194. Wang P., Ren L., He H., Liang F., Zhou X., Tan Z. A Phenol Quaternary Ammonium Porphyrin as a Potent Telomerase Inhibitor by Selective Interaction with Quadruplex DNA // *ChemBioChem*. 2006. Vol. 7, № 8. P. 1155–1159.
195. Gonçalves D.P.N., Rodriguez R., Balasubramanian S., Sanders J.K.M.

- Tetramethylpyridiniumporphyrazines—a new class of G-quadruplex inducing and stabilising ligands // *Chem. Commun.* 2006. № 45. P. 4685–4687.
196. Tahara H., Shin-ya K., Seimiya H., Yamada H., Tsuruo T., Ide T. G-Quadruplex stabilization by telomestatin induces TRF2 protein dissociation from telomeres and anaphase bridge formation accompanied by loss of the 3' telomeric overhang in cancer cells // *Oncogene*. 2006. Vol. 25, № 13. P. 1955–1966.
 197. Minhas G.S., Pilch D.S., Kerrigan J.E., LaVoie E.J., Rice J.E. Synthesis and G-quadruplex stabilizing properties of a series of oxazole-containing macrocycles // *Bioorg. Med. Chem. Lett.* 2006. Vol. 16, № 15. P. 3891–3895.
 198. Rzuczek S.G., Pilch D.S., LaVoie E.J., Rice J.E. Lysinyl macrocyclic hexaoxazoles: Synthesis and selective G-quadruplex stabilizing properties // *Bioorg. Med. Chem. Lett.* 2008. Vol. 18, № 3. P. 913–917.
 199. Harrison R.J., Gowan S.M., Kelland L.R., Neidle S. Human telomerase inhibition by substituted acridine derivatives // *Bioorg. Med. Chem. Lett.* 1999. Vol. 9, № 17. P. 2463–2468.
 200. Harrison R.J., Reszka A.P., Haider S.M., Romagnoli B., Morrell J., Read M.A., Gowan S.M., Incles C.M., Kelland L.R., Neidle S. Evaluation of by disubstituted acridone derivatives as telomerase inhibitors: the importance of G-quadruplex binding // *Bioorg. Med. Chem. Lett.* 2004. Vol. 14, № 23. P. 5845–5849.
 201. Cuenca F., Moore M.J.B., Johnson K., Guyen B., De Cian A., Neidle S. Design, synthesis and evaluation of 4,5-di-substituted acridone ligands with high G-quadruplex affinity and selectivity, together with low toxicity to normal cells // *Bioorg. Med. Chem. Lett.* 2009. Vol. 19, № 17. P. 5109–5113.
 202. Laronze-Cochard M., Kim Y.-M.M., Brassart B., Riou J.-F.F., Laronze J.-Y.Y., Sapi J. Synthesis and biological evaluation of novel 4,5-bis(dialkylaminoalkyl)-substituted acridines as potent telomeric G-quadruplex ligands // *Eur. J. Med. Chem.* 2009. Vol. 44, № 10. P. 3880–3888.
 203. Read M., Harrison R.J., Romagnoli B., Tanious F.A., Gowan S.H., Reszka A.P., Wilson W.D., Kelland L.R., Neidle S. Structure-based design of selective and potent G quadruplex-mediated telomerase inhibitors // *Proc. Natl. Acad. Sci.* 2001. Vol. 98, № 9. P. 4844–4849.
 204. Martins C., Gunaratnam M., Stuart J., Makwana V., Greciano O., Reszka A.P., Kelland L.R., Neidle S. Structure-based design of benzylamino-acridine compounds as G-quadruplex DNA telomere targeting agents // *Bioorg. Med. Chem. Lett.* 2007. Vol. 17, № 8. P. 2293–2298.

205. Schultes C.M., Guyen B., Cuesta J., Neidle S. Synthesis, biophysical and biological evaluation of 3,6-bis-amidoacridines with extended 9-anilino substituents as potent G-quadruplex-binding telomerase inhibitors // *Bioorg. Med. Chem. Lett.* 2004. Vol. 14, № 16. P. 4347–4351.
206. Burger A.M., Dai F., Schultes C.M., Reszka A.P., Moore M.J., Double J.A., Neidle S. The G-Quadruplex-Interactive Molecule BRACO-19 Inhibits Tumor Growth, Consistent with Telomere Targeting and Interference with Telomerase Function // *Cancer Res.* 2005. Vol. 65, № 4. P. 1489–1496.
207. Zambre V.P., Murumkar P.R., Giridhar R., Yadav M.R. Structural Investigations of Acridine Derivatives by CoMFA and CoMSIA Reveal Novel Insight into Their Structures toward DNA G-Quadruplex Mediated Telomerase Inhibition and Offer a Highly Predictive 3D-Model for Substituted Acridines // *J. Chem. Inf. Model.* 2009. Vol. 49, № 5. P. 1298–1311.
208. Lagah S., Tan I.-L., Radhakrishnan P., Hirst R.A., Ward J.H., O’Callaghan C., Smith S.J., Stevens M.F.G., Grundy R.G., Rahman R. RHPS4 G-Quadruplex Ligand Induces Anti-Proliferative Effects in Brain Tumor Cells // *PLoS One.* 2014. Vol. 9, № 1. P. e86187.
209. Mergny J.-L., Lacroix L., Teulade-Fichou M.-P., Hounsou C., Guittat L., Hoarau M., Arimondo P.B., Vigneron J.-P., Lehn J.-M., Riou J.-F., Garestier T., Helene C. Telomerase inhibitors based on quadruplex ligands selected by a fluorescence assay // *Proc. Natl. Acad. Sci.* 2001. Vol. 98, № 6. P. 3062–3067.
210. Hounsou C., Guittat L., Monchaud D., Jourdan M., Saettel N., Mergny J.-L., Teulade-Fichou M.-P. G-Quadruplex Recognition by Quinacridines: a SAR, NMR, and Biological Study // *ChemMedChem.* 2007. Vol. 2, № 5. P. 655–666.
211. Teulade-Fichou M.-P., Carrasco C., Guittat L., Bailly C., Alberti P., Mergny J.-L., David A., Lehn J.-M., Wilson W.D. Selective Recognition of G-Quadruplex Telomeric DNA by a Bis(quinacridine) Macrocyclic // *J. Am. Chem. Soc.* 2003. Vol. 125, № 16. P. 4732–4740.
212. Allain C., Monchaud D., Teulade-Fichou M.-P. FRET Templated by G-Quadruplex DNA: A Specific Ternary Interaction Using an Original Pair of Donor/Acceptor Partners // *J. Am. Chem. Soc.* 2006. Vol. 128, № 36. P. 11890–11893.
213. Koole R., Groeneveld E., Vanmaekelbergh D., Meijerink A., de Mello Donegá C. Size Effects on Semiconductor Nanoparticles // *Nanoparticles.* Berlin, Heidelberg, Heidelberg: Springer Berlin Heidelberg, 2014. P. 13–51.
214. Jasieniak J., Smith L., van Embden J., Mulvaney P., Califano M., Re-examination of the Size-Dependent Absorption Properties of CdSe Quantum Dots // *J. Phys. Chem. C.* 2009.

- Vol. 113, № 45. P. 19468–19474.
215. Rurack K., Spieles M. Fluorescence Quantum Yields of a Series of Red and Near-Infrared Dyes Emitting at 600–1000 nm // *Anal. Chem.* 2011. Vol. 83, № 4. P. 1232–1242.
 216. Laverdant J., Marcillac W.D. de, Barthou C., Chinh V.D., Schwob C., Coolen L., Benalloul P., Nga P.T., Maître A. Experimental Determination of the Fluorescence Quantum Yield of Semiconductor Nanocrystals // *Materials (Basel)*. 2011. Vol. 4, № 7. P. 1182–1193.
 217. Larson D.R., Zipfel W.R., Williams R.M., Clark S.W., Bruchez M.P., Wise F.W., Webb W.W. Water-soluble quantum dots for multiphoton fluorescence imaging in vivo. // *Science*. 2003. Vol. 300, № 5624. P. 1434–1436.
 218. Krivenkov V., Samokhvalov P., Solovyeva D., Bilan R., Chistyakov A., Nabiev I. Two-photon-induced Förster resonance energy transfer in a hybrid material engineered from quantum dots and bacteriorhodopsin // *Opt. Lett.* 2015. Vol. 40, № 7. P. 1440.
 219. Smith A.M., Mancini M.C., Nie S. Bioimaging: second window for in vivo imaging. // *Nat. Nanotechnol.* 2009. Vol. 4, № 11. P. 710–711.
 220. So P.T., Dong C.Y., Masters B.R., Berland K.M. Two-photon excitation fluorescence microscopy. // *Annu. Rev. Biomed. Eng.* 2000. Vol. 2. P. 399–429.
 221. Shen Y., Tan R., Gee M.Y., Greytak A.B. Quantum Yield Regeneration: Influence of Neutral Ligand Binding on Photophysical Properties in Colloidal Core/Shell Quantum Dots // *ACS Nano*. 2015. Vol. 9, № 3. P. 3345–3359.
 222. Grabolle M., Spieles M., Lesnyak V., Gaponik N., Eychmüller A., Resch-Genger U. Determination of the Fluorescence Quantum Yield of Quantum Dots: Suitable Procedures and Achievable Uncertainties // *Anal. Chem.* 2009. Vol. 81, № 15. P. 6285–6294.
 223. Pu S.-C., Yang M.-J., Hsu C.-C., Lai C.-W., Hsieh C.-C., Lin S.H., Cheng Y.-M., Chou P.-T. The empirical correlation between size and two-photon absorption cross section of CdSe and CdTe quantum dots. // *Small*. 2006. Vol. 2, № 11. P. 1308–1313.
 224. Makarov N.S., Drobizhev M., Rebane A. Two-photon absorption standards in the 550–1600 nm excitation wavelength range // *Opt. Express*. 2008. Vol. 16, № 6. P. 4029.
 225. Brassart B., Gomez D., Cian A.D., Paterski R., Montagnac A., Qui K.-H., Temime-Smaali N., Trentesaux C., Mergny J.-L., Gueritte F., Riou J.-F. A New Steroid Derivative Stabilizes G-Quadruplexes and Induces Telomere Uncapping in Human Tumor Cells // *Mol. Pharmacol.* 2007. Vol. 72, № 3. P. 631–640.
 226. Gomez D., Mergny J.-L., Riou J.-F. Detection of telomerase inhibitors based on g-quadruplex ligands by a modified telomeric repeat amplification protocol assay. // *Cancer Res.* 2002. Vol. 62, № 12. P. 3365–3368.

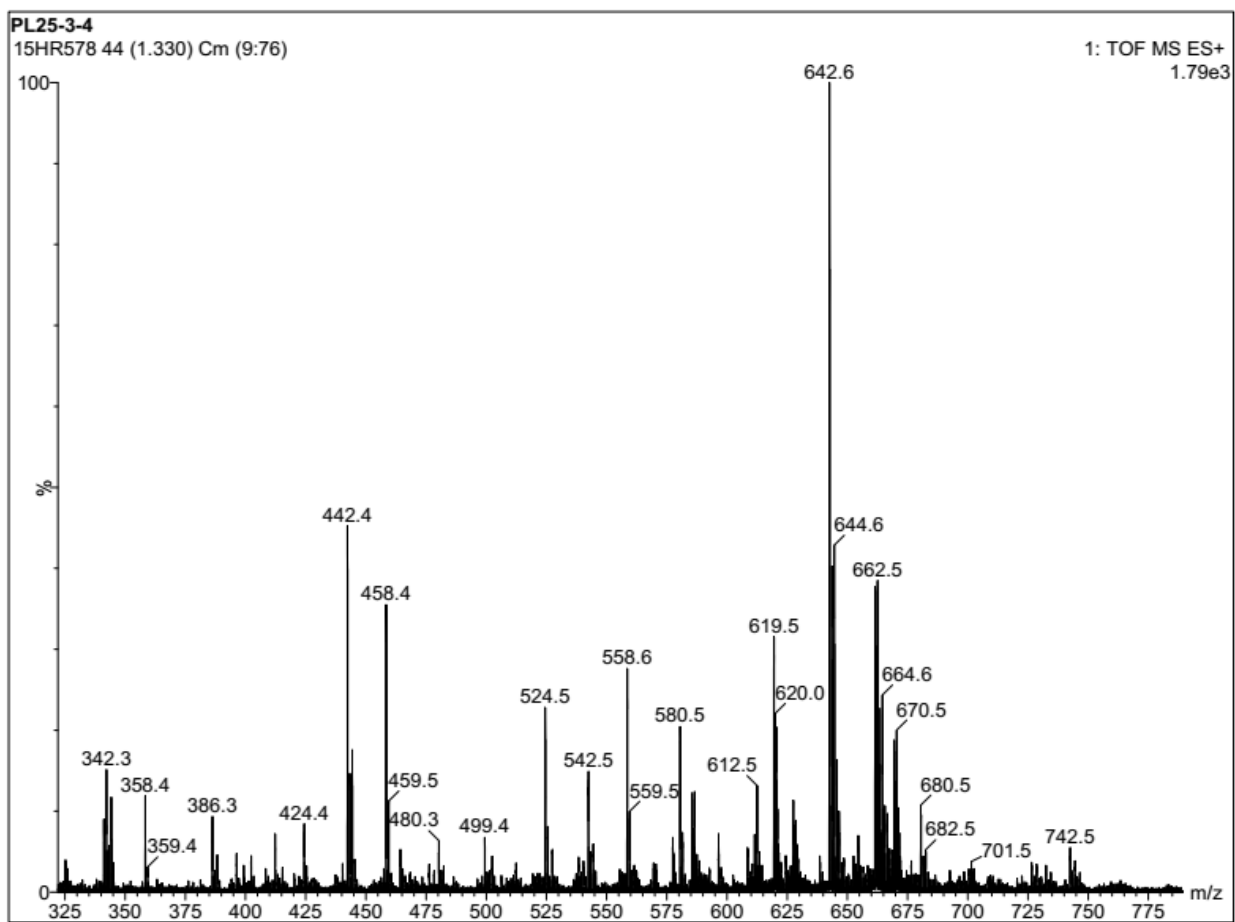
227. O'Hara T., Seddon B., O'Connor A., McClean S., Singh B., Iwuoha E., Fuku X., Dempsey E. Quantum Dot Nanotoxicity Investigations Using Human Lung Cells and TOXOR Electrochemical Enzyme Assay Methodology // *ACS Sensors*. 2017. Vol. 2, № 1. P. 165–171.
228. Shoemaker M., Cohen I., Campbell M. Reduction of MTT by aqueous herbal extracts in the absence of cells // *J. Ethnopharmacol.* 2004. Vol. 93, № 2–3. P. 381–384.
229. Shen Y., Gee M.Y., Tan R., Pellechia P.J., Greytak A.B. Purification of Quantum Dots by Gel Permeation Chromatography and the Effect of Excess Ligands on Shell Growth and Ligand Exchange // *Chem. Mater.* 2013. Vol. 25, № 14. P. 2838–2848.
230. Jang E., Jun S., Chung Y., Pu L. Surface Treatment to Enhance the Quantum Efficiency of Semiconductor Nanocrystals // *J. Phys. Chem. B*. 2004. Vol. 108, № 15. P. 4597–4600.
231. Chiron J., Galy J.-P. Reactivity of the Acridine Ring: A Review // *Synthesis*. 2004. № 3. P. 313–325.
232. Carole D.G., Michel D.M., Julien C., Florence D., Anna N., Séverine J., Gérard D., Pierre T.-D., Jean-Pierre G. Synthesis and antileishmanial activities of 4,5-di-substituted acridines as compared to their 4-mono-substituted homologues // *Bioorg. Med. Chem.* 2005. Vol. 13, № 19. P. 5560–5568.
233. Zhang A.J., Russell D.H., Zhu J., Burgess K. A method for removal of N-BOC protecting groups from substrates on TFA-sensitive resins // *Tetrahedron Lett.* 1998. Vol. 39, № 41. P. 7439–7442.
234. Li B., Bemish R., Buzon R.A., Chiu C.K.-F., Colgan S.T., Kissel W., Le T., Leeman K.R., Newell L., Roth J. Aqueous phosphoric acid as a mild reagent for deprotection of the t-butoxycarbonyl group // *Tetrahedron Lett.* 2003. Vol. 44, № 44. P. 8113–8115.
235. Maurice H.B., Phillips R., Karodia N. Design, Synthesis and biological evaluation of novel acridine-polyamine conjugates against prostate cancer // *J. Pharm. Pharmacol.* 2009. Vol. 3, № 12. P. 602–610.
236. Sulfo-NHS / EDC (carbodiimide) crosslinking reaction [Electronic resource]. URL: <https://www.thermofisher.com/ru/ru/home/life-science/protein-biology/protein-biology-learning-center/protein-biology-resource-library/pierce-protein-methods/carbodiimide-crosslinker-chemistry.html>.
237. Grabarek Z., Gergely J. Zero-length crosslinking procedure with the use of active esters. // *Anal. Biochem.* 1990. Vol. 185, № 1. P. 131–135.
238. Qu L., Peng X. Control of Photoluminescence Properties of CdSe Nanocrystals in Growth // *J. Am. Chem. Soc.* 2002. Vol. 124, № 9. P. 2049–2055.
239. Linkov P., Vokhmintcev K. V, Samokhvalov P.S., Nabiev I. Ultrasmall Quantum Dots: A

- Tool for in Vitro and in Vivo Fluorescence Imaging // *J. Phys. Conf. Ser.* 2017. Vol. 784. P. 12033.
240. Chen P.E., Anderson N.C., Norman Z.M., Owen J.S. Tight Binding of Carboxylate, Phosphonate, and Carbamate Anions to Stoichiometric CdSe Nanocrystals // *J. Am. Chem. Soc.* 2017. Vol. 139, № 8. P. 3227–3236.
 241. Frederick M.T., Achtyl J.L., Knowles K.E., Weiss E.A., Geiger F.M. Surface-Amplified Ligand Disorder in CdSe Quantum Dots Determined by Electron and Coherent Vibrational Spectroscopies // *J. Am. Chem. Soc.* 2011. Vol. 133, № 19. P. 7476–7481.
 242. Linkov P., Vokhmintcev K. V, Samokhvalov P.S., Nabiev I. Ultrasmall Quantum Dots for Fluorescent Bioimaging in vivo and in vitro // *Opt. Spectrosc.* 2017. Vol. 122, № 1. P. 8–11.
 243. Harrell S.M., McBride J.R., Rosenthal S.J. Synthesis of Ultrasmall and Magic-Sized CdSe Nanocrystals // *Chem. Mater.* 2013. Vol. 25, № 8. P. 1199–1210.
 244. Vengrenovich R., Ivanskii B., Panko I., Stasyk M. Size Distribution of Nanoparticles of ZnO and SnS in the Frame of Lifshits–Slezov–Wagner Modified Theory // *J. Phys. Chem. C.* 2013. Vol. 117, № 26. P. 13681–13687.
 245. Swain B., Hong M.H., Kang L.-S., Lee C.G. Understanding the isothermal growth kinetics of cdse quantum dots through microfluidic reactor assisted combinatorial synthesis // *J. Korean Phys. Soc.* 2016. Vol. 69, № 9. P. 1485–1492.
 246. Bouazra A., Naifar A., Abdi-Ben Nasrallah S., Said M. Mathematical modelling of optical properties of CdSe/ZnS core shell quantum dot // *Optik (Stuttg).* 2018. Vol. 158. P. 737–746.
 247. Dong C., Ren J. Measurements for molar extinction coefficients of aqueous quantum dots // *Analyst.* 2010. Vol. 135, № 6. P. 1395.
 248. Xu Y.-N., Ching W.Y. Electronic, optical, and structural properties of some wurtzite crystals // *Phys. Rev. B.* 1993. Vol. 48, № 7. P. 4335–4351.
 249. Tan R., Blom D.A., Ma S., Greytak A.B. Probing Surface Saturation Conditions in Alternating Layer Growth of CdSe/CdS Core/Shell Quantum Dots // *Chem. Mater.* 2013. Vol. 25, № 18. P. 3724–3736.
 250. Krivenkov V., Linkov P., Solovyeva D., Bilan R., Chistyakov A., Nabiev I. Energy Transfer Processes Under One-and Two-photon Excitation of Nano-biohybrid Structures based on Semiconductor Quantum Dots and Purple Membranes // *Phys. Procedia.* 2015. Vol. 73. P. 143–149.
 251. Bobrovsky A., Mochalov K., Oleinikov V., Sukhanova A., Prudnikau A., Artemyev M., Shibaev V., Nabiev I. Optically and electrically controlled circularly polarized emission

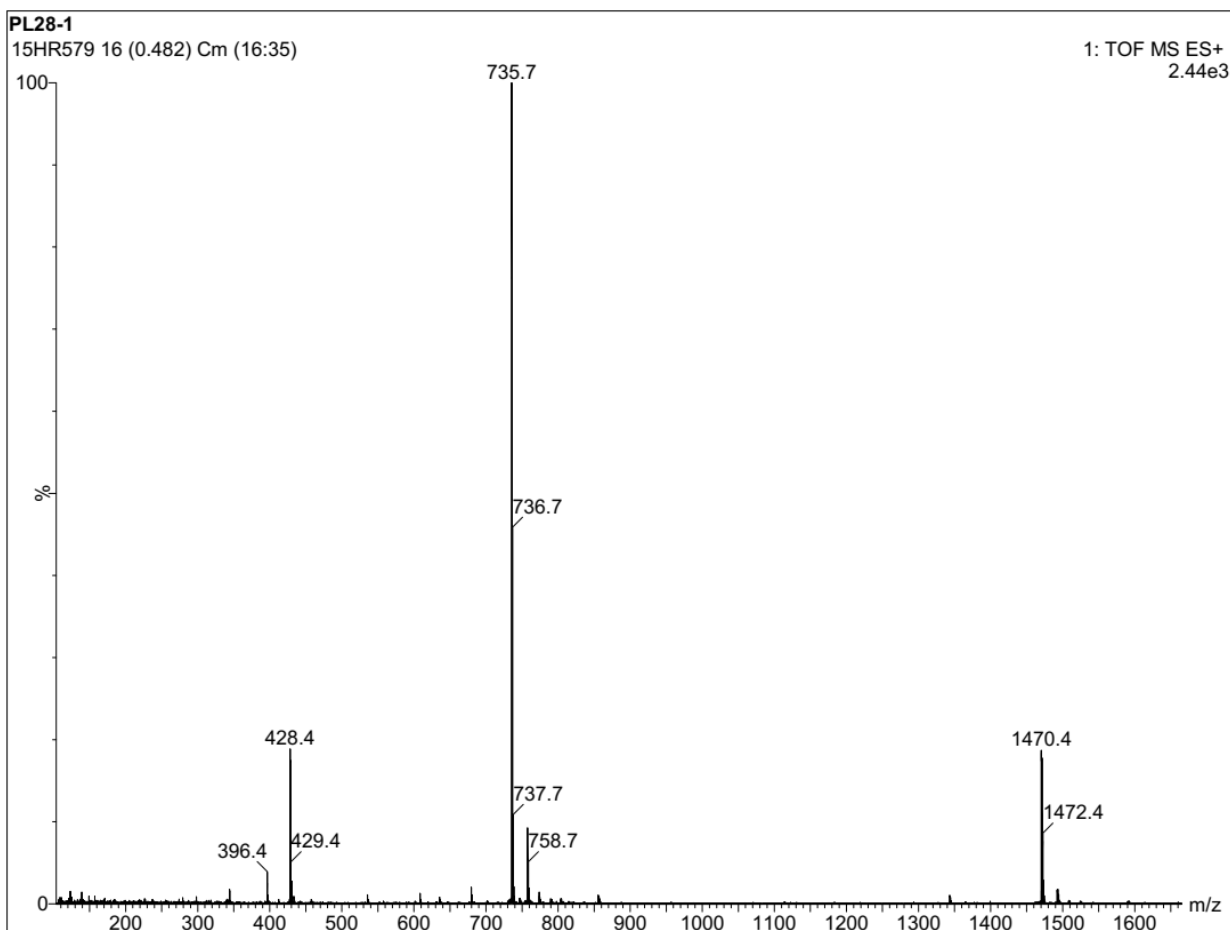
- from cholesteric liquid crystal materials doped with semiconductor quantum dots. // *Adv. Mater.* 2012. Vol. 24, № 46. P. 6216–6222.
252. Sukhanova A., Hafian H., Pluot M., Cohen J.H.M., Millot J.-M., Nabiev I., Turini M., Chames P., Baty D. Multiphoton imaging of tumor biomarkers in situ using highly oriented conjugates of single-domain antibodies and quantum dots // 2015 International Conference on Biomedical Engineering and Computational Technologies (SIBIRCON). IEEE, 2015. P. 119–121.
253. Pegg A. An encyclopedia of polyamines // *Trends Biochem. Sci.* 1998. Vol. 23, № 9. P. 366–367.
254. Cho A.-N., Chakravarthi N., Kranthiraja K., Reddy S.S., Kim H.-S., Jin S.-H., Park N.-G. Acridine-based novel hole transporting material for high efficiency perovskite solar cells // *J. Mater. Chem. A*. 2017. Vol. 5, № 16. P. 7603–7611.
255. Krzyimiński K., Malecha P., Zadykiewicz B., Wróblewska A., Błażejowski J. ¹H and ¹³C NMR spectra, structure and physicochemical features of phenyl acridine-9-carboxylates and 10-methyl-9-(phenoxy-carbonyl)acridinium trifluoromethanesulphonates – alkyl substituted in the phenyl fragment // *Spectrochim. Acta Part A Mol. Biomol. Spectrosc.* 2011. Vol. 78, № 1. P. 401–409.
256. Jasieniak J., Califano M., Watkins S.E. Size-Dependent Valence and Conduction Band-Edge Energies of Semiconductor Nanocrystals // *ACS Nano*. 2011. Vol. 5, № 7. P. 5888–5902.
257. Islam A., Murugan P., Hwang K.C., Cheng C.-H. Blue light-emitting devices based on 1,8-acridinedione derivatives // *Synth. Met.* 2003. Vol. 139, № 2. P. 347–353.
258. Liu I.-S., Lo H.-H., Chien C.-T., Lin Y.-Y., Chen C.-W., Chen Y.-F., Su W.-F., Liou S.-C. Enhancing photoluminescence quenching and photoelectric properties of CdSe quantum dots with hole accepting ligands // *J. Mater. Chem.* 2008. Vol. 18, № 6. P. 675.
259. Krivenkov V.A., Samokhvalov P.S., Linkov P.A., Solovyeva D.O., Kotkovskii G.E., Chistyakov A.A., Nabiev I. Surface ligands affect photoinduced modulation of the quantum dots optical performance // *SPIE Proc.* 2014. Vol. 9126. P. 91263N.
260. Pathakoti K., Hwang H.-M., Xu H., Aguilar Z.P., Wang A. In vitro cytotoxicity of CdSe/ZnS quantum dots with different surface coatings to human keratinocytes HaCaT cells. // *J. Environ. Sci. (China)*. 2013. Vol. 25, № 1. P. 163–171.
261. Delmas F., Avellaneda A., Di Giorgio C., Robin M., De Clercq E., Timon-David P., Galy J.-P. Synthesis and antileishmanial activity of (1,3-benzothiazol-2-yl) amino-9-(10H)-acridinone derivatives // *Eur. J. Med. Chem.* 2004. Vol. 39, № 8. P. 685–690.
262. Yu X.-M., Ramiandrasoa F., Guetzoyan L., Pradines B., Quintino E., Gabelle D., Forterre

- P., Cresteil T., Mahy J.-P., Pethe S. Synthesis and Biological Evaluation of Acridine Derivatives as Antimalarial Agents // *ChemMedChem*. 2012. Vol. 7, № 4. P. 587–605.
263. Di Giorgio C., Delmas F., Filloux N., Robin M., Seferian L., Azas N., Gasquet M., Costa M., Timon-David P., Galy J.-P. In Vitro Activities of 7-Substituted 9-Chloro and 9-Amino-2-Methoxyacridines and Their Bis- and Tetra-Acridine Complexes against *Leishmania infantum* // *Antimicrob. Agents Chemother.* 2003. Vol. 47, № 1. P. 174–180.

Annexes



Annex 1: Mass spectrum of 9-chloroacridine-4,5-dicarbonyl dichloride (23).



Annex 2: N4,N5-bis(*tert*-butyl-4-aminobutylcarbamate)-9-(3,4-difluorophenylamino)acridine-4,5-dicarboxamide (24a).

Single Mass Analysis

Tolerance = 5.0 PPM / DBE: min = -1.5, max = 50.0

Element prediction: Off

Number of isotope peaks used for i-FIT = 3

Monoisotopic Mass, Even Electron Ions

175 formula(e) evaluated with 1 results within limits (up to 50 best isotopic matches for each mass)

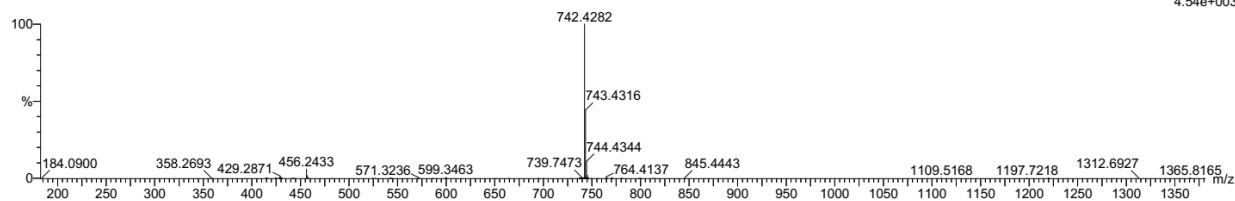
Elements Used:

C: 41-41 H: 0-1000 N: 0-7 O: 0-10 Na: 0-1

PL-43

16HR271 68 (2.204) AM (Cen,4, 80.00, Ar,5000.0,772.46,0.70,LS 20); Sm (SG, 1x1.00); Sb (5,40.00); Cm (67:68)

1: TOF MS ES+
4.54e+003



Mass	Calc. Mass	mDa	PPM	DBE	i-FIT	Formula
742.4282	742.4292	-1.0	-1.3	17.5	15.9	C41 H56 N7 O6

Annex 3: N4,N5-bis(*tert*-butyl-4-aminobutylcarbamate)-9-(4-(dimethylamino)phenylamino)acridine-4,5-dicarboxamide (24c).

Single Mass Analysis

Tolerance = 5.0 PPM / DBE: min = -1.5, max = 50.0

Element prediction: Off

Number of isotope peaks used for i-FIT = 3

Monoisotopic Mass, Even Electron Ions

187 formula(e) evaluated with 1 results within limits (up to 50 best isotopic matches for each mass)

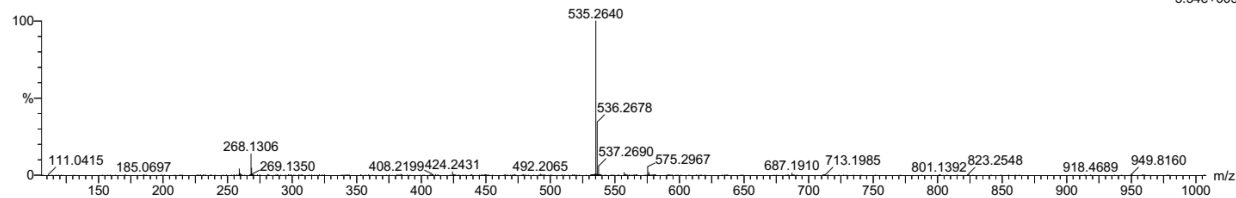
Elements Used:

C: 29-29 H: 0-1000 N: 6-6 O: 0-36 Na: 0-1 K: 0-1 F: 2-3

PL-32

16HR14 130 (4.146) AM (Cen,4, 80.00, Ar,5000.0,622.57,0.70,LS 20); Sm (SG, 1x1.00); Sb (5,40.00); Cm (127:131)

1: TOF MS ES+
5.54e+003



Minimum:

Maximum: 5.0 5.0 -1.5

Maximum: 50.0

Mass	Calc. Mass	mDa	PPM	DBE	i-FIT	Formula
535.2640	535.2633	0.7	1.3	15.5	2.1	C29 H33 N6 O2 F2

Annex 4: N4,N5-bis(4-aminobutyl)-9-(3,4-difluorophenylamino)acridine-4,5-dicarboxamide (25a).

Single Mass Analysis

Tolerance = 5.0 PPM / DBE: min = -1.5, max = 50.0

Element prediction: Off

Number of isotope peaks used for i-FIT = 3

Monoisotopic Mass, Even Electron Ions

157 formula(e) evaluated with 1 results within limits (up to 50 closest results for each mass)

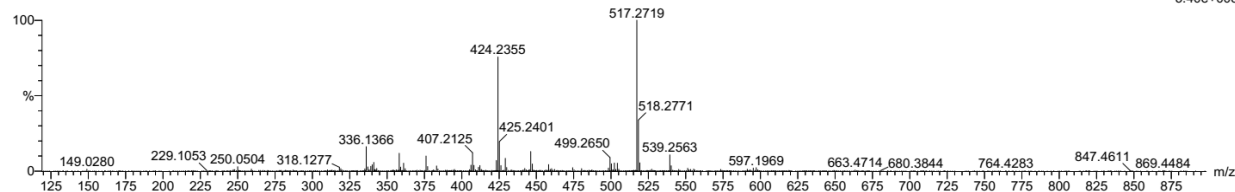
Elements Used:

C: 29-29 H: 0-200 N: 6-6 O: 0-20 F: 1-1 Na: 0-1 39K: 0-1 90Zr: 0-1

PL-56-5

16HR502 37 (1.118) AM (Cen,4, 80.00, Ar,5000.0,922.36,0.70,LS 20); Sm (SG, 1x1.00); Sb (5,40.00); Cm (35:37)

1: TOF MS ES+
5.40e+003



Minimum:

Maximum: 5.0 5.0 -1.5

Maximum: 50.0

Mass	Calc. Mass	mDa	PPM	DBE	i-FIT	Formula
517.2719	517.2727	-0.8	-1.5	15.5	4.7	C29 H34 N6 O2 F

Annex 5: N4,N5-bis(4-aminobutyl)-9-(4-fluorophenylamino)acridine-4,5-dicarboxamide (25b).

Publication list

Papers in the High-Impact Peer-Reviewed Journals

1. **Linkov, P.**, Artemyev, M., Efimov, A., Nabiev, I. (2013) Comparative advantages and limitations of the basic metrology methods applied to characterization of nanomaterials. *Nanoscale*, 5, 8781-8798. **IF=7.367.**
2. **Linkov, P.A.**, Vokhmintsev, K.V., Samokhvalov, P.S., Laronze-Cochard, M., Sapi, J., Nabiev, I.R. (2018) Effect of the semiconductor quantum dot shell structure on fluorescence quenching by acridine ligand. *JETP Letters*, 107 (4), 233–237. **IF=1.363.**
3. Dayneko, S., **Linkov, P.**, Martynov, I., Tameev, A., Tedoradze, M., Samokhvalov, P., Nabiev, I., Chistyakov, A. (2016) Photoconductivity of composites based on CdSe quantum dots and low-band-gap polymers. *Physica E: Low-dimensional Systems and Nanostructures*. 79, 206-211. **IF=2.399.**
4. Bugakov, M., Boiko, N., **Linkov, P.**, Samokhvalov, P., Efimov, A., Abramchuk, S., Shibaev, V. (2018) Fluorescent thermostable crosslinked poly(dodecylmethacrylate) composites based on porous polyethylene and CdSe/ZnS quantum dots. *Polymer International*, 67 (9), 1275-1281. **IF=2.070**
5. Melnikau, D., Hendel, T., **Linkov, P.A.**, Samokhvalov, P.S., Nabiev, I.R., Rakovich, Yu.P. (2018) Energy transfer between single semiconductor quantum dots and organic dye molecules. *Zeitschrift für Physikalische Chemie*. URL: www.doi.org/10.1515/zpch-2018-1144. **IF=1.144.**
6. **Linkov, P.** et al (2018) Enhanced Cell Penetrating Capacity of CdSe/ZnS Ultrasmall Quantum Dots for Labeling and Intracellular Tracking. To be published.
7. **Linkov, P.** et al. (2019) Synthesis and biological evaluation of 4,5,9-trisubstituted acridine derivatives as telomerase inhibitors. To be published.

Papers in the Other Peer-Reviewed Journals Cited in the Web-of-Science and/or Scopus Databases

8. **Linkov P.A.**, Vokhmintsev K.V., Samokhvalov P.S, Nabiev I.R. (2017) Ultrasmall quantum dots for fluorescent bioimaging in vivo and in vitro. *Optics and Spectroscopy*, 122 (1), 8–11. **IF=0.644.**

9. **Linkov, P.**, Krivenkov, V., Samokhvalov, P., Nabiev, I. (2016) High quantum yield CdSe/ZnS/CdS/ZnS multishell quantum dots for biosensing and optoelectronic applications. *Materials Today: Proceedings*, **3**, 104–108.
10. **Linkov, P.A.**, Vokhmintcev, K.V., Samokhvalov, P.S., Laronze-Cochard, M., Sapi, J., Nabiev, I.R. (2018) The effect of quantum dot shell structure on fluorescence quenching by acridine ligand. *KnE Energy & Physics*, 194–201.
11. **Linkov, P.**, Vokhmintcev, K.V., Samokhvalov, P.S. and Nabiev, I. (2017) Ultrasmall quantum dots: A tool for in vitro and in vivo fluorescence imaging. *Journal of Physics: Conference Series*, **784**, 012033.
12. **Linkov, P.**, Laronze-Cochard, M., Sapi, J., Sidorov, L., Nabiev, I. (2015) Multifunctional nanoprobe for cancer cell targeting, imaging and anticancer drug delivery. *Physics Procedia*, **73**, 216–220.
13. Samokhvalov, P.S., **Linkov, P.A.**, Zvaigzne, M.A., Kosmynceva, A.V., Petrova, I.O., Krivenkov, V.A., Sukhanova, A.V., Nabiev, I.R. (2018) Optical properties of core-multishell quantum dots. *KnE Energy & Physics*, 449–455.
14. Vokhmintcev, K.V., **Linkov, P.A.**, Samokhvalov, P.S., Nabiev, I.R. (2018) Two-stage ZnS shell coating on the CuInS₂ quantum dots for their effective solubilization. *KnE Energy & Physics*, 535–540.
15. Krivenkov, V., **Linkov, P.**, Solovyeva, D., Bilan, R., Chistyakov, A., Nabiev, I. (2015) Energy transfer processes under one- and two-photon excitation of nano-biohybrid structures based on semiconductor quantum dots and purple membranes. *Physics Procedia*, **73**, 143–149.
16. Krivenkov, V., **Linkov, P.**, Solovyeva, D., Bilan, R., Chistyakov, A., Nabiev, I. (2016) Two-photon-induced Förster resonance energy transfer in a quantum dot–bacteriorhodopsin hybrid material. *Materials Today: Proceedings*, **3**, A1–A5.
17. Samokhvalov, P., **Linkov, P.**, Michel, J., Molinari, M., Nabiev, I. (2014) Photoluminescence quantum yield of CdSe-ZnS/CdS/ZnS core-multishell quantum dots approaches 100% due to enhancement of charge carrier confinement. *Colloidal Nanoparticles for Biomedical Applications IX. Proceedings of SPIE*, Vol. **8955**, 89550S.
18. Krivenkov, V.A., Samokhvalov, P.S., **Linkov, P.A.**, Prokhorov, S.D., Martynov, I.L., Chistyakov, A.A., Nabiev, I. (2015) Effects of surface ligands and solvents on quantum dot

photostability under pulsed UV laser irradiation. *Quantum Optics and Quantum Information Transfer and Processing. Proceedings of SPIE, 9505*, 95050U.

19. Dayneko, S., Lypenko, D., **Linkov, P.**, Tameev, A., Martynov, I., Samokhvalov, P., Chistyakov, A. (2014) Effect of surface ligands on the performance of organic light-emitting diodes containing quantum dots. *Proc. of SPIE 9270, Optoelectronic Devices and Integration V*, 927009.
20. Krivenkov, V.A., Samokhvalov, P.S., **Linkov, P.A.**, Solovyeva, D.O., Kotkovskiy, G.E., Chistyakov, A.A., Nabiev, I.R. (2014) Surface ligands affect photoinduced modulation of the quanyum dots optical performance. *Nanophotonics V. Proc. of SPIE, 9126*, 91263N-1—91263N-8.
21. Dovzhenko, D., Osipov, E., Martynov, I., **Linkov, P.**, Chistyakov, A. (2015) Enhancement of spontaneous emission from CdSe/CdS/ZnS quantum dots at the edge of the photonic band gap in a porous silicon Bragg mirror. *Physics Procedia, 73*, 126–130.
22. Dovzhenko, D., Osipov, E., Martynov, I., **Linkov, P.** (2015) Spatial and spectral properties of CdSe/CdS/ZnS quantum dots luminescence in one-dimensional photonic structures based on porous silicon. *Proceedings of International Conference NANOMEETING 2015: Physics, Chemistry and Applications of Nanostructures – Reviews and Short Notes*, O-11, 144-147.
23. Dayneko, S., Lypenko, D., Sannikova, N., **Linkov, P.**, Tameev, A., Nikitenko, V., Samokhvalov, P., Chistyakov, A. (2016) Application of CdSe/ZnS/CdS/ZnS core–multishell quantum dots to modern OLED technology. *Materials Today: Proceedings, 3*, 211–215.
24. Dayneko, S., Tameev, A., Tedoradze, M., Martynov, I., **Linkov, P.**, Samokhvalov, P., Nabiev, I., Chistyakov, A. (2014) Hybrid bulk heterojunction solar cells based on low band gap polymers and CdSe nanocrystals. *Physics, Simulation, and Photonic Engineering of Photovoltaic Devices III. Proceedings of SPIE, 8981*, 898113.

Published Abstracts of Conferences and Symposia

1. **Linkov, P.**, Vokhmintcev, K., Samokhvalov, P., Laronze-Cochard, M., Sapi, J., Nabiev, I. (2017) The effect of quantum dot shell on fluorescence quenching by acridine ligand. *2nd International Symposium “Physics, Engineering and Technologies for Biomedicine”*, October 10–14, 2017, Moscow, Russia, 250–251.

2. **Linkov, P.**, Vokhmintcev, K.V., Samokhvalov, P.S., Nabiev, I. (2016) Ultrasmall quantum dots: a tool for in vitro and in vivo fluorescence imaging. *The First International Symposium "Physics, Engineering and Technologies for Bio-Medicine"*, October 18-23, 2016, Moscow, Russia.
3. **Linkov P.**, Krivenkov V., Samokhvalov P., Laronze-Cochard M., Sapi J., Nabiev I. (2016) CdSe/ZnS/CdS/ZnS QDs with advanced two-photon properties for tumor diagnosis and treatment. *PCNSPA Conference 2016—Photonic Colloidal Nanostructures: Synthesis, Properties, and Applications*, St. Petersburg, Russia, Jun 27–Jul 1, 2016, 55-56.
4. **Linkov, P.**, Krivenkov, V., Samokhvalov, P., Nabiev, I. (2015) High quantum yield CdSe/ZnS/CdS/ZnS multishell quantum dots for applications in biosensing and optoelectronics. *Advances in Functional Materials Conference 2015*, Stony Brook University, USA, Jun 29–Jul 3, 2015, AFM15-0722021-S7_MNJ7-O. *Oral presentation.*
5. **Linkov, P.A.**, Samokhvalov, P.S., Nabiev, I.R. (2014) CdSe/ZnS/CdS/ZnS multishell quantum dots with a fluorescence quantum yield reaching 100%. *XII International Conference on Nanostructured Materials (NANO 2014), Section: Biological and Biomedical Nanomaterials*, July 13–18, 2014, Moscow, Russia. *Oral presentation.*
6. Samokhvalov, P., **Linkov, P.**, Zvaigzne, M., Kosmynceva, A.V., Petrova, I.O., Krivenkov, V.A., Sukhanova, A., Nabiev, I. (2017) Optical properties of complex core-multishell quantum dots. *2nd International Symposium "Physics, Engineering and Technologies for Biomedicine"*, October 10–14, 2017, Moscow, Russia, 371–372.
7. Vokhmintcev, K., **Linkov, P.**, Samokhvalov, P., Nabiev, I. (2017) Two-stage shell coating of CuInS₂ quantum dots for efficient phase transfer. *2nd International Symposium "Physics, Engineering and Technologies for Biomedicine"*, October 10–14, 2017, Moscow, Russia, 429–430.
8. Krivenkov, V., **Linkov, P.**, Solovyeva, D., Bilan, R., Chistyakov, A., Nabiev, I. (2015) Two-photon-induced Förster resonance energy transfer in a quantum dot–bacteriorhodopsin hybrid material. *Advances in Functional Materials Conference 2015*, Stony Brook University, USA, Jun 29–Jul 3, 2015, AFM15-0794073-S7_RQYW-O. *Oral presentation.*
9. **Samokhvalov, P., Linkov, P., Nabiev, I.** (2014) Modeling of quantum dot growth: Towards rational development of nanomaterials with predictable properties. *Science of the Future: First International Conference*. St. Petersburg, 17-20 Sep 2014. *Oral presentation.*

10. Samokhvalov, P., Linkov, P., Nabiev, I. (2014) High quantum yield CdSe/ZnS/CdS/ZnS multishell quantum dots for applications in biosensing and optoelectronics. *Science of the Future: First International Conference*. St. Petersburg, 17-20 Sep 2014. *Oral presentation*.
11. Samokhvalov, P., Linkov, P., Michel, J., Molinari, M., Nabiev, I. (2014) Photoluminescence quantum yield of CdSe-ZnS/CdS/ZnS core-multishell quantum dots approaches 100% due to enhancement of charge carrier confinement. *SPIE Photonics West International Conference*, 1 - 6 February 2014, The Moscone Center San Francisco, California, US. Paper No. 8955-28, Tracking No. PW14B-BO501-41.
12. Krivenkov, V.A., Samokhvalov, P.S., Linkov, P.A., Prokhorov, S.D., Martynov, I.L., Chistyakov, A.A., Nabiev, I. (2015) Effects of surface ligands and solvents on quantum dot photostability under pulsed UV laser irradiation. *Conference/exhibition SPIE Optics + Optoelectronics 2015*. Prague, Czech Republic | April 13, 2015. *Oral presentation*.
13. Dayneko, S., Lypenko, D., Linkov, P., Tameev, A., Martynov, I., Samokhvalov, P., Chistyakov, A. (2014) Application of Quantum dots CdSe/ZnS in modern LED technology. *Science of the Future: First International Conference. St. Petersburg, 17-20 Sep 2014*.
14. Krivenkov, V.A., Samokhvalov, P.S., Linkov, P.A., Solovyeva, D.O., Kotkovskiy, G.E., Chistyakov, A.A., Nabiev, I.R. (2014) Surface ligands affect photoinduced degradation of the quanyum dots optical performance *SPIE Photonics Europe, Conference 9126 Nanophotonics*, Brussels, Belgium, 14 - 17 April 2014 Paper No. 9126-136.
15. Solovyeva, D., Lukashev, E., Linkov, P., Samokhvalov, P., Dayneko, S., Zaitsev, S., Oleinikov, V., Shemetov, A., Sukhanova, A., Nabiev, I., Chistyakov, A.A. Photovoltaic cells engineered from purple membranes of Halophilic bacteria and semiconductor quantum dots. *International Workshop "Laser Physics"*, Prague, Czech Republic, July 2013. *Oral presentation*.
16. Krivenkov, V.A., Solovyeva, D.O., Linkov, P.A., Nabiev, I.R., Chistyakov, A.A. Effect of highly intense laser radiation on the spectral characteristics of semiconductor quantum dots. *VII International Conference of Young Scientists and Specialists "Optika-2013"* [Optics 2013; in Russian], October 14–18, 2013, St. Petersburg, Russia.
17. Dovzhenko, D., Osipov, E., Martynov, I., Linkov, P. (2015) Spatial and spectral properties of CdSe/CdS/ZnS quantum dots luminescence in one-dimensional photonic structures based on porous silicon. *International Conference Nanomeeting 2015*, Minsk, Belarus, 26-29 May 2015, O-11. *Oral presentation*.

18. Dayneko, S., Lypenko, D., Sannikova N., **Linkov, P.**, Tameev, A., Nikitenko V., Samokhvalov, P., Chistyakov, A. (2015) Application of CdSe/ZnS/CdS/ZnS core–multishell quantum dots to modern OLED technology. *Advances in Functional Materials Conference 2015*, Stony Brook University, USA, Jun 29–Jul 3, 2015, AFM15-0803078-S7_2J58-O. *Oral presentation.*
19. Sukhanova, A., Bouchonville, N., Le Cigne, A., Molinari, M., **Linkov, P.**, Samokhvalov, P., Oleinikov, V., Nabiev, I. Biophotonics with nano-bio hybrid material with controlled FRET efficiency engineered from quantum dots and membrane protein bacteriorhodopsin. *International Workshop "Laser Physics"*, Prague, Czech Republic, July 2013.
20. Mochalov, K., Bobrovsky, A., Efimov, A., Oleinikov, V., **Linkov, P.**, Samokhvalov, P., Sukhanova, A., Nabiev, I. Circularly polarized emission from cholesteric liquid crystal material doped with quantum dots can be controlled both optically and electrically. *International Workshop "Laser Physics"*, Prague, Czech Republic, July 2013. *Oral presentation.*

Synthèse et caractérisation physico-chimique et optique de nanocristaux fluorescents pour des applications biomédicales

Le développement des nanoparticules fluorescentes, appelées quantum dots (QDs) est devenu l'un des domaines les plus prometteurs de la science des matériaux, influençant fortement la société moderne en raison de leurs nombreuses applications allant de la production d'énergie au diagnostic de maladies et à l'administration de médicaments. Ces dernières années, beaucoup d'efforts ont été consacrés à la résolution des problèmes se rapportant aux technologies liées aux QDs, telles que la réduction de leur taille, la maximisation du rendement quantique et la stabilité colloïdale dans les solutions biologiques. Dans cette étude une procédure avancée de synthèse contrôlable de QDs a été mise au point, comprenant (1) la synthèse de noyaux ultra-minces de CdSe, (2) la purification de noyau haute performance par la chromatographie de perméation de gel et (3) le revêtement central avec une coquille épitaxiale en ZnS d'une épaisseur déterminée. Cette approche a permis d'obtenir des QDs d'une taille de 1,5 nm possédant un rendement quantique supérieur à 70% et également d'améliorer considérablement leurs propriétés colloïdales. Les QDs développés ont été utilisés : (1) pour concevoir des conjugués de QDs compacts avec les nouveaux dérivés d'acridine synthétisés dans cette étude, ayant une affinité élevée pour le G-quadruplex des télomères; (2) pour démontrer l'efficacité fonctionnelle des conjugués lors des essais avec des acides nucléiques et des cellules, ainsi que leur effet inhibiteur sur la télomérase, une cible importante du traitement du cancer; et aussi (3) pour accélérer la pénétration transmembranaire des QDs ultracompacts dans les cellules monocytes tout en conservant une brillance élevée et une stabilité colloïdale. Les résultats de cette étude ouvrent la voie à l'ingénierie de nanosondes multifonctionnelles possédant une meilleure pénétration intracellulaire, une plus forte brillance et une stabilité colloïdale plus importante, permettant leur utilisation dans une multitude d'applications allant de l'administration de médicaments au diagnostic.

Mots clés : nanocristaux photoluminescents, « quantum dots », acridine, G-quadruplex, bioconjugaison, nanoprobés multifonctionnelles

The synthesis and physico-chemical and optical characterisation of fluorescent nanocrystals for biomedical applications.

Development of the fluorescent nanoparticles referred to as quantum dots (QDs) has become one of the most promising areas of materials sciences, strongly influencing modern society due to their numerous applications ranging from disease diagnostics to drug delivery. In recent years, much effort was concentrated on solving problems of QD-related technologies, such as minimizing their size and maximizing the quantum yield and colloidal stability in biological solutions. In this study, an advanced procedure of controllable synthesis of QDs, which includes (1) the synthesis of ultrasmall CdSe cores, (2) high-performance core purification by gel permeation chromatography, and (3) core coating with an epitaxial ZnS shell of a specified thickness has been developed. This approach has allowed obtaining 3.7 nm QDs with a quantum yield exceeding 70% and significantly improved their colloidal properties. The QDs developed have been used: (1) to engineer compact conjugates of QDs with the novel acridine derivatives synthesized in this study, which have a high affinity for the telomere G-quadruplex; (2) to demonstrate the functional effectiveness of the conjugate in tests with nucleic acids and cells, as well as their inhibitory effect on telomerase, an important target of anticancer therapy; and (3) to accelerate transmembrane penetration of ultrasmall QDs into monocyte cells while retaining a high brightness and colloidal stability. The results of this study pave the way to engineering of multifunctional nanoprobés with improved intracellular penetration, brightness, and colloidal stability, which will find use in a plethora of drug delivery and diagnostic applications.

Keywords : photoluminescent nanocrystals, quantum dots, acridine, DNA ligands, G-quadruplex, bioconjugation, multifunctional nanoprobés.

Discipline : CHIMIE

Spécialité : Pharmacie - SFS

l'Université d'Etat de Moscou

Laboratoire de thermochimie Département de
Chimie

1-3 Leninskiye Gory, 119991, Moscou, Russie



Université de Reims Champagne-Ardenne –

LRN - EA 4682

51 Rue Cognacq-Jay, 51100, Reims, France